Università degli Studi di Cagliari

Ph.D. degree in Chemical Science and Technology

Cycle XXXIII

Luminescent platforms for metal ions sensing

Scientific Disciplinary Sector:

CHIM/03 – Inorganic Chemistry

Ph.D. Student:	Mariangela Oggianu
Ph.D. Coordinator:	Prof. Stefano Enzo
Supervisors:	Prof. Maria Laura Mercuri
Co-supervisor:	Prof. Vito Lippolis Prof. Francesco Quochi

Final exam. Academic Year 2019 – 2020

Thesis defence: May 2021 Session

“Learn from yesterday,
live for today,
hope for tomorrow”

Albert Einstein

To my mum

Acknowledgements

I would like to thank my supervisors that guided me through these three years, Prof. Maria Laura Mercuri, Prof. Vito Lippolis and Prof. Francesco Quochi. I have appreciated your help, support and guidance on my PhD project.

A special thank is mandatory to Prof. Mercuri: you have believed in me even though I was a complete stranger in your lab. Your constant support, especially in the thesis writing, helped me to reach this goal without by sharing many hours of writing together on Skype.

I would like to thank Prof. Enzo Cadoni for his support and for helpful advices.

I thank Dr. Alessandra Garau for her guidance at the beginning on my PhD, for showing a pharmaceutical chemist how to move the first steps towards the sensing and supramolecular fields. I would like to thank Prof. Claudia Caltagirone for giving me the possibility to work in her lab.

Even though my time in Angers was drastically reduced due to the beginning of the pandemic, I would like to thank Prof. Narcis Avarvari for opening me the doors of his lab, for making me feel welcomed and for finding always time to discuss together about the project.

Table of Contents

GLOSSARY

A

AAS	Atomic Absorption Spectrometry
AFM	Atomic Force Microscopy
An	Anilate
APTES	3-aminopropyltriethoxysilane

C

CA	Contact Angle

D

DPP	Diketopyrrolo-[3,4-c]Pyrrole
DR	Diffuse Reflectance

E

EDTA	Ethylendiamine tetracetic acid
EPA	Environmental Protection Agency
ESI	Electrospray Ionization

F

FDA	Food and Drug Administration
FLUO	Fluorescein
FITC	Fluorescein isothiocyanate
FRET	Fluorescent Ratiometric Energy Transfer

I

ICP-AES	Coupled Plasma Atomic Emission Spectrometry
ICP-MS	Inductively Coupled Plasma Mass Spectrometry
ICT	Intramolecular Charge Transfer

K

KHClCNAn	Potassium chlorocyananilate

L

Ln	Lanthanide
LnCPs	Lanthanide Coordination Polymers
LnMOFs	Lanthanide Metal Organic Frameworks

M

MOF	Metal-Organic Framework
MOPS	3-N-morpholino-propansulfonic acid

N

NS	Nanosheets

P

PL	Photoluminescence

R

RFPs	Ratiometric Fluorescent Probes
RhO6G	Rhodamine 6G
RhOB	Rhodamine B

T

TDPP	Thiophene diketopyrrolo-pyrrole
TEOS	Tetraethoxysilane

W

WHO	World Health Organization

ABSTRACT

This work reports on the strategies for the design of novel luminescent chemosensors as valid alternative to conventional optical sensors, to recognize environmental pollutants, mainly heavy metal ions and nitroaromatics. Luminescent lab-on-chip devices, molecular and hybrid chemosensors and luminescent Nanosheets are the three platforms developed for sensing applications. Fluorescent dyes of the family of Xhantenes, Rhodamine (RhO) and Fluorescein (Fluo), Diketopyrrolopyrroles (DPPs) and 2,5 -dihydroxy-1,4-benzoquinone derivatives are the *old-fashioned* and *new* building blocks selected to fabricate these optical sensors, because of their unique luminescent properties. Rho, Fluo and thiofene diketopyrrolopyrrole (DPPT) are organic dyes emitting in the Visible region, that can be easily tailored by conventional organic synthetic methods, in order to interact selectively with a specific analyte. 2,3-dicyano-5,6-dichloro-1,4-benzoquinone, instead, was selected for it capability *i)* to produce two dimensional (2D) Coordination Polymers/Metal-Organic Frameworks (CPs/MOFs) and *ii)* to act as a good antenna ligand towards NIR and Vis. emitting Lanthanide ions. 2D CPs/MOFs, based on this linker, were obtained and miniaturized to 2D Nanosheets, which are challenging sensing platforms. The road map of the research is presented below.

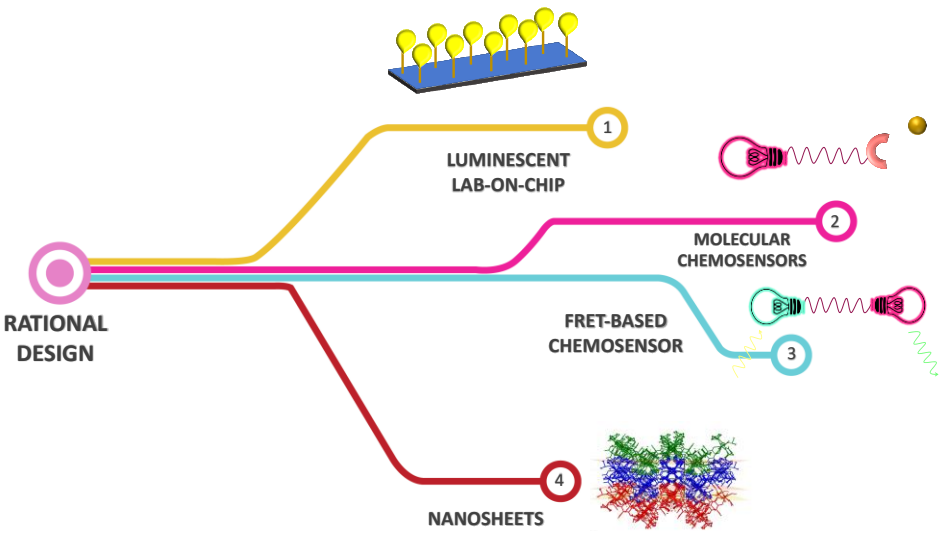

In **Chapter 2**, the design and the development of fluorescent silicon chips platforms for the selective recognition of copper ions in water solution, have been reported. Silicon chips were first functionalized with amino groups and Fluorescein organic dyes, used as sensing molecules, then covalently linked to the surface, *via* formation of thiourea groups. The fluorophore-analyte interaction mechanism at the basis of the reported fluorescence quenching, as well as the potential of performance improvements of the obtained sensing platforms, were also studied. The propose platform architecture, where recognition/fluorescent units are integrated on a silicon chip *via* a layer-by-layer functionalization approach, is very versatile owing to the possibility of fine tuning the selectivity towards other metal ions or different types of analytes by changing the fluorophore or the anchoring group.

In **Chapter 3,** a hybrid ratiometric fluorescent chemosensor, consisting of a dansyl moiety as donor unit and a rhodamine moiety, as acceptor unit, is reported. The proton-hybrid ratiometric platform interaction is studied in a wide range of pH, *via* a multi-technique approach, involving Uv-Vis Absorption, Photoluminescence (PL) and time-resolved PL Spectroscopy, Mass Spectrometry and potentiometric titrations. All experimental results are supported by Density Functional Theoretical (DFT) calculations. The proton mediated rhodamine spirolactam/ring-opening mechanism and the photophysical mechanism (FRET) at the basis of donor-acceptor units energy-transfer, in the hybrid ratiometric platform, is inferred by combining simoultaneously spectrophotometric and potentiometric titrations with DFT.

Chapter 4 is mainly focused on the research performed at the University of Angers, Laboratoire Moltech Anjou, under the supervision of Prof. N. Avarvari and, unfortunately, interrupted for COVID-19 emergency (1.5 months research stay over 5 months expected). Several molecular fluorescent chemosensors based on DPP derivatives, which represent a novelty in sensing field, have been synthesized and fully characterized. Their luminescence properties were also investigated in order to select the most promising derivatives to be anchored to various platforms, such as nanoparticles or silicon-based chips. This represents a viable and innovative strategy towards the fabrication of prototype devices for remote detection of a range of metal ions in water.

Chapter 5 reports on the use of Nanosheets technology as a challenging sensing technique, which provides a highly sensitivity and fast response towards a target analyte, specifically

nitroaromatics. Nanosheets of two mixed linkers (anilate/carboxylate)/Yb^{III}-based 2D layered CPs are reported. They are produced by exfoliation of bulk size CPs by the well-known top-down approach and characterized by Atomic Force Microscopy and High-Resolution Transmission Electron Microscopy. Remarkably, the powder X-ray diffraction patterns highlight that the crystallinity is retained at the nanoscale level. Nanosheets photophysics is investigated by an innovative Multiprobe Approach where lifetime, photoluminescence (PL) and integrated PL are simultaneously measured in order to study how these parameters can be affected by the presence of the different ligands. The present work contributes to the ongoing research on fabricating robust and crystalline luminescent hybrid (organic/inorganic sheetlike 2D sensing nanoplatforms.

Chapter 1

General Introduction

1.1 Fluorescent Materials

Global urbanization and industrialization are the major causes of ever-growing environmental pollution, which has become a huge threat for every living system.[1] Among various kinds of environmental pollution, water pollution has considered as one of lethal issues in recent years, mainly originated from anthropogenic sources such as industrial waste, resource mining, the use of fertilizers and pesticides, burning of fossil fuels *etc.*. Word Health Organization (WHO) has estimated that contaminated water cause almost 48500 deaths every year.[2] There are several typologies of pollutants in contaminated waters and among them chemical pollutants are the most toxic and dangerous.[3] Chemical pollutants are classified in two main categories, organic and inorganic. Depending on their charge, the organic ones can be classified into cationic, anionic and neutral; the commonly used herbicides, paraquat and diquat[4] have been considered as extremely toxic water pollutants among the organic cations. Inorganic pollutants, mainly oxyanions and/or inorganic metal cations such as heavy metal ions, including metal transitions cations, are generally more persistent in the environment than organic contaminants, therefore, when these pollutants enter the water supply, this becomes a serious problem due to their ill-effects, especially their toxicity to humans and wildlife, at ppm or even ppb level concentrations. In particular Hg^{II}, Pb^{II} and Cd^{II} [5,6], have attracted tremendous attention due to their lethal effects, while Zn^{II}, Cu^{II}, Fe^{II}, Fe^{III} [7–9] can also cause several issues when they are presents in excess of their law limits. Several traditional techniques are currently employed to recognize different kind of cationic pollutants in aqueous and biological environments, such as Inductively Coupled Plasma Atomic Emission Spectrometry (ICP-AES), Inductively Coupled Plasma Mass Spectrometry (ICP-MS) and Atomic Absorption Spectrometry (AAS). These techniques provide excellent detection limits but their practical applications are usually hampered by high-cost instrumentation, time-consuming sample preparation and highly trained personnel.[10–12] A valid alternative detection technique for sensing applications.[13–15] is photoluminescent (PL) spectroscopy,[16] given its advantageous features including high sensitivity, fast response, ability to detect low concentrations of analytes, and simple operations. Optical sensors are very well established, dating back to

the 1930s and they involve the reaction of a chemically selective substrate with a species of interest, to produce changes in the optical properties of the sensor. This may be a change in absorbance or fluorescence intensity and is typically detected colorimetrically or spectrally. Optical transducers exploit properties such as light absorption, fluorescence/phosphorescence, etc.[17] A *plethora* of materials has been developed as optical sensors and among them, molecular chemosensors, including FRET-based fluorescent probes up to luminescent lab-on-chip devices and luminescent Metal Organic Frameworks (LMOFs), also up to the nanoscale (nanosheets, nanoparticles)[18–20] are appealing materials employed as suitable platforms to recognize metal cations in aqueous environment, due to their versatility and the possibility to tailor their building blocks and their optical properties by a suitable rational design.

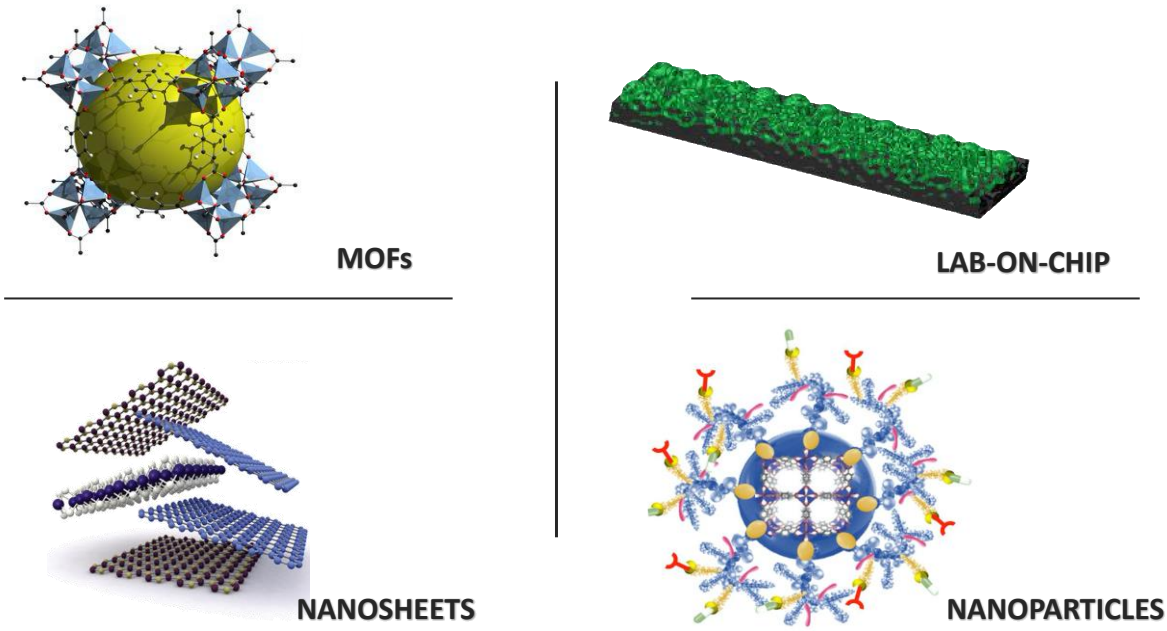

Figure 1. Selected Luminescent Materials.

Albert Einstein: "Learn from yesterday, live for today, hope for tomorrow."

1.2 Fluorescent Chemosensors

A chemical sensor is defined as "*a portable miniaturized analytical device"*, which can deliver *real-time* and *on-line* information in presence of specific compounds or ions in complex samples".[21] Chemical sensors can be divided into colorimetrical, fluorescent and electrochemical sensors, according to the type of signal transduction *i.e* color, fluorescence and redox potential.[22,23]

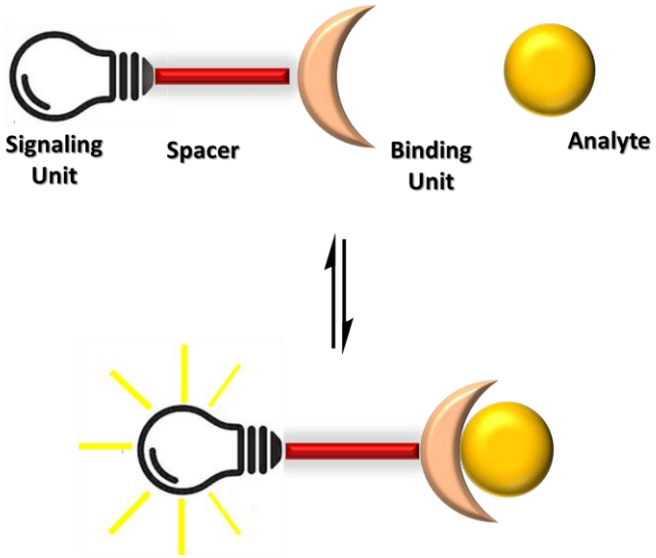

Figure 2. Interaction chemosensor-analyte.

Chemosensors based on fluorescence emission changes due to the interaction with a target substance, called analyte, are commonly known as fluorescent chemosensors,[22,26] whereas chemosensors involving the change in color upon binding with the specific analyte are termed as chromogenic or colorimetric chemosensors.[27]

Since the analyte detection occurs in two steps, *i.e*. molecular interaction and signal transduction, a chemosensor can be formed by three components, as reported in **Figure 2**: a recognition site or **receptor**, a **signaling unit** and a **spacer.**[7,25] The **receptor** should have the ability to bind selectively a specific target analyte. The formation of a selective receptor–analyte interaction depends on the size, shape and binding capability of the

receptor and the analyte compound. The **signaling unit** is an active component, whose properties should change upon interaction between receptor and analyte. In particular it measures the change in fluorescence/absorption intensity and/or wavelength and intensity decay lifetime. The **spacer** can lead to geometry modifications in the system, tuning the electronic interaction between the two former moieties. In the signal transduction step the receptor-analyte interaction is converted to a signal change that can be read and quantified by the signaling unit. Fluorescent chemosensors present remarkable advantages over conventional sensors, such as fast response times, high sensitivity and versatility in their synthesis through classical methods of organic chemistry.[28] In fact the proper choice of the fluorescent moiety can tailor the interaction with the analyte. Fluorescent dyes are often used as **signaling unit**. They are organic molecules that absorb/emit in a wide spectral range from ultraviolet (UV), Visible (Vis) up to near infrared (NIR).[29] Fluorescent dyes such as pyrene, cyanine, fluorescein, rhodamine, coumarin, BODIPY and diketopyrrolopyrrole (DPP) (**Figure 3**), are often used to fabricate fluorescent chemosensors providing a wide range of emission from UV to NIR region, where the analyte detection is achieved through one or more common photophysical mechanisms, including photoinduced electron transfer (PET),[30] fluorescence resonance energy transfer (FRET),[31] internal charge-transfer (ICT),[32] chelation induced enhanced fluorescence (CHEF).[33]

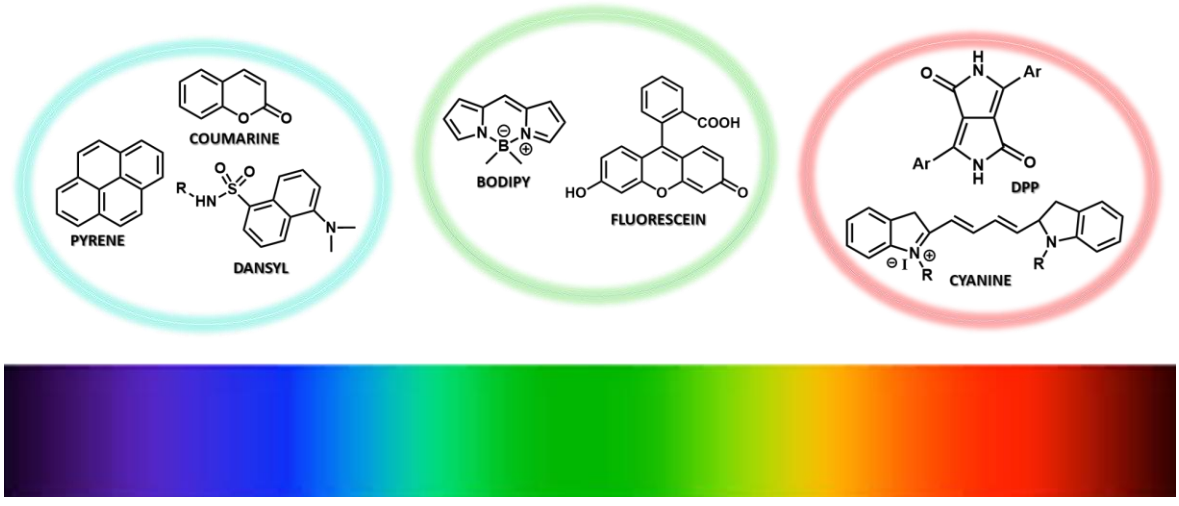

Figure 3. Structures of commonly used dyes to fabricate fluorescent chemosensors.

Pyrene, Coumarin and Dansyl derivatives are UV emitters, while BODIPY, Fluorescein, Rhodamine and DPP derivatives emit in the Vis and cyanines in the NIR region, respectively. Their different photophysical properties along with the possibility to tune their chemical make-up are fundamental prerequisites for choosing their specific application, by properly tailoring the dye for a specific target analyte. For example, amine-reactive probes are widely employed to modify proteins, peptides or other biomolecules[34] while functionalization of the dyes (*vide supra*) with isothiocyanate may be used to obtain, *via* thiourea formation, a covalent linkage to a solid support.[35] Furthermore the substituents on a fluorescent dye play a crucial role in fine tuning its emission intensity. For example, Rhodamine 6G and Rhodamine B, differing for the presence of a methyl group on the xanthene ring, exhibit different fluorescent properties.[36] Despite the progress made in the long-lasting field (about 150 years) of fluorescent chemosensors, several problems and challenges still exist. In fact, over the years, they have been increasingly applied in a wide variety of fields such as biology, physiology, pharmacology, diagnostic medicine and environmental sciences. In particular, enormous efforts have been addressed to design and synthesize fluorescent sensors able to recognize metal cations in aqueous environment, due to the key role that metal cations occupy in several aspect of human life.[37–39]

An overview on selected old-fashioned and new fluorescent dyes and analytes is presented in the following.

1.2.1 The Family of Xanthenes

Rhodamine and Fluorescein, the typical representatives of xanthene family, have been paid much attention in the design of fluorescence materials, due to their excellent photophysical properties including photostability, high molar absorption coefficient, high fluorescent quantum yield.[40,41] Rhodamine and Fluorescein are characterized by the presence of the tricyclic xanthene core (**Figure 4a**), consisting of a pyran heterocycle, as a central ring, fused to benzene rings on both sides of the molecule.

The main differences between Rhodamine and Fluorescein are the substituents on the xanthene core: amine groups are present in Rhodamine while Fluorescein possesses hydroxy groups as shown in **Figure 4b**, where Fluorescein and Rhodamine B and 6G are reported. The carboxyl group can be easily transformed to spirolactam or spirolactone ring, which could be employed as molecular scaffold to fabricated sensing probes.

Rhodamine was first synthesized in 1905, by Noelting and Dziewonsky, [42] but it was only in 1997 when Czarnik *e al.* presented the first example of rhodamine derivative able to act as sensing probe towards copper(II).[43] Since then, Rhodamine derivatives have been largely employed for the detection of several analytes. [44–46]

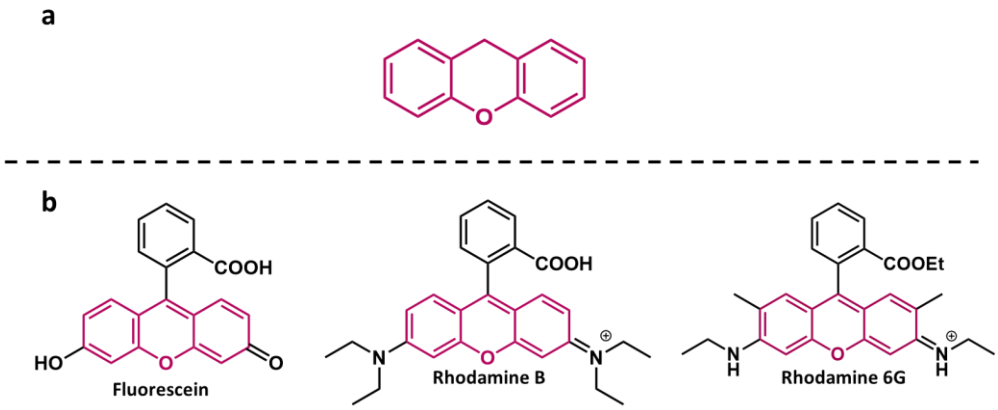

Figure 4. Molecular structures of the xanthene (a) and xanthene derivatives (b).

Rhodamine spirolactam/spirolactone derivatives are nonfluorescent and colorless, due to the separation of the xanthene ring from the aromatic ring, by a tetrahedral spiro carbon, whereas the ring-opening form gives rise to strong fluorescence emission and a red/pink color.[40,47] In general, a Rhodamine derivative shows a color change in acidic conditions or by adding specific metal ions, *via* activation of carbonylic group in the spirolactam moiety, as shown **Figure 5**.

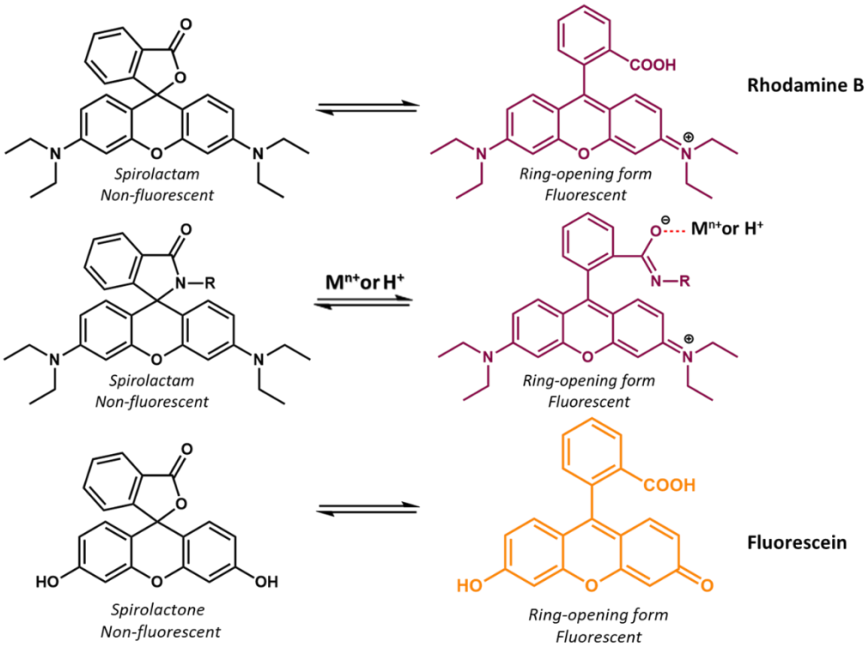

Figure 5. Ring-opening of spirocyclic xanthene.

Yoon *et al.* reported on a novel Rhodamine derivative for sensing Pb^{II} metal ion, exhibiting selectivity, among various metal ions, only for Pb^{II}, *via* fluorescence enhancement. The complexation has been confirmed by ESI Mass Spectrometry, NMR and IR Spectroscopy.[48] A novel dimeric system based on rhodamine derivatives with urea groups has been reported, showing selectivity towards Hg^{II}, through a fluorescence enhancement and colorimetric change due to the spirolactam opening, by interaction with urea groups.[49] A derivative based on rhodamine and benzothiazolinone has been synthesized by Peng's group for the recognition of Cu^{II} ions.[50] The interaction with copper ion led to an enhanced fluorescence emission and an absorption increase, due to the transformation of closed spirolactam to ring-opening form. This compound showed good selectivity, low detection limit, fast response and, interestingly, this system could recognize Cu^{II} ions in living cells.

Kan *et al.* designed and synthesized a Fe^{III}-specific probe, by reacting rhodamine B and ethylenediamine and, in a second step, the obtained product with pyridine-3-sulfonyl chloride, affording the N-TC probe.[51] N-TC exhibits the reversible ''turn-OFF-ON" fluorescence response to Fe^{III} in the EtOH/H_2O solution (1:1, v/v, HEPES, 0.5 mM, pH = 7.38), with high binding constant (1:1, binding stoichiometric ratio) and low detection limits. ^1H NMR titration experiments highlighted a downfield shift of proton in the xanthene ring, due to Fe^{III}-induced ring opening process. Interestingly N-TC was proven to be highly sensitive in monitoring trace Fe^{III} in environmental water specimens and in the detection of Fe^{III} in in living cells, animals and plant tissues, as demonstrated by biological experiments.

Fluorescein was first synthesized by von Bayer in 1871 and, since then, it has found many applications in several fields, particularly in biomedicine, fluorescent-labeling technology for bioanalytical purposes and environmental sciences.[52] Similarly to Rhodamine, Fluorescein derivatives are nonfluorescent in the lacton form and the ring opening form induces color change and fluorescence enhancement. Fluorescein has been largely employed as pH sensor since its photophysical properties are strongly pH-dependent.[53] Under acidic conditions Fluorescein is nonfluorescent, as the spirocyclic form dominates, while in basic or neutral conditions its ring-opening form, which is fluorescent, is present. Thus, when pH values of the environment decrease (for instance, from neutral to acidic conditions), Fluorescein derivatives show a fluorescence quenching signal (turn-OFF

process).[54] Fluorescein has been successfully used in the detection of transition metal ions in aqueous solutions and living cells,[55,56] while its derivatives containing thiocarbamide moiety have been used to bond thiophile metal ions (e.g. Ag^{I}, Hg^{II}).[57] Despite its excellent photophysical properties, the use of Fluorescein in developing molecular fluorescent chemosensors is limited, when compared to Rhodamine, due to the versatility in tailoring the chemical make-up of the latter. Instead, recent work highlights the capability of Fluorescein derivatives, mainly Fluorescein isothiocyanate (FITC), where Fluorescein has been functionalized with an isothiocyanate group (-N=C=S) and carboxy Fluorescein (-COOH), bearing a carboxylic group, to be covalently anchored to suitable solid supports for fabricating innovative fluorescent sensing platforms (*vide infra*).

1.2.2 Fluorescent detection platforms

Several fluorescent platforms have been developed, in recent years, for detection and/or monitoring of different chemical pollutants, especially heavy metal ions or small neutral molecules like nitroaromatics (explosives). The formers are essential for human survival, since they play a vital role in a range of physiological and pathological processes, conversely the latter threat to homeland safety and public health.

Zhang *et al.* reported on a fluorescent chemosensor where a dye-functionalized metal-organic-framework (MOF) is used as innovative detection platform toward silver metal ions in aqueous solution. The FITC-containing MOF, FITC@BTPY–NH_2 ([BTPY–NH_2 = $Zn_6(btb)_4(bipy–NH_2)_3$; btb = benzene-1,3,5-tribenzoate, bipy–NH_2 = 3-amino-4,4'-bipyridine) was synthesized, by post-grafting approach, by covalently binding FITC, *via* thiourea formation, to the large porous BTPY–NH_2 MOF. The FITC@BTPY–NH_2 performance has been tested in presence of various cations, showing high sensitivity towards Ag^{I}. This dye-functionalized MOF platform is very challenging, since it could be used in the selective and sensitive sensing of thiophilic metal ions in aqueous media. Furthermore, due to its heterogeneous features, it can be used in the separation, removal and enrichment of heavy-transition metal ions from drinking water.[58] By a similar approach, Zong *et al.*, fabricated a detection platform with selectivity toward Cu^{II} ions, based on fluorescent silica nanoparticles (NPs) where FITC has been grafted on the NPs surface by covalent linkage formation. The interaction between NPs and copper induces a fluorescence quenching

(turn-OFF) through the FRET mechanism.[59] Very recently, magnetic core-shell silica NPs (Fe_3O_4@SiO_2-NH_2) have been functionalized with Fluorescein. The obtained nanoplatforms showed a significative quenching in presence of Ni^{II} metal ions, with high selectivity and sensitivity, in neutral pH conditions. The performance of the nanoplatform has been evaluated in presence of different metal cations and biological macro-molecules, *i.e.* K^{I}, Na^{I}, Ca^{II}, Zn^{II}, Mn^{II}, Co^{II}, Ni^{II}, Fe^{II}, Fe^{III}, Pb^{II}, Cd^{II}, lysozymes and bovine serum albumin, showing its capability to detect Ni^{II} ion, at concentration as low as 0.8 nM.[60]

Ratiometric Fluorescent Probes (RFPs) are an emerging class of luminescent chemosensors that allow the simultaneous measurement of two fluorescent signals at different wavelengths. They are based on a photophysical mechanism, called Excitation Energy Transfer (EET), describing the energy transfer between two chromophores.[61] If both chromophores are fluorescent, the term Fluorescence Resonance Energy Transfer (FRET) is instead used. Upon photoexcitation, the electronic excitation energy of the Donor in its excited state can be transfer to the Acceptor in its ground state. FRET occurs if three prerequisites are satisfied: 1) the donor should have a high quantum yield; 2) the emission spectrum of the donor should overlap with the absorption spectrum of the acceptor; 3) the donor-acceptor distances should be less than 10 nm, through non radiative dipole-dipole coupling. Therefore, FRET is a process of non-radiative energy transfer through long-range dipole–dipole interactions between the donor–acceptor pair.[31,62] Generally, fluorescent platforms based on FRET mechanism are linked by a non-conjugated spacer, while probes characterized by a rigid conjugated linker are based on through-bond energy transfer (TBET) mechanism [63,64] (**Figure 6**).

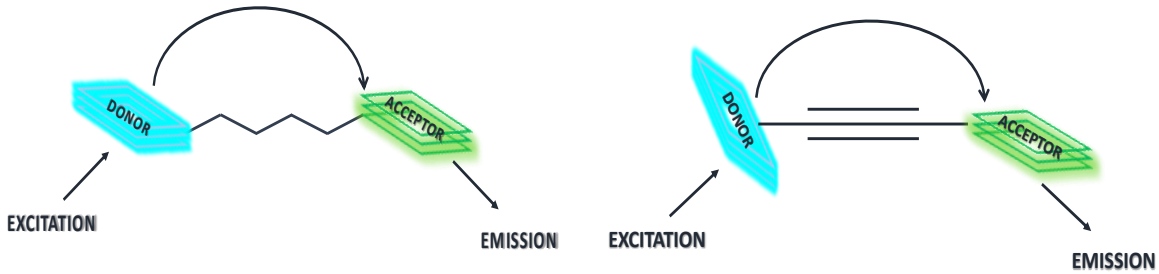

Figure 6. a) FRET and b) TBET energy transfer mechanisms.

The general strategy to fabricate FRET-based fluorescent probes is anchoring the donor–acceptor pair in close proximity in one single system or molecule. To fabricate the final FRET platform, a reactive unit, that can be used as a specific recognition group, is introduced synthetically. When FRET platforms interact with specific target analytes, the FRET process is initiated/prevented leading, as result, to a change in fluorescence signal which confirm the presence/absence of the target analytes. Initially, there is a little overlap between the absorption band of the non-fluorescent acceptor and the emission band of the donor. When the target analyte interacts with the non-fluorescent form of the acceptor a shift of the absorption band of the acceptor is observed, increasing overlap with the emission band of the donor and favoring FRET.

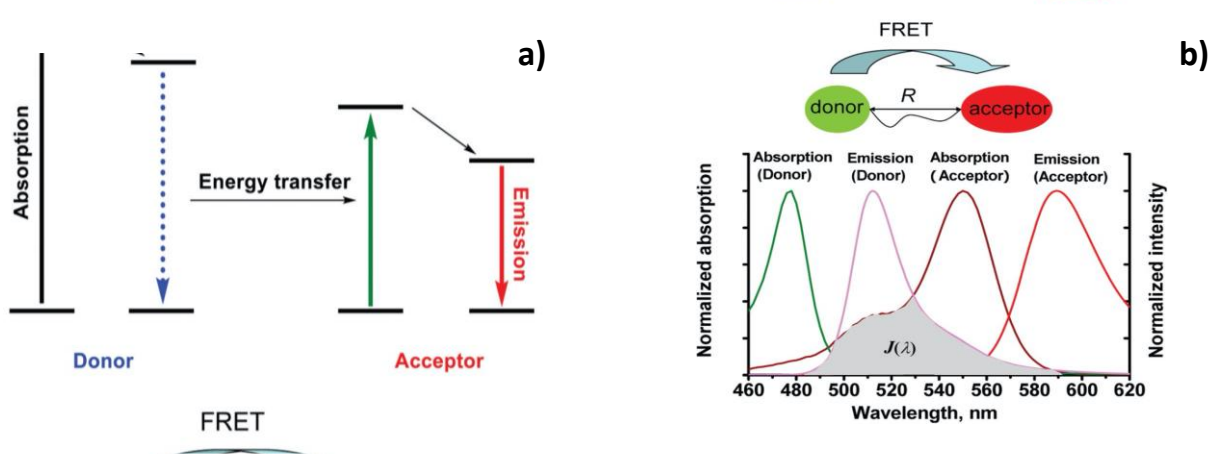

Figure 7. a) The mechanism of Förster resonance energy transfer (FRET). R is the distance between the energy donor and acceptor, J(λ) represents the degree of spectral overlap between the donor emission and the acceptor absorption. Reproduced with permission from ref.[65]

BODIPY, Fluorescein, Rhodamine and Coumarin are the main fluorophores used in the construction of FRET scaffolds. Particularly, rhodamines have attracted ever-growing interest as energy acceptors, given their excellent photophysical properties, *i.e.* absorption and emission bands at longer wavelength (*c.a* 580 nm), high fluorescence quantum yields and large molar absorption coefficients. Moreover, they can undergo fuorescence enhancement *via* a structural change from the spirolactam (non-fluorescent) to the ring-open (fluorescent) form, induced by the target analyte. Rhodamine is a convenient platform to construct "OFF–ON" ratiometric chemosensors, with naphthalimide[62] and

coumarin as energy donors and currently several Rhodamine-based FRET platforms have been successfully designed, synthesized and applied. Luxamy *et al*[66] synthesized a reversible probe for the recognition of Hg^{II} where Naphthalimide and Rhodamine were covalently linked to form a donor-acceptor platform. The system displays a blue emission centered at 485 nm due to naphtalimide unit. The addition of Hg^{II} to the solution induces a gradual intensity decrease of the emission peak at 485 nm and an increase of the intensity peak at 585 nm, due to spirolactam opening of Rhodamine, consistent with a turn-ON FRET process. In 2015, Goswami *et al*. developed a FRET platform able to recognize Cd^{II}, consisting of a quinoline benzothiazole unit as donor and rhodamine unit as acceptor. As prepared, the probe showed a band at 470 nm, that was ascribed to the emission of the quinoline–benzothiazole fluorophore, thus suggesting that Rhodamine moiety is present as non -fluorescent spirolactam. After the addition of Cd^{II} a new absorption band at 565 nm appeared, indicating the spirolactam ring-opening of the rhodamine moiety. Moreover, the shift of the emission peak from 485 nm to 585 nm confirmed the energy transfer (FRET process) between donor and acceptor.[67] Yu *et al*. reported on a FRET fluorescent platform for the recognition of Copper, consisting of napthalimide donor and Rhodamine acceptor. The probe exhibited an emission peak at 525 nm, due to napthalimide donor. Upon addition of copper, the intensity of the peak at 525 nm decreased and, gradually, the intensity of the new band at 580 nm, attributed to the ring-opening of spirolactam, increases, confirming the turn-ON FRET process.[68]

1.2.3 Family of Diketopyrrolo-pyrrole

Diketopyrrolopyrrole (DPP) was discovered by Farnum et al in 1974.[69] DPPs are organic dyes based on dilactam 2,5-dihydropyrrolo [3,4-c] pyrrole-1,4-dione (**Figure 8**) and two flanked aromatic rings. The DPP chromophoric unit presents several reactive centers including *i)* aryl rings that undergo electrophilic and nucleophilic substitutions, and *ii)* the bicyclic lactam unit containing three different functional groups C=C double bonds, carbonyl groups and secondary amine that undergo several synthetic modifications.[70]

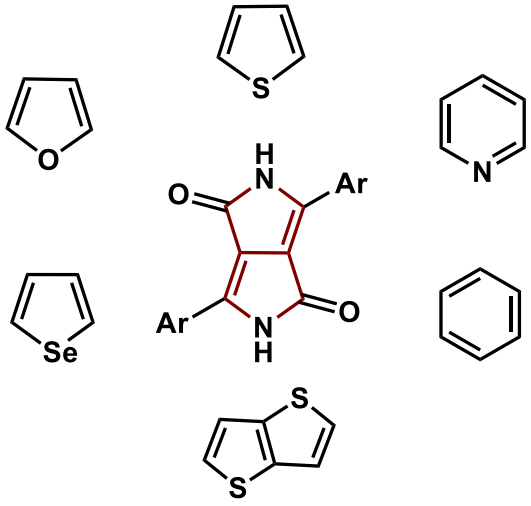

Figure 8. Some Ar-DPP derivatives (Ar=benzene, pyridine, thiophen, furane, selenophene thienothiophene).

The bicyclic symmetric system contains 8 π-electrons that generate π–π stacking intermolecular interactions, while the two lactam units are able to originate hydrogen bonds between the NH and C=O groups. The strong intermolecular interactions are the cause of the insolubility of DPPs in most common solvents (110 mg/L in DMF, at 25 °C) and of their consequent chemical *inertia*;[71] furthermore, they are characterized by a high melting point (> 350 °C) and absorption in the visible: their solutions in N-methylpyrrolidone exhibit a maximum absorption centered at 504 nm, with a ε = 33000 M^{-1} cm^{-1}. In the solid state, instead, DPP shows, like most pigments, a bathochromic shift, due to the greater electronic density,[72] because of the intermolecular hydrogen bonds, with maximum absorption centered at 583 nm. Since DPPs derivatives show excellent electronic properties, good thermal and photostability, high quantum yield and high molar absorption coefficients, they have found application in several research field, ranging from semiconductor materials to organic solar cells.[73] To date, DPP-based high-performance materials have been largely developed, while the DPPs ability to recognize biologically important species still remains relatively underestimated. In last few years several research groups developed DPP-based systems for the recognition of heavy metal ions. In 2017 Liang *et al.*[74] fabricated a surfactant-free-micelle like organic nanoparticles (ONPs) to recognize Hg^{II} in aqueous solution. The interaction between the amine group (unit receptor) and the analyte allows for molecular aggregation leading to

fluorescence quenching and color change. Furthermore, the formation of the DPP complex with Hg^{II} was confirmed by ^{1}H NMR. The signal (singlet) at δ=11.39 ppm corresponds to -NH proton of DPP derivative. Upon interaction with Hg^{II}, the signal for the −NH proton disappeared, demonstrating the deprotonation of lactam moiety and the formation of a N−Hg−N bond, which is similar to that involved in the well-known thymine(T)−Hg−T model system.

1.2.4 Analytes

Metal Cations. Detection of metal cations is of great interest to many researchers in different fields including chemistry, biology, clinical biochemistry and environment sciences. Sodium, Magnesium, Calcium and Potassium are involved in some important biological processes such as muscle contraction, signal transduction, nerve impulse transmission *etc.*[75] Iron is the most abundant metal transition in the human body and it is involved in various physiological processes such as oxygen transport and electron transport in the mitochondrial respiration. A low iron concentration can cause several disorders: anemia, low blood pressure, diabetes and decreased immunity, however an excessive concentration into living cells leads to the reactive oxigen species (ROS) formation by free radical reaction. ROS are responsible to damage nucleic acids, proteins and lipids.[76,77] Zinc is the second most abundant metal ions in the human body and it is employed in several biological processes such as gene transcription, brain activity cellular transport, it is essential for the DNA synthesis during the cellular turnover in particular in gastric apparatus and immune system. A Zinc excess leads to some neurodegenerative disease, Alzheimer's disease epilepsy, ischemia, while its depletion leads to several malfunctions like growth retardation, diarrhea and sexual delayed.[78,79]

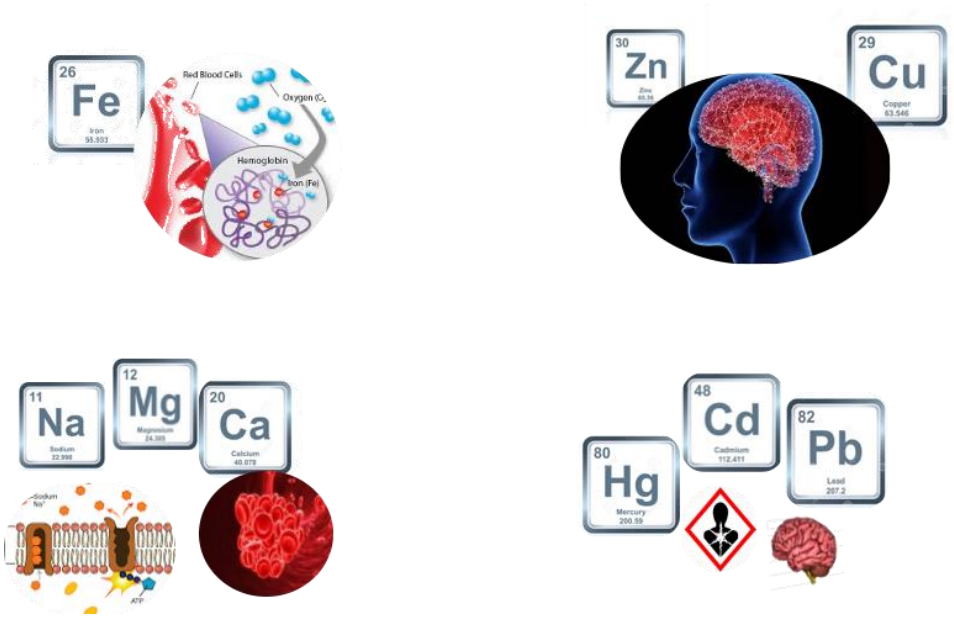

Figure 9. Graphical representation of biological process in which are involved metal cations.

Copper is the third most abundant metal ions in human body, taking part to various aspect of metabolism, including free radical detoxification, neurotransmitter synthesis, mitochondrial oxidative phosphorylation and iron metabolism. It is present in two oxidation states, either oxidized (Cu^{II}) or reduced (Cu^{I}). Cu^{I} is thought to be the dominant oxidation state of labile copper in cells, where this speciation is largely ascribed to the function of membrane reductases that reduce extracellular Cu^{II} prior to import as well as the reducing environment maintained within the cytosol. It is present in high concentrations in the environment and can leads to various disorders: Alzheimer's disease, amyotrophic lateral sclerosis, Menkes disease, Parkinson's disease, and Wilson's disease.[80,81] Lead, Cadmium and Mercury, well known as heavy metal ions, are highly soluble in the aquatic environments and they can be absorbed by living organisms. Once they enter the food chain, large concentrations of heavy metals may accumulate in the human body. They are highly toxic and do not play a useful role in the living body.[82,83] Among them lead is the most ubiquitous. Lead is largely distributed in air, soil and water due to widespread use in battery, gasoline and pigments. Low concentrations can cause several pathologies to human life including memory disruption, reduced IQs, physical growth impairments, anemia, particularly in young kids. Cadmium is a well- known metal used in industries such as batteries, paint, pigments, plastic, and electronic devices. An

excess of Cadmium concentration leads to several effect such as renal dysfunction, calcium metabolism disorders and increase of different forms of cancer. Mercury and its derivatives can be released from a variety industrial and natural sources such as agriculture, electronics industry, gold mining, and fossil fuel combustion, pharmaceutical industries.[84,85] Mercury is considered as the most hazardous and dangerous because of it is highly affinity to thiol groups in proteins and enzymes, causing several health problems. Elemental and ionic forms can be converted to metilmercury by microorganism in the environment, which accumulated into the body, causing several diseases including carcinogenic effect, nervus system and endocrine damage. To avoid toxic effects of heavy metal ions these metals have been forbidden for use in electronic devices by the European Union's Restriction of Hazardous Substances (RoHS). United States Environmental Protection Agency (EPA) and World Health Organization (WHO) have established allowable limits in potable water.

Nitroaromatics. Nitroaromatics are a family of organic compounds characterized by aromatic rings bearing one or more nitro (NO_2) groups. Most of nitroaromatics compounds have been synthesized, *i.e.* nitrobenzene, p-nitrotoluene, p-nitrochlorobenzene, whereas a limited amount of them are biosynthesized by Streptomyces bacteria.[86] Even though these compounds find a large application as pesticides, dyes and building blocks for polymers, they are very sensitive to heat and vibrations, therefore they can be considered like explosive materials. This feature was indeed exploited, especially in the military field. For example, 2,4,6-trinitrotoluene (TNT) is one of the most common explosive materials and it is used as a reactant to synthesize more complex explosives molecules. Other known explosives are 1,3,5-trinitroperhydro-1,3,5-triazine (RDX) and picric acid (PA). Given their chemical versatility and applications, nitroaromatics are involved in environmental pollution; they have been detected in different ecosystems and even in the human food chain. Their accumulation take place in the soil and underneath waters and although organic pollutants, they are quite persistence in the environment, due to the presence of the nitro group, which cannot be degraded in oxidative conditions. Moreover, some studies highlighted the possible mutagenic, cancerogenic and cytotoxic effect on human and other mammals, especially at epatic level. Their accumulation *in vivo* brings to the formation to the radical oxygen species (ROS) and to DNA damages. Therefore, many nitroaromatic compounds have been considered as dangerous for the human health and listed as

pollutants by the Environmental Protection Agency in the US.[87] Considered the high risk for the human health and the environment, a suitable detection technology is needed. In this context, the development of fluorescent platforms and/or sensor materials for rapid and selective detection of nitroaromatic, including chemical explosives, at trace levels, up to their removal from the environment, is of paramount importance for public health and homeland security.[88]

pH. Monitoring pH values is fundamental for understanding physiological and pathological processes in human body. It is also well known that intracellular pH plays an important role in many physiological processes, such as calcium regulation, cell-cycle progression and apoptosis, homeostasis and ion transport.[89] In normal conditions, the concentration of H^+ is 40 nM (pH 7.40),[90] but some pathologies, such as cancer or Alzheimer disease, are associated with abnormal pH values **(Figure 9)**. Traditional methods to measure pH, *i.e.* potentiometric titrations, nuclear magnetic resonance (NMR) and molecular spectroscopy, require expensive instrumentations, complex operations and possibility to have interference from other factors. Fluorescent chemosensors are finding ever-growing applications in numerous fields, such as analytical chemistry, bio-imaging,[91,92] and as biosensors, given the advantages of fluorescence spectroscopy, compared with traditional techniques (*vide supra*) such as high selectivity, sensitivity and rapid operations.

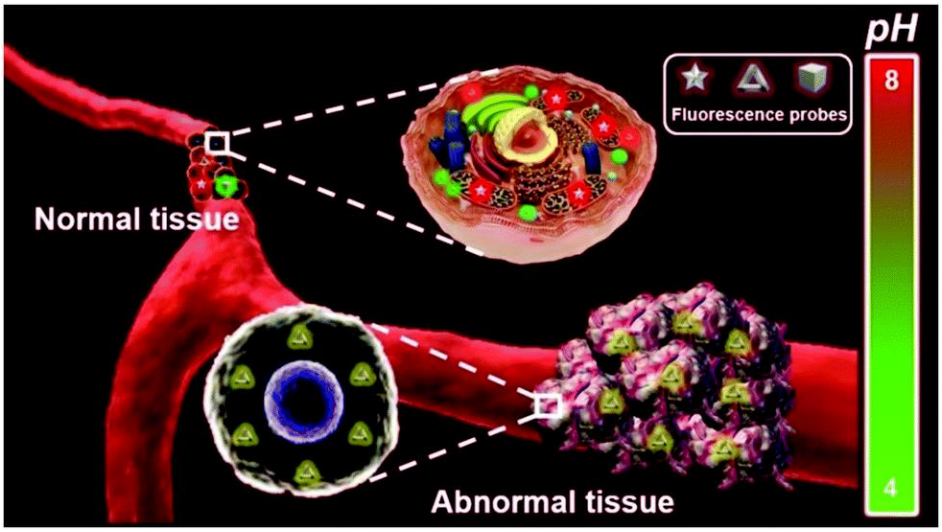

Figure 10. The illustration of fluorescent probes for imaging the physiological pH. . Reproduced with permission from ref [93].

1.3 Coordination Polymers and Metal-Organic Frameworks

Recently MOFs and CPs have attracted a great interest in sensing field because of the possibility to tailor their composition by a proper combination of multitopic organic ligands (linkers) and metal ions (nodes). According to IUPAC, a CP is *"A coordination compound with repeating coordination entities extending in 1, 2, or 3 dimensions"*.[94] The crystallinity degree is not a requirement for CPs. Generally, the prefix 1D, 2D and 3D, is used to indicate the dimensionality of the coordination network. The IUPAC definition for MOFs is "*A metal-organic framework, abbreviated to MOF, is a coordination network with organic ligands containing potential voids*".[94] Potential voids are important requirements to define a system as a MOF, but no physical measurements of porosity are demanded.

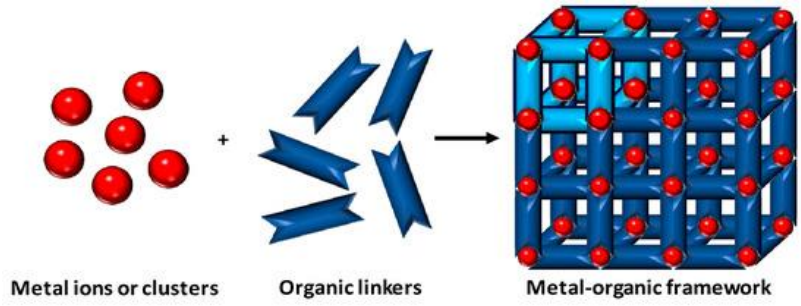

Figure 11. Schematic representation of a MOF[95].

Their large surface areas, tunable pore size, framework versatility in "tailor-made" functionalities endow MOFs to be promising candidates for applications in several field, spanning from gas storage, separation and sorption, catalysis, to biomedicine, up to chemical sensing. [96–99] **Figure 11** shows a schematic representation of their most appealing applications.

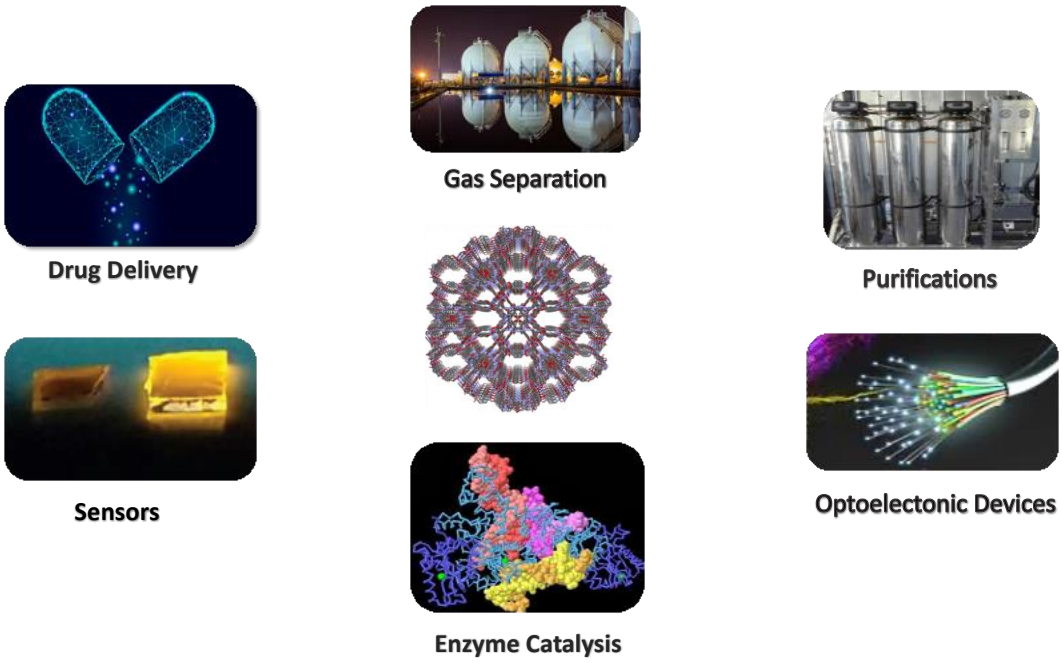

Figure 12. MOFs Applications.

Luminescent MOFs (LMOFs), as a subclass of MOFs, are an emerging class of luminescent materials employed in sensory.[98,100] Generally, the luminescent properties of LMOFs generate from metal nodes and organic linkers with aromatic or π-conjugated systems. Remarkably organic Ligands play a fundamental role in the photophysical properties of LMOFs. Especially π-electron rich ligands have been found to be able to absorb light and emit it via fluorescence or phosphorescence processes. Besides organic linker-based emission, metal ion-based emission has found to play a key role in LMOFs. In particular lanthanide-based MOFs (LnMOFs) have attracted ever-growing attention among LMOFs, because of the unique luminescent properties of lanthanide ions, such as long lifetime, characteristic sharp emissions, large Stokes shifts, and high color purity, with high quantum yields in the near-infrared and visible regions.[101,102] Optical properties of Lanthanide ions (Ln^{3+}) originate from the electronic configuration [Xe] $4f^{n}$ (n= 0 to 14). [103,104] Except La^{III} and Lu^{III}, Ln^{III} exhibit luminescent f-f emissions covering the entire spectrum, indeed Eu^{III}, Tb^{III}, Sm^{III}, and Tm emit in the visible region with the color red, green, orange, and blue, respectively; Pr^{III}, Nd^{III}, Sm^{III}, Dy, Ho^{III}, Er^{III}, Tm^{III}, and Yb^{III} show emissions in the near-infrared region, while Ce^{III} shows a broadband emission from 370 to 410 nm because of the 5d–4f

transition. Given the forbidden f-f transitions, Lanthanides are characterized by very low molar absorption coefficients and low quantum yield and consequent low emission properties, if excited directly. To overcome this problem, the lanthanide emission enhancement is possible by introducing an organic chromophore (molar absorption coefficient ~10^4) that transfer its energy to the lanthanide ion. This process is well known as Antenna Effect.[105]

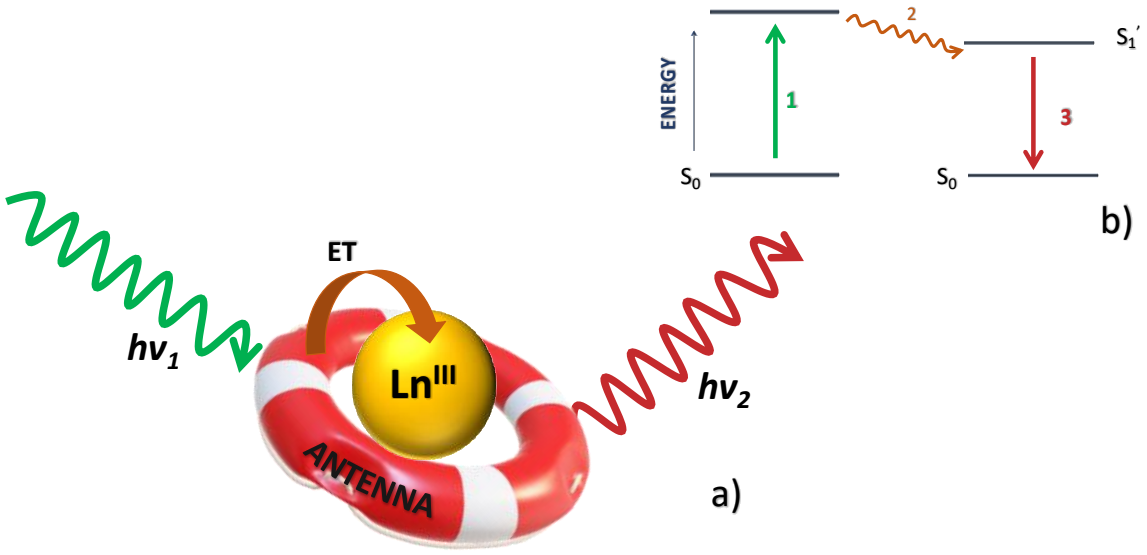

Figure 13. a) Scheme of indirect excitation mechanism of a Ln^{III} ion through an "antenna" ligand (hv_1= excitation energy; ET=energy transfer; hv_2=emission energy). b) Steps involved in the "Antenna Effect".

Antenna effect involves three different steps (**Figure 12**): *i)* the organic ligand absorbs light, upon excitation, at a certain wavelength and transits to triplet state (S_1-T_1); *ii)* the energy is transferred from the ligand to Ln^{III} *via* an intramolecular energy transfer; *iii)* Ln^{III} emits light of a different wavelength, by a radiative process.[106] LMOFs are generally fabricated through the following approaches: *i)* pre-synthetic or post-synthetic functionalization of MOFs; *ii)* inclusion of luminescent guests or luminophores inside the network and *iii)* the employment of ligands or emitting ions. All these approaches can be employed for sensing applications through the turn-OFF or turn-ON processes, induced by the interaction between the luminescent probe and a targeting analyte. Recently, Yan and co-workers anchored Eu^{III} ions on the UiO-66 (Zr)-$(COOH)_2$ MOF, through a post-synthetic strategy, to

obtain a turn-ON sensor. After the incorporation of Eu^{III} ions, a red emission was observed, which is confirmed by a five emission peaks at 591nm, 614nm, 650nm and 695nm. An enhancement in fluorescence was observed after interaction with Cd^{II}.[107] By a similar approach, a UIO-66-type MOF doped with Eu^{III} (isophthalic acid and 2,6-pyridinedicarboxylic acid and zirconium chloride served as the organic connectors and metal precursor, respectively) was prepared by a post-synthetic modification. The obtained LnMOFs exhibited good photothermal and luminescence stability in aqueous solution. As a luminescent probe, dispersion of this UIO-66-type MOFs can selectively recognize Hg^{II}, through a quenching of luminescence (turn-OFF process).[108] Fluorescein isothiocyanate (FITC) has been grafted on $[Zn_6(btb)_4(bipy–NH_2)_3$ *via* thiourea formation, to obtain a dye-functionalized MOF, FITC@BTPY–NH_2 (btb = benzene-1,3,5-tribenzoate, bipy–NH_2 = 3-amino-4,4'-bipyridine). The obtained system has been studied towards different cations, showing a turn-OFF response after the interaction with Ag^{I}.[58]

Despite numerous advantages of MOFs as luminescent probes, several studies demonstrated that sensing capabilities depend on diffusion processes of the analyte into the voids of the porous network, the interactions between functional sites and the target analyte leading to a slow response of the luminescent signal. Noteworthy, 2D MOFs have become a promising tool for sensing metal ions and biomolecules,[109–111] since the pioneering work of H. Zhang and Z. Zhang, on the use of nanosheets (NS), based on transition metal chalcogenides and graphene oxide, as luminescent challenging sensing platforms. Their high surface area/thickness ratio, ultrathin thickness, large surface area and more active sites on the surface are crucial elements to obtain suitable nanoplatforms with high sensitivity and fast response towards target analytes (**Figure 13**), when compared with other luminescent sensors.[111,112]

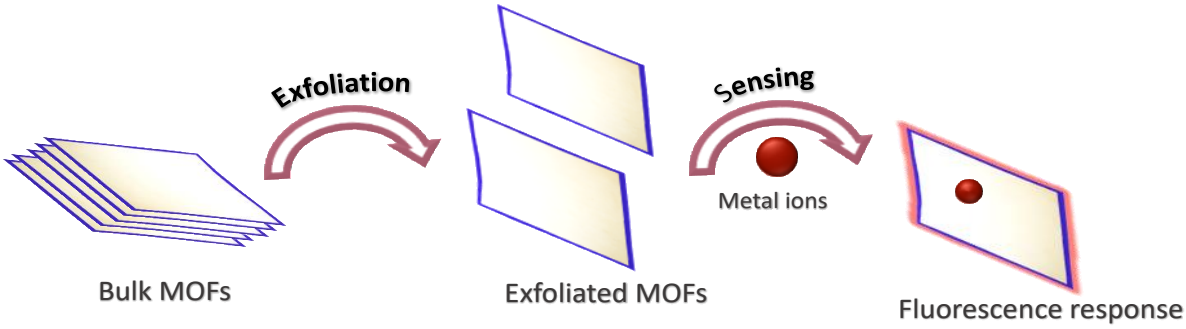

Figure 14. Schematic illustration of the fabrication of a fluorescent probe based on Nanosheets.

In 2016, Hui Xu *et al.* reported on the first example of luminescent NS based on 2D MOF containing 2,5-dihydroxyterephthalic acid (H_2DOBDC). This material was exfoliated by a top- down approach to obtain luminescent NS capable to recognize metal cations in aqueous environment. In particular these NS have shown, a high sensitivity and an ultra-fast response time (10 seconds) towards Fe^{III}, by a luminescent turn-OFF process, in comparison with conventional fluorescent probes.[113]

To date, the design of new luminescent probes based on NS technology is a challenging and innovative topic, that should be explored in order to fabricate highly sensitive and fast reponsive sensor prototypes for the recognition of environmental pollutants.

Among the organic linkers, derivatives of 2,5 dihydroxybenzoquinone, hereafter called anilates, have shown the abilities to build 2D CPs/MOFs with conducting and/or magnetic and luminescent properties depending on the involved metal node (transition metal or lanthanide ions respectively[114,115]). 2,3-dicyano-5,6-dichloro-1,4-benzoquinone, is the first example of a heterosubstituted anilate,[116] where the cyano group modifies the electronic properties, breaking the symmetry and conferring luminescent properties to the anilato moiety. In fact, the dianionic form is a green luminophore showing emission at 550 nm, able to transfer energy, acting as good antenna, towards Ln^{III} metal ions. For more details see *Annex III.*

1.4 Aim of the work

Despite the enormous scientific efforts addressed to fabricate optical sensors able to monitor and/or detect chemical pollutants, mainly *i)* metal cations in aqueous environment, for health protection and global sustainability; *ii)* nitroaromatics which represent a severe threat for homeland security; *iii)* pH, which is crucial in many physiological and pathological processes, several problems and challenges still exist in this field. *The present Work* contributes to the ongoing research on Luminescent sensors, the current emerging technology, with the aim to design novel luminescent chemosensors and/or sensing platforms with promising applications in the real-time detection/monitoring of environmental pollutants. Dye-functionalized silicon-based integrated fluorescent platforms, molecular hybrid ratiometric and intensity-based fluorescent chemosensors and luminescent nanosheets are prepared, by using the conventional methods of organic chemistry, material chemistry and supramolecular chemistry and characterized, through a multi-technique approach, involving X-Ray Diffraction (powder and single-crystal), Atomic Force Microscopy, Transmission Electron Microscopy, Mass Spectrometry, Photoluminescence (PL) and Time-Resolved PL Spectroscopy. In this context particular attention has been devoted to the choice of molecular building blocks employed in the development of the fluorescent chemosensors. Fluorescein, Rhodamine, Diketopyrrolopyrroles and 2,5 -dihydroxy-1,4-benzoquinone derivatives are selected, due the possibility to fine tune their chemical make-up for tailoring properly the chemosensor-analyte interaction.

The research Work has been carried out as follow:

- **Chapter 1**. ***General Introduction***

  Overview on Fluorescent Chemosensors, selected Organic Fluorophores, Detection Platforms, including FRET-based and molecular Chemosensors and Target Analytes.

- **Chapter 2. *Silicon-based Fluorescent Platforms for Copper(II) Detection in Water***

  Rational design and fabrication of a fluorescent silicon-based Platform, by conjugation of a dye of the xanthene family (FITC) to an amino-modified silicon chip, which results in a practical sensing platform for detection of copper(II) in water.

This approach can lead to effective metal-ion fluorescent sensors. An original fluorophore-analyte reversible sensing mechanism is proposed, widely supported by control experiments. These results provide new and original scientific knowledgement on selective sensing of toxic metal ions at functionalized silicon surfaces in aqueous environment and, remarkably, the use of fluorescent silicon chips may facilitate sensor integration in remote analysis systems for real-time water monitoring.

- **Chapter 3.** ***Hybrid Ratiometric Fluorescent Platforms***

  Rational design and development of a hybrid fluorescent ratiometric platform, by combining a dansyl moiety, as donor unit and a rhodamine derivative, as acceptor unit. Study of the proton - hybrid platform interaction, to investigate the proton-mediated spirolactam/ring opening mechanism and the photophysical mechanism/s at the basis of energy-transfer, *via* a multi-technique approach, involving Uv-Vis Absorption, Photoluminescence (PL) and time-resolved PL Spectroscopies, Mass Spectrometry and Potentiometric titrations, supported by theoretical calculations.

- ***Chapter 4. Rhodamine and Thiophene Diketopyrrolo-Pyrrolo based Fluorescent Chemosensors***

  Rational design and synthesis and luminescent characterization of ligands based on Rhodamine and Diketopyrrolopyrrole. In particularly, due to the novelty in the sensing field we focused our interesting in DPP monoalkylated derivatives due to the possibility to anchor these luminescent molecules to solid support in order to obtain suitable probes for the recognition of toxic metal ions.

- **Chapter 5.** ***Luminescent Nanosheets as Unique Platforms for Chemical Sensing***

  Rational design and synthesis of Nanosheets, based on NIR (Yb^{III}) and UV-Vis (Tb^{III} and Eu^{III}) emitters. Photophysics of Nanosheets based on Yb ^{III}, consisting of $ClCNAn^{2-}$ and carboxylates, is compared to the corresponding bulks is investigated by an innovative Multiprobe Approach where lifetime, photoluminescence (PL) and integrated PL are simultaneously measured in order to study how these parameters can be affected by the presence of the different solvents.

- **SUMMARY.** ***Conclusions and Perspectives***

- **ANNEXES**

  ANNEX I. Overview on Luminescence and Lanthanide and their luminescent properties.

  ANNEX II. Overview on Anilate Ligands and their CPs/MOFs.

  ANNEX III. Exfoliation Methods.

1.5 References

1 A. J. Howarth, Y. Liu, J. T. Hupp and O. K. Farha, *CrystEngComm*, 2015, **17**, 7245–7253.

2 P. Samanta, A. V. Desai, S. Let and S. K. Ghosh, *ACS Sustain. Chem. Eng.*, 2019, **7**, 7456–7478.

3 H. K. Okoro, S. O. Ayika, J. C. Ngila and A. C. Tella, *Appl. Water Sci.*, 2018, **8**, 1–10.

4 R. J. Drout, L. Robison, Z. Chen, T. Islamoglu and O. K. Farha, *Trends Chem.*, 2019, **1**, 304–317.

5 L. T. Gibson, *Chem. Soc. Rev.*, 2014, **43**, 5163–5172.

6 M. Li, H. Gou, I. Al-Ogaidi and N. Wu, *ACS Sustain. Chem. Eng.*, 2013, **1**, 713–723.

7 Z. Xu, J. Yoon and D. R. Spring, *Chem. Soc. Rev.*, 2010, **39**, 1996–2006.

8 G. Sivaraman, M. Iniya, T. Anand, N. G. Kotla, O. Sunnapu, S. Singaravadivel, A. Gulyani and D. Chellappa, *Coord. Chem. Rev.*, 2018, 357, 50–104.

9 S. Sen, S. Sarkar, B. Chattopadhyay, A. Moirangthem, A. Basu, K. Dhara and P. Chattopadhyay, *Analyst*, 2012, **137**, 3335–3342.

10 Y. Liu, P. Liang and L. Guo, *Talanta*, 2005, **68**, 25–30.

11 J. S. Becker, A. Matusch, C. Depboylu, J. Dobrowolska and M. V. Zoriy, *Anal. Chem.*, 2007, **79**, 6074–6080.

12 A. P. S. Gonzáles, M. A. Firmino, C. S. Nomura, F. R. P. Rocha, P. V. Oliveira and I. Gaubeur, *Anal. Chim. Acta*, 2009, **636**, 198–204.

13 J. S. Lee, A. Baldridge, S. Feng, Y. Siqiang, Y. K. Kim, L. M. Tolbert and Y. T. Chang, *ACS Comb. Sci.*, 2011, **13**, 32–38.

14 N. L. Han, K. M. K. Swamy, K. K. Sook, J. Y. Kwon, Y. Kim, S. J. Kim, J. Y. Yeo and J. Yoon, *Org. Lett.*, 2007, **9**, 243–246.

15 Y. Yan, L. Meng, W. Zhang, Y. Zheng, S. Wang, B. Ren, Z. Yang and X. Yan, *ACS Sensors*, 2017, **2**, 1369–1376.

16 J. H. Goldman, S. A. Rounds and J. A. Needoba, *Environ. Sci. Technol.*, 2012, **46**, 4374–4381.

17 S. Anbu, A. Paul, G. J. Stasiuk and A. J. L. Pombeiro, *Coord. Chem. Rev.*, 2021, **431**, 213744.

18 K. Y. Wu, M. Chen, N. H. Huang, R. T. Li, W. L. Pan, W. H. Zhang, W. H. Chen and J. X. Chen, *Talanta*, 2021, **221**, 121399.

19 S. Wang, X. Wang, Z. Zhang and L. Chen, *Colloids Surfaces A Physicochem. Eng. Asp.*, 2015, **468**, 333–338.

20 X. Zhao, L. Zhang, J. Bai, P. Wu, Y. Li, L. Liang, L. Xie and J. Wang, *Spectrochim. Acta - Part A Mol. Biomol. Spectrosc.*, 2020, **243**, 118794.

21 A. Hulanicki, S. Glab and F. Ingman, *Pure Appl. Chem.*, 1991, **63**, 1247–1250.

22 A. P. De Silva, H. Q. N. Gunaratne, T. Gunnlaugsson, A. J. M. Huxley, C. P. McCoy, J. T. Rademacher and T. E. Rice, *Chem. Rev.*, 1997, **97**, 1515–1566.

23 A. W. Czarnik, 1993, 1–9.

24 A. W. Czarnik, *Acc. Chem. Res.*, 1994, **27**, 302–308.

25 L. Prodi, F. Bolletta, M. Montalti and N. Zaccheroni, *Coord. Chem. Rev.*, 2000, **205**, 59–83.

26 N. Kwon, Y. Hu and J. Yoon, *ACS Omega*, 2018, **3**, 13731–13751.

27 J. Huang, Y. Xu and X. Qian, *Dalt. Trans.*, 2009, 1761–1766.

28 K. P. Carter, A. M. Young and A. E. Palmer, *Chem. Rev.*, 2014, 114, 4564–4601.

29 R. M. Christie, *Fluorescent dyes*, Woodhead Publishing Limited, 2011, vol. 1.
30 B. Daly, J. Ling and A. P. De Silva, *Chem. Soc. Rev.*, 2015, **44**, 4203–4211.
31 X. Zhou, F. Su, H. Lu, P. Senechal-Willis, Y. Tian, R. H. Johnson and D. R. Meldrum, *Biomaterials*, 2012, **33**, 171–180.
32 R. K. Meka and M. D. Heagy, *J. Org. Chem.*, 2017, **82**, 12153–12161.
33 J. W. Nugent, H. Lee, H. S. Lee, J. H. Reibenspies and R. D. Hancock, *Chem. Commun.*, 2013, **49**, 9749–9751.
34 R. F. Chen, *Anal. Biochem.*, 1968, **25**, 412–416.
35 L. K. Chaganti, N. Venkatakrishnan and K. Bose, *Biosci. Rep.*, 2018, **38**, 1–8.
36 S. G. Stratton, G. H. Taumoefolau, G. E. Purnell, M. Rasooly, W. L. Czaplyski and E. J. Harbron, *Chem. - A Eur. J.*, 2017, **23**, 14064–14072.
37 R. Azadbakht, T. Almasi, H. Keypour and M. Rezaeivala, *Inorg. Chem. Commun.*, 2013, **33**, 63–67.
38 J. H. Hu, J. Bin Li, J. Qi and Y. Sun, *Sensors Actuators, B Chem.*, 2015, **208**, 581–587.
39 H. M. Zhang, W. F. Fu, S. M. Chi and J. Wang, *J. Lumin.*, 2009, **129**, 589–594.
40 H. N. Kim, M. H. Lee, H. J. Kim, J. S. Kim and J. Yoon, *Chem. Soc. Rev.*, 2008, **37**, 1465–1472.
41 K. Tanaka, T. Miura, N. Umezawa, Y. Urano, K. Kikuchi, T. Higuchi and T. Nagano, *J. Am. Chem. Soc.*, 2001, **123**, 2530–2536.
42 Z. Kenntniss, B. Ii--vii, D. Wir and D. Arbeit, .
43 V. Dujols, F. Ford and A. W. Czarnik, *J. Am. Chem. Soc.*, 1997, **119**, 7386–7387.
44 Y. Xiang and A. Tong, *Org. Lett.*, 2006, **8**, 1549–1552.
45 M. Suresh, A. Shrivastav, S. Mishra, E. Suresh and A. Das, *Org. Lett.*, 2008, **10**, 3013–3016.
46 Z. Yang, M. She, B. Yin, J. Cui, Y. Zhang, W. Sun, J. Li and Z. Shi, *J. Org. Chem.*, 2012, **77**, 1143–1147.
47 M. Atzori, F. Pop, T. Cauchy, M. L. Mercuri and N. Avarvari, *Org. Biomol. Chem.*, 2014, **12**, 8752–8763.
48 J. Y. Kwon, Y. J. Jang, Y. J. Lee, K. M. Kim, M. S. Seo, W. Nam and J. Yoon, *J. Am. Chem. Soc.*, 2005, **127**, 10107–10111.
49 J. H. Soh, K. M. K. Swamy, S. K. Kim, S. Kim, S. H. Lee and J. Yoon, *Tetrahedron Lett.*, 2007, **48**, 5966–5969.
50 Y. Jiao, L. Zhou, H. He, J. Yin, Q. Gao, J. Wei, C. Duan and X. Peng, *Talanta*, 2018, **184**, 143–148.
51 F. Song, X. Shao, J. Zhu, X. Bao, L. Du and C. Kan, *Tetrahedron Lett.*, 2019, **60**, 1363–1369.
52 M. Łukarska, A. Jankowska, J. Gapiński, S. Valable, C. Anfray, B. Ménard, S. Mintova and S. Kowalak, *New J. Chem.*, 2017, **41**, 9969–9976.
53 E. Lanz, M. Gregor, J. Slavík and A. Kotyk, *J. Fluoresc.*, 1997, **7**, 317–319.
54 Y. Tian, E. Fuller, S. Klug, F. Lee, F. Su, L. Zhang, S. H. Chao and D. R. Meldrum, *Sensors Actuators, B Chem.*, 2013, **188**, 1–10.
55 C. Queirós, A. M. G. Silva, S. C. Lopes, G. Ivanova, P. Gameiro and M. Rangel, *Dye. Pigment.*, 2012, **93**, 1447–1455.
56 S. C. Burdette, G. K. Walkup, B. Spingler, R. Y. Tsien and S. J. Lippard, *J. Am. Chem. Soc.*, 2001, **123**, 7831–7841.
57 H. Mu, R. Gong, L. Ren, C. Zhong, Y. Sun and E. Fu, *Spectrochim. Acta - Part A Mol. Biomol. Spectrosc.*, 2008, **70**, 923–928.

58 L. Zhang, Y. Jian, J. Wang, C. He, X. Li, T. Liu and C. Duan, *Dalt. Trans.*, 2012, **41**, 10153–10155.

59 C. Zong, K. Ai, G. Zhang, H. Li and L. Lu, *Anal. Chem.*, 2011, **83**, 3126–3132.

60 M. T. Shah, A. Balouch and E. Alveroglu, *J. Mater. Chem. C*, 2018, **6**, 1105–1115.

61 E. M. Obeng, E. C. Dullah, M. K. Danquah, C. Budiman and C. M. Ongkudon, *Anal. Methods*, 2016, **8**, 5323–5337.

62 R. Zhang, F. Yan, Y. Huang, D. Kong, Q. Ye, J. Xu and L. Chen, *RSC Adv.*, 2016, **6**, 50732–50760.

63 G. S. Jiao, L. H. Thoresen and K. Burgess, *J. Am. Chem. Soc.*, 2003, **125**, 14668–14669.

64 J. Fan, M. Hu, P. Zhan and X. Peng, *Chem. Soc. Rev.*, 2013, **42**, 29–43.

65 L. Wu, C. Huang, B. P. Emery, A. C. Sedgwick, S. D. Bull, X. P. He, H. Tian, J. Yoon, J. L. Sessler and T. D. James, *Chem. Soc. Rev.*, 2020, **49**, 5110–5139.

66 V. Luxami, M. Verma, R. Rani, K. Paul and S. Kumar, *Org. Biomol. Chem.*, 2012, **10**, 8076–8081.

67 K. Aich, S. Goswami, S. Das, C. Das Mukhopadhyay, C. K. Quah and H. K. Fun, *Inorg. Chem.*, 2015, **54**, 7309–7315.

68 C. Yu, Y. Wen, X. Qin and J. Zhang, *Anal. Methods*, 2014, **6**, 9825–9830.

69 D. G. Farnum, G. Mehta, G. G. I. Moore and F. P. Siegal, *Tetrahedron Lett.*, 1974, **15**, 2549–2552.

70 M. Kaur and D. H. Choi, *Chem. Soc. Rev.*, 2015, **44**, 58–77.

71 R. Lenz, .

72 J. Mizuguchi and G. Wooden, *Berichte der Bunsengesellschaft für Phys. Chemie*, 1991, **95**, 1264–1274.

73 R. Beninatto, G. Borsato, O. De Lucchi, F. Fabris, V. Lucchini and E. Zendri, *Dye. Pigment.*, 2013, **96**, 679–685.

74 K. Nie, B. Dong, H. Shi, Z. Liu and B. Liang, *Anal. Chem.*, 2017, **89**, 2928–2936.

75 B. Valeur and I. Leray, *Coord. Chem. Rev.*, 2000, **205**, 3–40.

76 T. Kobayashi and N. K. Nishizawa, *Plant Sci.*, 2014, **224**, 36–43.

77 D. Vlascici, E. Fagadar-Cosma, I. Popa, V. Chiriac and M. Gil-Agusti, *Sensors (Switzerland)*, 2012, **12**, 8193–8203.

78 E. Kimura and S. Aoki, *BioMetals*, 2001, **14**, 191–204.

79 K. H. Brown, S. E. Wuehler and J. M. Peerson, *Food Nutr. Bull.*, 2001, **22**, 113–125.

80 B. Witt, D. Schaumlöffel and T. Schwerdtle, *Int. J. Mol. Sci.*, 2020, 21

81 Z. Xu, Q. Meng, Q. Cao, Y. Xiao, H. Liu, G. Han, S. Wei, J. Yan and L. Wu, *Anal. Chem.*, 2020, **92**, 2201–2206.

82 W. Su, S. Yuan and E. Wang, *J. Fluoresc.*, 2017, **27**, 1871–1875.

83 T. Rasheed, M. Bilal, F. Nabeel, H. M. N. Iqbal, C. Li and Y. Zhou, *Sci. Total Environ.*, 2018, **615**, 476–485.

84 E. M. Nolan and S. J. Lippard, *Chem. Rev.*, 2008, **108**, 3443–3480.

85 P. Venkatesan, N. Thirumalivasan and S. P. Wu, *RSC Adv.*, 2017, **7**, 21733–21739.

86 K.-S. Ju and R. E. Parales, *Microbiol. Mol. Biol. Rev.*, 2010, **74**, 250–272.

87 L. Yuan, W. Lin, Y. Xie, B. Chen and S. Zhu, *J. Am. Chem. Soc.*, 2012, **134**, 1305–1315.

88 D. Wu, A. C. Sedgwick, T. Gunnlaugsson, E. U. Akkaya, J. Yoon and T. D. James, *Chem. Soc. Rev.*, 2017, **46**, 7105–7123.

89 K. Ehrlich, T. R. Choudhary, M. Ucuncu, A. Megia-Fernandez, K. Harrington, H. A. C.

Wood, F. Yu, D. Choudhury, K. Dhaliwal, M. Bradley and M. G. Tanner, *Sensors (Switzerland)*, 2020, **20**, 1–12.
90 J. T. Hou, W. X. Ren, K. Li, J. Seo, A. Sharma, X. Q. Yu and J. S. Kim, *Chem. Soc. Rev.*, 2017, **46**, 2076–2090.
91 Y. Chen, *Anal. Biochem.*, 2021, **612**, 113900.
92 J. Han and K. Burgess, *Chem. Rev.*, 2010, **110**, 2709–2728.
93 Y. Han, C. Ding, J. Zhou and Y. Tian, *Anal. Chem.*, 2015, **87**, 5333–5339.
94 A. V. Chadwick and J. N. Sherwood, *Point Defects in Solids*, 1975, **85**, 441–475.
95 S. Carrasco, *Biosensors*, 2018, **8**, 92-122
96 H. Li, L. Li, R.-B. Lin, W. Zhou, Z. Zhang, S. Xiang and B. Chen, *EnergyChem*, 2019, **1**, 100006.
97 D. Yang and B. C. Gates, *ACS Catal.*, 2019, **9**, 1779–1798.
98 P. Kumar, A. Deep and K. H. Kim, *TrAC - Trends Anal. Chem.*, 2015, **73**, 39–53.
99 A. Ray Chowdhuri, D. Bhattacharya and S. K. Sahu, *Dalt. Trans.*, 2016, **45**, 2963–2973.
100 F. Y. Yi, D. Chen, M. K. Wu, L. Han and H. L. Jiang, *Chempluschem*, 2016, **81**, 675–690.
101 Y. Zhang, D. Geng, X. Kang, M. Shang, Y. Wu, X. Li, H. Lian, Z. Cheng and J. Lin, *Inorg. Chem.*, 2013, **52**, 12986–12994.
102 Y. Zhang, X. Li, K. Li, H. Lian, M. Shang and J. Lin, *ACS Appl. Mater. Interfaces*, 2015, **7**, 2715–2725.
103 K. Binnemans, *Chem. Rev.*, 2009, **109**, 4283–4374.
104 J. C. G. Bünzli, *Chem. Rev.*, 2010, **110**, 2729–2755.
105 G. Bao, *J. Lumin.*, 2020, **228**, 117622.
106 M. D. Allendorf, C. A. Bauer, R. K. Bhakta and R. J. T. Houk, *Chem. Soc. Rev.*, 2009, **38**, 1330–1352.
107 J. N. Hao and B. Yan, *Chem. Commun.*, 2015, **51**, 7737–7740.
108 Z. Xiaoxiong, Z. Wenjun, L. Cuiliu, Q. Xiaohong and Z. Chengyu, *Inorg. Chem.*, 2019, **58**, 3910-3915.
109 C. Tan, P. Yu, Y. Hu, J. Chen, Y. Huang, Y. Cai, Z. Luo, B. Li, Q. Lu, L. Wang, Z. Liu and H. Zhang, *J. Am. Chem. Soc.*, 2015, **137**, 10430–10436.
110 J. Xu, X. Chen, Y. Xu, Y. Du and C. Yan, *Adv. Mater.*, 2020, **32**, 1–17.
111 M. Zhao, Y. Wang, Q. Ma, Y. Huang, X. Zhang, J. Ping, Z. Zhang, Q. Lu, Y. Yu, H. Xu, Y. Zhao and H. Zhang, *Adv. Mater.*, 2015, **27**, 7372–7378.
112 S. Guo and S. Dong, *J. Mater. Chem.*, 2011, **21**, 18503–18516.
113 H. Xu, J. Gao, X. Qian, J. Wang, H. He, Y. Cui, Y. Yang, Z. Wang and G. Qian, *J. Mater. Chem. A*, 2016, **4**, 10900–10905.
114 S. Ashoka Sahadevan, N. Monni, A. Abhervé, D. Marongiu, V. Sarritzu, N. Sestu, M. Saba, A. Mura, G. Bongiovanni, C. Cannas, F. Quochi, N. Avarvari and M. L. Mercuri, *Chem. Mater.*, 2018, **30**, 6575–6586.
115 S. A. Sahadevan, A. Abhervé, N. Monni, C. Sáenz De Pipaón, J. R. Galán-Mascarós, J. C. Waerenborgh, B. J. C. Vieira, P. Auban-Senzier, S. Pillet, E. E. Bendeif, P. Alemany, E. Canadell, M. L. Mercuri and N. Avarvari, *J. Am. Chem. Soc.*, 2018, **140**, 12611–12621.
116 M. Atzori, F. Artizzu, L. Marchiò, D. Loche, A. Caneschi, A. Serpe, P. Deplano, N. Avarvari and M. L. Mercuri, *Dalt. Trans.*, 2015, **44**, 15786–15802.

Chapter 2

Silicon-based Fluorescent Platforms for Copper(II) Detection in Water

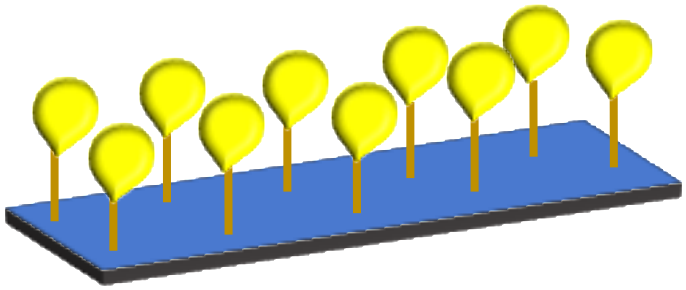

2.1 Introduction

Several traditional techniques are currently employed for detecting trace toxic metal ions in aqueous and biological environments, including Inductively Coupled Plasma Atomic Emission Spectrometry (ICP-AES),[1] Inductively Coupled Plasma Mass Spectrometry (ICP-MS)[2] and Atomic Absorption Spectrometry (AAS).[3] These techniques provide excellent detection limits but require high cost instrumentation, time-consuming sample preparation and well-trained operators. Colorimetric and fluorescence sensor devices are fast-growing technologies showing remarkable advantages over conventional techniques, such as fast response times, non-destructive analysis and remote operation, while attaining competitive performances in terms of detection limits, sensitivity, selectivity and reversibility by rational device design.[4–8] Fluorescent probes, which have found widespread use in biomedical applications,[9,10] are being increasingly studied for real-time and remote environmental monitoring such as detection of toxic metals in water and biological media.[4,11–14] In a molecular-type approach, a fluorescent probe, which represents the sensitive part of the fluorescent device, basically consists of a recognition (binding) moiety linked to or included into a fluorescent species (usually an organic dye) whose emission properties, such as peak wavelength and quantum yield, are modified by the interaction with the analyte. The chemical nature of both the binding and fluorescent units can be tailored to optimize the probe for any specific analyte and/or application.

Typically, fluorescent probes are designed to work in solution. However, depending on the application an improvement in the sensing performance can be obtained by covalently anchoring fluorescent probes to different substrates, e.g. biomolecules,[15,16] silica-based nanocomposites[17–20] and metal-organic frameworks.[21–23] Grafting fluorescent probes to silicon-based planar platforms represents a promising route towards sensor integration with silicon photonics technology and realization of Lab-on-Chip devices.[24,25] To this aim, the sol-gel technique based on organosilane derivatives[26,27] is one of the most suitable strategies for the fabrication of robust, low-cost and functional silicon-based device platforms. In particular, the use of 3-aminopropyltriethoxysilane (APTES) as organosilane derivate allows to insert amino groups capable to covalently link fluorophores on the silicon surfaces, *via* the formation of amides, ureas, thioureas and imines as linking functional groups.[28–31] Although step-by-step silanization of silicon substrates has already been

investigated for the fabrication of fluorescent platforms,[32–34] the potential of silicon-based on-chip fluorescence sensors for the detection of trace metal ions in aqueous environment is yet to be demonstrated.

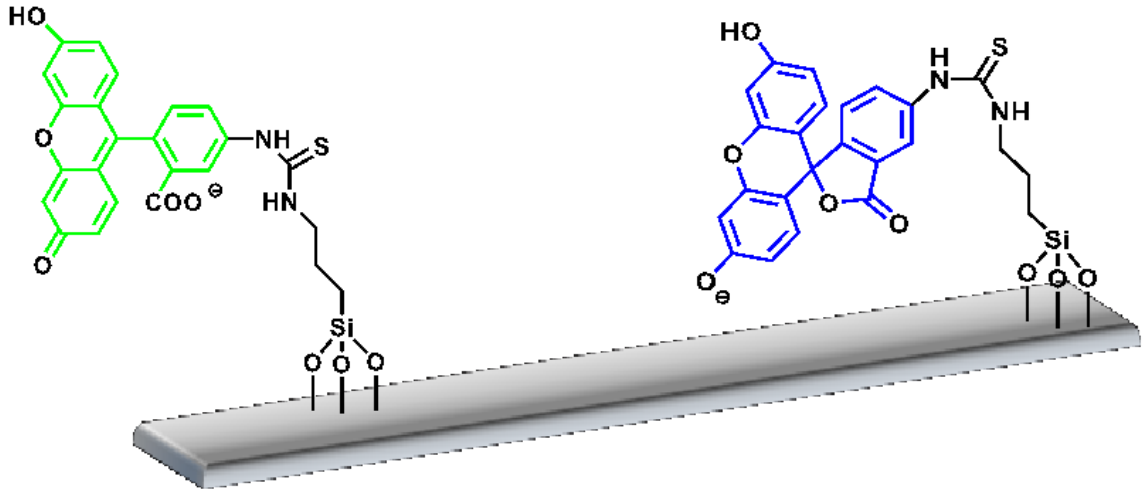

Figure 1. Schematic representation of the fluorescent silicon chip.

A fundamental study on silicon-based fluorescent platforms for detection of trace metal ions in aqueous environment is herein presented. Fluorescein isothiocyanate (FITC) was covalently linked to APTES-prefunctionalized silicon substrates via thiourea formation to realize silicon-based on-chip devices integrating both recognition and fluorescent units. On the one hand, FITC is highly suitable to serve as prototypical fluorescent sensing unit because of its remarkable photophysical properties;[35–37] on the other hand, thiourea groups have been demonstrated effective in binding metal cations such as Cu^{II}, Cd^{II}, and Hg^{II} in water, in fact enabling metal-ion fluorescent sensors with competitive performances.[38–40] Selectivity to copper(II), high sensitivity and low limit of detection were reported. Successful surface regeneration was achieved using ethylenediaminetetraacetic acid (EDTA) chelating agent, yielding insight into the mechanism responsible for metal binding at the sensor surface.

The performance of the device in terms of sensing capability towards common toxic metal ions in aqueous environment (together with its selectivity, sensitivity and regeneration properties) is investigated and the best performance is achieved with copper(II) metal ion. It's well known that copper is the third most abundant metal ion after iron and zinc in the human body and it plays an important role in different biological processes,[41] *i.e.* in the

functionality of many enzymes such as cytochrome C Oxidase (COX), tyrosinase, dismutases, copper amine oxidases, dopamine b hydroxylase.[42] On the other hand, a misregulation can lead to various genetic disorders, such as Menkes and Wilson's diseases,[43] and neurodegenerative diseases including Alzheimer's, Parkinson's and Prion. Consequently, EPA (US Environmental Protection Agency) and WHO (World Health Organization) have set the maximum copper level in drinking waters to 1.3 and 2 mg L^{-1}, respectively.

2.2 Results and Discussion

2.2.1. Design and surface characterization

Silicon surface modification steps are reported in **Figure 2.** Firstly, ultrathin silica layers are deposited on (100)-oriented silicon chips by (i) the sol-gel technique by using TEOS as silica precursor (**Scheme 1**) and (ii) the spin-coating deposition method (**Step 1**). Subsequently, amino groups were introduced on the Si@SiO_2 surface by using APTES (**Step 2**). FITC was covalently anchored to the Si@SiO_2@APTES surface *via* thiourea formation (**Step 3**).

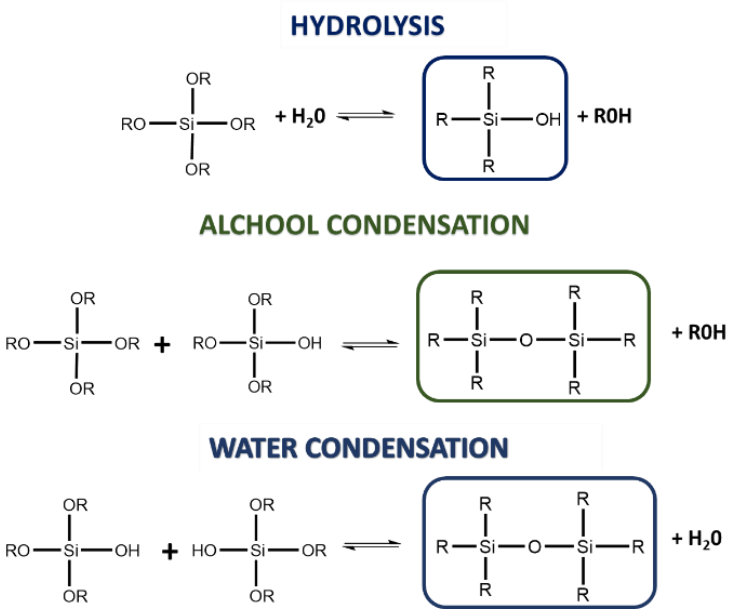

Scheme 1.Reaction involved in sol-gel process.

To monitor how each functionalization step modified the morphological and optical properties of the silicon surface,[45] samples were investigated following a multivariate approach, adopting CA measurements, AFM, Reflectance and Fluorescence Spectroscopy.

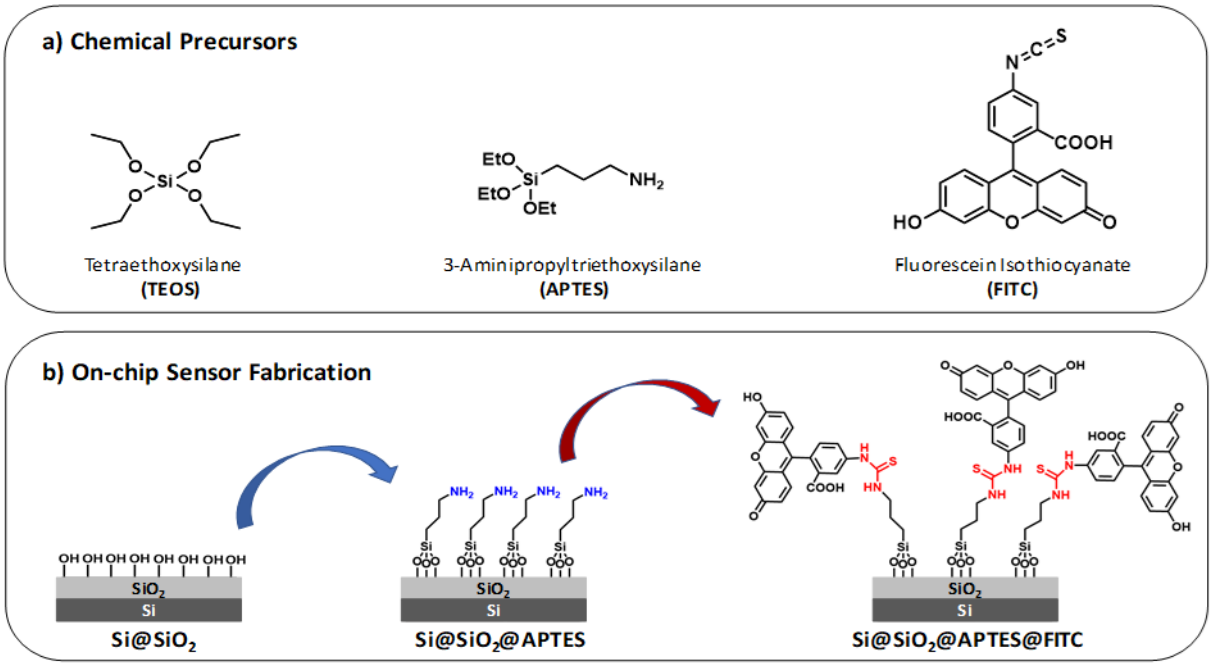

Figure 2. (a) Chemical precurosrs used to fabricate the fluorescent sensor (b) Step 1: Surface silica layer deposition bearing hydroxy groups via the sol-gel method using TEOS (left); Step 2: Amino-functionalization of the silica surface with APTES (centre, amino groups highlighted in blue). Step 3: Functionalization with FITC (right), leading to the formation of thiourea groups (highlighted in red).

CA measurements, using water as solvent, were performed to evaluate surface wettability. As shown in **Figure 3**, data revealed a decreasing surface wettability of the silicon chip upon amino-modification by APTES and subsequent FITC linkage. In fact, the mean CA, which was found to be 38.3(0.5)° in the $Si@SiO_2$ chip, increased up to 54.4(0.7)° after silanization with APTES[46] and then up to 72.1(0.9)° upon functionalization with FITC.[47] These results could be easily rationalized as a decreased surface hydrophilicity due to the functionalization of the silica layer (bearing hydroxy groups, -OH) with the amino ($–NH_2$) groups of APTES and then with FITC, which contains hydrophobic aromatic rings (**Figure 3A**). To confirm the homogeneous deposition and/or functionalization, measurements were performed on different points. This result was confirmed at the nanoscale by AFM height images, showing

lack of topographic reliefs and root mean square (RMS) values of the surface roughness lower than 1 nm (**Figure 3B**).

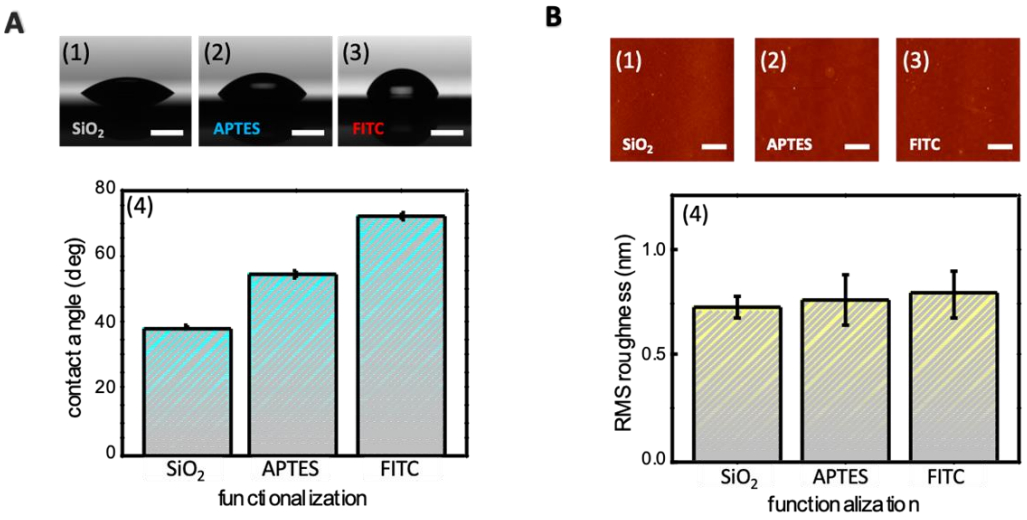

FIgure 3. A) Pictures of a distilled water drop laid onto: (1) A silica layer on silicon substrate (Si@SiO_2); (2) APTES grafted onto the silica layer (Si@SiO_2@APTES); (3) FITC-conjugated system (Si@SiO_2@APTES@FITC). Horizontal white bars correspond to 2 mm. (4) Histograms showing the evolution of the mean water contact angle value after each deposition step. Standard errors are indicated. B) AFM surface topography of silicon-chip structures1) Image of the surface of a sol-gel silica layer (Si(100)@SiO_2 structure). (2) Same as (1) but for an Si(100)@SiO_2@APTES structure. (c) Same as (b) but for a Si(100)@SiO_2@APTES@FITC structure. White bars: 10 µm. (4) Histogram depicting the evolution of the RMS surface roughness after each deposition step. Standard errors are indicated.

2.2.2 Optical Characterization

VIS reflectance spectroscopy was used to evaluate the thickness of the layers deposited through the various functionalization steps. Measurements were performed in hemispherical geometry to collect both specular and diffuse reflectance. The results are reported in **Figure 4**. Spectral reflectance ratio $R_i(\lambda)/R_{i-1}(\lambda)$ was calculated after fabrication Step i. Silica deposition resulted in 10-15% decrease in reflectance across the visible spectrum (**Figure 4a**), as the silica layer acted as an antireflection coating on silicon. Knowing the index of refraction of silica from previous work done with similar sol-gel precursor concentrations and physical deposition parameters,[48] it was possible to calculate

the thickness of the silica layer with high degree of accuracy. The estimated value of 28(1) nm implies that reflectance was very sensitive to any increase in thickness caused by subsequent functionalization steps. In the actual experimental setup, this sensitivity resulted to be ~1 nm. In the inset of **Figure 4a**, the reflectance ratio R/R_0, where R (R_0) is the reflectance of theSi@SiO_2 structure (bare silicon chip) at 700 nm, is plotted against the SiO_2 layer thickness.

The high sensitivity of the reflectance ratio to the thickness of the APTES and FITC layers was readily deduced from the slope of the black line at the intersection with the blue and red vertical bars, depicting the APTES and FITC layers, respectively. **Figures 4 b,c** show that reflectance remained practically unchanged upon functionalization of APTES and FITC, allowing to conclude that these functionalization steps were well-controlled and involved the deposition of monolayers. Indeed, a dip was observed in the spectrum of the reflectance ratio measured after FITC deposition (Fig. 3c); its very small depth (~0.003) was found to be compatible with the optical absorption of a dense monolayer of FITC in the visible.

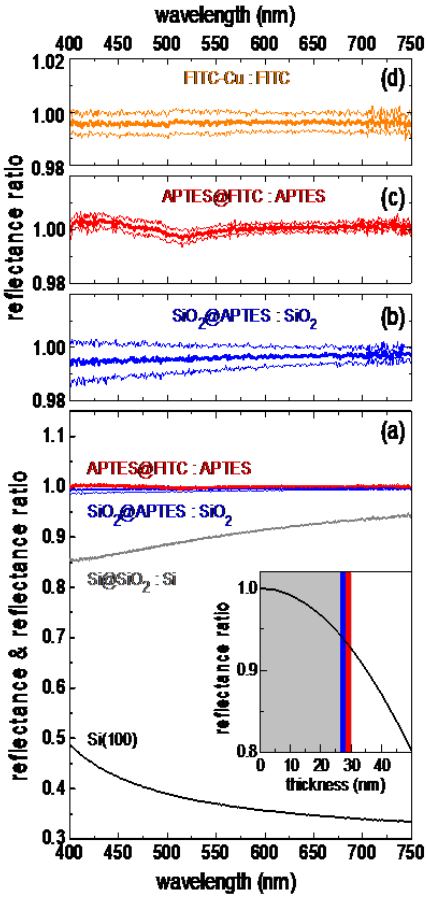

Figure 4. Reflectance spectrum of n-doped (100)-oriented silicon substrate (black line); Spectral reflectance ratios measured upon sequential layer deposition/functionalization: Si@SiO_2-to-Si, Si@SiO_2@APTES-to-Si@SiO_2, and Si@SiO_2@APTES@FITC-to-Si@SiO_2@APTES ratios (grey, blue and red lines, respectively).

Furthermore, combined Cw/time-resolved fluorescence spectroscopy was applied to check for surface functionalization with FITC and to gain information on the xanthene-centered fluorescence efficiency upon FITC linkage to the silicon surface. The fluorescence spectrum of the sensing device is shown in **Figure 4a.** The main emission peak, centered at 540 nm (red curve), was readily assigned to FITC xanthene unit, while comparative measurements on Si@SiO_2 bare chip (grey curve) allowed to attribute the short-wavelength shoulder (centered at 420 nm) to the silica fluorescence spectrum.

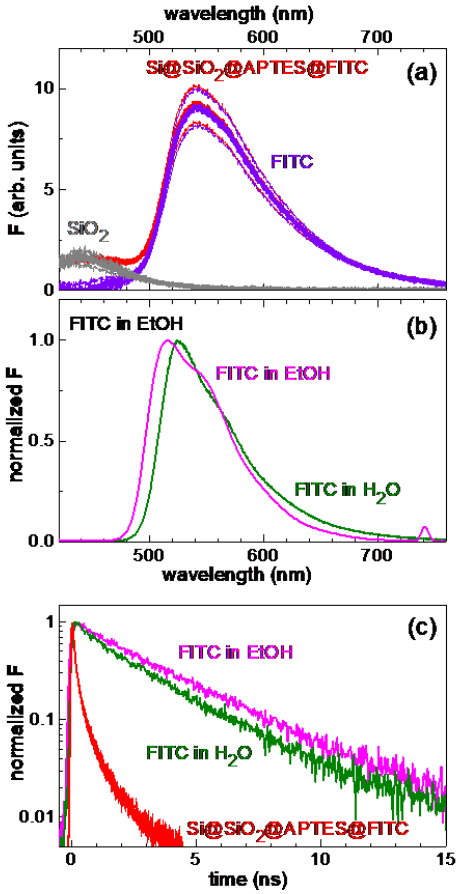

Figure 5. (a) Fluorescence intensity (F) spectrum of the Si@SiO_2@APTES@FITC device. Red curves: Fluorescence spectrum in air. FITC and SiO_2 contributions to the whole spectrum are shown as the violet and grey lines, respectively. Thick lines are the mean signal values; Thin lines are the mean values increased and decreased by their standard errors. (b) Normalized fluorescence spectrum of FITC in ethanol (1.2×10^{-5} mol L^{-1}) and water (< 10^{-5} mol L^{-1}) solutions (magenta and olive line, respectively). (c) Normalized fluorescence decay curves of FITC in ethanol and water solution (magenta and olive line, respectively). Red curve: Fluorescence decay transient of the device. Excitation wavelength was 355 nm.

For reference, emission spectra were also collected for FITC dissolved in water and ethanol (**Figure 5b**). FITC grafting resulted in loss of fluorescence efficiency, as deduced from the stretched exponential decay of the fluorescence intensity with reduced lifetime as compared to that of the nearly mono-exponential decay observed in solution.

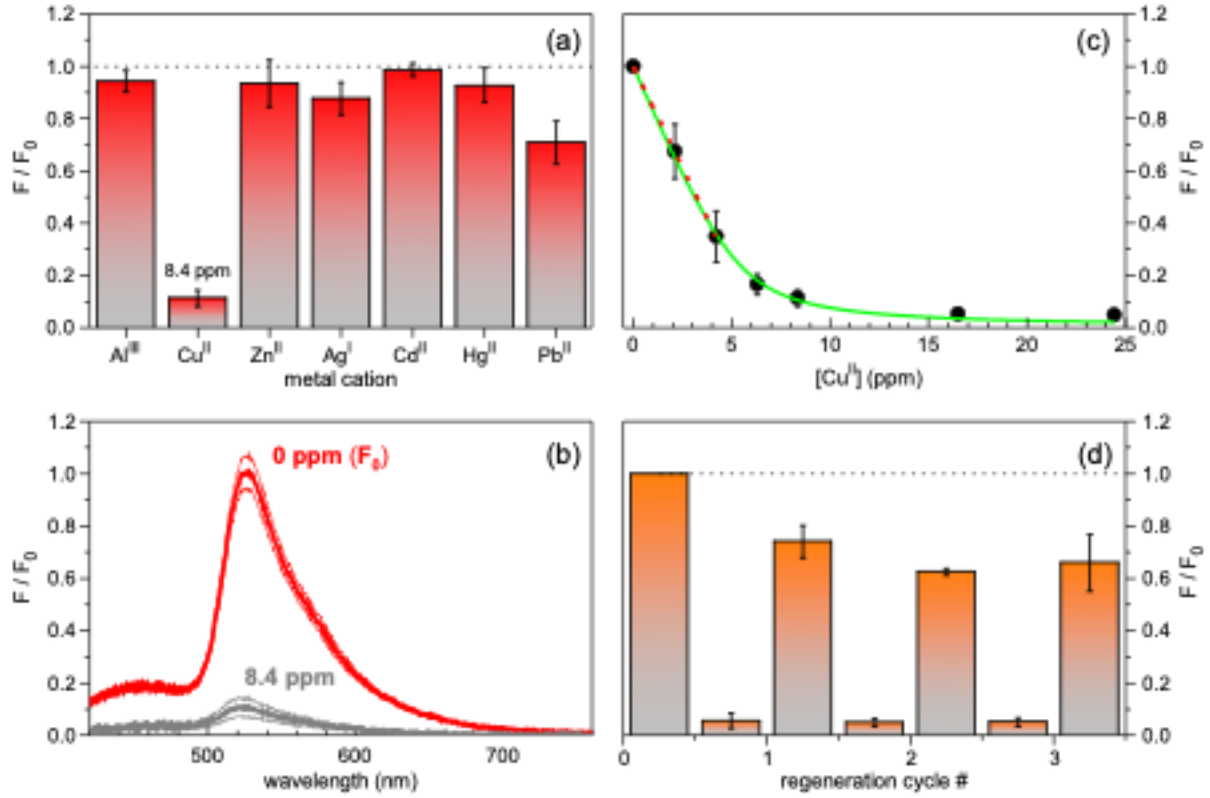

Figure 6. Performance characterization of silicon-chip fluorescence sensors in MOPS buffer at pH = 7.2 (excitation wavelength of 355 nm). (a) Spectrally-integrated fluorescence intensity changes in response to equimolar (1.3×10^{-4} mol·L^{-1}) solutions of various metal ions. (b) Red lines: Fluorescence spectrum of the unperturbed sensor; Grey lines: Fluorescence spectrum measured upon addition of 8.4 ppm of Cu^{II} ions. Thick lines are the mean signal values; thin lines are the mean values augmented and diminished by their standard errors. (c) Titration curve for the fluorescence intensity reduction (F/F_0) vs. Cu^{II} concentration. (d) Sensor regeneration tests.

2.2.3 Sensing Measurements

The silicon-chip sensor performance was evaluated by a preliminary screening, using several metal cations (Al^{III}, Cu^{II}, Zn^{II}, Ag^{I}, Cd^{II}, Hg^{II}, Pb^{II}) in MOPS buffer solutions at pH = 7.2, at a fixed molar concentration of 1.3×10^{-4} mol L^{-1} (**Figure 6a**). Among the investigated ions, Cu^{II} only lead to a neat fluorescence turn-off behavior (see also the fluorescence spectra in **Figure 5b**). The device sensitivity toward Cu^{II} was determined by fluorescence-intensity titration curves as a function of Cu^{II} concentration. The decrease in fluorescence intensity measured as the Cu^{II} concentration increased was fitted with an exponential decay curve, yielding 0.3 ppm^{-1} as the characteristic decay constant (or, equivalently, 30% reduction at 1 ppm level) in the low-concentration

regime below 10 ppm **(Figure 6c**). A constant superimposed to the exponential decay allowed to best fit the model curve to the experimental data, showing a stabilization of fluorescence quenching for Cu^{II} concentration values larger than 20 ppm. Finally, regeneration tests carried out in EDTA water solution showed stabilization of the fluorescence signal recovery level at ~60% already after the second regeneration cycle (**Figure 6d**), thereby demonstrating good reversibility of the sensor-analyte interaction. Several Cu^{II}-sensor interaction mechanisms could in principle be envisaged for the present on-chip devices. Fluorescence sensing of Cu^{II} by a rhodamine B derivative conjugated to silica nanoparticles through a thiourea group was previously shown to yield Cu^{II} complexes exhibiting an optical absorption band partly overlapping with the fluorophore emission band, thus acting as fluorescence quencher *via* photoinduced Forster's resonance energy transfer (FRET).[17] However, the minimum detectable change in the optical reflectance of the sensor surface was not low enough to allow for demonstrating, upon device dipping into Cu^{II} aqueous solution, the appearance of additional absorption bands (**Figure 4d**).

2.2.4 Sensing Mechanism

Redox processes involving Cu^{II} reduction to Cu^{I}, thiourea oxidation to a disulfide moiety, and concomitant formation of Cu^{I}-thiourea complexes, were also demonstrated experimentally in solution.[49–51] In the present on-chip devices, however, surface oxidation with formation of disulfide (-S-S-) bonds would presumably cause irreversible modification of the sensor surface, in contrast with regeneration tests by using EDTA. Thiourea-induced copper(II) reduction was therefore discarded as a possible metal sensing mechanism.

Thiourea groups may indeed not be directly involved in Cu^{II} sensing. Experiments performed on FITC dilute solutions in ethanol/water, where thiourea groups are not present, showed that Cu^{II} can selectively interact with FITC, leading to a decrease in both absorbance and fluorescence intensity without formation of new optical absorption bands. FRET-type processes were therefore ruled out. A new FITC-Cu^{II} interaction mechanism was in turn suggested, which involves the formation of a fluorescein lactonic species where π-conjugation interruption leads to vanishing of the xanthene-centred optical transition moment[52] and, hence, to fluorescence quenching. This mechanism was further supported

by mass and tandem mass spectrometry data. A model-based analysis of the sensor response for varying Cu^{II} concentration is also reported.

An intramolecular charge-transfer process, triggered by Cu^{II} coordination to the quinonic oxygen atom at the 3 position of the xanthene moiety, is envisaged as a possible cause of

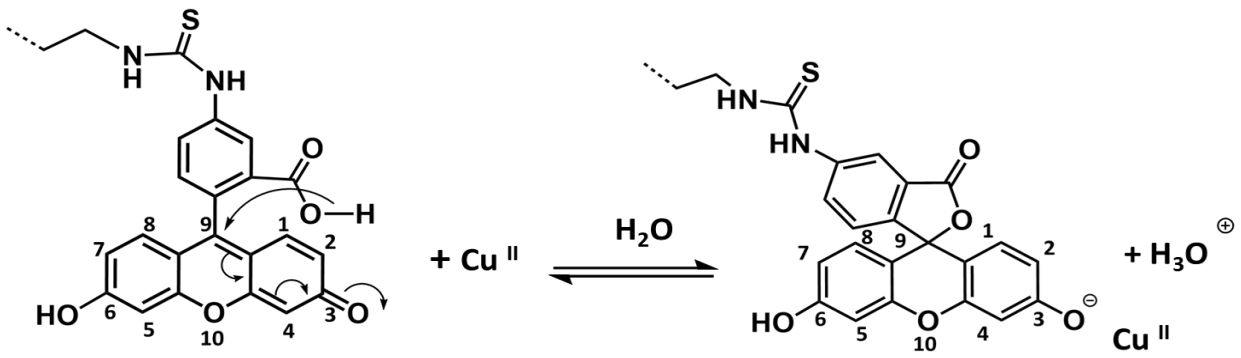

Scheme 2. Cu^{II}-triggered charge-transfer to the quinonic oxygen and lactonic fluorescein formation on the surface of the $Si@SiO_2$@APTES@FITC device.

the observed fluorescence quenching of the $Si@SiO_2$@APTES@FITC device (**Scheme 2**). The process leads to the formation of a spiranic lactone, resulting in fluorescein conjugation interruption, with consequent vanishing of the fundamental optical transition moment and fluorescence quenching.[52] This process, which is alternative to Cu^{II}-S interaction at the thioureidic groups of the device, clearly distinguishes the $Si@SiO_2$@APTES@FITC device from the thiourea-based fluorescent chemosensors reported in literature.

In order to provide experimental support to the suggested FITC-Cu^{II} interaction mechanism, FITC, FITC/Zn^{II} and FITC/Cu^{II} dilute solutions in 1:1 v/v EtOH/H_2O and pure EtOH were studied by Fluorescence, UV-Vis-Spectroscopy, and ESI mass (MS) and Collision-Induced Dissociation (CID) tandem mass (MS/MS) Spectrometry.

Addition of Cu^{II} to a FITC (~10^{-5} mol L^{-1}) solution led to a reduction in both Vis absorbance and fluorescence intensity of FITC (**Figure 7**). In EtOH/H_2O (1:1 v/v) (**Figure 7a**), the reduction in fluorescence intensity was of the same order of magnitude as that reported on the Si@SiO_2@APTES@FITC sensor, whereas, in pure EtOH (**Figure 7b**), it resulted in a 10-fold increase in terms of sensitivity towards Cu^{II} as compared to the on-chip device. The same experiment performed on FITC/Zn^{II} solutions produced no response in EtOH/H_2O, hence demonstrating FITC selectivity towards Cu^{II} in aqueous environment; in EtOH, a large signal reduction in both absorbance and fluorescence intensity was instead observed, showing a significant response also to Zn^{II}. Correlated reductions in Vis absorbance and fluorescence intensity, that is, the progressive conversion of FITC into a colorless and nonfluorescent species, is consistent with the formation of spiranic lactones in the FITC/metal ions mixed solutions.

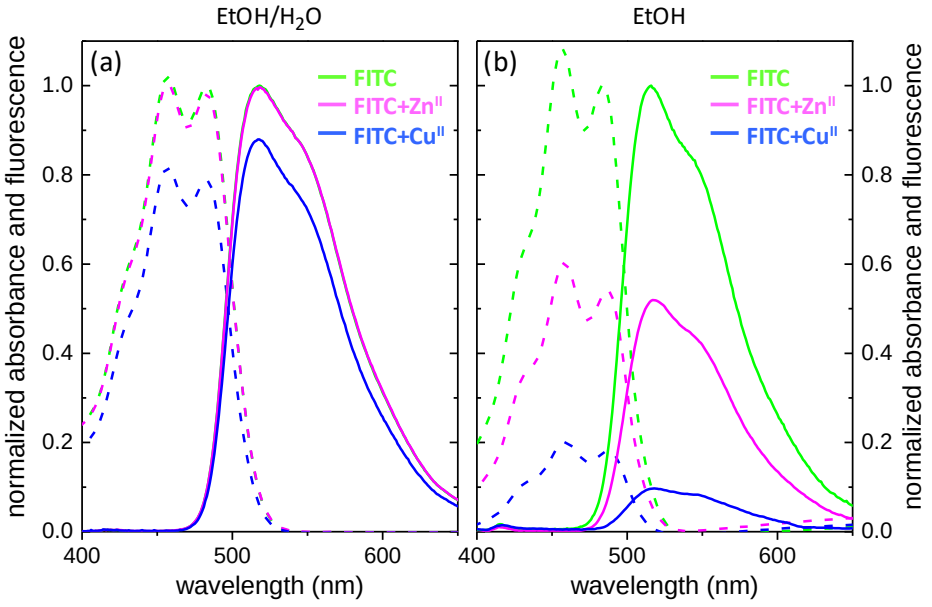

Figure 7. Absorbance spectra (dashed lines) and fluorescence spectra, photoexcited at 370 nm (solid lines) of FITC (green), FITC/Zn^{II} (magenta) and FITC/Cu^{II} (blue) in (a) 1:1 v/v EtOH/H_2O, and (a) EtOH. FITC concentration is 1.2×10^{-5} mol·L^{-1}; Zn^{II} and Cu^{II} concentrations are 1.2×10^{-4} mol·L^{-1} (a) and 1.2×10^{-5} mol·L^{-1} (b). Data are normalized to the 483 nm absorbance peak value and maximum fluorescence intensity of pure FITC solutions.

ESI-MS spectra of FITC and FITC/Cu^{II} ethanol solutions, acquired in positive ion mode, are reported in Figure **8a**, showing no evidence of the formation of FITC-Cu^{II} adducts.

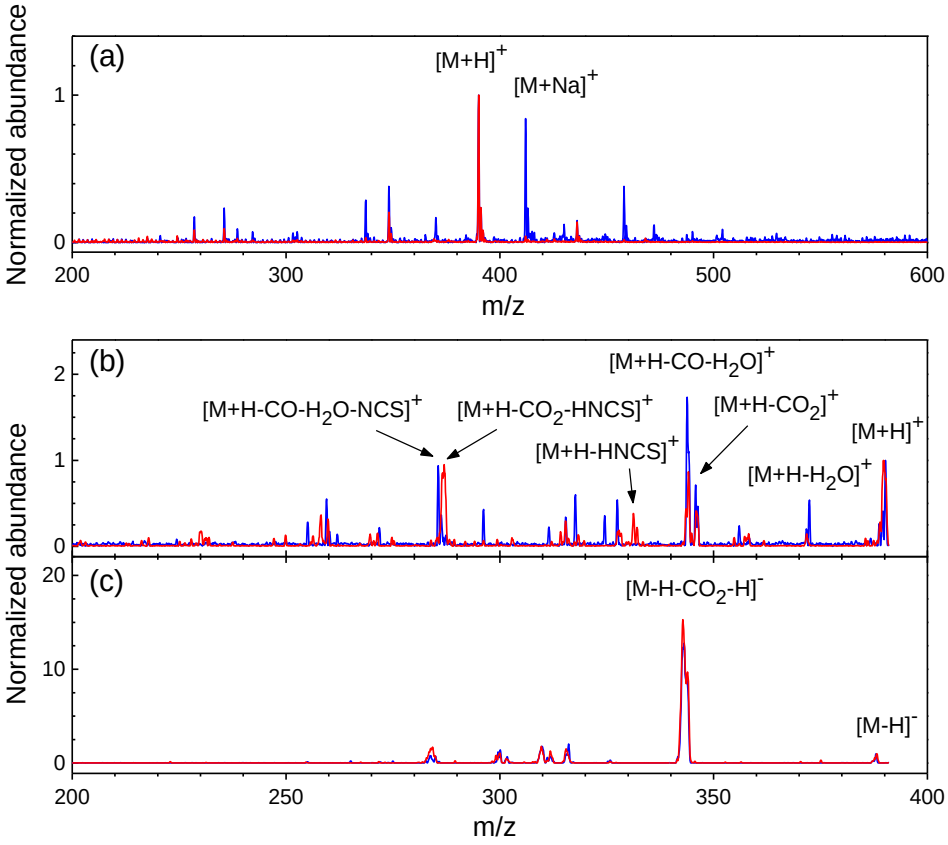

Figure 8. (a), ESI-CID MS/MS spectra in positive mode (b), and ESI-CID MS/MS spectra in negative mode (c) of FITC (blue lines) and FITC/Cu^{II} equimolar solution (red lines). All spectra are normalized to the $[M\pm H]^{\pm}$ parent peak intensity. Relevant peak assignments are displayed.

In positive ion mode, the lactonic anion is supposed to be stabilized in a double protonation process, shown in **Scheme 3.**

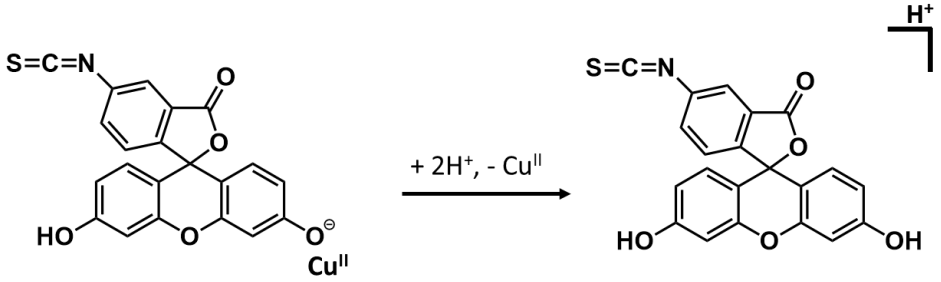

Scheme 3. Double protonation process of lactonic fluorescein anion by ESI in positive ion mode.

Structural isomers obtained in positive ion mode could be distingu ished in ESI-CID MS/MS spectra. $[M+H]^+$ fragmentation spectrum of the pure FITC sample revealed a much larger loss of water, carbon monoxide and carbon dioxide than that of FITC/Cu^{II} equimolar solution, which is consistent with the formation of a lactonic species in the FITC/Cu^{II} solution (**Figure 7b**). Further confirmation of the formation of lactonic fluorescein comes from the observation of the $[M+H-HNCS]^+$ mass peak (m/z = 331), only in the FITC/Cu^{II} solution. The fragmentation mechanism is shown in **Scheme 4.**

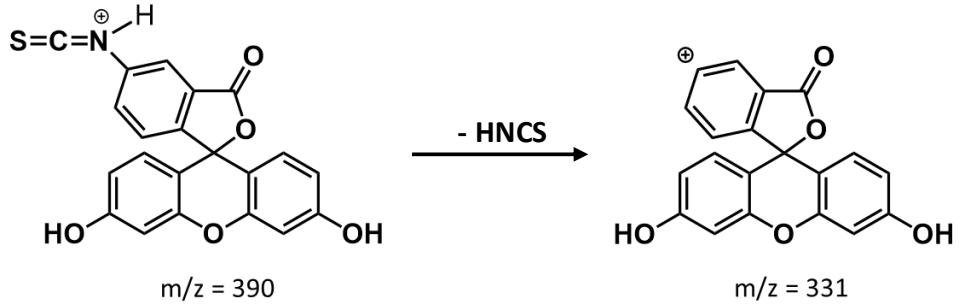

Scheme 4. Fragmentation of protonated lactonic fluorescein leading to the formation of phenyl carbocation with moderate stability.

Remarkably, in the protonated open FITC, the same fragmentation mechanism would result in an excess of positive charge on the phenyl ring, compared to the lactonic form, owing to the negative mesomeric effect by the quinonic oxygen *via* the phenyl/xanthene conjugated system (not shown), and can thus be ruled out.

In negative ion mode, FITC lactonic form is transformed into the open structure (**Scheme 5**), and, consequently, FITC fragmentation spectrum should be the same in both FITC and FITC/Cu^{II} solutions.

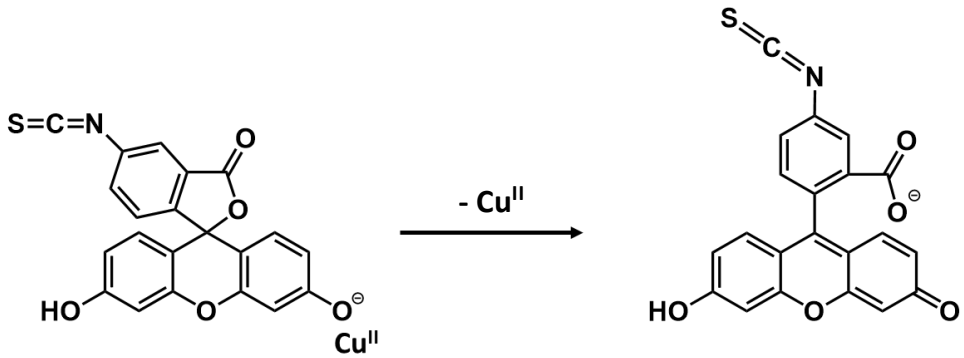

Scheme 5. Lactonic-into-open fluorescein anion conversion by ESI in negative ion mode.

This was actually verified experimentally: both FITC and FITC/Cu^{II} negative ion ESI-CID (20 eV) MS/MS spectra (**Figure 8**c) exhibited a very intense base peak at m/z = 343, which was identified as [M-H-CO_2-H]$^-$, that is, a stable radical anion obtained from deprotonated FITC, through sequential loss of CO_2 and a hydrogen atom (**Scheme 6**).

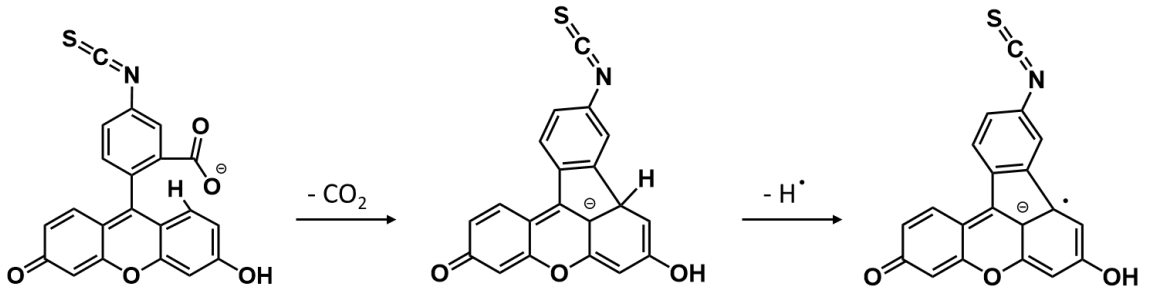

Scheme 6. Deprotonated FITC undergoing sequential loss of carbon dioxide and a hydrogen atom towards the formation of a cyclic radical anion with m/z = 343.

Results of ESI-mass and CID MS/MS experiments on ethanol solutions were confirmed in EtOH/H_2O solutions.

Optical and ESI-CID MS/MS data are consistent with the formation of a lactonic fluorescein species in the FITC/Cu^{II} solutions, suggesting the possibility of a direct FITC-Cu^{II} interaction mechanism at the surface of the Si@SiO_2@APTES@FITC sensor.

It is also worth discussing on the Limit of Detection (LoD) of the chip sensors. LoD is defined as the analyte concentration that produces a response signal equal to a given threshold level, which is usually set to three standard deviations of the reference signal (F_0) from its mean value. In principle, the reference signal-to-noise ratio can be made as large as wanted simply by increasing signal averaging, which means that the LoD can virtually be lowered down to any desired value instrumentally. In practice, time constraints due to a limited system stability and/or extrinsic application requirements put an upper bound to the amount of time that can be used for signal averaging, and thus a lower bound to the sensor LoD. In the reported silicon-based sensors, although step-by-step characterization confirmed a good quality of the planar platforms, surface disorder appeared to result in non-negligible sample-to-sample fluctuations of the sensor fluorescence intensity (**Figure 6c**). The resulting standard error bars of data points in **Figure 6d** currently set the Cu^{II} LoD to a few ppm, compatible with current limits for copper in drinking waters. More

meaningful is the sensitivity value of 0.3 ppm^{-1}, which could in principle be exploited to greatly improve the LoD in silicon-based sensors with reduced chip-to-chip signal fluctuations.

Another point of interest resides in the fluorescence efficiency that can be achieved upon fluorophore conjugation to the silicon substrate. The strong reduction reported for the FITC fluorescence lifetime upon surface grafting (180 ps against the 2.6 ns value found in water solution, **Figure 5c**) hints to a strong sensitivity of FITC fluorescence to surface loading, possibly arising from the sizable absorption-emission spectral overlap, which causes fluorescence self-quenching through FITC-to-FITC photoinduced energy transfer at the sensor surface.[53] This issue, often encountered in bioanalytical applications of fluorescence, opens up to the use of organic dyes with shorter critical (Foerster's) energy transfer distance and, hence, less sensitive to fluorescence self-quenching.

2.3 Experimental Section

2.3.1 Materials

Tetraethoxysilane (TEOS, purity >99%), aminopropyltriethoxysilane (APTES, purity >97%), fluorescein isothiocyanate (FITC, purity >95%), 3-(N-morpholino)propanesulfonic acid (MOPS, purity >99%), ethylenediaminetetraacetic acid (EDTA, purity >99%), metal perchlorates (Al^{III}, Cu^{II}, Zn^{II}, Ag^{I}, Cd^{II}, Hg^{II}, Pb^{II}, purity >99%), absolute ethanol (EtOH, purity >99%), and hexane (purity >99%), were used as received without further purification. It was used Fresh distilled water purified by a Milli-Q system (Millipore) was used for each measurement.

All reactants and solvents were purchased from Sigma Aldrich, exception made for FITC (Tokyo Chemical Industry, TCI). Silicon wafers (100 orientation, P/B doped, resistivity 5–10 Ω-cm, thickness 380 µm) were purchased from Siegert Wafer.

2.3.2 Silica synthesis and deposition

The silica sol precursor was prepared by mixing TEOS, EtOH and distilled water under stirring at room temperature (RT). Subsequently, HCl was added to the sol and the mixture was maintained under stirring at 60 °C overnight. The molar ratio of the starting solution was TEOS : H_2O : EtOH : HCl = 1 : 5 : 6 : 0.065. A diluted solution was prepared by mixing freshly prepared TEOS solutions with a proper amount of EtOH (volume ratio 1:10) in a closed vessel at RT. Silica films were deposited on 100-oriented silicon substrates cut into ~15×15 mm^2 pieces for morphological and optical characterization, and ~7×7 mm^2 pieces for sensing measurements. After deposition, samples were dried at RT for 24 h.

2.3.3 Silica@APTES functionalization

The functionalization of the ultrathin silica films on silicon substrates with amino groups was done by immersion of the substrates in a 1 mM APTES/hexane solution for 10 s. The films were then rinsed with hexane followed by acetone to remove the excess of APTES.

2.3.4 Silica@APTES@FITC functionalization

A FITC in EtOH solution was prepared by dissolving 8 mg (0.02 mmol) of FITC in 10 mL of EtOH. Silica@APTES films on silicon substrates, *vide supra*, were immersed in the FITC solution for 30 min. The reaction was performed at RT in dark conditions. Upon completion of the reaction, the FITC-functionalized silicon substrates were rinsed with EtOH and acetone to remove the excess of FITC, and then kept in 20 mL of milli-Q water for 20 minutes before characterization measurements.

2.3.5 Morphological characterization

A NT-MDT Solver-Pro atomic-force microscopy (AFM) was used to study the topography and roughness of the sample surface. AFM measurements were performed at 0.5-1 Hz scan speed in semi-contact mode in air. Topography image analysis and calculation of surface roughness were performed by using WSxM 5.0 Develop3.2 software.[44] The measurements

were performed on at least three different points of the same sample to assess the uniformity of the layers.

2.3.6 Surface wettability experiments

Water Contact Angle (CA) measurements on the functionalized sample surfaces were performed at 22 °C by using a Kruss drop shape analyzer (DSA 30S) and analyzed by the Kruss Advance software. A sessile drop method was used to measure a contact angle of a 1 μL distilled water drop. The measured CA was the average between the left and right contact angles. The measurements were performed on at least three different points of the same sample to assess the uniformity of the layers.

2.3.7 Optical spectroscopy and fluorescence lifetime measurements

Reflectance spectroscopy measurements were made under sample direct illumination in a dual-beam spectrophotometer (Agilent Technologies Cary 5000 UV-Vis-NIR) equipped with a diffuse reflectance accessory. Fluorescence spectra for samples in air and in a MOPS buffer in a quartz cuvette were measured under 355-nm irradiation of the samples by a passively Q-switched powerchip laser (Teem Photonics PNV-M02510) operating in pulsed regime (350-ps pulses, 1-kHz repetition rate). The fluorescence was spectrally resolved using a single-grating spectrometer (Princeton Instruments Acton SpectraPro 2300i) and acquired by a thermoelectrically cooled Vis CCD camera (AndorNewton^{EM}). Fluorescence lifetime in air were measured under sample irradiation at 350 nm by an optical parametric amplifier (Light Conversion TOPAS-C) pumped by a regenerative Ti:Sapphire amplifier (Coherent Libra-HE), delivering 200-fs-long pulses at 1 kHz repetition rate. The fluorescence was spectrally dispersed using a single-grating spectrometer (Princeton Instruments Acton SpectraPro2300i) and acquired by a Vis streak camera (Hamamatsu C1091). Pump fluence was kept below 50 $\mu J/cm^2$ per pulse in all fluorescence experiments to prevent sample degradation.

2.3.8 Sensing Measurements

Sensing performances towards different metal cations were assessed by fluorescence spectroscopy with the silicon-chip sensors placed in a 1-cm-thick quartz cuvette. The cuvette was then filled with 1500 μL of aqueous MOPS buffer (70 mM, pH = 7.2) and 60 μL of 0.1 mM aqueous solution of various perchlorate salts (Al^{III}, Cu^{II}, Zn^{II}, Ag^{I}, Cd^{II}, Hg^{II}, Pb^{II}) was added. The sensitivity towards Cu^{II} ions was evaluated through fluorescence titration experiments in the 0-120 μL range. A waiting time of 3 min was set before each measurement to ensure that the device-analyte interaction had reached equilibrium. Device regeneration after immersion into Cu^{II} solution was accomplished by sensor chip sonication in 3 mL of EDTA solution (0.1 M) for 10 min. Three generation cycles were performed on each chip sensor.

2.3.9 Mass spectrometry

Mass spectra were recorded using a triple quadrupole QqQ Varian 310-MS mass spectrometer using the atmospheric-pressure Electrospray Ionization (ESI) technique. Sample solutions (20 μL) were injected into the ESI source by a Rheodyne® model 7125 injector connected to a HPLC Varian 212 LC pump, with a 50 L min^{-1} methanol flow. Experimental conditions: Dwell time 2 s, needle voltage 3000 V, shield voltage 600 V, source temperature 60 °C, drying gas pressure 20 psi, nebulizing gas pressure 20 psi, detector voltage 1600 V. Mass spectra were recorded in the 100–600 m/z range. Collision-Induced Dissociation (CID) tandem mass (MS/MS) experiments were performed using argon as the collision gas (1.8 psi). Collision energy was varied from 20 to 40 eV.

2.4 Conclusion

Silicon-based fluorescent chips for the detection of metal ions in water were reported[54], where the xanthene-based fluorophore, FITC, was covalently linked to an amino-silanized silicon surface *via* thiourea formation. These solid-state hybrid platforms exhibited selectivity towards copper(II) with good detection limit, competitive sensitivity, and regeneration capability using a metal-chelating agent. An original FITC-Cu^{II} reaction mechanism involving the formation of a lactonic

fluorescein species, exhibiting disappearance of the fundamental optical transition moment, is proposed as a possible cause of fluorescence quenching. The sensing platform architecture, where recognition/fluorescent units are integrated on a silicon chip *via* a layer-by-layer functionalization approach, is very versatile owing to the possibility of tuning the selectivity to other metal ions or different types of analytes by changing the fluorophore or the anchoring group. This represents a viable strategy towards silicon-integrated fluorescent devices for remote detection of a range of metal ions in water.

2.5 References

1 Y. Liu, P. Liang and L. Guo, *Talanta*, 2005, **68**, 25–30.
2 J. S. Becker, A. Matusch, C. Depboylu, J. Dobrowolska and M. V. Zoriy, *Anal. Chem.*, 2007, **79**, 6074–6080.
3 A. P. S. Gonzáles, M. A. Firmino, C. S. Nomura, F. R. P. Rocha, P. V. Oliveira and I. Gaubeur, *Anal. Chim. Acta*, 2009, **636**, 198–204.
4 K. P. Carter, A. M. Young and A. E. Palmer, *Chem. Rev.*, 2014, 114, 4564–4601.
5 C. Guo, A. C. Sedgwick, T. Hirao and J. L. Sessler, *Coord. Chem. Rev.*, 2021, **427**, 213560.
6 S. P. Wu, K. J. Du and Y. M. Sung, *Dalt. Trans.*, 2010, **39**, 4363–4368.
7 M. Li, H. Gou, I. Al-Ogaidi and N. Wu, *ACS Sustain. Chem. Eng.*, 2013, **1**, 713–723.
8 D. Wu, A. C. Sedgwick, T. Gunnlaugsson, E. U. Akkaya, J. Yoon and T. D. James, *Chem. Soc. Rev.*, 2017, **46**, 7105–7123.
9 G. P. C. Drummen, *Molecules*, 2012, **17**, 14067–14090.
10 Y. Fu and N. S. Finney, *RSC Adv.*, 2018, **8**, 29051–29061.
11 Y. Zhao, X. B. Zhang, Z. X. Han, L. Qiao, C. Y. Li, L. X. Jian, G. L. Shen and R. Q. Yu, *Anal. Chem.*, 2009, **81**, 7022–7030.
12 L. Lvova, F. Caroleo, A. Garau, V. Lippolis, L. Giorgi, V. Fusi, N. Zaccheroni, M. Lombardo, L. Prodi, C. Di Natale and R. Paolesse, *Front. Chem.*, 2018, **6**, 1–10.
13 N. De Acha, C. Elosúa, J. M. Corres and F. J. Arregui, *Sensors (Switzerland)*, , DOI:10.3390/s19030599.
14 F. Le Guern, V. Mussard, A. Gaucher, M. Rottman and D. Prim, *Int. J. Mol. Sci.*, 2020, **21**, 1–23.
15 L. Petri, P. A. Szijj, Á. Kelemen, T. Imre, Á. Gömöry, M. T. W. Lee, K. Hegedus, P. Ábrányi-Balogh, V. Chudasama and G. M. Keseru, *RSC Adv.*, 2020, **10**, 14928–14936.
16 A. J. Counsell, S. J. Walsh, N. S. Robertson, H. Sore and D. R. Spring, *Org. Biomol. Chem.*, 2020, 4739–4743.
17 C. Zong, K. Ai, G. Zhang, H. Li and L. Lu, *Anal. Chem.*, 2011, **83**, 3126–3132.
18 L. Wang, B. Li, L. Zhang, L. Zhang and H. Zhao, *Sensors Actuators, B Chem.*, 2012, **171**–**172**, 946–953.
19 Y. Qiao and X. Zheng, *Analyst*, 2015, **140**, 8186–8193.
20 C. M. Carbonaro, F. Orrù, P. C. Ricci, A. Ardu, R. Corpino, D. Chiriu, F. Angius, A.

Mura and C. Cannas, *Microporous Mesoporous Mater.*, 2016, **225**, 432–439.
21 N. Zhang, G. Li, Z. Cheng and X. Zuo, *J. Hazard. Mater.*, 2012, **229**–**230**, 404–410.
22 Y. Zhang, B. Li, H. Ma, L. Zhang and W. Zhang, *J. Mater. Chem. C*, 2017, **5**, 4661–4669.
23 F. Rouhani, A. Morsali and P. Retailleau, *ACS Appl. Mater. Interfaces*, 2018, **10**, 36259–36266.
24 J. P. Lafleur, A. Jönsson, S. Senkbeil and J. P. Kutter, *Biosens. Bioelectron.*, 2016, **76**, 213–233.
25 E. Luan, H. Shoman, D. M. Ratner, K. C. Cheung and L. Chrostowski, *Sensors (Switzerland)*, 2018, 18.
26 M. Zhu, M. Z. Lerum and W. Chen, *Langmuir*, 2012, **28**, 416–423.
27 T. J. Lee, L. K. Chau and C. J. Huang, *Langmuir*, 2020, **36**, 5935–5943.
28 J. A. Howarter and J. P. Youngblood, *Langmuir*, 2006, **22**, 11142–11147.
29 V. K. S. Hsiao, J. R. Waldeisen, Y. Zheng, P. F. Lloyd, T. J. Bunning and T. J. Huang, *J. Mater. Chem.*, 2007, **17**, 4896–4901.
30 X. Chen, A. Yamaguchi, M. Namekawa, T. Kamijo, N. Teramae and A. Tong, *Anal. Chim. Acta*, 2011, **696**, 94–100.
31 J. Klug, L. A. Pérez, E. A. Coronado and G. I. Lacconi, *J. Phys. Chem. C*, 2013, **117**, 11317–11327.
32 T. Baumgärte, C. von Borczyskowski and H. Graaf, *Beilstein J. Nanotechnol.*, 2013, **4**, 218–226.
33 S. W. Han, S. Lee, J. Hong, E. Jang, T. Lee and W. G. Koh, *Biosens. Bioelectron.*, 2013, **45**, 129–135.
34 R. Kateklum, B. Gauthier-Manuel, C. Pieralli, S. Mankhetkorn and B. Wacogne, *Sensors Actuators, B Chem.*, 2017, **248**, 605–612.
35 A. Imhof, M. Megens, J. J. Engelberts, D. T. N. De Lang, R. Sprik and W. L. Vos, *J. Phys. Chem. B*, 1999, **103**, 1408–1415.
36 C. Zhong, Y. Wang, G. Ma and R. Li, *Anal. Methods*, 2016, **8**, 3809–3815.
37 Y. Zhou, J. Ding, T. Liang, E. S. Abdel-Halim, L. Jiang and J. J. Zhu, *ACS Appl. Mater. Interfaces*, 2016, **8**, 6423–6430.
38 T. Anand and M. Sankar, *Anal. Methods*, 2020, **12**, 4526–4533.
39 M. Vonlanthen and N. S. Finney, *J. Org. Chem.*, 2013, **78**, 3980–3988.
40 R. S. Kathayat, L. Yang, T. Sattasathuchana, L. Zoppi, K. K. Baldridge, A. Linden and N. S. Finney, *J. Am. Chem. Soc.*, 2016, **138**, 15889–15895.
41 Z. Xu, Q. Meng, Q. Cao, Y. Xiao, H. Liu, G. Han, S. Wei, J. Yan and L. Wu, *Anal. Chem.*, 2020, **92**, 2201–2206.
42 G. Sivaraman, M. Iniya, T. Anand, N. G. Kotla, O. Sunnapu, S. Singaravadivel, A. Gulyani and D. Chellappa, *Coord. Chem. Rev.*, 2018, **357**, 50–104.
43 A. K. Boal and A. C. Rosenzweig, *Chem. Rev.*, 2009, **109**, 4760–4779.
44 I. Horcas, R. Fernández, J. M. Gómez-Rodríguez, J. Colchero, J. Gómez-Herrero and A. M. Baro, *Rev. Sci. Instrum.*, , DOI:10.1063/1.2432410.
45 P. Pallavicini, G. Dacarro, M. Galli and M. Patrini, *J. Colloid Interface Sci.*, 2009, **332**, 432–438.
46 J. Kim, P. Seidler, L. S. Wan and C. Fill, *J. Colloid Interface Sci.*, 2009, **329**, 114–119.
47 S. Zhang, L. Ding, F. Lü, T. Liu and Y. Fang, *Spectrochim. Acta - Part A Mol. Biomol. Spectrosc.*, 2012, **97**, 31–37.
48 F. Floris, C. Figus, L. Fornasari, M. Patrini, P. Pellacani, G. Marchesini, A. Valsesia, F.

Artizzu, D. Marongiu, M. Saba, A. Mura, G. Bongiovanni, F. Marabelli and F. Quochi, *J. Phys. Chem. Lett.*, 2014, **5**, 2935–2940.

49 S. Krzewska and H. Podsiadły, *J. Inorg. Nucl. Chem.*, 1980, **42**, 83–86.

50 S. Krzewska, H. Podsiadły and L. Pajdowski, *J. Inorg. Nucl. Chem.*, 1980, **42**, 87–88.

51 S. Krzewska, H. Podsiadły and L. Pajdowski, *J. Inorg. Nucl. Chem.*, 1980, **42**, 89–94.

52 C. Liu, S. Huang, H. Yao, S. He, Y. Lu, L. Zhao and X. Zeng, *RSC Adv.*, 2014, **4**, 16109–16114.

53 G. Hungerford, J. Benesch, J. F. Mano and R. L. Reis, *Photochem. Photobiol. Sci.*, 2007, **6**, 152–158.

54 M.Oggianu, C. Figus, S.Ashoka-Sahadevan,N.Monni, D.Marongiu, M. Saba, A. Mura, G. Bongiovanni,C.Caltagirone, V. Lippolis, C. Cannas, E. Cadoni,M. L. Mercuri and F. Quochi. *J. Mater. Chem. C*, 2021, **submitted**.

Chapter 3

Hybrid Ratiometric Fluorescent Platforms

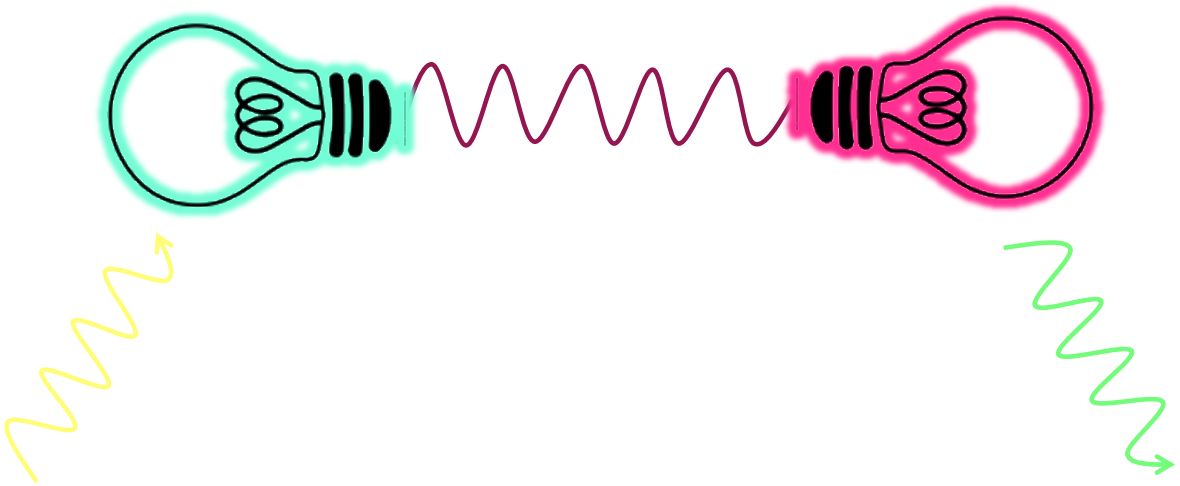

3.1 Introduction

The design of fluorescent probes has been receiving much attention as alternative analytical method given their remarkable advantages such as selectivity, sensitivity, low-cost, simple operations and real time monitoring.[1,2] Fluorescent probes are classified into two types: intensity-based and ratiometric chemosensors. The main limitation of intensity-based chemosensors is that the probe concentration, environment and/or excitation intensity may influence the intensity measurements.[3] Given their excellent photophysical properties compared to conventional intensity based fluorescent probes, the smart design of Ratiometric Chemosensors is a recent challenge. Ratiometric Fluorescent Probes (RFPs) allow the simultaneous measurement of two fluorescence signals at different wavelengths followed by calculation of their intensity ratio, which can provide more precise measurement results than intensity-based fluorescent probes. RFPs are commonly based on Fluorescent Resonance Energy Transfer (FRET) and Intramolecular charge transfer (ICT).[4] FRET is a nonradiative process in which an excited dye donor transfers energy to a dye acceptor in the ground state.[5] Ratiometric Fluorescent platforms should consist of an energy donor, a linker and an energy acceptor, as shown in **Figure 1**.

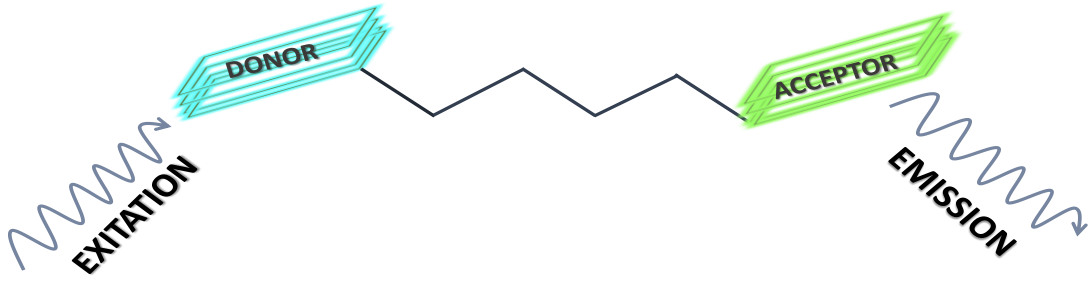

Figure 1. Schematic representation of a FRET based chemosensor

Rhodamine fluorophores, given their excellent photophysical properties *i.e.* excitation and emission in the visible region, high fluorescence quantum yield, high extinction coefficient and good photostability, have been largely employed as acceptors to fabricate FRET based platforms.[6]

Under neutral conditions, the rhodamine amide derivatives in their spirolactam form, are colorless and not fluorescent. Metal ions or acidic conditions can induce a fluorescence

enhancement due to a structural change from the spirocyclic to the ring opening-form, showing a strong fluorescence emission and a significant color change.[7,8] The protonation mechanism of the carbonyl group leads to a resonance-stabilized intermediate (**Scheme 1, II**), when the positive charge is delocalized between nitrogen and oxygen. The spirolactam opening is due to the electronic rearrangement that breaks the intermediate, producing a conjugated moiety. The absorption and emission spectra of the opening-form show a band at in the 550-580 nm range, thus making rhodamines optimal energy acceptors in FRET based systems.

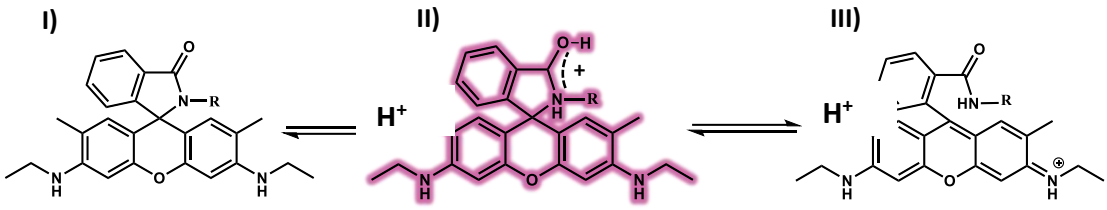

Scheme 1. Spirolactam opening mechanism

Rhodamine 6G (RhO6G) and Rhodamine B (RhOB), given their low-cost, are the most employed to fabricate fluorescence probes. The main difference between Rho 6G and Rho B (**Figure 2a**) is the presence of two methyl groups in 2 and in 7 positions, which, due to the steric effects, make RhO 6G much more sensitive than RhOB.[9,10]

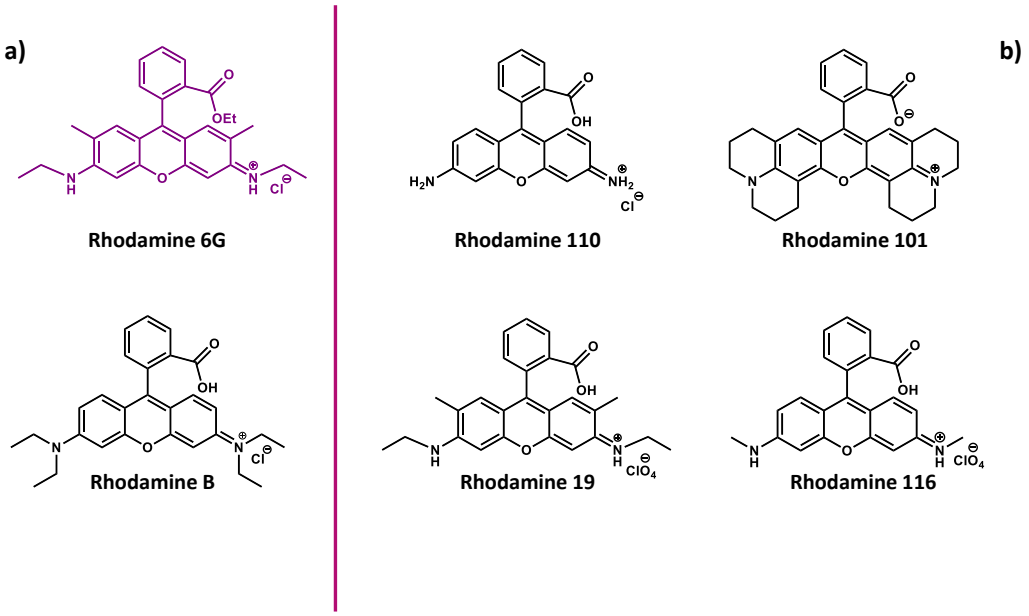

Figure 2 a-b. Commercially available Rhodamines.

By modifying rhodamine skeleton in three different positions, the xanthene ring, the carboxyphenilic ring or the carboxylic acid group, different rhodamine derivatives can be obtained, suitable for the conjugation with proper fluorophores to construct FRET chemosensors.[11–13] To date, several rhodamine based FRET platforms have been synthesized for detection/monitoring of different analytes in water and physiological environments. Very recently James *et al.*[5] traced a roadmap on the design principles required for the construction of FRET-based small-molecule probes, providing, interestingly, several donor–acceptor combinations for FRET scaffolds, since 2008 and a basic tutorial on how they work. For example, a naphtalimide-rhodamine fluorescent platform was synthesized, by using an ethylenediamine moiety as spacer, by Fang *et al*.[14] showing a good selectivity towards Hg^{II}, with a limit of detection up to $8 \cdot 10^{-7}$ M. At pH=7.2 the probe displayed a blue fluorescence peak, centered at 485 nm, when it is excited at 410 nm. Upon addition of Hg^{II}, the intensity of the peak at 485 nm, due to the naphtalimidic core, decreases and a new peak, centered at 585 nm, attributed to rhodamine moiety, gradually increases. Qin *et al.*[15] developed a FRET based chemosensor consisting of a hydroxy quinoline moiety as donor unit, which emits at 440 nm and overlaps the absorption band of rhodamine. This probe shows a good selectivity towards Fe^{III}. The interaction between the probe and the target ion leads to a decrease of quinoline emission and an increase of rhodamine emission, centered at 550 nm.

Dansyl amide derivatives are well-known fluorescent compounds largely employed in the construction of FRET ratiometric chemosensors, given their peculiar photophysical properties, in particular large Stokes shifts, due to the charge-transfer process of the singlet excited state of the electron-withdrawing sulfonamidic group and the dimethylamino electron-donating moiety on the naphthalenic core. The dansyl moiety exhibits a strong and broad emission in the 450-650 nm visible range, which overlaps the absorption band of rhodamine 6G in its ring opening-form, providing the optimal conditions for FRET process.[16]

The synthesis and characterization of the novel fluorescent ratiometric chemosensor (**RhO-L_3**) is, herein, reported, by conjugating, *via* an ethylenediamine spacer, the RhO 6G derivative, **RhO-L_1**, as acceptor unit, with the dansyl moiety, **RhO-L_2**, as donor unit, (**Figure 3)**. The interaction between this hybrid platform and the proton is studied in a wide range of pH, through a multi-technique approach, involving Uv-Vis Absorption,

Photoluminescence (PL) and time-resolved PL Spectroscopies, Mass Spectrometry and Potentiometric titrations. The aim is to get deep insight into the proton-mediated spirolactam/ring opening mechanism. All experimental results are supported by preliminary Density Functional Theoretical (DFT) calculations. Monitoring pH is of paramount importance in environmental sciences and biomedicine.[17] In particular intracellular pH plays a key role in many cellular processes such as cellular metabolism,[18] apoptosis, cellular proliferation and chemotaxis.[19] Most of commercially available fluorescent probes work well in the 4-9 pH range,[20–22] but they are not capable to detect very low pH ranges (1-4). Some media as industrial waste water and the fluid into the human stomach are extremely acid and some microorganisms including *Helicobacter pylori* and acidophiles species prefer such extreme conditions, therefore the development of fluorescent platforms for pH monitoring, in highly acidic media, although the progress made in this field, still represents a challenge.

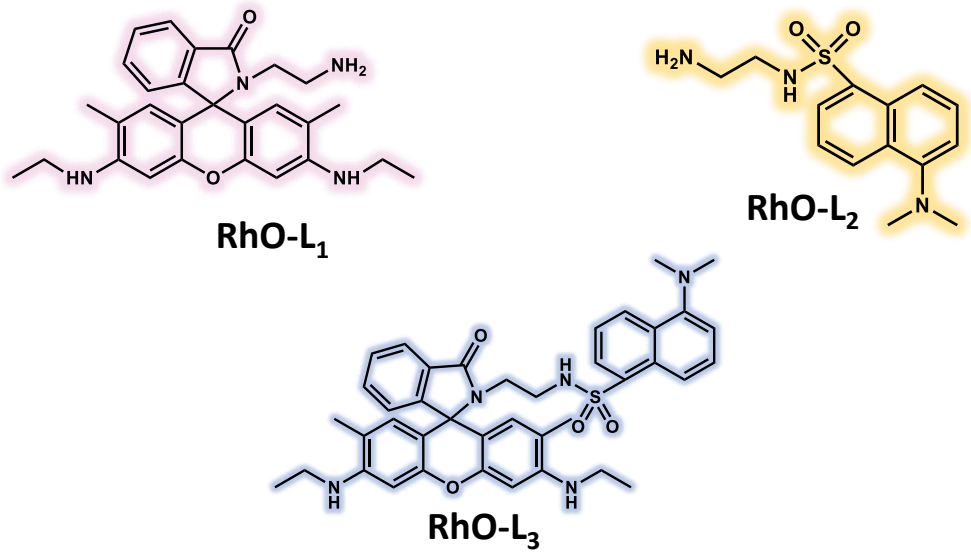

Figure 3. Synthesized Fluorescent FRET Units.

3.2 Results and Discussion

3.2.1 Synthesis and Characterization

RHO-L$_3$ has been synthesized starting from Rhodamine ethylenediamine (**RHO-L$_1$**) and Dansyl chloride, as shown in **Scheme 2**. **RHO-L$_2$** has been synthesized as reference for photophysical measurements.

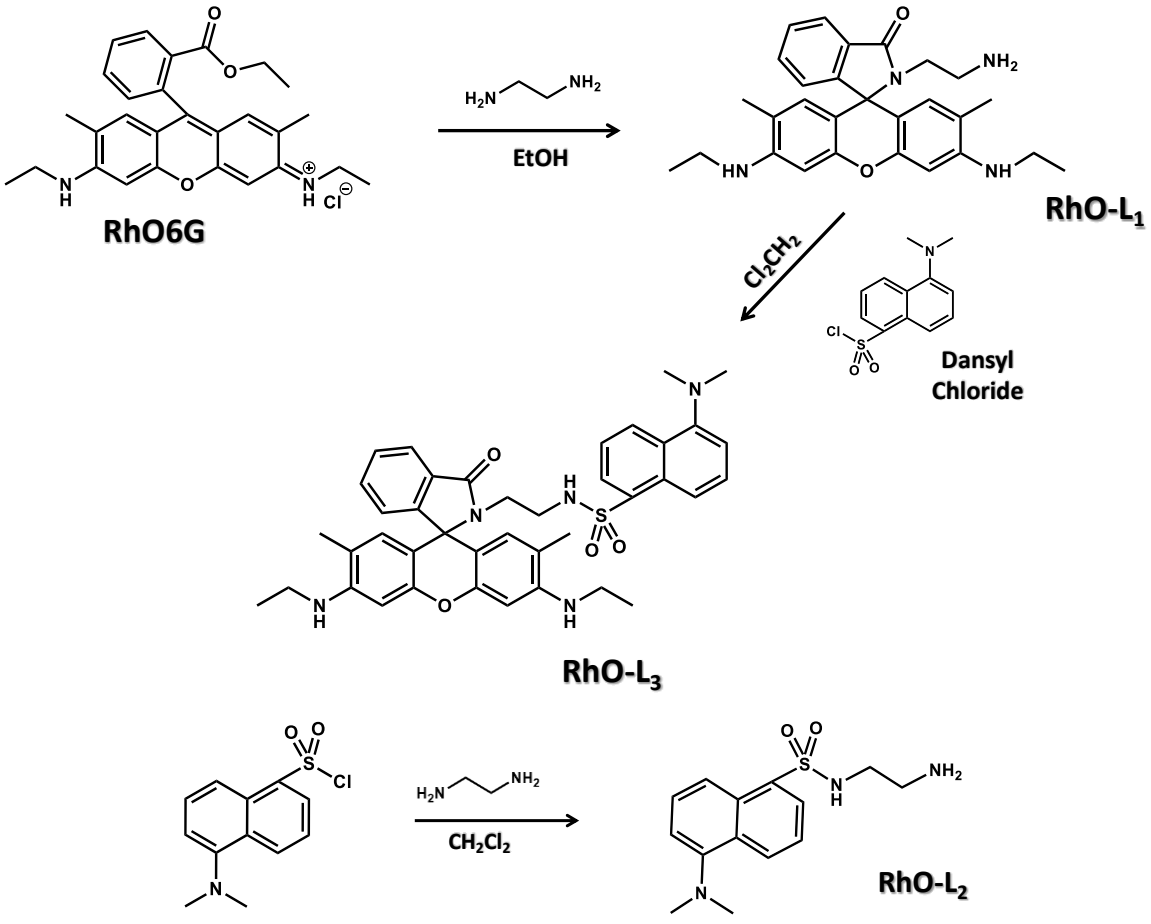

Scheme 2. Synthesis of **RhO-L$_1$**, **RhO-L$_2$**, **RhO-L$_3$**.

The absorption spectrum of **RhO-L$_3$**, shown in **Figure 4a**, displays two peaks at 303 nm and 333 nm, highlighting that **RhO-L$_3$** is the combination of **RhO-L$_1$** and **RhO-L$_2$** and suggesting that the rhodamine moiety, in neutral pH conditions, is in the ring-closed spirolactam form.

Figure 4b shows that **RhO-L$_2$** and **RhO-L$_3$**, consisting of dansyl amide moiety, emit at 520 nm, while **RHO-L$_1$**, which is presents in the spirolactam form, doesn't show fluorescence.

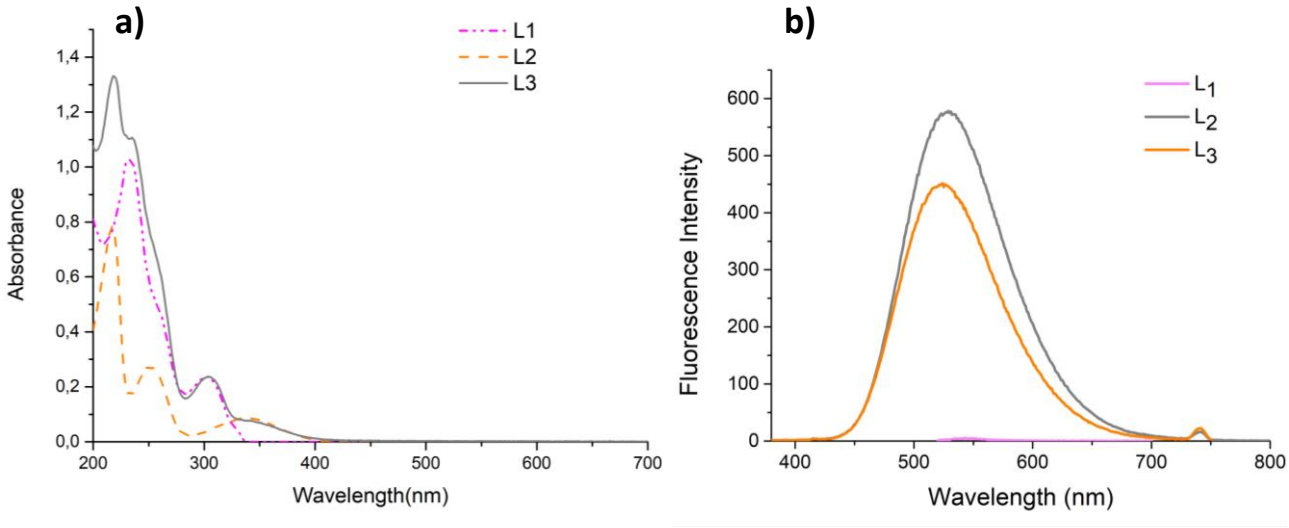

Figure 4. **a)** Absorbance and **b)** Fluorescence spectra of **RHO-L$_1$**, **RHO-L$_2$** **RHO-L$_3$**.

Figure 5 shows the spectral-overlap between the absorption band of the acceptor unit (Rhodamine) and the emission band of the donor unit (Dansyl), which is a crucial prerequirement for FRET process.

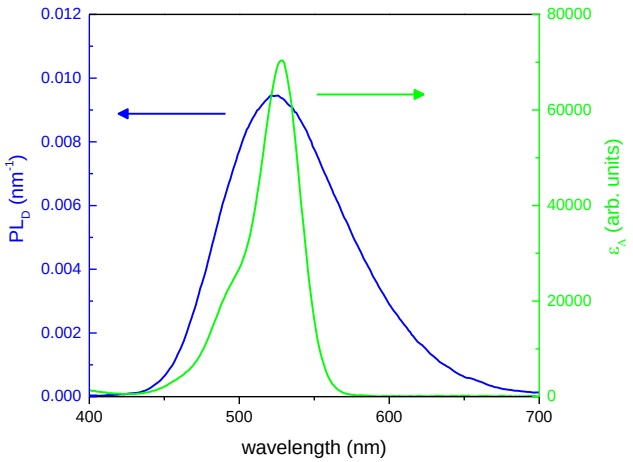

Figure 5. Dansyl-centered emission spectrum (PL$_D$, blue curve) and rhodamine-centered absorption spectrum (green curve) showing donor-acceptor spectral overlap, enabling a dansyl-to-rhodamine FRET process in **RhO-L$_3$**.

Interestingly, an increase of absorbance *vs* time is observed in the Uv-VIS spectra of **RhO-L_3**, performed at different times, as shown in **Figure 6 (d-f)**.

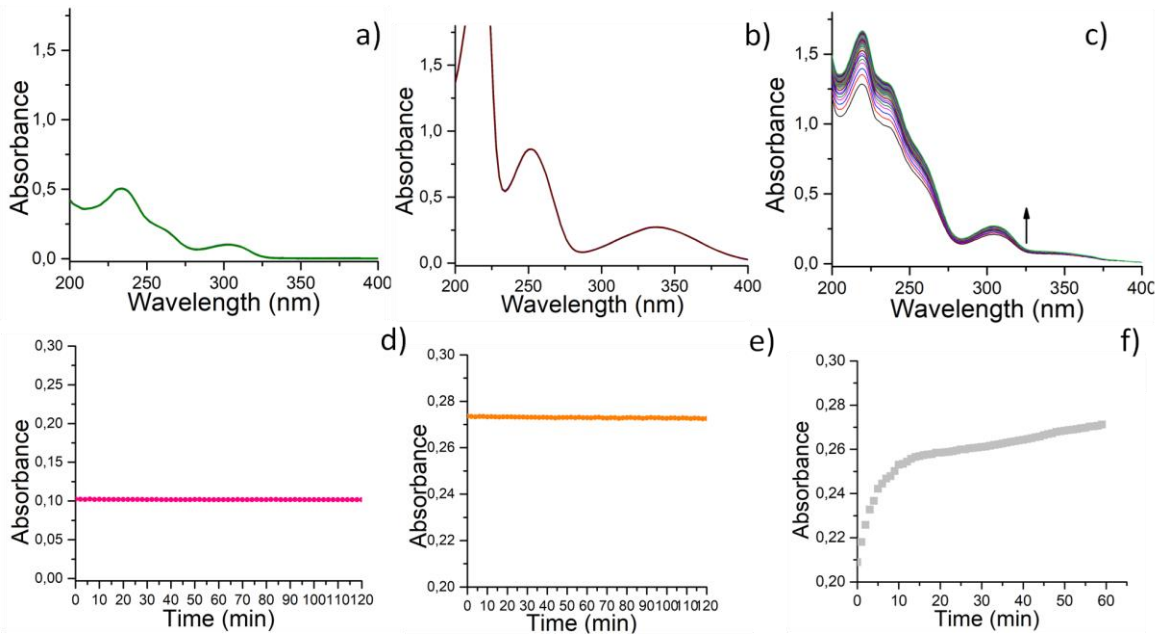

Figures 6. UV spectra of: **a) RhO-L_1**, **b) RhO-L_2** and **c) RhO-L_3**, recorded every minute *vs* time (120 min); d-f) Plots of absorbance *vs* time for **d) RhO-L_1**, **e) RhO-L_2** and **f) RhO-L_3**.

Figures 6, d-f, clearly show that absorbance increase is observed only for **RhO-L_3**. The time dependent increase of absorbance, observed within two hours, can be due to the presence of an intramolecular hydrogen bonding (H-bonding) between solfonamidic proton and lactamic oxygen, in the solid state. The cleavage of this bond, which occurs during the **RhO-L_3** solubilization, in a CH_3CN/H_20 (4:1) mixture, is a slow process due to the presence of the CH_3CN aprotic solvent, which has a dielectric constant lower than water. Noteworthy DFT calculations evidenced the presence of the intramolecular H-bonding which is highlighted in **Scheme 3.**

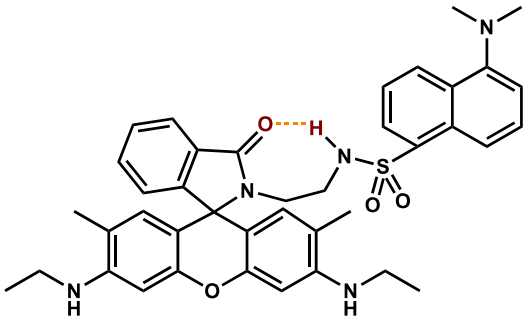

Scheme 3. Schematic representation of the hydrogen bonding.

Also, the calculated absorbance, in presence (**a**)/lack (**b**) of H-bonding, supports these findings, as shown in **Figure 7**.

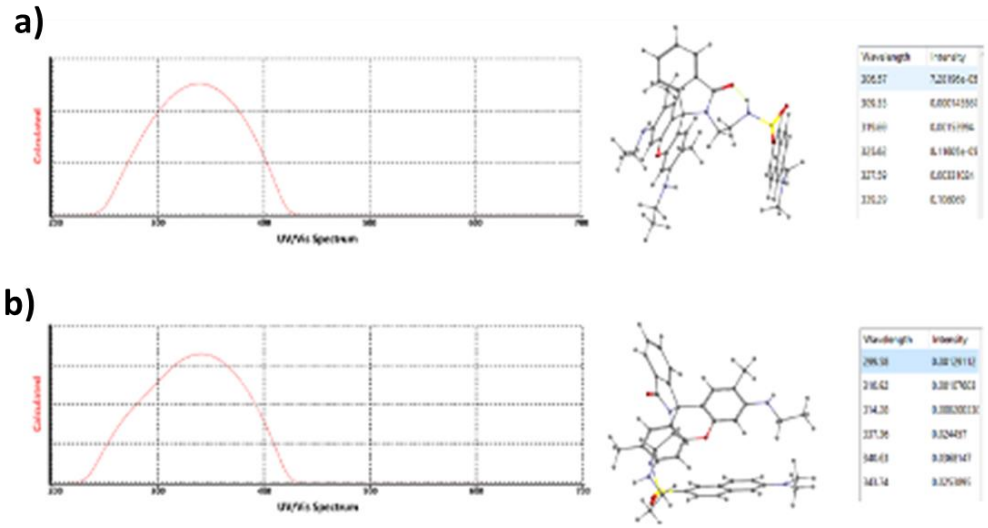

Figure 7. Calculated absorbance in presence (**a**)/lack(**b**) of H-bonding.

Ms/ms Mass spectra performed on **RhO-L$_3$** samples, freshly prepared and after 2 hs, are consistent with UV-Vis. data and theoretical calculations. The m/z 414 ion, observed only in the fresh **RhO-L$_3$** sample (**Figure 8 A**), is formed when still H-bonding is present, conversely, m/z 383 ion formation is strictly related to the lack of H-bonding with lactamic oxygen. Finally, m/z 355 ion abundance is higher, when H-bonding is not present, because of the major double bond character shown by the C (carbonylic)-C(aromatic) bond. Fragmentation mechanisms are reported in **Scheme 5**.

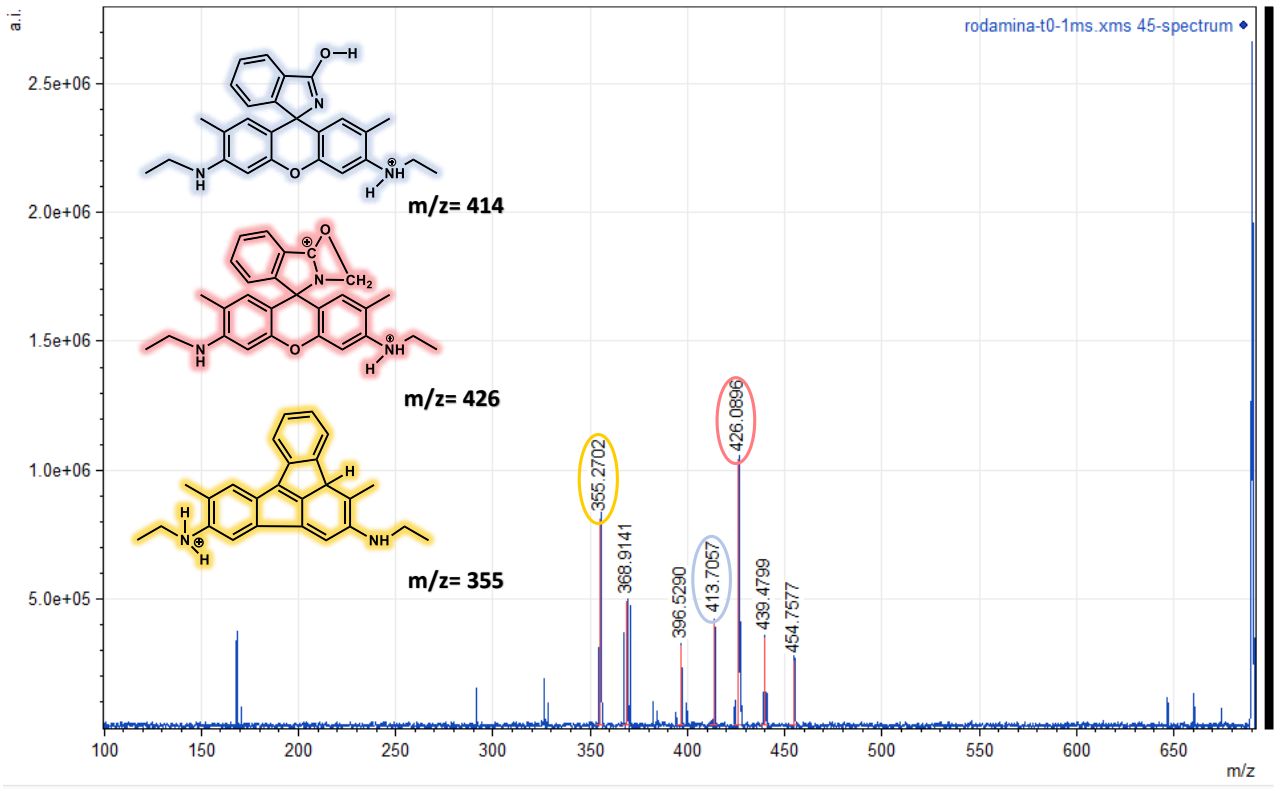

Figure 8A. ESI-CID MS/MS recorded at time=0 (fresh **RhO-L$_3$** sample).

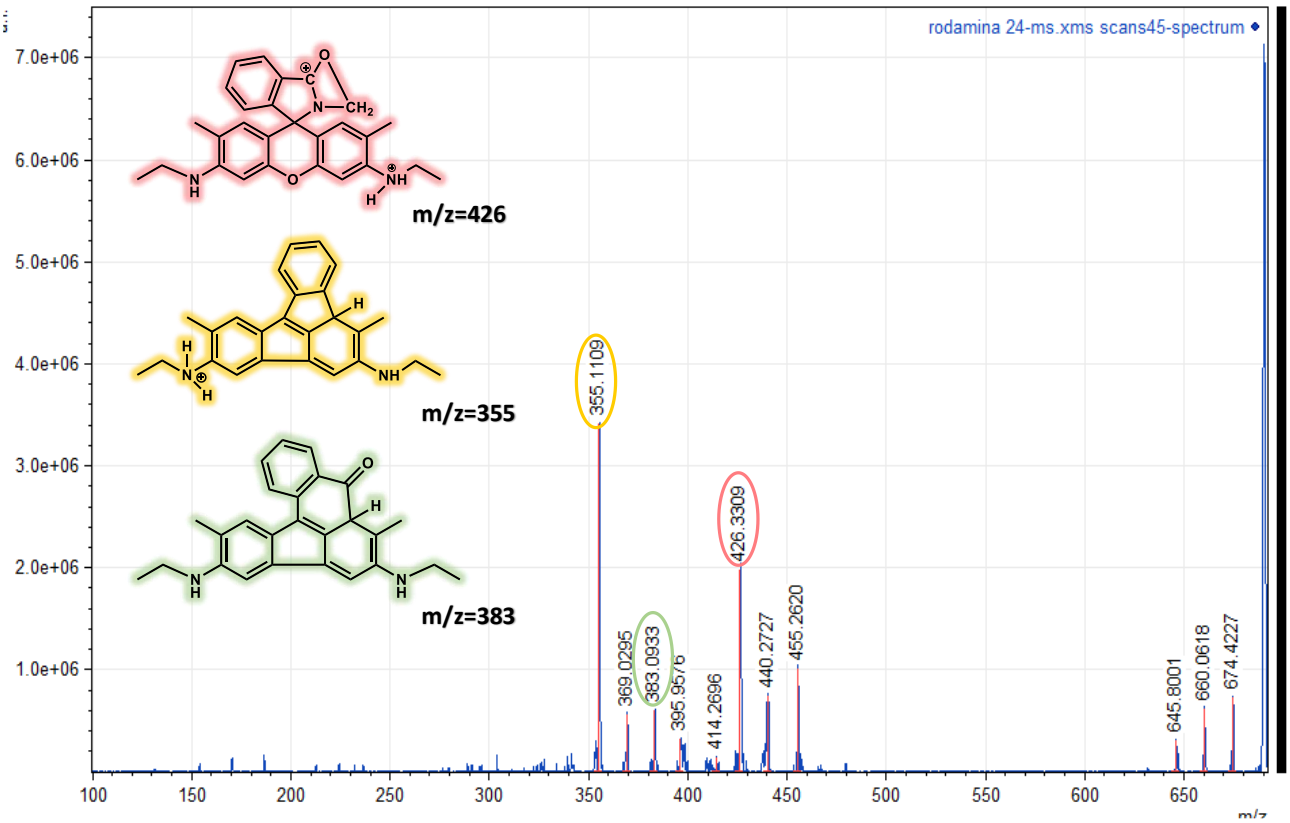

Figure 8B. ESI-CID MS/MS recorded **RhO-L$_3$** sample after 2 h.

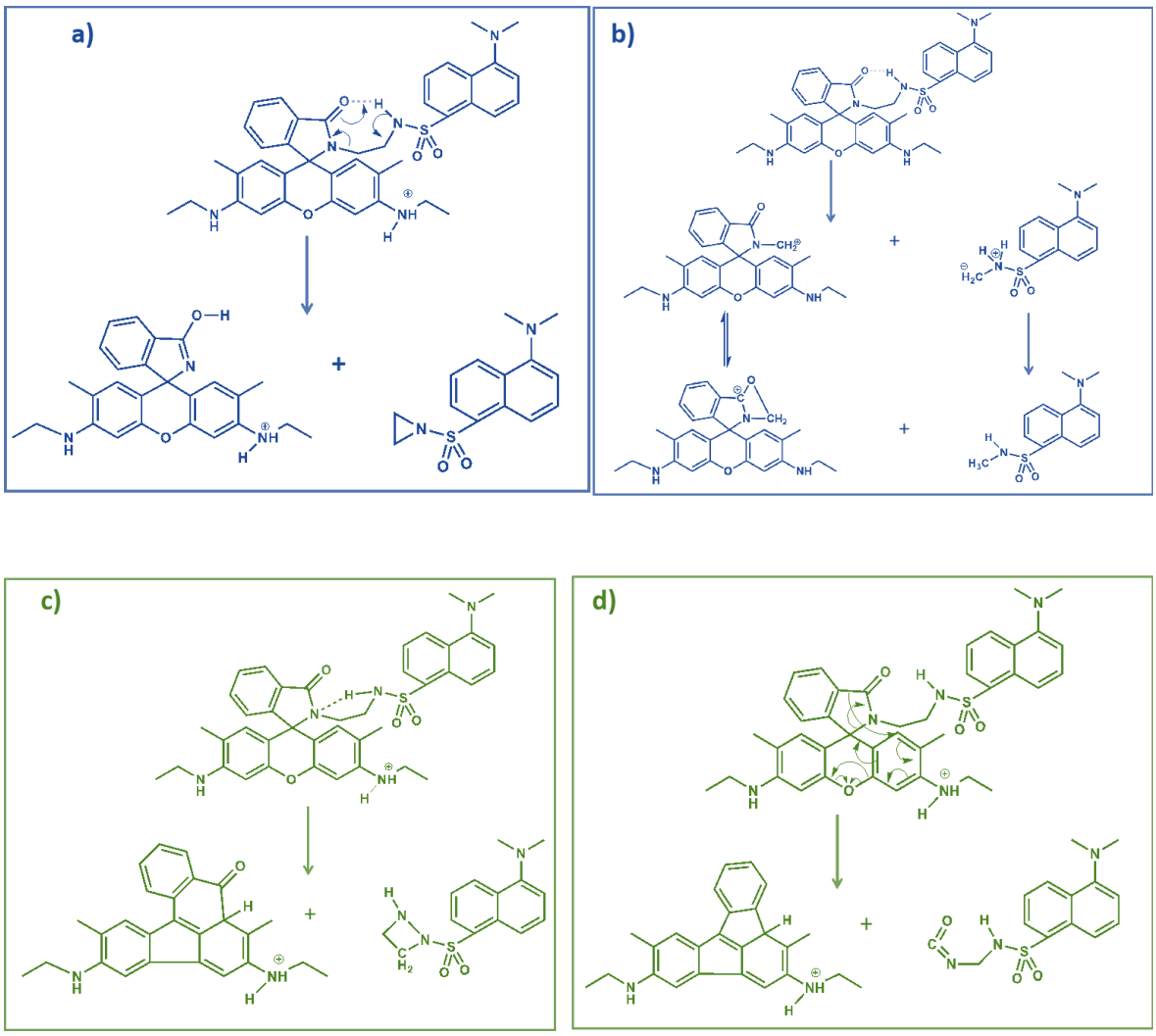

Scheme 4. Fragmentation mechanisms: **a)** m/z 414; **b)** m/z 426; **c)** m/z 355; **d)** m/z 383.

3.2.2 Theoretical Calculations

DFT calculations were carried out to study conformation and energy of neutral and variously protonated forms of **RhO-L$_1$**-**RhO-L$_3$**, with the aim to determine the most probable protonation sequence and the reaction mechanism responsible of the fluorescence emission pH dependent. All the calculations were performed in gas phase and by applying the conductor-like polarizable continuum model (CPCM). A 43.1 value as static dielectric constant for 4:1 acetonitrile/water mixture at 298 K was used[23] for CPCM. CPCM was applied to account the solvent effects in quantum chemical calculations. With this

model the solvent is thought as a dielectric polarizable continuum while the studied molecule is placed in a cavity of proper molecular shape. Polarization charges on the surface of the cavity determine the solvent reaction field. At first, the molecular electrostatic potential maps (MEP) were investigated as a useful descriptor for the molecules' reactive behavior and sites, especially for noncovalent interactions.[12,13] The electrostatic potential $V(\mathbf{r})$ is a physical observable that can be determined computationally,[13] and represented spatially as a colored surface where the electrostatic potential increases in the order red < orange < yellow < green < blue, showing electron rich, slightly electron rich, slightly electron deficient, and electron deficient regions, respectively.

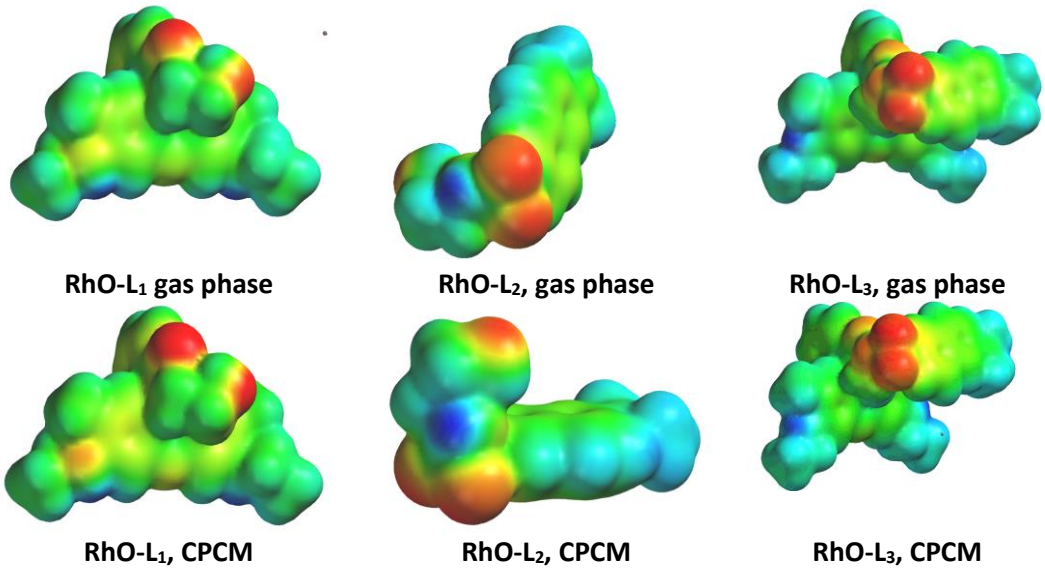

Figure 9. Electrostatic potential surface maps of **RhO-L$_1$**- **RhO-L$_3$**in gas phase (upper) and with CPCM (bottom). Red areas refer to regions containing electron-rich and blue areas refer to regions containing electron-poor sites (from -319.0 kJ/mol to 232.6 kJ/mol).

MEPs of **RhO-L$_1$**, **RhO-L$_2$** and **RhO-L$_3$** in gas and CPCM phase (**Figure 9**) show several regions of negative surface potential Vs(r) localized on nitrogen and oxygen atoms. The shield of electrostatic potential ranging from -319.0 kJ/mol to 232.6 kJ/mol enables interactions with protons, implying nitrogen and oxygen atoms as potential nucleophilic species. However, as shown in the following sections, not only the charge density defines the proton-binding

sites, but also the different stability of the variously protonated charged species, due mainly to the charge delocalization.

HOMO and LUMO Orbitals

Frontier orbitals, highest occupied molecular orbital (HOMO) and lowest unoccupied molecular orbital (LUMO), were calculated to observe the difference in HOMO-LUMO gap for **RhO-L_1-RhO-L_3**. The difference in energy between these two frontier orbitals can be exploited to predict the strength and stability of molecules and derivatives (metal complexes or protonated species), as well as their Uv-Vis absorption and emission. Orbital energy and HOMO, LUMO orbitals are shown in **Figure 10** for CPCM.

The HOMO-LUMO gap was observed for **RhO-L_1** (≈ 4.8 eV). The two frontier orbitals were localized in two different part of the molecule, being LUMO centered on the xantene moiety and HOMO on the phenyl moiety. As regards **RhO-L_2** and **RhO-L_3**, the energy gap values were ≈ 3.9 eV and ≈ 4.0 eV, respectively. In **RhO-L_2** both LUMO and HOMO are localized mainly on the aromatic rings, while in **RhO-L_3** they are both localized mainly on the dansyl moiety.

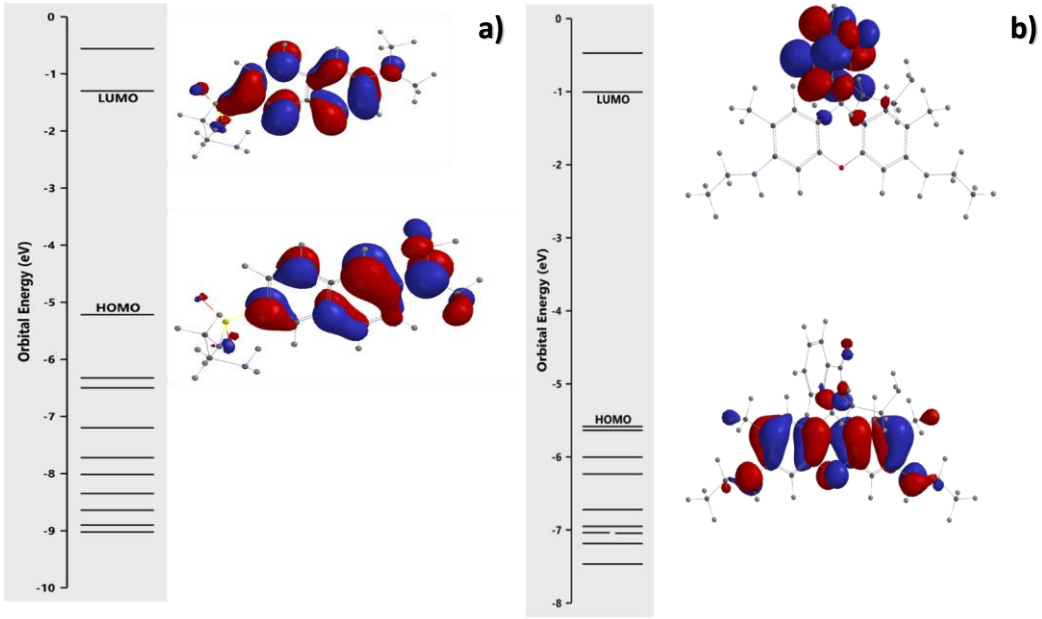

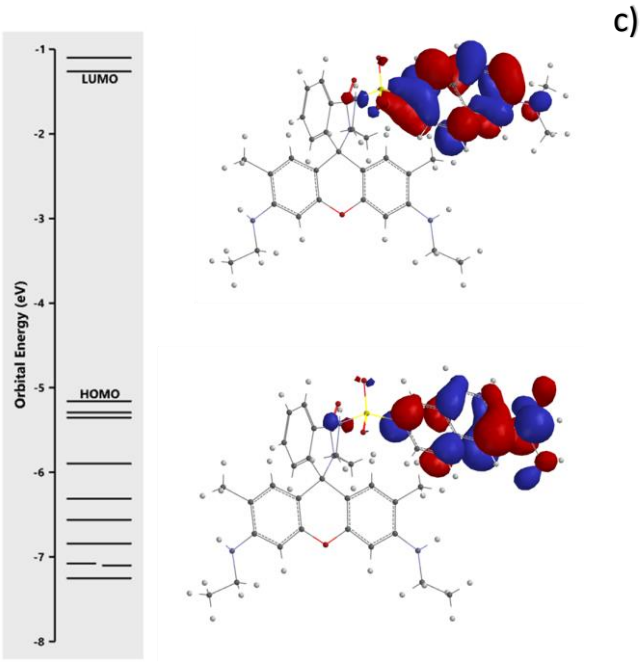

Figure 10. Molecular orbital energy and HOMO – LUMO surfaces for **RhO-L$_1$** (**A**), **RhO-L$_2$** (**B**) and **RhO-L$_3$** (**C**)

3.2.3 Protonation sequence

To define the protonation site(s), all the possible conformers were built and the relative geometries were optimized to determine the most stable species. For **RhO-L$_1$**, it has been found that: *i*) when the proton is coordinated by the spiranic nitrogen N1, its bond with the proximal spiranic carbon extends until it breaks; *ii*) when the proton is coordinated by the carbonyl oxygen, the O-H bond extends to bring the proton into the area of the NH_2 group; *iii*) when the proton is bonded to NH_2 group the most stable conformer is formed. The behaviors (*i*) and (*ii*) were observed also for the subsequent protonation steps. The protonation sequence reported in **Figure 11A** was then assessed. The species LH_4^{4+}, responsible of the fluorescence emission, undergoes to a structural rearrangement with the opening of the spirocycle, as shown **in Figure 11B**. Several resonant structures, where the positive charge could be delocalized in the two aromatic rings, define the stability of the rhodamine open form.

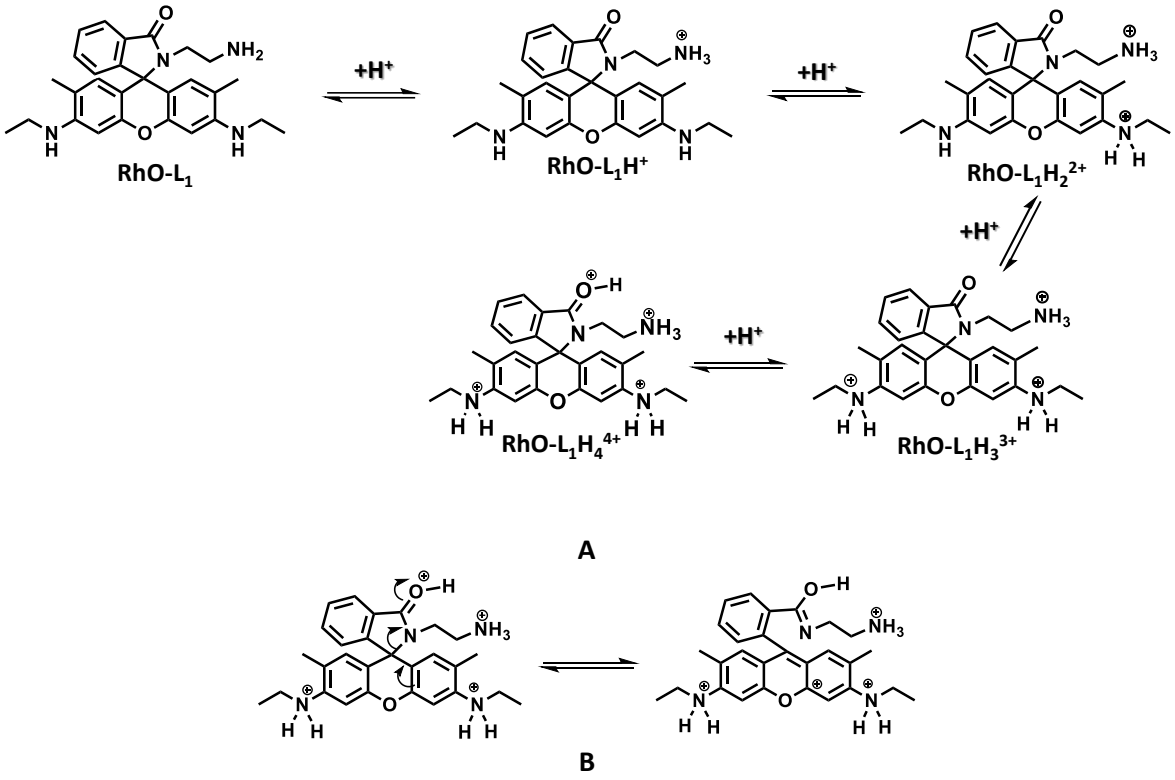

Figure 11. Protonation sequence for **RhO-L$_1$** (**A**) and ring-opening (**B**).

As for **RhO-L$_2$**, the protonation involves the aminic nitrogen, the dansylic amine and, finally, the nitrogen proximal to the sulfonic group (**Figure 12**).

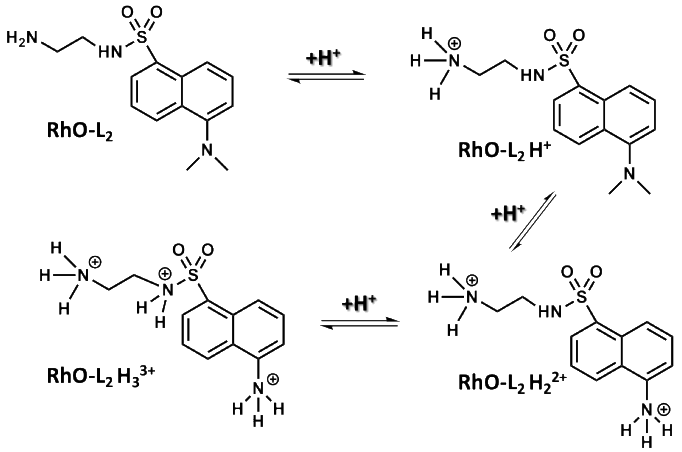

Figure 12. Protonation sequence for **RhO-L$_2$**

As for **RhO-L$_3$**, the protonation involves one aminic nitrogen of the xanthine moiety, the dansylic amine, the second aminic nitrogen of the xanthine moiety, and, finally, the oxygen of the carbonilic group (**Figure 12A**). The positive charge on the oxygen atom leads to the ring opening with a pathway shown in **Figure 13B**.

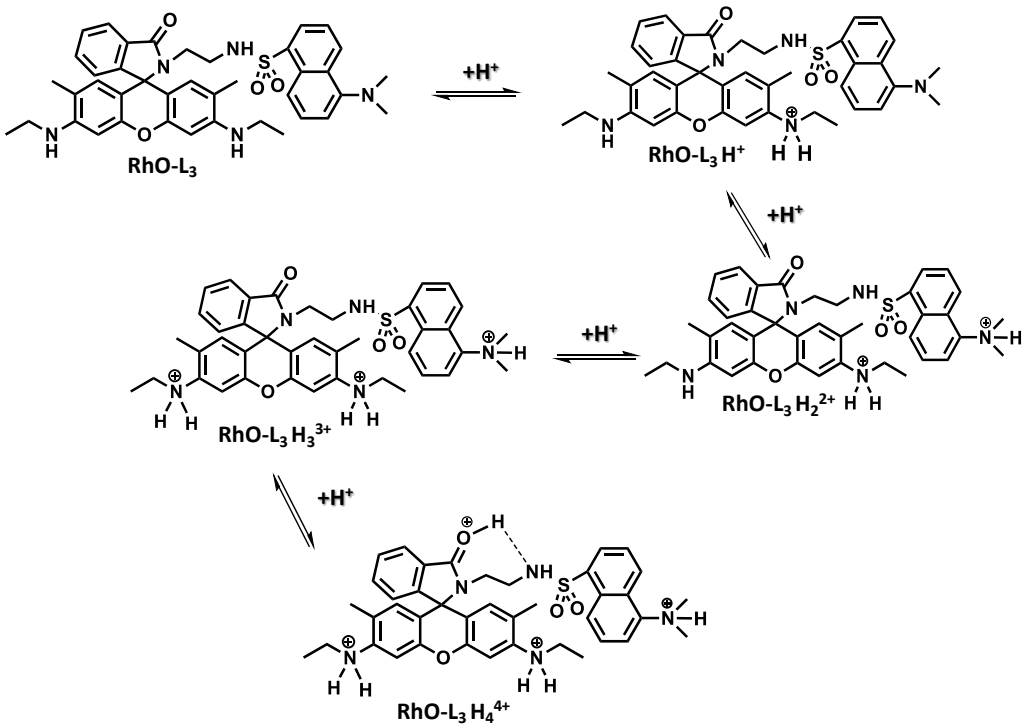

A

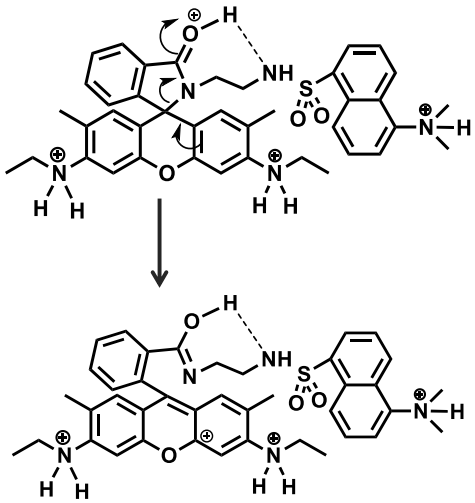

B

Figure 13. Protonation sequence for **RhO-L$_3$** (**A**) and ring-opening process (**B**).

3.2.4 Spectrophotometric and Potentiometric Titrations

A batch titration was performed for **RhO-L_1**, **RhO-L_2** and **RhO-L_3**, due to the slow kinetic shown by the absorbance data. Fifty solutions containing the same amount of each fluorophore were prepared. Various amount of HCl or NaOH were added to span the entire pH range. After 24 h, absorbance and pH values were read. In **Figures 14-16** selected spectra recorded during the batch titrations for **RhO-L_1**, **RhO-L_2** and **RhO-L_3**, respectively, are reported. Absorbance values, at selected wavelengths, were also reported as a function of pH or H^0 (the H^0 acid scale was used for high acidity solutions, since activity coefficients differ significatively from 1) (**Figure 17**).

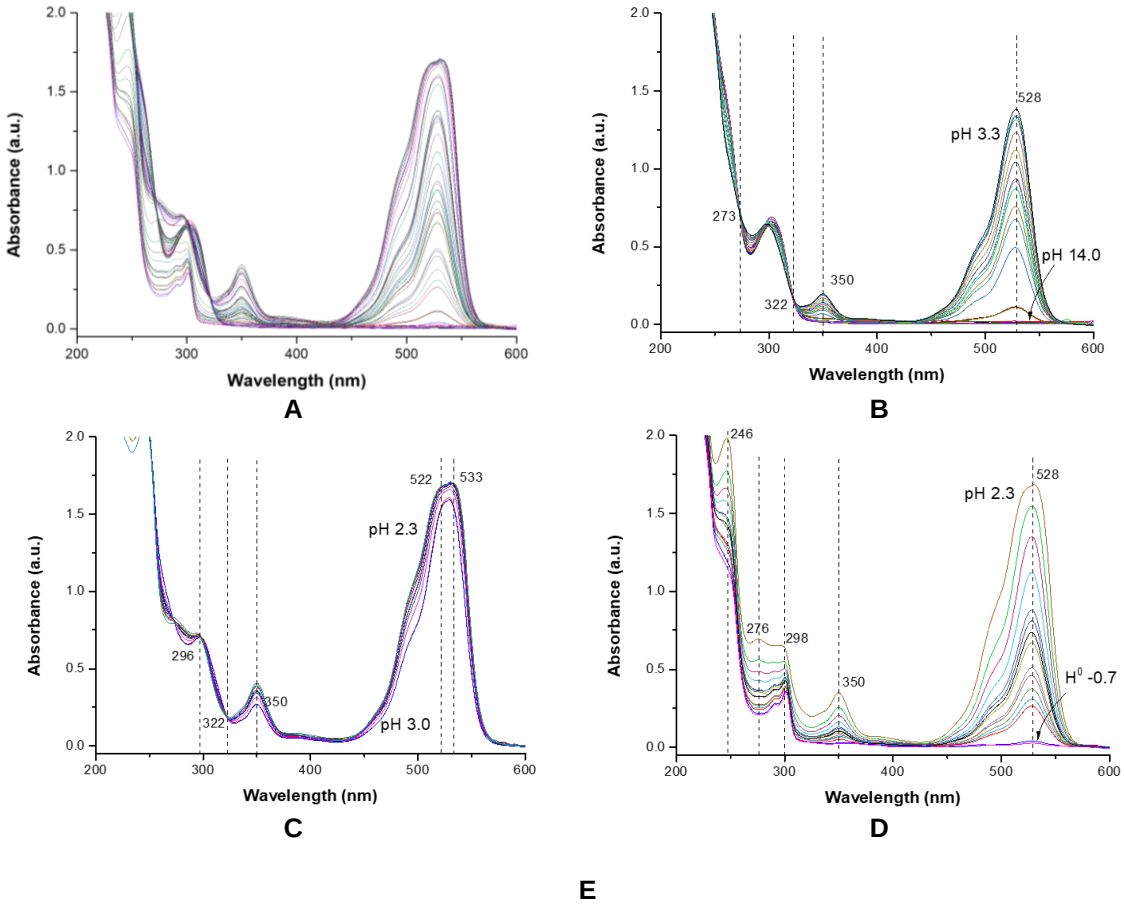

Figure 14. Selected spectra recorded during the spectrophotometric titration of **RhO-L_1**, from pH 14 to H^0 -0.7 (**A**), from pH 14 to pH 3.3 (**B**), from pH 3.0 to pH 2.3 (**C**), from pH 2.3 to H0 -0.7 (**D**).

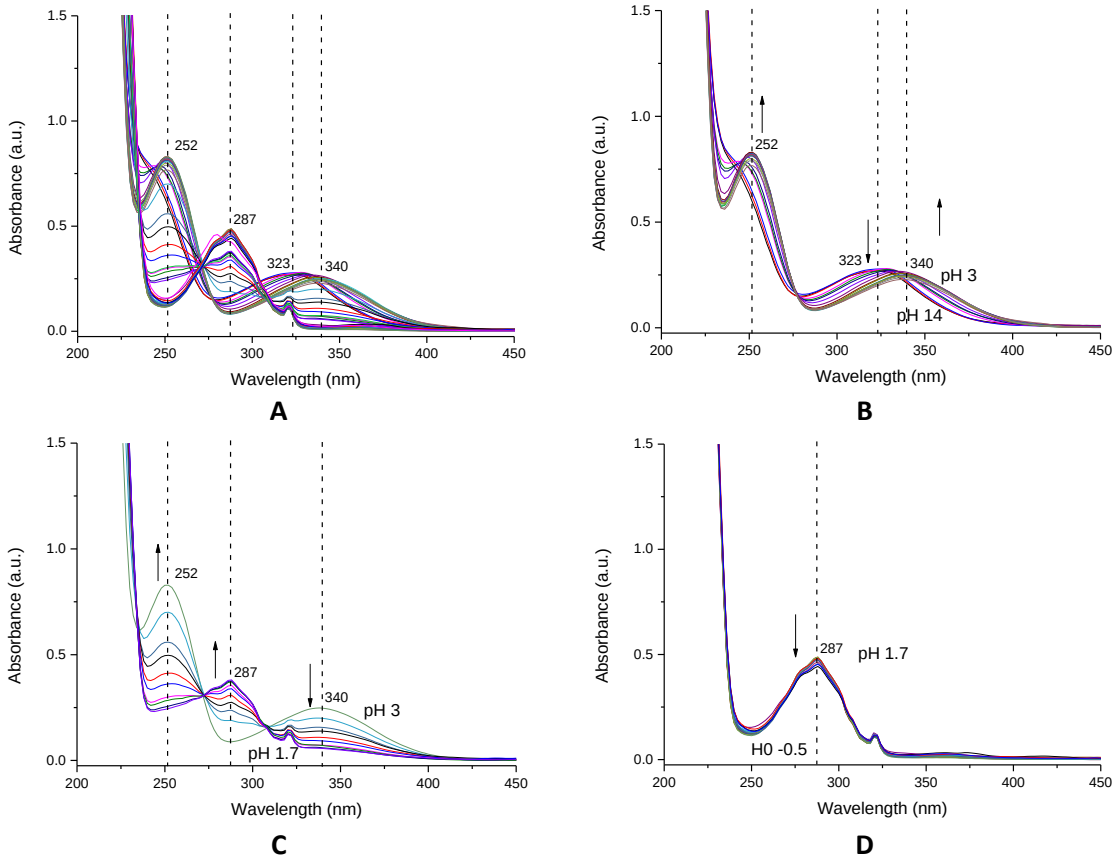

Figure 15. Selected spectra recorded during the spectrophotometric titration of **RhO-L_2**, from pH 14 to H^0 -0.5 (**A**), from pH 14 to pH 3 (**B**), from pH 3 to pH 1.7 (**C**), from pH 1.7 to H0 -0.5 (**D**).

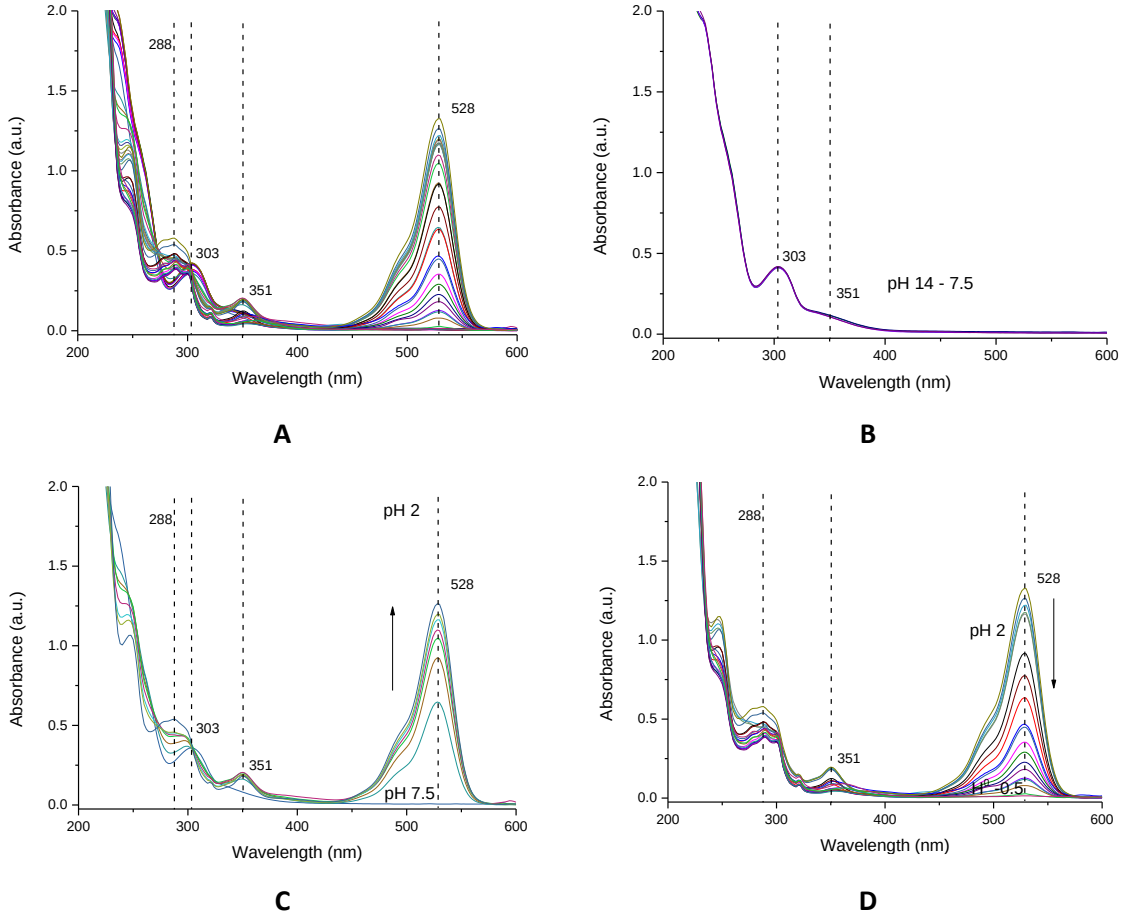

Figure 16. Selected spectra recorded during the spectrophotometric titration of **RhO-L$_3$**, from pH 14 to H^0 -1 (**A**), from pH 14 to pH 7.5 (**B**), from pH 7.5 to pH 2 (**C**), from pH 2 to H0 -1 (**D**).

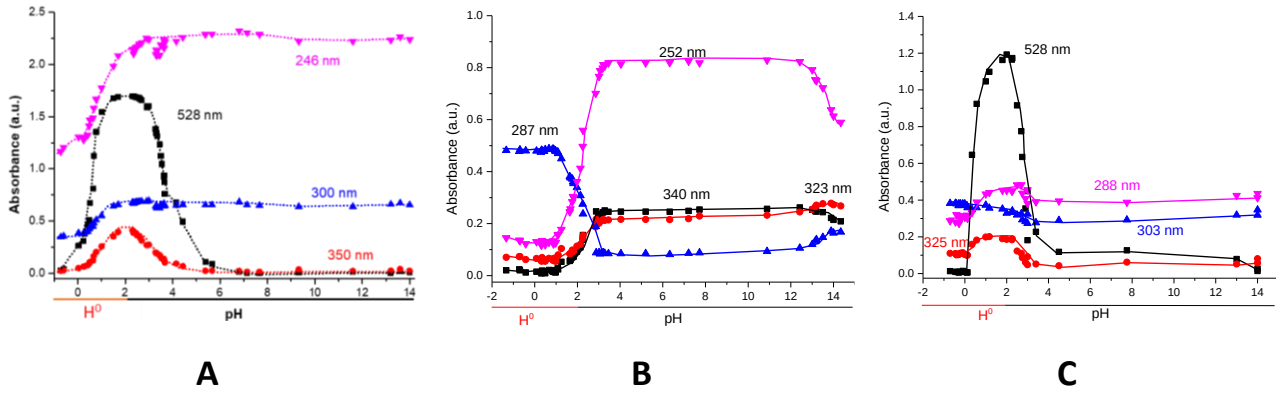

Figure 17. Absorbance values at selected wavelengths were also reported as a function of pH or H^0 for **RhO-L$_1$** (**A**), **RhO-L$_2$** (B) and **RhO-L$_3$** (C).

As it can be seen in **Figures 14-17**, an absorption in the visible region was observed in the 4-13 pH range, only for **RhO-L$_2$**; for **RhO-L$_1$** and **RhO-L$_3$** an absorption peak at 528 nm was evidenced at acidic pH (pH < *ca.* 3) due to the ring-opening process. Interestingly, at very

acidic pH (<2), this absorption peak disappeared with the feasible modification of the molecules.

The optimized geometry of the opening-form of **RhO-L$_3$** was calculated, together with the MOs and MEP.

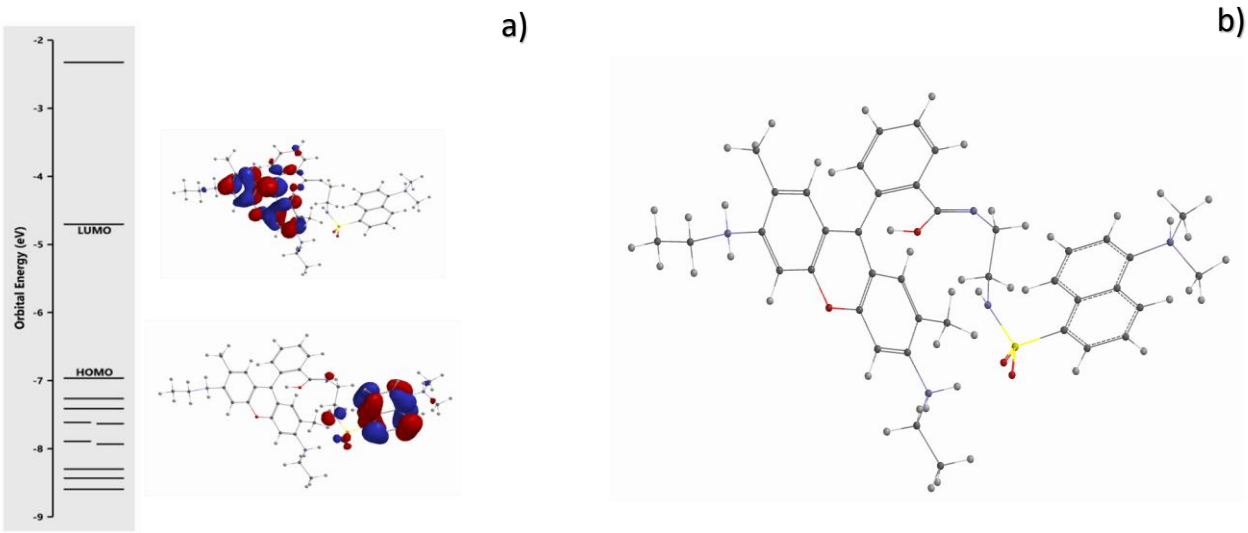

Figure 18. a) Optimised geometry of H_4L^{4+} species of **RhO-L$_3$** opening-form; **b)** Orbital energy and shape of HOMO, LUMO orbitals of H_4L^{4+} species of **RhO-L$_3$**, opening-form.

The HOMO-LUMO gap between the MOs is *ca.* 2.3 eV, favoring the HOMO-LUMO transition, thus supporting the strong absorption observed in the visible region.

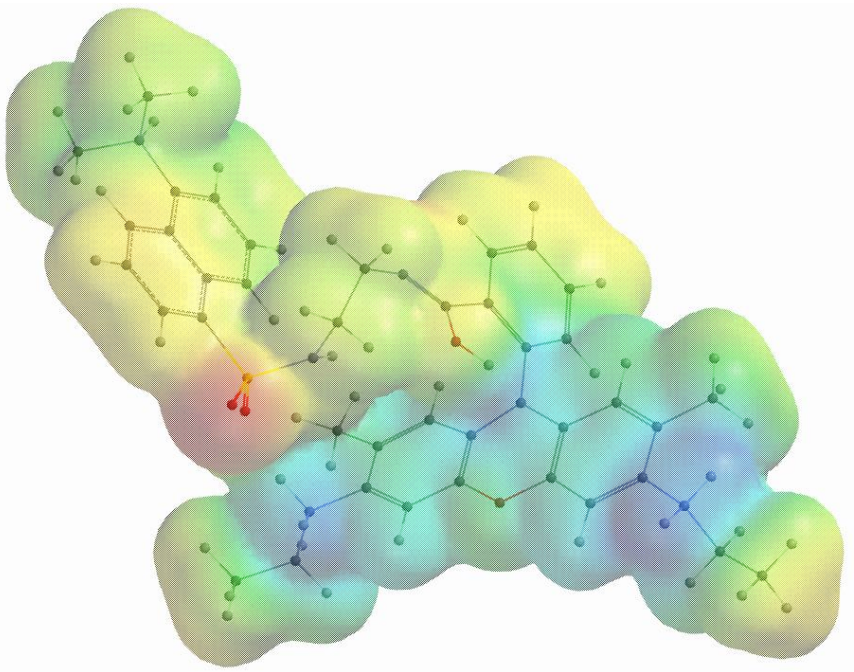

Figure 19. Electrostatic potential map of of H_4L^{4+} species of **RhO-L$_3$**, opening-form

The MEP of of H_4L^{4+} species of **RhO-L$_3$**, opening-form, shows that the positive charge on the carbon atom is slightly delocalized on the xanthene moiety, due to the positive charges already present on the two aminic groups. A summary of total energies of **RhO-L$_3$** protonated species is reported in **Table 1**.

Table 1. Total energy of **RhO-L$_3$** (L) protonated species

Species	**Energy (Hartree units)**	**ΔE**	**Energy (Hartree units)**	**ΔE**
	Gas phase		**Solution**	
L	-2522.98540	-	-2523.02992	-
LH^+	-2523.39038	0.40498	-2523.47714	0.44722
LH_2^{2+}	-2523.69951	0.30913	-2523.92729	0.45015
LH_3^{3+}	-2523.96131	0.26180	-2524.37150	0.44421
LH_4^{4+}	-2524.14461	0.18315	-2524.79931	0.42781
LH_4^{4+} opening-form	-2624,02830	0.11631	Work in progress	-

3.2.5 Photoluminescence Measurements

Preliminary photoluminescence (PL) and time-resolved PL data were acquired on **RhO-L$_3$** in both neutral conditions (pH ~7.5) and acidic conditions (pH ~2.5) near the predicted maximum for the FRET process. The PL intensity spectra are reported in **Figure 20**.

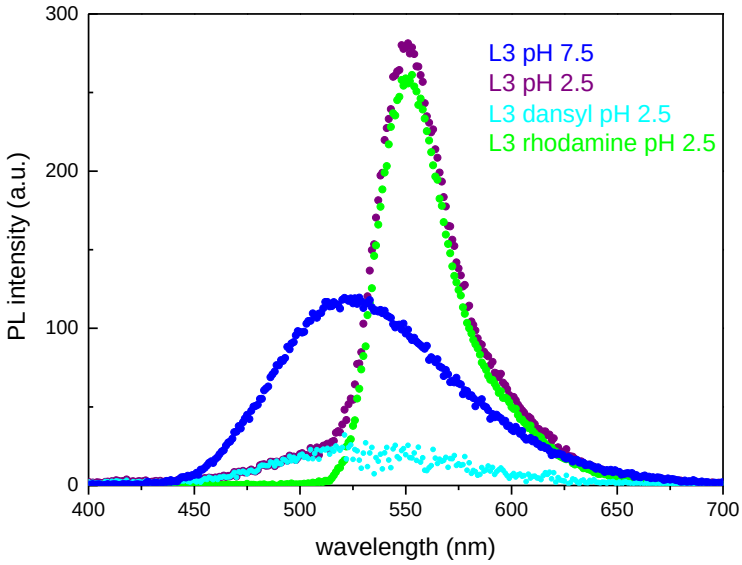

Figure 20. PL spectra of **RhO-L$_3$**. Blue dots: Spectrum at pH ~7.5. Violet dots: Spectrum at pH ~2.5, corrected for self-absorption in the sample cuvette. Cyano (green) dots: Dansyl- (rhodamine-) centered spectrum deduced from spectral decomposition of self-absorption corrected **L$_3$** spectrum.

At pH ~7.5, the emission spectrum of **RhO-L$_3$** only exhibits a dansyl-centered band. Lowering the pH to ~2.5 strongly renormalizes the emission spectrum: The dansyl-centered band becomes weaker (magenta dots), while the rhodamine-centered emission dominates the system response (green dots) as a consequence of the spirolactam ring-opening.

Time decays of the **RhO-L$_3$** PL bands were measured to possibly detect a dansyl-to-rhodamine FRET process directly in the time domain. Decay profiles are shown in **Figure 21**. As clearly visible, the dansyl-centered emission decays monoexponentially with a characteristic time (~13 ns) that is nearly independent of pH. The rhodamine-centered emission can be well fitted with a three-exponential decay curve. The longest component is traced back to the dansyl contribution in the integration spectral window 510-650nm. Characteristic times deduced from curve fitting are summarized in **Table 2**.

Table 2. Decay characteristics times (τ) and fractional amplitudes ($\%A$) at different pH values

L3 band	pH	τ_1 (ns)	$\%A_1$	τ_2 (ns)	$\%A_2$	τ_3 (ns)	$\%A_3$
dansyl	7.5	13.7(1)	100	-	-	-	-
dansyl	2.5	12.4(2)	100	-	-	-	-
rhodamine	2.5	0.97(1)	59	4.1(1)	38	12.4	3

The dansyl-centered emission decay profile acquired in acidic conditions (cyano dots) shows no evidence for a fast PL component owing to the mole fraction of dyads able to undergo the FRET mechanism. This is attributed to the fact that a quantitative FRET process with nearly unitary quantum efficiency is expected to result in a dansyl-centered (donor) lifetime that is possibly many orders of magnitude shorter than the reference (donor in the absence of the acceptor) lifetime of 12-13 ns, hence considerably shorter also than the resolution of the experimental apparatus (~60 ps).

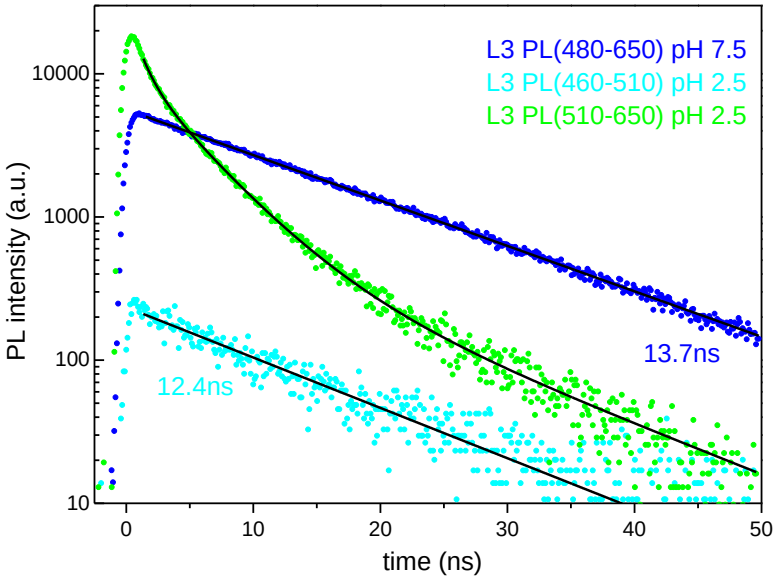

Figure 21. PL intensity decay profiles measured in **RhO-L3**. Profile of the dansyl-centered band at pH ~7.5 (blue dots), Dansyl-centered band at pH ~2.5 (cyano dots), and rhodamine-centered band at pH ~2.5 (green dots). Spectral integration windows are shown in the color legend. Continuous lines are fits of monoexponential (dansyl) and three-exponential (rhodamine) curves to experimental profiles.

3.3 Experimental Section

3.3.1 Materials

All reagents are purchase from Sigma Aldrich and used as received without further purifications**. RhO-L_1**, **RhO-L_2** and **L RhO-L_3** synthesis reactions were performed in oven-dried glassware under a slight positive pressure of nitrogen. ^{1}H-NMR (300 MHz or 500 MHz) spectra were determined on a Bruker Advance 300 MHz or on a Varian VXR500. Chemical shifts for 1 H-NMR are reported in parts per million (ppm), calibrated to the residual solvent peak set, with coupling constants reported in Hertz (Hz). The following abbreviations are used for spin multiplicity: s = singlet, d = doublet, t = triplet, and m = multiplet. Uv-Vis absorption spectra were recorded at 298.1 K on a Varian Cary-100 spectrophotometer equipped with a temperature control unit.

3.3.2 Synthesis of RhO- L_1

Rhodamine 6G (958 mg, 2 mmol) was dissolved in 25 mL of hot ethanol, followed by addition of ethylenediamine (0.67 mL, 10 mmol). The reaction mixture was refluxed for 6 hours till the fluorescence of the solution was disappeared. After cooling to room temperature, the solution was kept in fridge overnight. The precipitate was collected and washed with 10 mL of cold ethanol. L_1 was obtained as white solid in 78 %. ^{1}H-NMR (300MHz,$CDCl_3$, 298K): δ 7.94 (d, 1H), 7.47 (t, 2H), 7.05 (d, 1H), 6.35 (s, 2H), 6.23 (s, 2H), 3.50 (t, 2H), 3.24 (t, 4H), 2.39 (t, 2H), 1.90 (s, 6H), 1.36 (t, 6H).

3.3.3 Synthesis of RhO-L_3

A mixture of dansyl chloride (100 mg, 1.0 mmol) in anhydrous dichloromethane (10 mL) was added drop to drop to a solution of **RhO-L_1** and triethylamine (0.5 mL) in anhydrous dichloromethane (20 mL), After refluxing for 24 h the reaction is cooled to room temperature. The precipitate was collected by filtration under vacuum and washed with dichloromethane and acetone. was obtained as white solid in 82%. ^{1}H-NMR (300 MHz, $CDCl_3$ 298K): δ 8.52 (d, 2 H), 8.34 (m, 2 H), 7.97 (m, 1 H), 7.48(m, 4 H), 7.07 (m, 2 H), 6.37 ~ 6.17 (m, 6 H), 3.37 (q, 8 H), 3.08 (t, 2 H), 2.82 (s, 6 H), 2.78 (t, 2 H), 2.34 (t, 4 H), 2.04 (t, 2 H), 1.79 (br, s), 2,55 (t, 6H), 2.33(t, 4H), 2.21 (m 2H), 1.85 (s, 6H).

3.3.4 Synthesis of RhO-L_2[24]

A solution of dansyl chloride (100 mg, 0.37 mmol) in dichloromethane (6 mL) was dropped into 1,2-ethylenediamine (6.5 mL, 200 mg, and 3.20 mmol) while stirring and cooling over ice. The mixture was stirred for 1 h. The reaction mixture was acidified with dilute HCl and then extracted with dichloromethane (3× 20 mL). The aqueous layer was made with NaOH and again extracted with dichloromethane (3 × 20 mL). The organic layer was dried over Na_2SO_4, and the solvent removed under reduced pressure to give (2-aminoethyl)-dansylamide as a yellow solid (100 mg, 92%).

3.3.5 Mass Spectrometry Measurements

Mass spectra were recorded using a triple quadrupole QqQ Varian 310-MS mass spectrometer using the atmospheric-pressure Electrospray Ionization (ESI) technique. Sample solutions (20 μL) were injected into the ESI source by a Rheodyne® model 7125 injector connected to a HPLC Varian 212 LC pump, with a 50 $\mu L \cdot min^{-1}$ methanol flow. Experimental conditions: Dwell time 2 s, needle voltage 3000 V, shield voltage 600 V, source temperature 60 °C, drying gas pressure 20 psi, nebulizing gas pressure 20 psi, detector voltage 1600 V. Mass spectra were recorded in the 100–600 m/z range. Collision-Induced Dissociation (CID) tandem mass (MS/MS) experiments were performed using argon as the collision gas (1.8 psi). Collision energy was varied from 20 to 40 eV.

3.3.6 Computational Studies

Geometry optimization of neutral and protonated forms of **RhO-L_1-L_3** were performed on an Intel-i7 based system using Spartan'18, Wavefunction inc., using B3LYP as the density functional theory and 6-31G* for the basis set. IR frequency calculations were carried out to verify the nature of the minima of each optimization by assessing the absence of calculated negative frequencies. Heat of formation, Gibbs energy, molecular electrostatic potential, electrostatic,[25,26] natural,[27] Mulliken charges,[28,29] and HOMO and LUMO orbitals were also calculated.

3.3.7 Spectroscopic Measurements

UV-visible spectroscopic measurements were carried out on a Varian Cary 60 UV-vis spectrophotometer in the 200–600 nm wavelength range using a 1 cm quartz cell, at 25 °C. The protonation constants of **RhO-L_1**- **RhO-L_3** at pH < 3 were determined at 25 °C by spectrophotometric titration of the ligand with HCl, in acetonitrile:water 4:1 solution and with 0.05 M NaCl ionic buffer.

3.3.8 Potentiometric Measurements

Potentiometric titrations were carried out in a thermostatated vessel with a Mettler-Toledo Seven Compact pH/Ion-meter equipped with a Mettler-Toledo InLab Micro Pro combined glass electrode with an integrated temperature probe. Potentiometric titrations were performed at 25 °C in 0.05 M ionic strength (NaCl) under N_2 atmosphere. The glass electrode was calibrated daily by titration of a known amount of HCl with carbonate-free NaOH solution. Electrode standard potential (E0), water ionic product (pKw), electrode response and carbonate content of the titrant solution were checked with Gran's procedure [30] using the Glee program [31]. The reversibility of all the studied equilibria was checked by back-titration with standard HCl. The overall stability constants were determined with the Hyperquad2003 program. [32]

3.3.9 Photophysical Measurements

Time-resolved fluorescence was excited at 370 nm by 200 fs long pulses delivered by an optical parametric amplifier (Light Conversion TOPAS-C) pumped by a regenerative Ti:sapphire amplifier (Coherent Libra-HE) running at a repetition frequency of 1 kHz, wavelength dispersed by a single-grating spectrometer (Princeton Instruments Acton SpectraPro2300i) and detected by a Vis streak camera (Hamamatsu C1091). Time resolution of the apparatus was about 50 ps.

3.4 Conclusions

The synthesis and characterization of the novel ratiometric fluorescent platform, **RhO-L$_3$**, formed by a rodamine derivative, **RhO-L$_1$**, as acceptor unit and dansyl moiety, **RhO-L$_2$**, as donor unit, is reported. This hybrid platform was investigated in a wide range of pH, from 14 up to 0.7 and its response to protonation was studied, by a multi-technique approach, involving UV-Visible, PL and time-resolved PL spectroscopies, potentiometric titrations and Mass Spectrometry. Both rhodamine and dansyl acceptor/donor units were selected because of spectral-overlap between the absorption band of the acceptor unit (rhodamine) and the emission band of the donor unit (dansyl), a crucial prerequisite for the occurrence of a FRET process. Noteworthy, the proton-mediated rhodamine spirolactam/ring-opening mechanism and the photophysical mechanism (FRET) at the basis of energy-transfer was inferred by the simultaneous combination of spectrophotometric and potentiometric titrations, supported by DFT calculations. Interestingly, the latter showed the formation of a stable H_4L^{4+} (L=**RhO-L$_3$**) species, through a multiple protonation sequence. Furhermore the frontier orbitals study highlighted that the HOMO-LUMO gap decreases, as a consequence of **RhO-L$_3$** ring-opening process. The energy gap decrease is consistent with the strong absorption observed in the visible spectrum, in highly acidic conditions (pH <*ca.* 3), due to **RhO-L$_3$** ring-opening form. The proton interaction with **RhO-L$_3$** probe influences significantly HOMO/LUMO energy levels of rhodamine and dansyl moiety and it was found that the HOMO–LUMO energy gap of the H_4L^{4+} species (≈2.3 eV) becomes lower than that one of the free **RhO-L$_3$** chemosensor (**RhO-L$_3$** ≈ 4.0 eV). Remarkably, when **RhO-L$_3$** probe is in its spirolactam form, the HOMO–LUMO energy gap of acceptor rhodamine moiety is greater than that one of dansyl donor, suppressing the dansyl-to-rhodamine energy transfer. However, in acidic conditions (pH <*ca.*3), spirolactam ring is opened up, as a consequence of proton interaction, showing a significant decrease of the energy gap in the rhodamine moiety, which, matching dansyl unit energy gap, can favor FRET process.[33] Theoretical calculations seem to be a potential approach to predict the occurrence of FRET processes, even though a systematic study on several donor/acceptor combinations of model FRET-based chemosensors is required to confirm these findings. Dansyl- and rhodamine-centered PL intensity titration experiments are now under way with the aim to detect and quantify the FRET process. Furthermore donor–acceptor pair distance (typically

10–100 Å) in the present hybrid ratiometric platform should be determined in order to rationalise the FRET distance dependency and its efficiency.

3.5 References

1 S. Saravana Kumar, R. Selva Kumar and S. K. Ashok Kumar, *Inorganica Chim. Acta*, 2020, **502**, 119348.

2 K. P. Carter, A. M. Young and A. E. Palmer, *Chem. Rev.*, 2014, 114, 4564–4601.

3 E. M. Obeng, E. C. Dullah, M. K. Danquah, C. Budiman and C. M. Ongkudon, *Anal. Methods*, 2016, **8**, 5323–5337.

4 S. Pal, B. Sen, M. Mukherjee, K. Dhara, E. Zangrando, S. K. Mandal, A. R. Khuda-Bukhsh and P. Chattopadhyay, *Analyst*, 2014, **139**, 1628–1631.

5 L. Wu, C. Huang, B. P. Emery, A. C. Sedgwick, S. D. Bull, X. P. He, H. Tian, J. Yoon, J. L. Sessler and T. D. James, *Chem. Soc. Rev.*, 2020, **49**, 5110–5139.

6 S. L. Shen, X. F. Zhang, S. Y. Bai, J. Y. Miao and B. X. Zhao, *RSC Adv.*, 2015, **5**, 13341–13346.

7 J. Park, B. A. Rao and Y. A. Son, *Fibers Polym.*, 2015, **16**, 953–960.

8 H. J. Lee, M. J. Cho and S. K. Chang, *Inorg. Chem.*, 2015, **54**, 8644–8649.

9 W. L. Czaplyski, G. E. Purnell, C. A. Roberts, R. M. Allred and E. J. Harbron, *Org. Biomol. Chem.*, 2014, **12**, 526–533.

10 L. Yuan, W. Lin and Y. Feng, *Org. Biomol. Chem.*, 2011, **9**, 1723–1726.

11 X. Zhang, Y. Xiao and X. Qian, *Angew. Chemie - Int. Ed.*, 2008, **47**, 8025–8029.

12 K. Umezawa, M. Kamiya and Y. Urano, *Angew. Chemie - Int. Ed.*, 2018, **57**, 9346–9350.

13 L. Yuan, W. Lin, Y. Xie, B. Chen and S. Zhu, *J. Am. Chem. Soc.*, 2012, **134**, 1305–1315.

14 Y. Fang, Y. Zhou, J. Y. Li, Q. Q. Rui and C. Yao, *Sensors Actuators, B Chem.*, 2015, **215**, 350–359.

15 J. C. Qin, Z. Y. Yang and G. Q. Wang, *J. Photochem. Photobiol. A Chem.*, 2015, **310**, 122–127.

16 J. Piao, J. Lv, X. Zhou, T. Zhao and X. Wu, *Spectrochim. Acta - Part A Mol. Biomol. Spectrosc.*, 2014, **128**, 475–480.

17 Q. J. Ma, H. P. Li, F. Yang, J. Zhang, X. F. Wu, Y. Bai and X. F. Li, *Sensors Actuators, B*

Chem., 2012, **166**–**167**, 68–74.

18 B. Shi, Y. Gao, C. Liu, W. Feng, Z. Li, L. Wei and M. Yu, *Dye. Pigment.*, 2017, **136**, 522–528.

19 M. A. Croxen, G. Sisson, R. Melano and P. S. Hoffman, *J. Bacteriol.*, 2006, **188**, 2656–2665.

20 T. Hirano, Y. Noji, T. Shiraishi, M. Ishigami-Yuasa and H. Kagechika, *Tetrahedron*, 2016, **72**, 4925–4930.

21 X. Gao, Y. Zhang and B. Wang, *Org. Lett.*, 2003, **5**, 4615–4618.

22 Q. Liu, X. Hong Su, L. Ying Wang, W. Sun, Y. Bo Lei and Z. Yi Wen, *J. Lumin.*, 2014, **154**, 124–130.

23 L. G. Gagliardi, C. B. Castells, C. Ràfols, M. Rosés and E. Bosch, *J. Chem. Eng. Data*, 2007, **52**, 1103–1107.

24 E. L. Doyle, C. A. Hunter, H. C. Phillips, S. J. Webb and N. H. Williams, *J. Am. Chem. Soc.*, 2003, **125**, 4593–4599.

25 L. E. Chirlian and M. M. Francl, *J. Comput. Chem.*, 1987, **8**, 894–905.

26 C. M. Breneman and K. B. Wiberg, *J. Comput. Chem.*, 1990, **11**, 361–373.

27 A. E. Reed, R. B. Weinstock and F. Weinhold, *J. Chem. Phys.*, 1985, **83**, 735–746.

28 R. S. Mulliken, *J. Chem. Phys*, 1955, **23**, 1833.

29 R. S. Mulliken, *J. Chem. Phys.*, 1955, **23**, 2338–2342.

30 K. V. GROVE-RASMUSSEN, *Dan. Tidsskr. Farm.*, 1961, **35**, 236–242.

31 P. Gans and B. O'Sullivan, *Talanta*, 2000, **51**, 33–37.

32 T. Pivetta, F. Trudu, E. Valletta, F. Isaia, C. Castellano, F. Demartin, R. Tuveri, S. Vascellari and A. Pani, *J. Inorg. Biochem.*, 2014, **141**, 103–113.

33 S. Mondal, S. K. Manna, K. Maiti, R. Maji, S. S. Ali, S. Manna, S. Mandal, M. R. Uddin and A. K. Mahapatra, *Supramol. Chem.*, 2017, **29**, 616–626.

Chapter 4

Rhodamine and Thiophene Diketopyrrolo-Pyrrolo Fluorescent Chemosensors

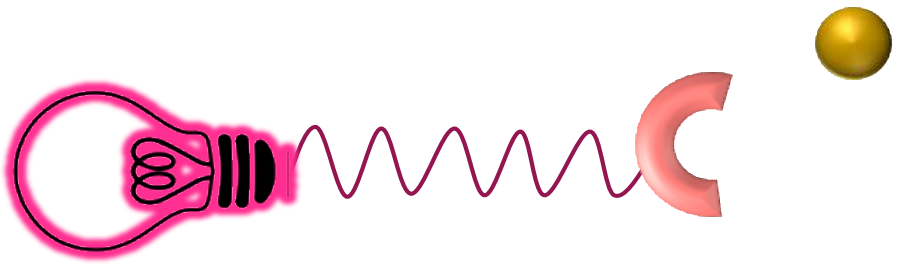

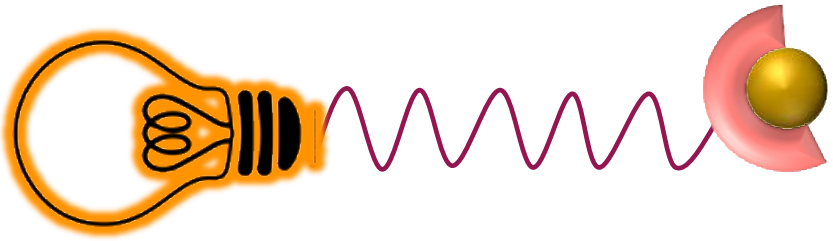

4.1 Introduction

Lead, Cadmium and Mercury, well-known as toxic metal ions, are highly soluble in the aquatic environment and they can be absorbed by living organisms leading to harmful effects.[1–3] Among them mercury is the most dangerous given its ability to react with various biomolecules.[4] Mercury exists in nature in three different forms: as element, as component of inorganic compounds and organic complexes, which can be released from a variety of industrial and natural sources such as electronics industry, gold mining, fossil fuel combustion, geothermal activity and pharmaceutical industries.[5–7] Mercury metal and metal ion can be converted by microorganisms in the environment to Methyl-mercury, which accumulated into the body can cause several diseases, damaging the intestine, lungs, kidney, nervous system and DNA causing Minamata and neurological diseases.[8–11] Due to its toxicity, international organizations such as the EPA and FDA have established mercury values for drinking water, being 0.002 ppm and 2 ppb respectively. Several instrumental techniques, such as ICP-MS[12], ICP-AES [13]and AAS[14] have been widely used for detecting toxic metal ions. Since these instrumental techniques require skillful operation and high costs, nowadays alternative detection methods have been receiving much attention. Particular promising approaches for a sensing strategy would involve the use of a fluorescence-based chemosensors[15–17] given their peculiar properties including high sensitivity, sensibility and real-time response.[18,19] A fluorescent chemosensor, basically, consists of a three components (**Figure.1**): a receptor (the interacting part with a target analyte), an active unit (whose emission properties, such as peak wavelength and quantum yield, are modified by the interaction with the analyte) and, eventually a spacer that can change the geometry of the system.[20]

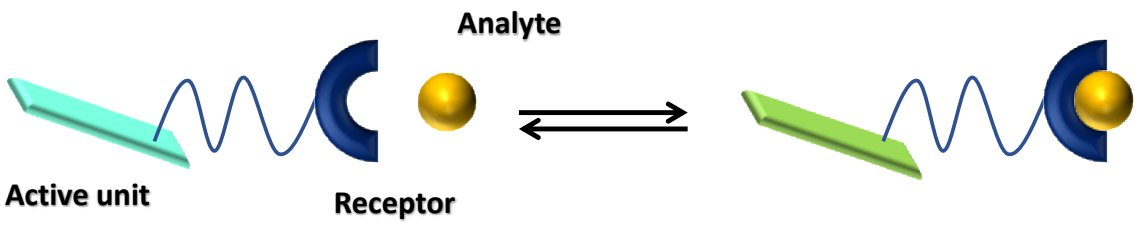

Figure 1. General representation of a chemosensor and its interaction with an analyte.

Among the various fluorophores, the family of rhodamines has found a large employment as active unit in the fabrication of fluorescent chemosensors, including the hybrid ratiometric

platforms discussed in **Chapter 3**, given their unique photophysical properties *i.e* high extinction coefficients, excellent quantum yields, long emission and absorption wavelengths and a great photostability.[21] Rhodamine spirolactam derivatives are nonfluorescent and colorless due to the separation of the xanthene ring from the aromatic ring by a tetrahedral spiro carbon and the interruption of the conjugation in the xanthene ring, whereas ring-opening form gives rise to strong fluorescence emission and a typical red/pink color.[22–24] In general, a rhodamine derivative shows a color change in acidic conditions *via* activation of the carbonylic group on the spirolactam moiety, as shown in **Scheme 1**, and in the same way the spirolactam derivative can be transformed to the open ring form by adding a specific metal ion, differently from FRET based chemosensors where a donor-acceptor energy transfer is crucial for opening the spirolactam ring. This dual response,[25,26] both fluorometric and colorimetric, due to a structural transformation, plays a crucial role in the fabrication of new chemosensors for the recognition of metal ions in the environment.

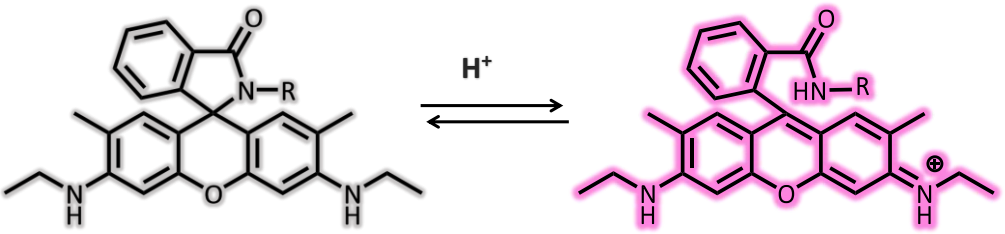

Scheme 1. Spirolactam ring-opening process of rhodamine derivative. The non-fluorescent close ring and the fluorescent forms are highlighted in grey and pink, respectively.

RhO-L$_4$ and **RhO-L$_5$** rhodamine derivatives have been synthesized, according to the literature, and studied as turn-ON chemosensors towards different metal cations. In particular, **RhO-L$_4$** consists of a rhodamine unit, as active unit and two branched primary amine groups, as binding sites, while **RhO-L$_5$** contains a *N*-dipodal binding moiety as shown in **Figure 2.**

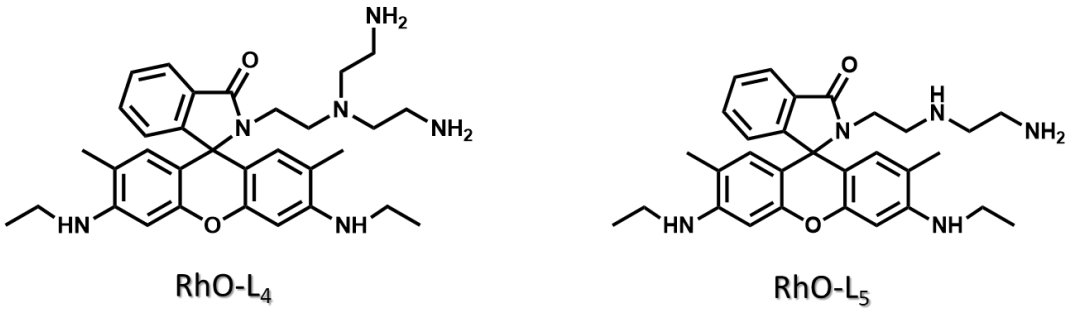

Figure 2. Synthesized rhodamine ligands.

Rhodamine based systems are largely studied since 1997, when Czarnik reported on the first example of rhodamine sensors.[27] Therefore, it represents a challenge to develop new chemosensors based on different fluorescent organic dyes. Among them, coumarin, fluorescein and cyanine have been widely employed in the design of several fluorescent chemosensors for the recognition of mercury and other toxic metal ions (lead, cadmium, etc.). However, in the last years, diketopyrrolo-[3,4-c]pyrroles (hereafter DPPs) have attracted ever-growing scientific interest as a valid alternative to rhodamine derivatives for obtaining new fluorescent sensing probes. DPPs, synthesized by the reaction of an aromatic nitrile with dialkyil succinate, are interesting organic dyes, employed in several research fields as Organic Field-Effect Transistors (OFTEs) and Organic Photovoltaics (OPVs).[28–31] Recently, given their excellent optical properties such as strong absorption and emission in the visible region, high photostability, and large Stokes shift,[32–34] they were employed in the design of fluorescent probes to detect chemical analytes.[35–38] Generally, DPP derivatives, containing two amine units and two carbonyil groups[33] (**Scheme 2**) in the core, together with two flanked aromatics groups, have a planar structure and can induce strong intermolecular H-bonding and π–π stacking with neighboring molecules. Taking into account that thymine is one of selective receptors for Hg^{II},[39] a DPP derivative with similarity with thymine was tailored for the interaction with Hg^{II}. DPP-Hg^{II}-DPP complexation has been firstly reported by Kaixuan Nie and Bo Dong in 2017.[40] They synthesized a thiophene diketopyrrolo-pyrrole (**DPPT**) derivative, with a hydrophilic chain able to form micelles in aqueous environment. The complexation with Hg^{II} induces rigidity on the molecular structure and this phenomenon leads to molecular aggregation.[41] Molecular aggregations cause a change in the absorbance and emission spectra making **DPPT** derivatives promising sensors for the recognition of Hg^{II}.

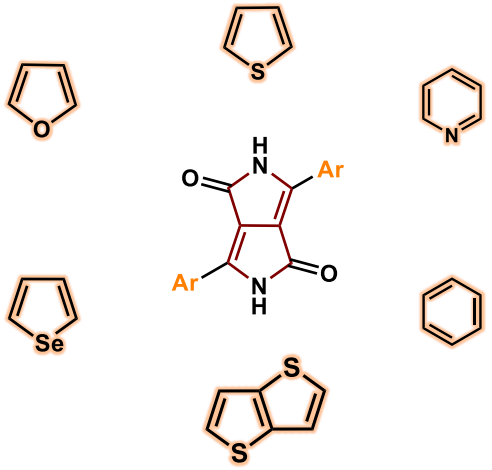

Scheme 2. Some Ar-DPP derivatives (Ar=benzene, pyridine, thiophen, furane, selenophene thienothiophene).

All fluorescent and colorimetric chemosensors based on DPP framework are reported in **Figure 3**. **DPP-L_1**, **DPP-L_2**, **DPP-L_3** and **DPP-L_4**, have been synthesized and characterized at the Moltech-Anjou Laboratory (University of Angers), under the supervision of Prof. Narcis Avarvari and Dr. Flavia Pop. The work performed in Angers was interrupted due to the coronavirus Emergency, but the synthesis of the organic dyes has continued in Cagliari, under the supervision of Prof. Avarvari in the laboratory of Prof. Mercuri at University of Cagliari.

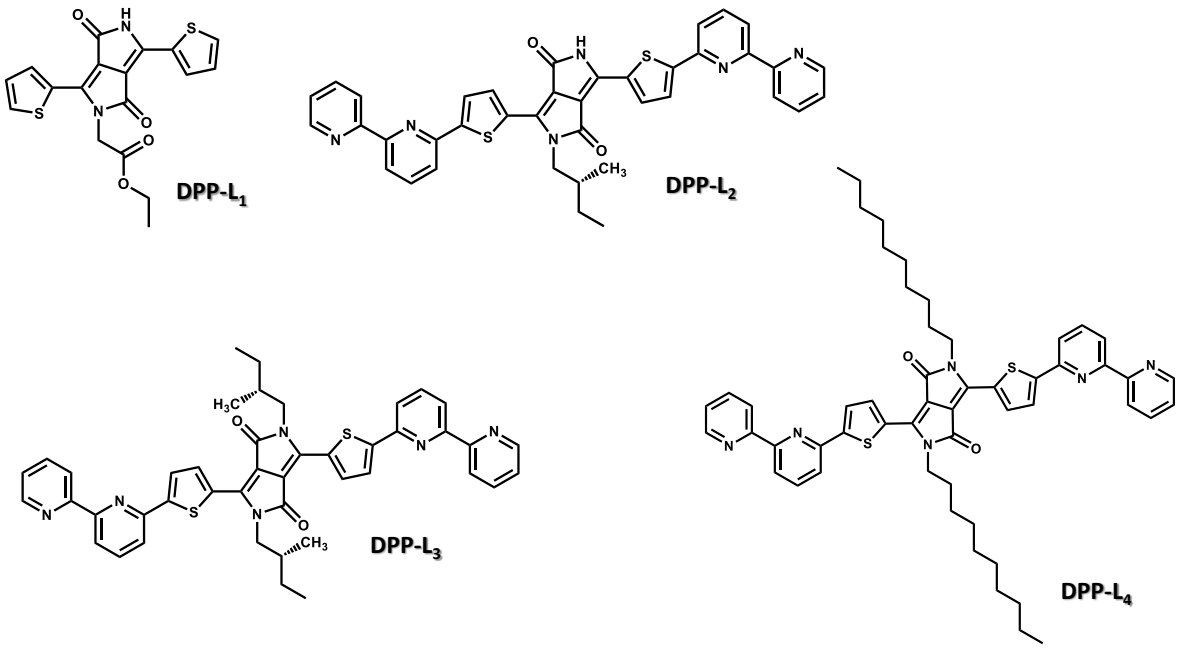

Figure 3. DPP based ligands used in the project.

DPP-L$_1$ and **DPP-L$_2$** are monoalkylated derivatives, in which the free-amide group is the binding site towards mercury cation. Particularly interesting is **DPP-L$_2$** consisting of two bipyridine moieties. Bipyridine, being a bidentate ligand, could be a binding site towards different transition metal ions. Monoalkylated derivatives, based on **DPPT** skeleton, show a low solubility and to overcome this issue, **DPP-L$_3$** and **DPP-L$_4$** have been synthesized as bi-alkylated compounds.

4.2A Results and Discussion (RhO Derivatives)

4.2A.1 Synthesis and Characterization

RhO-L$_4$ consists of a rhodamine moiety (spirolactam form) and two branched primary amine groups. Here, the rhodamine portion acts as a signaling unit while the alkyl amine spacer allows Hg^{II} interaction. In addition, we prepared a similar compound, **RhO-L$_5$** (containing a *N*-dipodal moiety) to compare with **RhO-L$_4$**, to deeper insight into the mechanism interaction between

and Hg^{2+}. In **Scheme 4,** the reaction of rhodamine 6G with an excess of tris (2-aminoethyl) amine (TREN) or diethylenetriamine is reported, using as solvent MeOH, to afford **RhO-L*4*** and **RhO-L*5***.

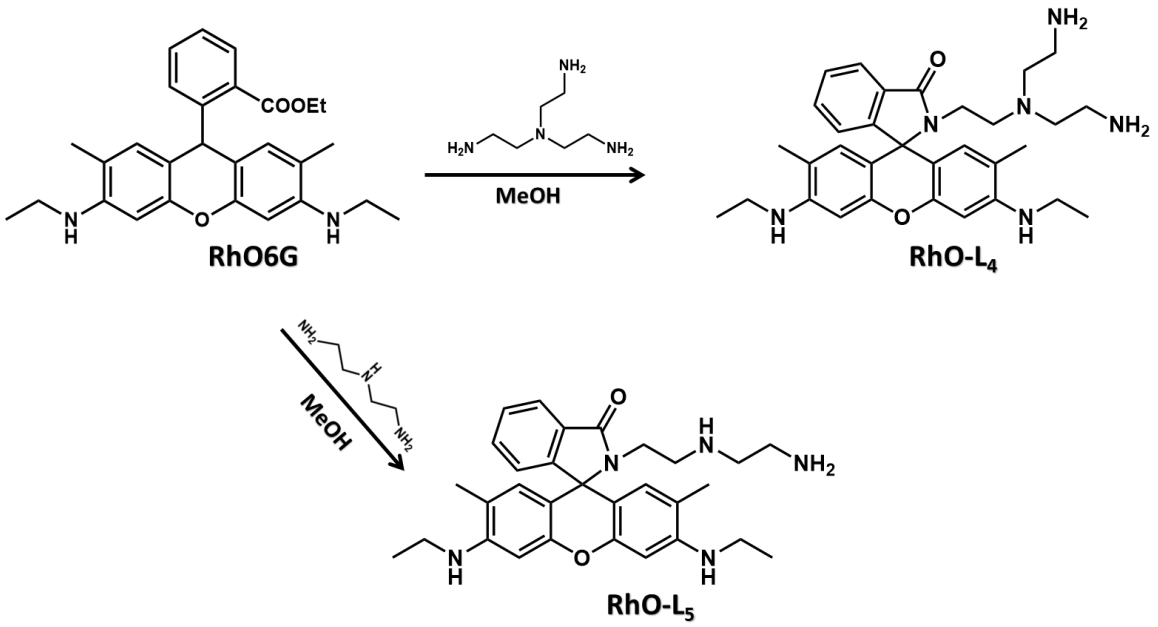

Scheme 3. Reaction scheme of RhO-L_4 and RhO-L_5.

Figure 4 shows the photophysical characterization of the synthesized chemosensors. The solutions of **RhO-L*4*** and **RhO-L*5*** in CH_3CN/H_2O (ratio 4:1 v/v) are colorless. Absorption spectra have been carried out in neutral and acidic conditions in order to study the spirolactam and ring-opening forms of **RhO-L*4*** and **RhO-L*5***. In neutral conditions, the band at 310 nm, characteristic of rhodamine derivatives in their spirolactam form, is observed while in acidic conditions (pH=2) the ring-opening, induced by proton interaction, occurs and new bands, at 350 and 550 nm, appear in according with rhodamine derivatives in their ring-opening forms.[42] The PL spectra **RhO-L*4*** and **RhO-L*5*** were performed by sample excitation at 510nm. An emission band, centered at 550 nm, is observed only in acidic conditions, typically attributed to rhodamine derivatives in their ring-opening form.[42]

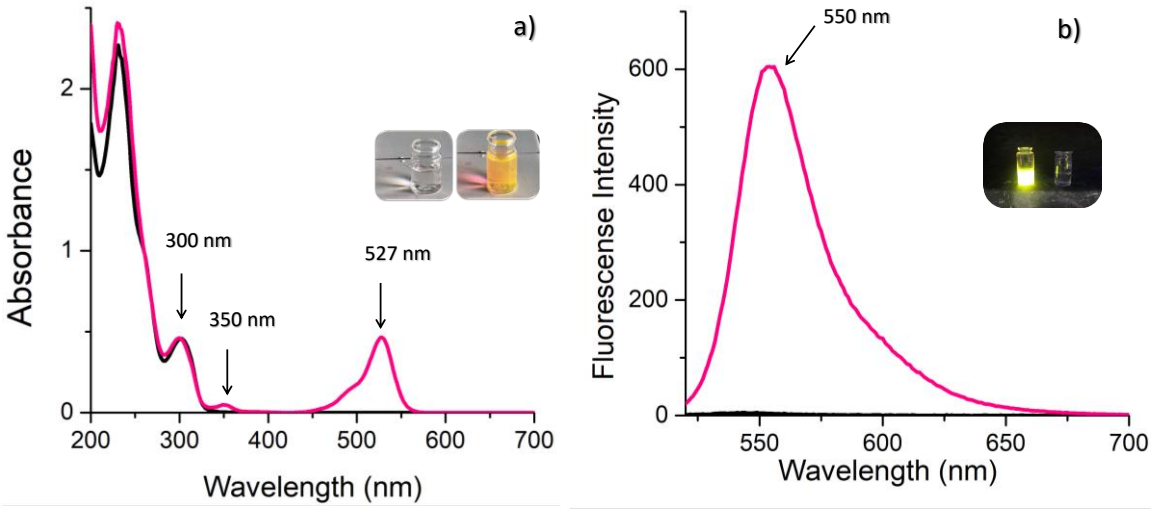

Figure 4. a) Absorption and **b**) Fluorescence spectra of **RhO-L$_4$** and **RhO-L$_5$** derivatives ($2 \cdot 10^{-5}$ M) in neutral (black line) and acidic (pink line) conditions.

Since the fluorescence intensity of rhodamine derivatives are affected by pH conditions, acid–base titrations have been performed to evaluate the behavior of **RhO-L$_4$** and **RhO-L$_5$**. **Figure 5** shows that the spirolactam undergoes a ring-opening and a strong fluorescence band, centered at 550 nm, is observed for pH < 4, while no fluorescence variation is found in the 5.0 - 10.0 pH range.

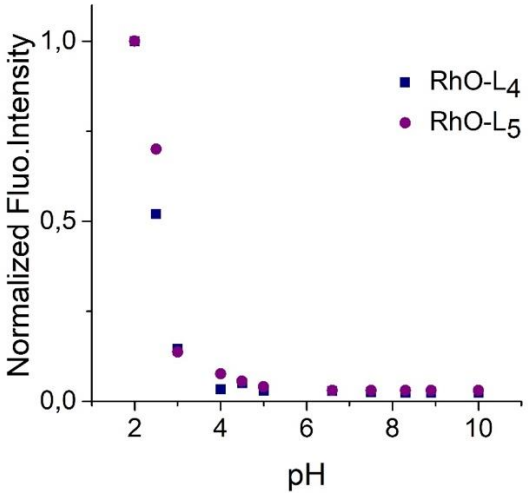

Figure 5. RhO-L$_4$ and **RhO-L$_5$** Fluorescence Intensity *vs* pH in the 2 – 10 range, in acetonitrile–water (4:1 v/v) mixture (λ_{ex} = 510 nm).

4.2A.2 Selectivity Studies

A spectrophotometric and spectrofluorimetric screening in presence of several cations (as nitrate or perchlorate salts), in particular Cd^{II}, Cu^{II}, Fe^{III}, Al^{III} Hg^{II} , Ni^{II}, Zn^{II} and Pb^{II}, has been performed, in order to evaluate the **RhO-L$_4$** capability in detecting metal cations. The absorption spectrum of **RhO-L$_4$**, in CH_3CN/H_2O (4:1 v/v) mixture, at pH 7.4 (MOPS buffer, MOPS = 3-N-morpholino-propansulfonic acid) shows two bands, at 231 nm (ε =10000 M^{-1} cm^{-1}) and 302 nm (ε = 57479 M^{-1} cm^{-1}) (**Figure 6 a-b**). Selectivity experiments are reported in **Figure 6c**, showing the best performance towards Hg^{II}. Interestingly, only the interaction with Hg^{II} induces the spirolactam opening, confirmed by the appearance of two new absorbance peaks at 350 and 530 nm (**Figure 6a**) and an increase of fluorescence intensity, generally attributed, to its ring-opening form (**Figure 6b**). In normal conditions, when cations are not present, **RhO-L$_4$** did not show any fluorescence band in the 450-600 nm region due to the spirolactam form, while a remarkable fluorescence band, centered at 550 nm, upon addition of Hg^{II} appears in acid conditions (**Figure 6b)**.

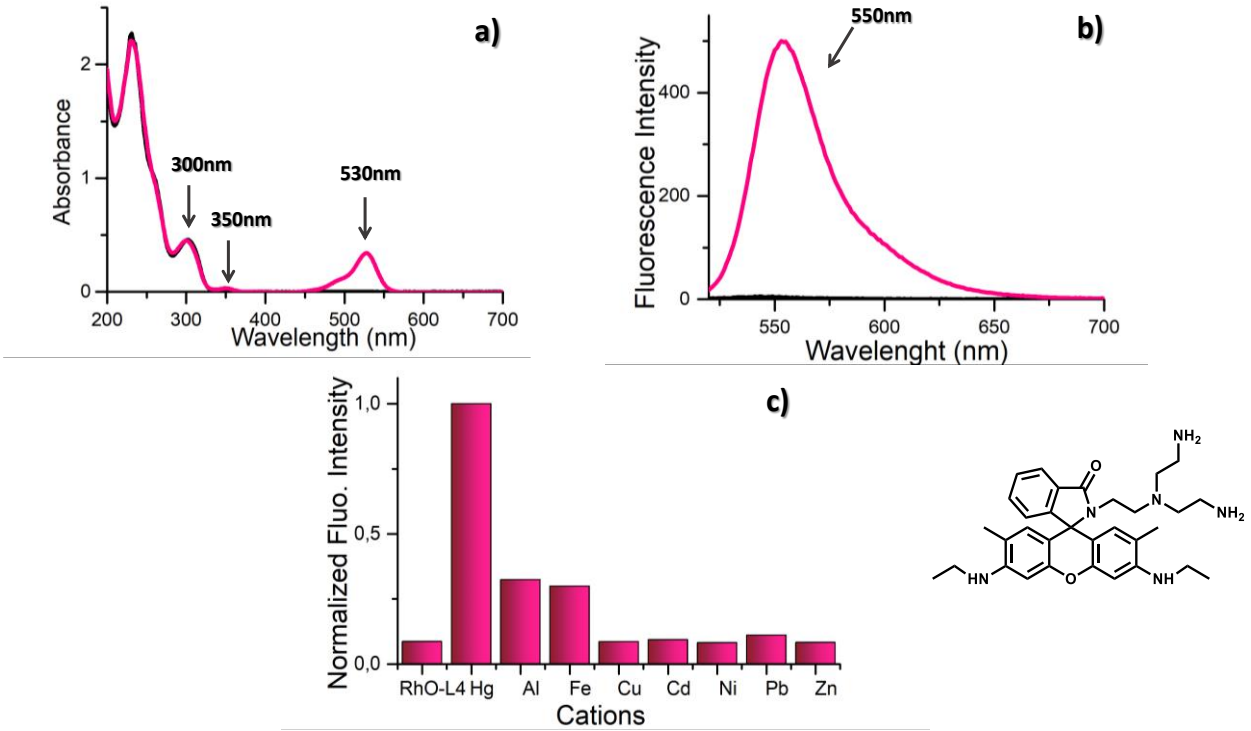

Figure 6. RhO-L$_4$ ($2 \cdot 10^{-5}$ M) **a)** Absorption and **b)** Fluorescence spectrum, before (black line) and upon adding of Hg^{II} (pink line). **c)** Selectivity experiments towards various metal cations.

In order to investigate the mechanism interaction between **RhO-L$_4$** and mercury cation, **RhO-L$_5$**, bearing one N-dipodal arm, has been synthesized and then characterized in terms of emission and absorption properties and tested with several metal cations. Selectivity studies are carried out following the same procedure used for **RhO-L$_4$**. Interestingly **Figure 6c** and **7c** show that the mechanism involved in **RhO-L$_4$**-Hg^{II} and **RhO-L$_5$**-Hg^{II} interaction is different, suggesting that both N-dipodal arms, present in **RhO-L$_4$**, play a crucial role in chelating mercury ions, as reported in **Scheme 4.** In fact, **RhO-L$_5$** shows a change in absorbance and fluorescence intensity only upon adding of Al^{III} and Fe^{III} (**Figure 7c**).

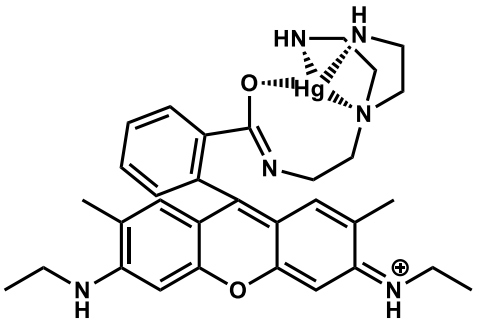

Scheme 4. Proposed mechanism of the interaction between **RhO-L$_4$** and Hg^{II}

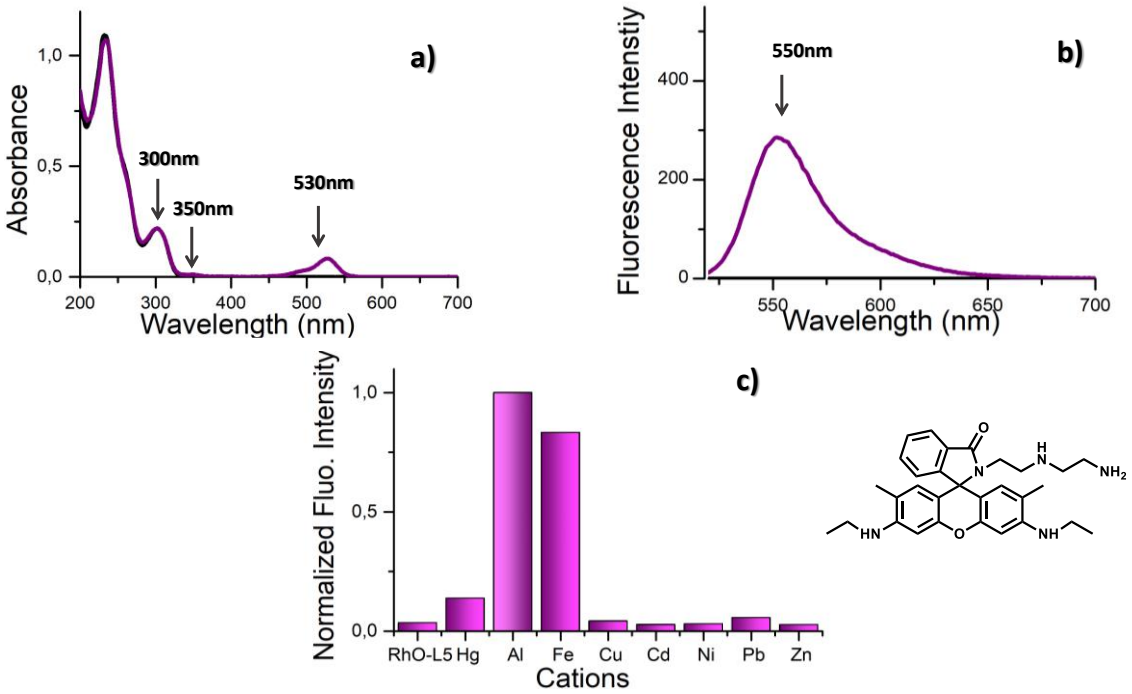

Figure 7. RhO-L$_5$ ($2\cdot10^{-5}$ M) **a)** Absorption and **b)** Fluorescence spectrum, before (black line) and upon adding of Al^{III} (pink line). **c)** Selectivity experiments towards various metal cations.

RhO-L$_4$ performance in the detection of mercury cation was monitored by UV-Vis. and Fluorescence titration experiments. The spectral titration of **RhO-L$_4$** (2.1 10^{-5} M) with Hg^{II} was performed in CH_3CN/H_2O (4:1 v/v) mixture, at pH 7.4 (MOPS buffer). It can be seen in **Figure 8** that the absorption and emission bands, centered at 530 nm and 550 nm, respectively, are enhanced with the increase of Hg^{II} concentration in the 0-50 equivalents (eq.). The calculated Limit of Detection (LoD) for Hg^{II} is 4.3 ppm, over the allowable 0.02 ppm limit.

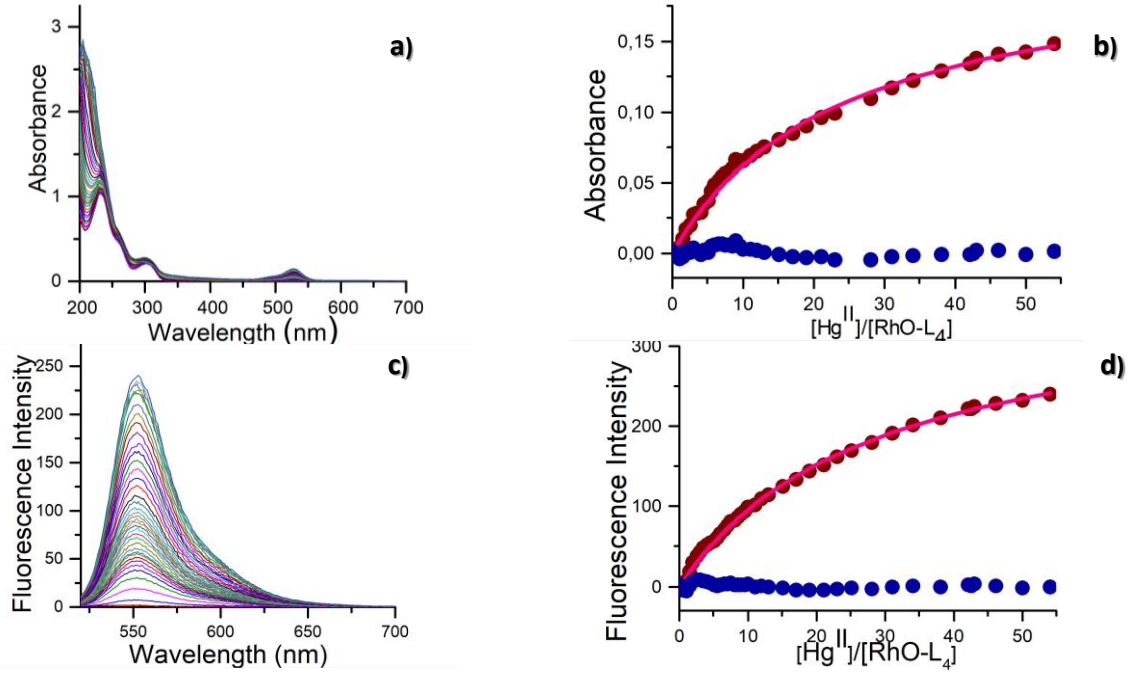

Figure 8. UV-Vis absorption (**a**) and fluorescence (**c**) spectra of **RhO-L$_4$** with various concentrations of Hg^{II}, bottom-to-top, Hg^{II}: 0, 10, 20, 30, 40 and 50 eq. Plots of the **b)** absorbance (*A*) at 530 nm and **d)** the Fluorescence intensity (*F*) at 550 nm *vs.* the concentration of Hg^{II}, with fitting curves in red (λ_{ex}: 510 nm, slit width: 5 nm). The blue dots represent Aborbance and Fluorescence of free **RhO-L$_4$.**

4.3A Experimental Section

4.3A.1 Materials

All reagents are purchase from Sigma Aldrich and used without further purifications**. RhO-L_4** and **RhO-L_5** synthesis reactions were performed in oven-dried glassware under a slight positive pressure of nitrogen. ^{1}H-NMR (300 MHz or 500 MHz) spectra were determined on a Bruker Advance 300 MHz or on a Varian VXR500. Chemical shifts for ^{1}H-NMR are reported in parts per million (ppm), calibrated to the residual solvent peak set, with coupling constants reported in Hertz (Hz). The following abbreviations are used for spin multiplicity: s = singlet, d = doublet, t = triplet, and m = multiplet. UV-Vis absorption spectra were recorded at 298.1 K on a Varian Cary-100 spectrophotometer equipped with a temperature control unit. Fluorescence emission spectra were recorded at 298.1 K on a Varian Cary-Eclipse spectrofluorimeter and the spectra are uncorrected.

4.3A.2 Synthesis of RhO-L_4

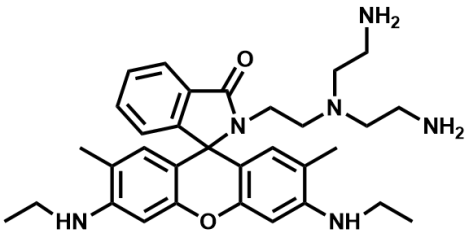

RhO-L_4

RhO-L_4 was synthesized following a literature procedure.[43] Rhodamine 6G (958 mg, 2 mmol) was dissolved in 25 mL of methanol. Tris(2-aminoethyl) amine was added slowly to Rhodamine solution. The reaction was refluxed until the solution changed from pink tom orange. After cooling to room temperature, the solvent was evaporated under vacuum. Then, CH_2Cl_2 and water were added and the organic layer was separated. The organic phase was washed with water and dried with anhydrous Na_2SO_4. NMR ^{1}H NMR (300 MHz, $CDCl_3$ 298K): 7.91 (m, 1H), 7,45 (m ,2H), 7,02 (m, 1H), 6,33(s, 2H), 6.14 (s, 2H), 3,35 (broad s, 2H), 3,20 (m, 6H), 2,55 (t, 6H), 2.33(t, 4H), 2.21 (m 2H), 1.85 (s, 6H).

4.3A.3 Synthesis of RhO-L_5

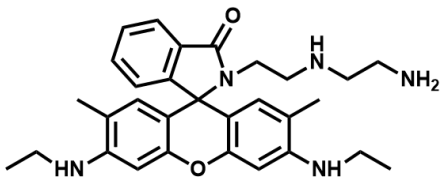

RhO-L_5

RhO-L_5 was synthesized optimizing a Rhodamine 6G[43] (958 mg, 2 mmol) was dissolved in 25 mL of methanol. Tris(2-aminoethyl) amine was added slowly to the Rhodamine solution. The reaction was refluxed until the solution changed from pink to orange. After cooling to room temperature, the solvent was evaporated under vacuum. Then, CH_2Cl_2 and water were added, and the organic layer was separated. The organic phase was washed with water and dried with anhydrous Na_2SO_4. L_1 was obtained as a pale pink solid. ^1H NMR (300 MHz, $CDCl_3$ 298K): 7.91 (m, 1H), 7,45 (m ,2H), 7,02 (m, 1H), 6,33(s, 2H), 6.14 (s, 2H), 3,35 (br s, 2H), 3,20 (m, 6H), 2,55 (t, 6H), 2.33(t, 4H), 2.21 (m 2H), 1.85 (s, 6H).

4.3A.4 Selectivity Studies

RhO-L_4 and RhO-L_5. Stock solutions of various metal ions (2.5×10^{-3} M) were prepared in deionized water. Stock solutions of **RhO-L_4** (2×10^{-5} M) and **RhO-L_5** (1.8×10^{-5} M) was prepared in CH_3CN:H_2O (4:1 ratio v/v). Spectral data were recorded after the addition of the ions. In the selectivity experiments, the test samples were prepared by placing an appropriate amount of the cations stock into 2 ml of solution of **RhO-L_4** (2×10^{-5}M). In the titration experiments, a solution of **RhO-L_4** (1×10^{-5} M) was placed in a quartz optical cuvette of 1 cm optical path length, and the ion stock solutions were added into the quartz optical cell gradually by using a micropipette.

4.2B Results and Discussion (DPP Derivatives)

4.2B.1 Synthesis and Characterization

This work, performed in Moltech Anjou Laboratory, University of Angers, under the supervision of Prof. Narcis Avarvari and Dr. Flavia Pop, has been interrupted due to Coronavirus Emergency (1,5 month stay over 5 expected months).

DPP-L_1, DPP-L_2, DPP-L_3 and **DPP-L_4**, have been synthesized as fluorescent chemosensors for the recognition of metal cations, with two different design approaches.

Based on the strong binding affinity of lactam-N in DPP dyes for transition metal ions, two fluorescent chemosensors, **DPP-L_1** and **DPP-L_2**, have been designed for the recognition of metal cations in aqueous environment. **DPP-L_1** is a monoalkylated **DPPT** derivative, consisting of a free-amide group, as binding site to interact with mercury cation, and an ester group, as alkylating chain, which could be hydrolyzed and anchored to silica nanoparticles. The design approach, to obtain the sensing fluorescent platform, is reported in **Figure 9.**

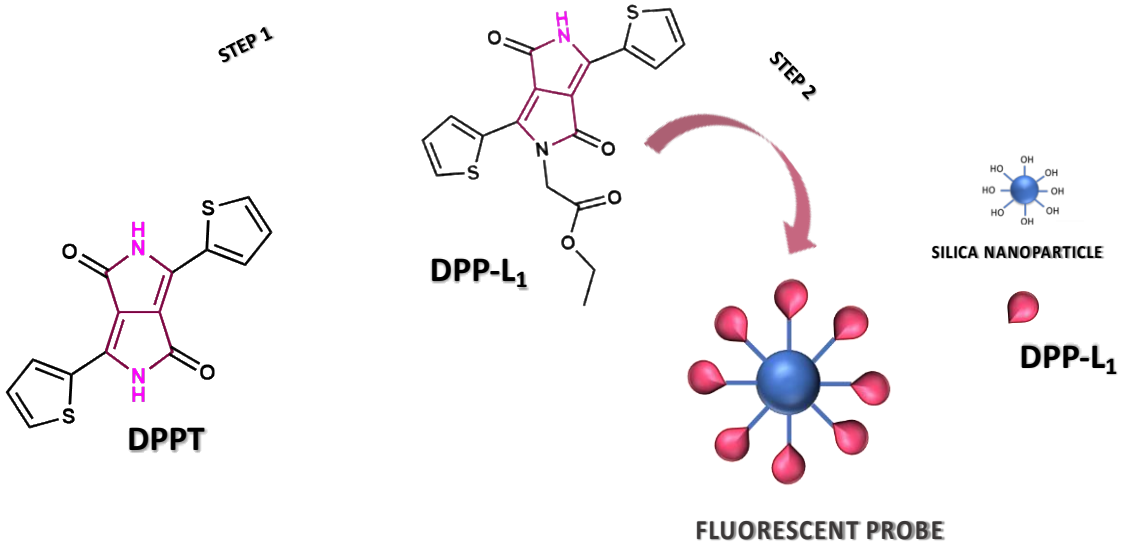

Figure 9. Step 1: synthesis of **DPP-L_1** starting from **DPPT** precursor; **Step 2**: functionalization of silica nanoparticles.

DPP-L_1 was synthesized (**Scheme 5**), starting from DPP, according to similar procedures described by F. Pop *et al.*[44] by using one equivalent of the alkyl halide derivative. When two equivalents of alkylating agent were added bis-alkylated derivative was obtained exclusively

whereas using fewer equivalents both derivatives, mono (**DPP-L$_1$**) and dialkylate one were obtained. They were separated by flash column chromatography.

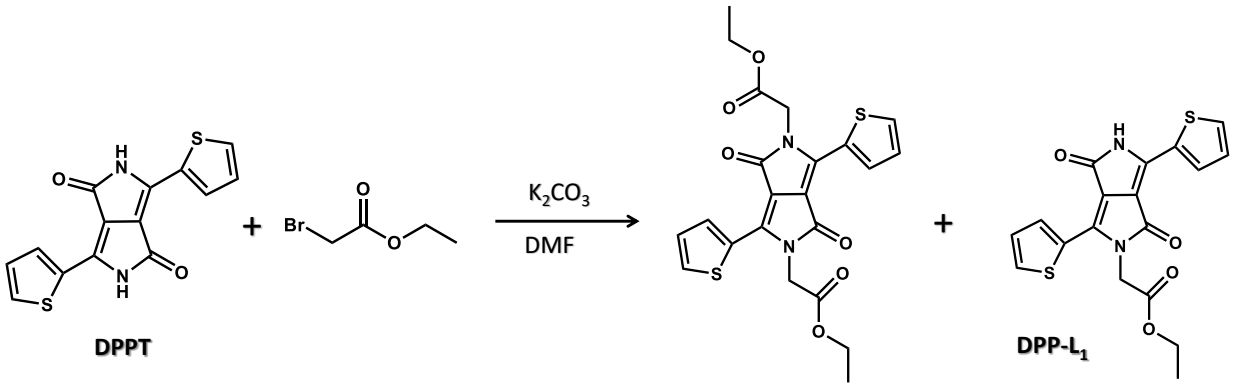

Scheme 5. Reaction synthesis of **DPP-L$_1$**.

In a previous work, performed in Montelch-Anjou Laboratory, by Avarvari *et al*., platinum complexes based on DPPT-Bipyridine derivatives were synthesized and characterized. Platinum complexes shown a change in the optical properties, quenching of emission and a decrease of absorbance, compared to the free ligands. On these basis, **DPP-L$_2$** (**Scheme 6**), a monoalkylated derivative, consisting of two bipyridine skeletons, which being a good bidentate chelating ligand, offers several coordination sites for the interaction with metal ions and an increase of elating the system conjugation, has been synthesized.

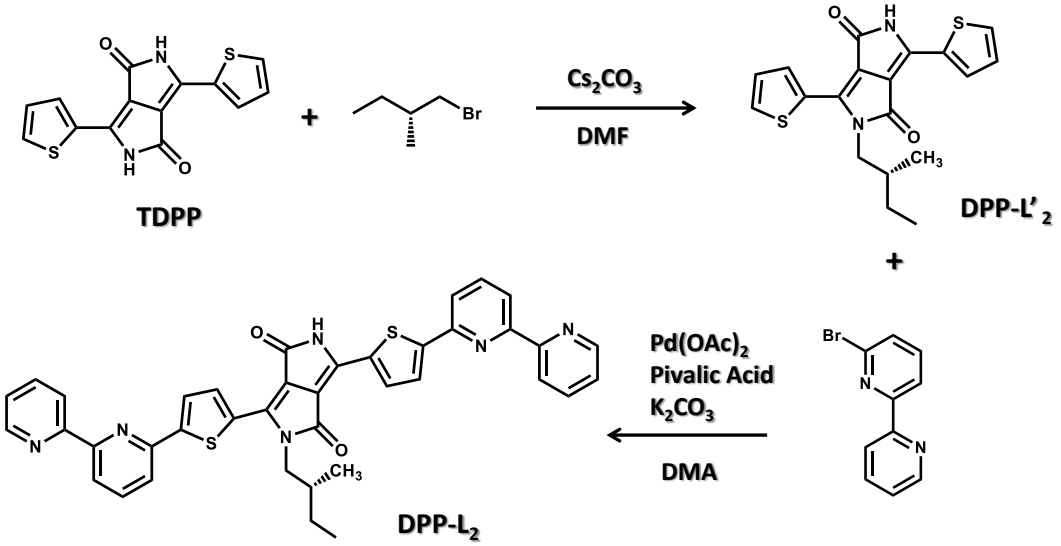

Scheme 6. Reaction synthesis of **DPP-L$_2$**.

Firstly, **DPPT** moiety has been alkylated, in order to obtain the monoalkylated derivative, then the bipyridine moiety has been attached to thiophene by the microwave method. The mono-alkylated derivatives, **DPP-L$_1$** and **DPP-L$_2$** are low soluble because of the strong intermolecular hydrogen bonding of the free NH units. In order to increase the solubility, the synthesis of **DPP-L$_3$** and **DPP-L$_4$**, as di-alkylated compounds, has been performed.

After alkylation of DPPT precursor, compounds, **DPP-L'$_2$** and **DPP-L'$_3$**, were obtained with yields of 26 % and 8%, respectively. The synthesis of the compounds **DPP-L$_3$**, (**Scheme 7**) was performed using the microwave method. After purification by chromatography, the compounds were obtained with a yield of 30%. Monosubstituted ligands and bis-substituted ones show different colors.

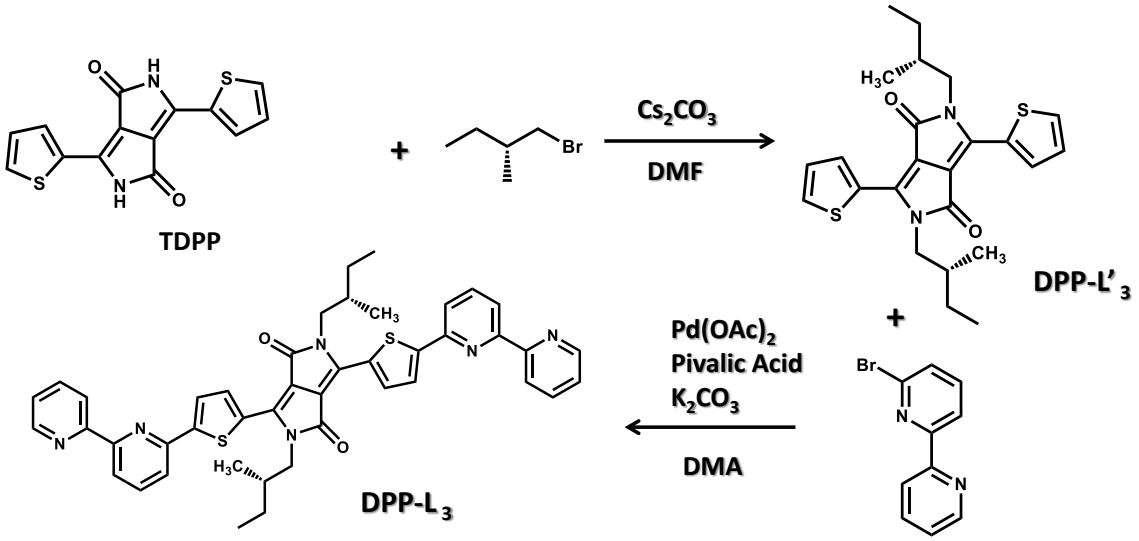

Scheme 7. Reaction synthesis of **DPP-L$_3$**.

DPP-L$_4$ was prepared from the unit C_{10}-dithiophene- diketopyrrolopyrrole and 6-bromo-2,2'-bipyridine (**Scheme 8**), by using the microwave method.

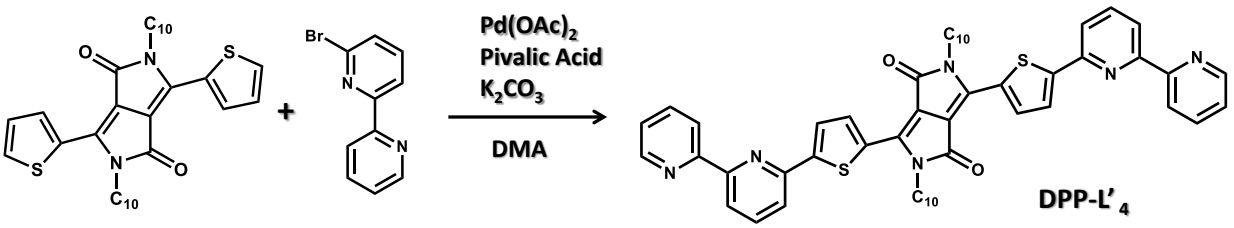

Scheme 8. Reaction synthesis of **DPP-L$_4$**

The obtained mono-bipyridine and the bis-bipyridine compounds were separated by chromatography. It was possible to control the formation of the mono or bis-functionalized ligand by adding 1 or 2 equivalents of 6-bromo-2,2'-bipyridine and the compounds were obtained with yields of 39 % for the mono-substituted compound and 5% for **DPP-L$_4$**. The solution of the mono-substituted compound is purple, while the solution of **DPP-L$_4$** is dark-violet. The change in color is expected and it will be later correlated with the increase of the conjugation length of the aromatic part.

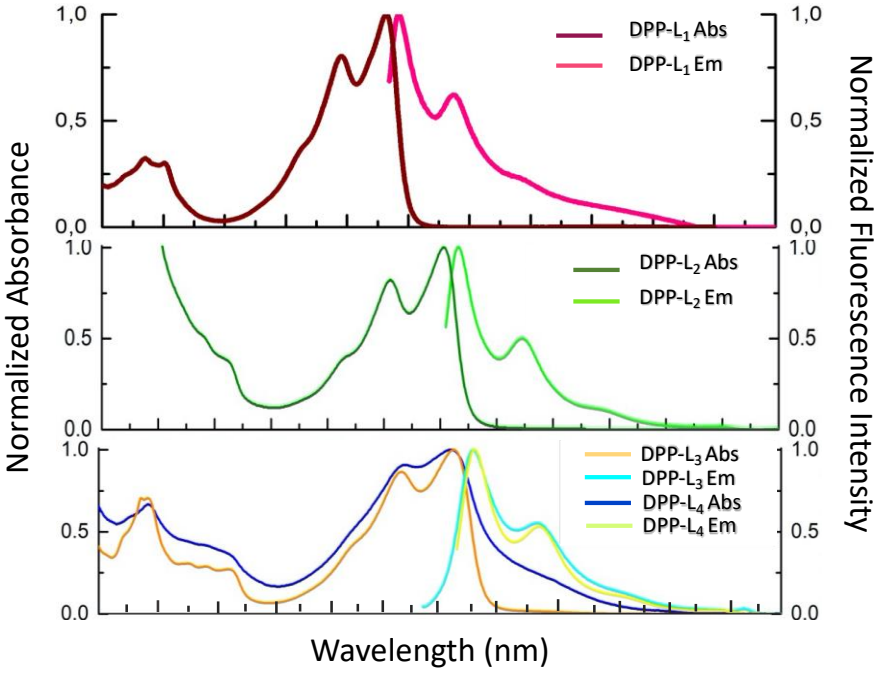

Figure 10. Absorption and emission spectra performed in THF

The shape of the absorption and emission bands are characteristic of **DPPT** based compounds. However, a bathochromic shift is observed between the compound without bipyridine and the bi-bipyridine derivative, showing that absorption and emission properties have been tuned by increasing the π-conjugated system. Conversely, the absorption is not influenced by the alkyl substituents on the DPP lactam unit. Absorption spectra exhibit dual band absorption profiles common for compounds with a donor–acceptor primary structure.[19] The absorption profiles show intense visible bands, centered at 500 nm and weaker high energy bands at around 340 nm, attributed to strong intramolecular interactions from the thiophenyl donor to the DPP acceptor and π–π transitions localized on either the donor or the acceptor, respectively.

4.2B.2 Selectivity Experiments

DPP-L$_1$, as shown in **scheme 5**, has been synthesized as monoalkylated derivative for the interaction with mercury cation, based on the strong binding affinity of lactam-N in DPP dyes for transition metal ions, *via* analogous T-Hg-T complexation, two DPP dyes can form a DPP–Hg-DPP. To demonstrate this mechanism, the spectroscopic properties of the precursor DPPT and the monoalkylated derivative, upon addition of Hg^{II} were studied. In normal conditions, **DPPT** exhibited a characteristic maximum absorption peak centered at 526 nm. Upon addition of Hg^{II}, the maximum absorption intensity decreased, and a new absorption band, centered at 598 nm, appeared, as shown in **Figure 11a**. The interaction between N-lactam and mercury allows fluorophore aggregation, evidenced by the absorption band at 598 nm. By adding 1 eq. of Hg^{II}, a color change by naked eyes was observed (**Figure 11d**). A similar behavior has been observed also for **DPP-L$_1$**. Upon addition of increasing concentrations of Hg^{II}, the maximum absorption intensity decreases and a new absorption band, centered at 550 nm, appeared and increased. This increase is due to **DPP-L$_1$** aggregation.

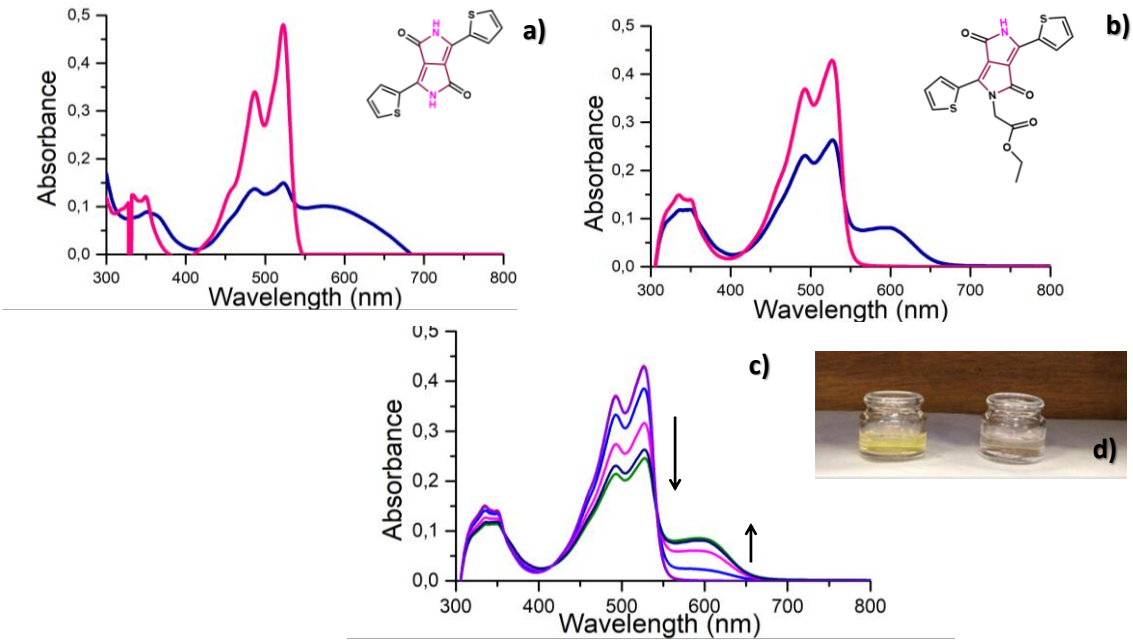

Figure *11*. UV–vis absorption spectra of (**a**) **DPPT** and (**b**) **DPP-L$_1$** with (line blue) and without (line pink) the addition of Hg^{II}. (**c**) Hg^{II} titration performed on **DPP-L$_1$** and (**d**) color variation due to Hg^{II} addition (yellow to colorless solution).

4.3B Experimental Section

4.3B.1 Materials

All reagents are purchase from Sigma Aldrich and used as received without further purifications**.** **L_1**, **L_2** and **L_3** synthesis reactions were performed in oven-dried glassware under a slight positive pressure of nitrogen. **L_4** has been synthesized using the microwaves method. ^{1}H-NMR (300 MHz or 500 MHz) spectra were determined on a Bruker Advance 300 MHz or on a Varian VXR500. Chemical shifts for ^{1}H-NMR are reported in parts per million (ppm), calibrated to the residual solvent peak set, with coupling constants reported in Hertz (Hz). The following abbreviations are used for spin multiplicity: s = singlet, d = doublet, t = triplet, and m = multiplet. UV-Vis absorption spectra were recorded at 298.1 K on a Varian Cary-100 spectrophotometer equipped with a temperature control unit. Fluorescence emission spectra were recorded at 298.1 K on a Varian Cary-Eclipse spectrofluorimeter and the spectra are uncorrected.

4.3B.2 Synthesis of DPP-L_1

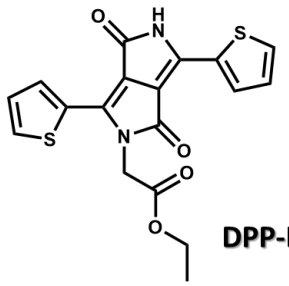

DPP-L_1

A solution of thiophene diketopyrrolopyrrole (1,3 mmol, 0,400 g) and K_2CO_3 (1.3 mmol, 0,179 g) was heated. When the temperature has reached 106°C it was added Ethyl Bromoacetate (1.3 mmol, 0.222 g). the reaction was left at 106°C overnight. After cooling the temperature H_20 was added to the reaction, a violet precipitate appeared. It was filtered under vacuum and washed three times in order to avoid DMF and carbonate. The precipitate was solubilized by DCM. The organic solution was dried with Mg_2SO_4 filtered and concentrated under vacuum. The compound was purified through chromatography column using DCM/Ethylacetate as eluents mixture. A dark red solid was obtained (yield 15 %) 1H NMR (500 MHz, DMSO-*d*6) δ 11.54 (s, 1H), 8.62 (dd, *J* = 3.9, 1.2 Hz, 1H), 8.26 (dd,

J = 3.8, 1.2 Hz, 1H), 8.06 (dd, *J* = 5.0, 1.1 Hz, 1H), 8.03 (dd, *J* = 5.0, 1.2 Hz, 1H), 7.38 (dd, *J* = 5.0, 3.8 Hz, 1H), 7.34 (dd, *J* = 5.0, 3.8 Hz, 1H), 4.86 (s, 2H), 4.17 (q, *J* = 7.1 Hz, 2H), 1.18 (t, *J* = 7.1 Hz, 3H).

4.3B.3 Synthesis of DPP-L'$_2$

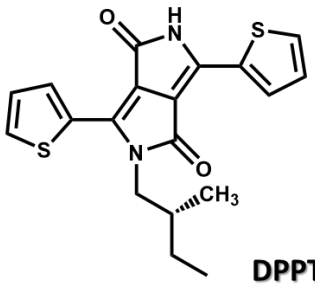

DPPT- L'$_2$

A solution of thiophene diketopyrrolopyrrole (1 mmol 0.307) and Cs_2CO_3 (2.5 eq) in DMF (3 mL mmol^{-1}) was prepared and, when the temperature has reached T=100 °C, (S)-(+)-1-bromo-methylbutane (1 eq) was added the and the mixture was left at 100 °C for 6 h. The crude product was extracted with H_2O saturated with NaCl and THF, the organic phase was dried with Mg_2SO_4 anhydrous, filtered and concentrated under vacuum. The crude product was purified by column chromatography (CH_2Cl_2, AcOEt/CH_2Cl_2 20/80%); a red solid was obtained (yield 8%) The ^{1}H-NMR is in accord to the literature. [45]

4.3B.4 Synthesis of DPP-L'$_3$

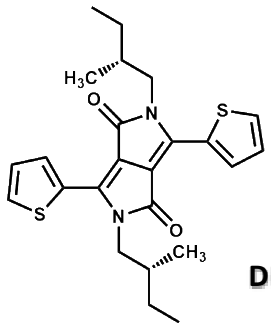

DPP-L'$_3$

A solution of thiophene diketopyrrolopyrrole (1 mmol) and Cs_2CO_3 (2.5 eq) in DMF (3 mL mmol^{-1}) was prepared and, when the temperature has reached 100 °C, (S)-(+)-1-bromo-methylbutane (2 .1 eq) was added the and the mixture was left at 100 °C for 6 h. The crude product was extracted with H_2O and CH_2Cl_2, the organic phase was dried with Mg_2SO_4 anhydrous, filtered and concentrate under vacuum. CH_3OH was added,

the precipitate was filtered and dissolved in CH_2Cl_2, while the solution in CH_3OH was concentrated under vacuum and purified by column chromatography (Hexane/CH_2Cl_2 10/90%); a red solid was obtained. After concentrate CH_2Cl_2 phase, the product was washed with CH_3OH and a red solid was obtained (yield 26 %). The ^{1}H-NMR is in accord to the literature.[45]

4.3B.5 Synthesis DPP-L_2

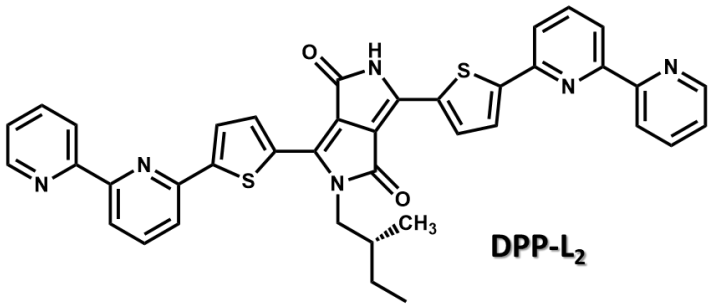

DPP-L_2

Under argon, **DPP-L'$_2$** (1 mmol), 6-bromo-2,2'-bipyridine (2 eq), K_2CO_3 (2 eq), $Pd(OAc)_2$ (0.1 eq) and pivalic acid (0.2 eq) were mixed together in a solution of anhydrous dimethylacetamide (DMA) (9.5 mL mmol^{-1}); the mixture was placed in the microwave for 40 min (T=180 °C, P=10 bar). The crude product was extracted with H_2O saturated with NaCl and THF, the organic phase was dried with Mg_2SO_4 anhydrous and concentrated under vacuum. The crude product was purified by column chromatography (start with CH_2Cl_2 and add gradually AcOEt until 50% in CH_2Cl_2); a violet solid was obtained after washing with CH_3OH (yield 18%). The solution of the product was violet.

^{1}H-NMR (300 MHz, TDF), δ: 8.71 (d, 1H, *J* = 4.1 Hz), 8.65 (d, 2H, *J* = 4.0 Hz), 8.59 (d, 2H, *J* = 8.0 Hz), 8.43 (dt, 2H, *J* = 6.4, 2.1 Hz), 7.94 – 7.86 (m, 8H), 7.40 – 7.33 (m, 3H), 4.74 (s, 1H), 4.28 – 4.02 (m, 2H), 1.06 – 1.01 (m, 9H).

4.3B.6 Synthesis DPP-L_3

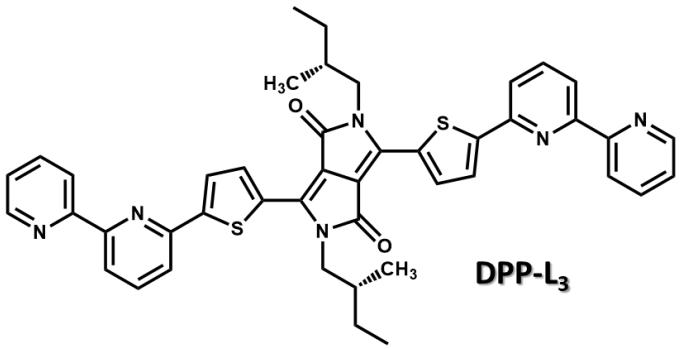

DPP-L_3

Under argon, **DPP-L'$_3$** (1 mmol), 6-bromo-2,2'-bipyridine (1 eq), K_2CO_3 (2 eq), $Pd(OAc)_2$ (0.1 eq) and pivalic acid (0.2 eq) were mixed together in a solution of anhydrous DMA (9.5 mL $mmol^{-1}$); the mixture was placed in the microwave for 40 min (T=180 °C, P=10 bar). The product was extracted with H_2O saturated with NaCl and THF, the organic phase was dried with Mg_2SO_4 anhydrous and concentrated under vacuum. The crude product was purified by column chromatography (starting with CH_2Cl_2 and adding gradually AcOEt until 50% in CH_2Cl_2); the two fractions obtained correspond to the mono- (not characterized in this thesis) and the di-substituted (**DPP-L_3**), yielding 30% and 5%, respectively. ^{1}H-NMR (300 MHz, $CDCl_3$) δ: 9.13 (d, 1H, J = 4.3 Hz), 8.98 (d, 1H, J = 3.9 Hz), 8.68 (d, 1H, J = 3.8 Hz), 8.54 (d, 1H, J = 8.0 Hz), 8.37 (d, 1H, J = 7.8 Hz),7.90 – 7.81 (m, 2H), 7.74 (t, 2H, J = 8.1, 4.5 Hz), 7.62 (d, 1H, J = 4.9 Hz), 7.36 – 7.30 (m, 1H), 7.27 (d, 1H, J = 4.2 Hz), 4.10 (t, 2H, J = 6.6, 7.8 Hz), 3.99 (dd, 2H, J = 7.3, 4.9 Hz), 2.18-1.84 (m,3H), 1.36-1.13 (m, 3H), 1.02-0.97 (m, 6H), 0.92 (t, 6H, J=7.2, 8.1).

4.3B.7 Synthesis DPP-L_4

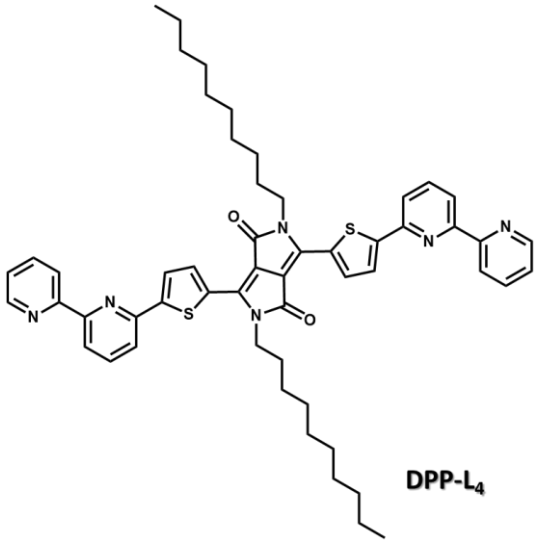

Under argon **C_{10}-DPP** (1 mmol), 6-bromo-2,2'-bipyridine (1 eq), K_2CO_3 (2 eq), $Pd(OAc)_2$ (0.1 eq) and pivalic acid (0.2 eq) were mixed together in a solution of anhydrous DMA (9.5 mL $mmol^{-1}$); the mixture was placed in the microwave for 40 min (T=180 °C, P=10 bar). The crude product was extracted with H_2O saturated with NaCl and THF, the organic phase was dried with Mg_2SO_4 anhydrous and concentrated under vacuum. The crude product was purified by column chromatography (start with CH_2Cl_2 and add gradually AcOEt until 30% in CH_2Cl_2); a violet solid was obtained after washing with CH_3OH (yield 39%). The solution of the product was purple. ^{1}H-NMR (300 MHz, $CDCl_3$), : 9.07 (d, 1H, *J* = 4.2 Hz), 8.95 (d, 1H, *J* = 3.8 Hz),8.68 (dd, 1H, *J* = 5 1.6 Hz), 8.53 (d, 1H, *J* = 7.9 Hz), 8.35 (d, 1H, *J* = 7.7 Hz), 7.84 (t, 2H,*J* = 7.8, 2.4 Hz), 7.75-7.68 (m, 2H), 7.61 (d, 1H, *J* = 4.9 Hz), 7.34 (dd, 1H, *J* = 7.4, 4.8Hz), 7.28 – 7.25 (m, 1H), 4.17 (t, 2H, *J* = 7.6, 7.4 Hz), 4.05 (t, 2H, *J* = 7.9, 7.9 Hz), 1.79 (m, 4H), 1.61-1.40 (m, 6H), 1.45 – 1.11 (m, 22H), 0.94 – 0.83 (m, 6H).

4.3B.8 Selectivity Experiments

DPPT (10 µM) in CH_3OH/H_2O (1:1, v/v) and **DPP-L_1** (10 µM) in water (containing 0.1% DMF) were added into 5 mL plastic sample tubes. The Hg^{II} (10 mM) was added and mixed thoroughly for 60 min at room temperature. Then, all the UV−Vis and fluorescence spectra were recorded at 25 °C unless another temperature was noted. The color changes were documented under natural light as well as under a UV lamp (365 nm).

4.4 Conclusions and Perspectives

Novel Rhodamine and Diketopoyrrolopyrrole derivatives have been prepared with the aim to develop fluorescent chemosensors able to detect Hg^{II}. In particular, this chapter, mainly focused on the work performed in Laboratoire Moltech-Anjou, report on the synthesis, characterization and luminescent properties of four DPP derivatives *i.e.* **DPP-L_1**, **DPP-L_2**, **DPP-L_3** and **DPP-L_4**.

To date DPP derivatives, despite their employment in several research fields as Organic Field-Effect Transistors (OFTEs) and Organic Photovoltaics (OPVs), are rarely investigated for the fabrication of fluorescent probes. A rational design for developing DPP-based fluorescent probes is presented. Following the well- known thymine-Hg^{II} binding process, where the nitrogen group of is able to interact with Hg^{II}, **DPP-L_1** and **DPP-L_2** have been synthesized as monolakilated derivatives. The studies performed on **DPP-L_1** showed a variation in photophysical properties upon addition of Hg^{II}, due to an aggregation process Hg^{II}-mediated resulting in a luminescence quenching. Furthermore, **DPP-L_3** and **DPP-L_4**, conjugating the bipyridine moiety to the DPP core, have been synthesized and characterized. Bipyridine, being a good bidentate chelating, offers several coordination sites for the interaction with metal ions and an increase in the conjugation system. Remarkably the DPP derivatives are very versatile fluorescent probes owing to the possibility of tuning the chemical make-up to properly tailor their selectivity to other metal ions or different types of analytes by simply changing the substituents.

Future work will involve the study of sensing performances of the synthesized DPP-fluorescent probes, towards several metal cations in aqueous environment. The probes showing the best sensing performance will be grafted, *via* the layer-by-layer functionalization approach, on silicon-based platforms (discussed in **Chapter 2**), to fabricate silicon-integrated fluorescent devices for remote detection of a wide range of metal ions in water.

4.5 References

1 T. Rasheed, M. Bilal, F. Nabeel, H. M. N. Iqbal, C. Li and Y. Zhou, *Sci. Total Environ.*, 2018, **615**, 476–485.

2 B. Valeur and I. Leray, *Coord. Chem. Rev.*, 2000, **205**, 3–40.

3 N. Ullah, M. Mansha, I. Khan and A. Qurashi, *TrAC - Trends Anal. Chem.*, 2018, **100**, 155–166.

4 C. Wu, J. Wang, J. Shen, C. Bi and H. Zhou, *Sensors Actuators, B Chem.*, 2017, **243**, 678–683.

5 T. Rasheed, M. Bilal, F. Nabeel, H. M. N. Iqbal, C. Li and Y. Zhou, *Sci. Total Environ.*, 2018, **615**, 476–485.

6 B. K. Bansod, T. Kumar, R. Thakur, S. Rana and I. Singh, *Biosens. Bioelectron.*, 2017, **94**, 443–455.

7 P. B. Tchounwou, W. K. Ayensu, N. Ninashvili and D. Sutton, *Environ. Toxicol.*, 2003, **18**, 149–175.

8 Y. Jiao, L. Zhou, H. He, J. Yin and C. Duan, *Talanta*, 2017, **162**, 403–407.

9 J. Ni, B. Li, L. Zhang, H. Zhao and H. Jiang, *Sensors Actuators, B Chem.*, 2015, **215**, 174–180.

10 P. Samanta, A. V. Desai, S. Sharma, P. Chandra and S. K. Ghosh, *Inorg. Chem.*, 2018, **57**, 2360–2364.

11 E. M. Nolan and S. J. Lippard, *Chem. Rev.*, 2008, **108**, 3443–3480.

12 C. Prohaska, K. Pomazal and I. Steffan, *Fresenius. J. Anal. Chem.*, 2000, **367**, 479–484.

13 E. Bakkaus, R. N. Collins, J. L. Morel and B. Gouget, *J. Chromatogr. A*, 2006, **1129**, 208–215.

14 J. Y. Cabon, P. Giamarchi and A. Le Bihan, *Anal. Chim. Acta*, 2010, **664**, 114–120.

15 L. Lvova, F. Caroleo, A. Garau, V. Lippolis, L. Giorgi, V. Fusi, N. Zaccheroni, M. Lombardo, L. Prodi, C. Di Natale and R. Paolesse, *Front. Chem.*, 2018, **6**, 1–10.

16 L. Lvova, C. Di Natale, R. Paolesse, L. Giorgi, V. Fusi, A. Garau and V. Lippolis, *Procedia Eng.*, 2016, **168**, 346–350.

17 A. Garau, A. Bencini, A. J. Blake, C. Caltagirone, L. Conti, F. Isaia, V. Lippolis, R. Montis, P. Mariani and M. A. Scorciapino, *Dalt. Trans.*, 2019, **48**, 4949–4960.

18 C. Guo, A. C. Sedgwick, T. Hirao and J. L. Sessler, *Coord. Chem. Rev.*, 2021, **427**, 213560.

19 K. P. Wang, Y. Lei, S. J. Zhang, W. J. Zheng, J. P. Chen, S. Chen, Q. Zhang, Y. B. Zhang and Z. Q. Hu, *Sensors Actuators, B Chem.*, 2017, **252**, 1140–1145.

20 L. Prodi, F. Bolletta, M. Montalti and N. Zaccheroni, *Coord. Chem. Rev.*, 2000, **205**, 59–83.

21 G. Li, F. Tao, H. Wang, L. Wang, J. Zhang, P. Ge, L. Liu, Y. Tong and S. Sun, *RSC Adv.*, 2015, **5**, 18983–18989.

22 L. Liu, P. Guo, L. Chai, Q. Shi, B. Xu, J. Yuan, X. Wang, X. Shi and W. Zhang, *Sensors Actuators, B Chem.*, 2014, **194**, 498–502.

23 J. Wan, K. Zhang, C. Li, Y. Li and S. Niu, *Sensors Actuators, B Chem.*, 2017, **246**, 696–702.

24 H. N. Kim, M. H. Lee, H. J. Kim, J. S. Kim and J. Yoon, *Chem. Soc. Rev.*, 2008, **37**, 1465–1472.

25 C. Liu, S. Huang, H. Yao, S. He, Y. Lu, L. Zhao and X. Zeng, *RSC Adv.*, 2014, **4**, 16109–16114.

26 T. Rasheed, C. Li, Y. Zhang, F. Nabeel, J. Peng, J. Qi, L. Gong and C. Yu, *Sensors Actuators, B Chem.*, 2018, **258**, 115–124.

27 V. Dujols, F. Ford and A. W. Czarnik, *J. Am. Chem. Soc.*, 1997, **119**, 7386–7387.

28 S. H. Eom, S. Y. Nam, H. J. Do, J. Lee, S. Jeon, T. J. Shin, I. H. Jung, S. C. Yoon and C. Lee, *Polym. Chem.*, 2017, **8**, 3612–3621.

29 M. M. Wienk, M. Turbiez, J. Gilot and R. A. J. Janssen, *Adv. Mater.*, 2008, **20**, 2556–2560.

30 C. Zhao, Y. Guo, Y. Zhang, N. Yan, S. You and W. Li, *J. Mater. Chem. A*, 2019, **7**, 10174–10199.

31 H. Luo, C. Yu, Z. Liu, G. Zhang, H. Geng, Y. Yi, K. Broch, Y. Hu, A. Sadhanala, L. Jiang, P. Qi, Z. Cai, H. Sirringhaus and D. Zhang, *Sci. Adv.*, 2016, **2**, 1–11.

32 M. Grzybowski and D. T. Gryko, *Adv. Opt. Mater.*, 2015, **3**, 280–320.

33 M. Kaur and D. H. Choi, *Chem. Soc. Rev.*, 2015, **44**, 58–77.

34 Z. Hao and A. Iqbal, *Chem. Soc. Rev.*, 1997, **26**, 203.

35 T. Yamagata, J. Kuwabara and T. Kanbara, *Tetrahedron Lett.*, 2010, **51**, 1596–1599.

36 W. Li, L. Wang, H. Tang and D. Cao, *Dye. Pigment.*, 2019, **162**, 934–950.

37 X. Yang, L. Zheng, L. Xie, Z. Liu, Y. Li, R. Ning, G. Zhang, X. Gong, B. Gao, C. Liu, Y. Cui, G. Sun and G. Zhang, *Sensors Actuators, B Chem.*, 2015, **207**, 9–24.

38 D. Udhayakumari, S. Velmathi, W. C. Chen and S. P. Wu, *Sensors Actuators, B Chem.*, 2014, **204**, 375–381.

39 S. Wen, T. Zeng, L. Liu, K. Zhao, Y. Zhao, X. Liu and H. C. Wu, *J. Am. Chem. Soc.*, 2011, **133**, 18312–18317.

40 K. Nie, B. Dong, H. Shi, Z. Liu and B. Liang, *Anal. Chem.*, 2017, **89**, 2928–2936.

41 H. Langhals, M. Limmert, I. P. Lorenz, P. Mayer, H. Piotrowski and K. Polborn, *Eur. J. Inorg. Chem.*, 2000, **13**, 2345–2349.

42 Z. Q. Hu, M. Li, M. D. Liu, W. M. Zhuang and G. K. Li, *Dye. Pigment.*, 2013, **96**, 71–75.

43 H. Ju, M. H. Lee, J. Kim, J. S. Kim and J. Kim, *Talanta*, 2011, **83**, 1359–1363.

44 F. Pop, W. Lewis and D. B. Amabilino, *CrystEngComm*, 2016, **18**, 8933–8943.

45 F. Pop, J. Humphreys, J. Schwarz, L. Brown, A. Van Den Berg and D. B. Amabilino, *New J. Chem.*, 2019, **43**, 5783–5790.

Chapter 5

Fluorescent Nanosheets as Unique Platforms for Chemical Sensing

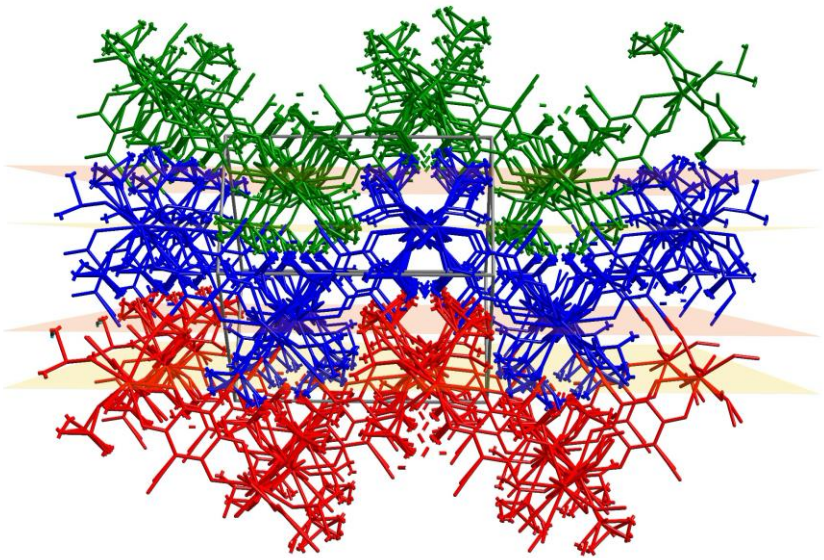

5.1 Introduction

During the last years, Luminescent Coordination Polymers (LCPs) and Metal-Organic Frameworks (LMOFs) have attracted considerable interest in material science given their peculiar supramolecular architectures extending in 1, 2 or 3 dimensions (1D, 2D 3D) and richness in optical properties.[1] Due to the possibility of tailoring their composition by choosing appropriate metal ions and organic linkers, LMOFs and LCPs can find applications in social and industrial fields, ranging from telecommunications and information storage to biomedicine and sensing.[2–5]

Among luminescent MOFs, Lanthanide MOFs (Ln-MOFs) have attracted much attention because of their luminescent properties, *i.e.* long lifetime, characteristic sharp emission, large Stokes shifts and high quantum yield in the near infrared and visible region.[6–8] It is well known that Ln^{III} centers cannot efficiently absorb light due to forbidden 4f–4f transitions.[9] To overcome this issue, a strategy for the fabrication of Ln-based materials is the incorporation of luminescent linkers as antennas, thereby able to absorb and transfer energy to the lanthanide center.[10–13] Indeed, Ln-MOFs have been largely studied as chemical sensors showing luminescence enhancement (**turn-ON response**) or quenching (**turn-OFF response**) upon interaction with the analyte of interest.[12,14–20] Their use as luminescent probes is gradually becoming a hot topic due to their fast and effective luminescent response for the targeted substance.

3,6-disubstituted-2,5-dihydroxy-1,4-benzoquinone derivatives, most commonly known as anilates, are widely employed as valuable antenna ligands and building blocks to produce 2D Ln-CPs showing interesting optical properties.[21] In 2015, the first example of heterosubstituted anilate, 3-chloro-6-cyano-2,5-dihy-droxybenzoquinone, (KHClCNAn salt), reported in **Figure 1**, was synthesized,[22] that showed a good performance as antenna ligand towards NIR emissive Er^{III}, Yb^{III} and Nd^{III} ions.[23] By combining the ligand $ClCNAn^{2-}$ with Er^{III}, Yb^{III} and Nd^{III} ions, 2D $[Ln_2(ClCNAn)_3(DMF)_6]\cdot(DCM)x\}_n$ (Ln^{III} = Yb (x = 0), Nd, and Er (x = 2)) CPs have been obtained and they have been successfully exfoliated in ultrathin nanosheets.[23]

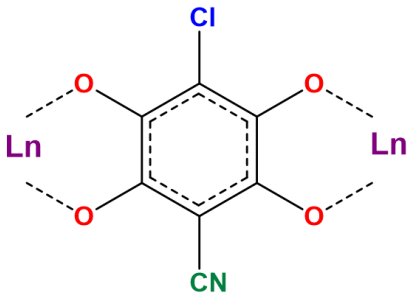

Figure 1.Coordination mode of the ligand $ClCNAn^{2-}$.

Since the pioneering work of H. Zhang and Z. Zhang on transition metal chalcogenides nanosheets (NS) and graphene oxide nanosheets for metal ions sensing applications, 2D materials have become a promising tool for sensing metal ions and biomolecules.[21,24,25] Their high surface area/thickness ratio, ultrathin thickness, large surface area and more active sites on the surface are crucial elements to obtain suitable nanoplatforms with high sensitivity and fast response towards target analytes (see **Figure 2**), when compared with other luminescent sensors.[25,26]

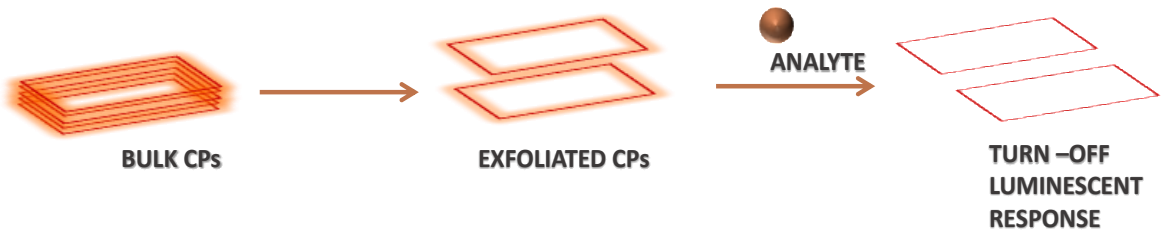

Figure 2. Schematic illustration of the fabrication of a nanosheet-based luminescent nanoplatform.

Nitroaromatic compounds are widely used for several applications such as synthesis of pesticides, explosives, polymers and other intermediates. Their wastes are prevalently found in water, soils and in some common food causing several health problems due to their mutagenic and carcinogenic effects.[14,27,28] For this reason, it is of great interest the development of new systems for their detection and the use of the novel nanosheet technology, which has been successful in frontier cellular research, represents a challenge.[29] Furthermore, 2D nanosheets can be dispersed in water or other solvents and deposited for developing ultrathin nanodevices. Recently, Maka.V.K. *et al.*[30] have

developed a new fluorescent **turn-OFF** probe, based on fluorescent nanosheets, for the detection of nitroaromatic explosives, by using a highly-symmetric 6-connecting hexaacid linker **H_6TPA** based on a 1,3,5-triphenylbenzene.

Sensing metal ions is of great significance in environmental and ecological systems. Transition-metal cations, such as Cu^{II}, Fe^{II}, Fe^{III} and Zn^{II}, are in fact essential in biological processes and an alteration in their concentration can lead to several diseases, such as Alzheimer's disease, Wilson's disease, anemia, etc.[31,32] Hg^{II}, Pb^{II}, and Cd^{II}, known as toxic metal ions, can cause serious damage to the human body.[33,34] Therefore, the design and preparation of efficient and straightforward metal ion probes are urgently needed. Interestingly, Chen *et al*. reported on a new Ln-MOF $[Eu(PDC)_{1.5}(DMF)](DMF)_{0.5}(H2O)_{0.5}$ (PDC=pyridine-3,5-dicarboxylate, DMF = dimethylformamide), where pyridyl is the binding basic site for Cu^{II} ions.[35] This system shows a good selectivity towards copper(II) among other metal ions *via* a **turn-OFF** response. The interaction between pyridyl nitrogen atoms and the analyte could lead to a reduction of the antenna effect of the PDC resulting in luminescence quenching. Based on this sensing mechanism, several Ln-MOFs containing Lewis basic sites have been synthesized as sensing metal ions.[15,36,37] Zheng *et al.* developed $[Eu(L_1)(BPDC)_{0.5}(NO_3)]H_3O]$ for Fe^{III} detection (H_2L_1 = 2,5-di(pyridin-4-yl) terephthalic acid, BPDC = biphenyl-4,40-dicarboxylic acid). This probe shown an excellent luminescence **turn-OFF** response with a remarkable detection limit (5×10^{-7} mol/L).[38]

In 2017, Ji and coworkers[16] reported a luminescence sensor for detecting Pb^{II} based on a millimeter-sized Tb-MOF $\{[Tb(L)(H_2O)_5]_n$ H_2L^-= 3,5-dicarboxy-phenol anion ligand}. This MOF is the first high-efficiency MOF-based luminescence sensor for Pb^{II} at a very low concentration and with the detection limit up to 10^{-7} M.

Xu H. *et al*[39] reported on 2D luminescent materials based on $Ti_2(HDOBDC)_2(H_2$-DOBDC) (H_2DOBDC = 2,5-dihydroxyterephthalic acid). This material was delaminated by a top-down approach in order to obtain the first example of nanosheet for the recognition of metal cations in aqueous environment. In particularly, these nanosheets have shown, by a fluorescence quenching, a high sensitivity and an ultra-fast response time (10 seconds) towards Fe^{III} in comparison with conventional fluorescent probes.

Since the emission of lanthanide NIR-emitters is relatively quenched in water, due to the presence of O-H vibrational quenchers, 2D Ln-MOFs/CPs based on Tb^{III} and Eu^{III} Vis-emitting ions, which have characteristic green emission at around 541 nm and red emission at

around 614 nm,[40] respectively, have been developed in order to obtain suitable 2D platforms for the cation recognition in water solution. The $ClCNAn^{2-}$ organic linker has been used for its capability to build 2D architectures, a fundamental requirement to produce nanosheets.

Nanosheets of two mixed linker (anilate/carboxylate)/Yb^{III}-based 2D layered coordination polymers (CPs) are herein reported, hereafter called **1-NS** and **2-NS** (CPs=$[Yb_4(ClCNAn)_5(DOBDC)_1(DMSO)_{10}]_n \cdot (DMSO)_2$ **(1)** and $[Yb_2(ClCNAn)_2(F_4\text{-}BDC)(DMSO)_6]_n$ (**2**), respectively). **1-NS** and **2-NS**, are produced by exfoliation of bulk CPs by the well-known top-down approach, *via* the sonication-assisted solvents method[41,42] and characterized by atomic force microscopy (AFM) and high resolution transmission electron microscopy (HRTEM). Powder X-ray diffraction (PXRD) studies are performed in order to check if crystallinity is retained at the nanoscale level. The photophysic of the Nanosheets is investigated by an innovative Multiprobe Approach where lifetime, photoluminescence (PL) and integrated PL are simultaneously measured in order to study how these parameters can be affected by the presence of the different ligands. Bulk 2D isostructural layered CPs, formulated as **$[Tb_2(ClCNAn)_3(DMSO)_6]_n$ (4)** and **$[Eu_2(ClCNAn)_3(DMSO)_6]_n$, (5)** are prepared and fully characterized. Single-crystal X-Ray diffraction and optical and magnetic properties are performed on bulk size **4** CP. **4-NS** are fabricated using the same top-down approach as that considered for the preparation of **1-NS** and **2-NS** and characterized by AFM.

5.2 Results and Discussion

5.2.1. 2D Materials based on NIR-Emitters

5.2.1.1. Synthesis and Morphological Characterization of 1-2 Nanosheets

CPs **1** and **2**, prepared according to the literatura,[43] were exfoliated by sonication of isopropanol suspensions of crystals. To confirm the formation of the delaminated 1-NS and 2-NS, AFM and HR-TEM measurements were carried out to examine their topography and morphology, respectively. **3-NS**[23] (Yb-Homoleptic, $[Yb_2(ClCNAn)_3(DMF)_6](CH2Cl_2)_x\}_n$) were also synthesized according to the literature. Suspensions of **1-2-NSs** in isopropanol were deposited on Si/SiO_2 substrates and were analyzed by AFM. AFM characterization of dropcast suspensions, obtained by crystal sonication, revealed the 2D nature of the compounds (**Figure 3a-c**). Micrometer-sized nanosheets were obtained with heights ranging from one to eight in number of layers. Monolayer-thick portions of nanosheets are shown for **1-NS** and **2-NS** in **Figure 3b-d**.

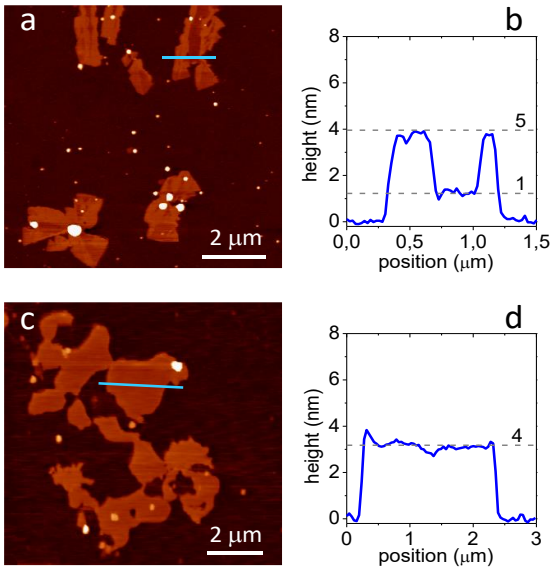

Figure 3. AFM characterization of dropcast nanosheets of compounds **1-2**. (a) Height image of **1-NS**; (b) Height profile of **1-NS** along the line depicted in panel (a). (c, d) Same as in panels a,b but for **2-NS**. Numbered dashed lines mark the heights of the corresponding numbers of layers.

TEM images confirm the presence of overlapped sheets for both, **1-NS** and **2-NS** samples (**Figure 4, a-b**). The contrast of the TEM images indicates that the layers are very thin. High resolution images for **1-NS** and **2-NS** are reported in Figure4 along with those for the reference 3-NS (Figure 4c-f). Well defined lattice fringes with interplanar average distances of 3.0 Å, 2.6 Å and 1.8 Å, were observed for both compounds which can be ascribed to the reticular planes (3 0 0) at 2.98 Å, (0 6 0) at 1.80 Å and (-3 2 0) at 2.6 Å for **1-NS** and (1 -3 3) at 2.98 Å and (2 3 3) at 1.80 Å for **2-NS**.

Crystalline nanodomains with different orientations can be observed showing that the 2D nansheets are made of a multi-nanodomains crystalline structure. It is worth noting the excellent stability of 1-2 NS under electron beam irradiation over time, as already highlighted in the AFM images (*vide supra*), which makes them suitable nanoplatforms for advanced photophysical studies. Heteroleptic **1-NS** and **2-NS** are the most robust and reliable nanoplatforms in the anilato-based CPs/MOFs, even when compared with the **3-NS** homoleptic ones.[44–46] Lattice fringes are rarely observed in MOF-based nanosheets,[25,47,48] due to their instability under the irradiation exposure.

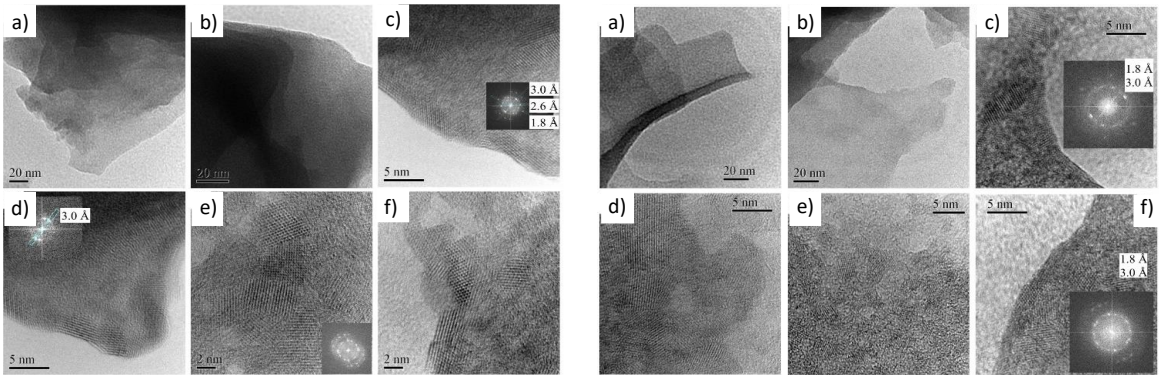

Figure 4. TEM (a,b) and HR-TEM (c-f) of 1-NS (left) and 2-NS (right).

The successful delamination of 1-CP and 2-CP to obtain **1-NS** and **2-NS** was further confirmed for both samples by powder x-ray diffraction (PXRD, **Figure 5**) as the diffraction peaks associated with the exfoliation plane (*i.e.* 1-11 and -101 for compound 1 and 2, respectively), was found to significantly decrease or disappear in the NS PXRD patterns in comparison with the bulk materials. Furthermore, PXRD of 1-NS and 2-NS showed that the crystallinity of the bulk CPs was preserved after the exfoliation, but generally with peaks of

lower intensity in the nanosheet patterns than the bulk ones as expected after the exfoliation.

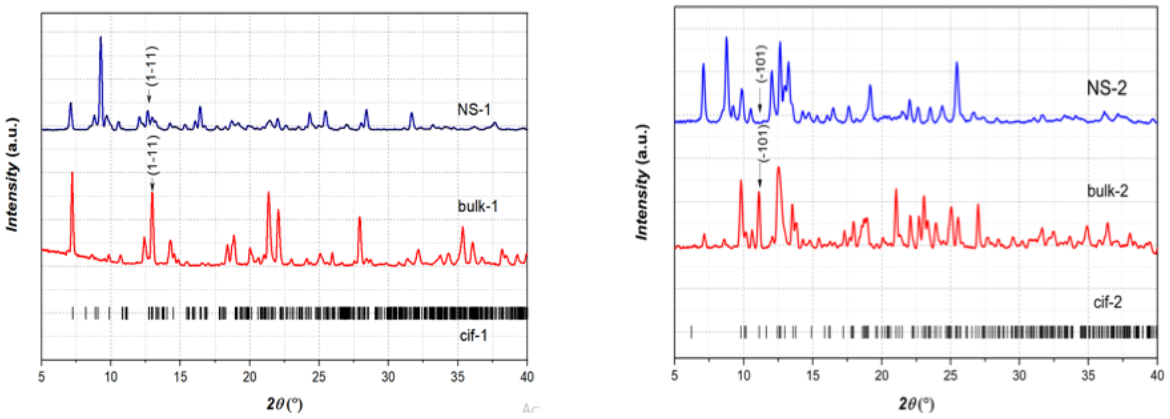

Figure 5. NSs samples, bulk materials and simulated PXRD patterns of compounds **1** (left) and **2** (right) and **1-NS** and **2-NS**.

5.2.1.2 Photophysical Studies

Advanced 1-NS and 2-NS Photophysics. A comparison between the intrinsic Photophysical Properties of Bulky Sized **1** and **2** and corresponding **1-NS**/**2-NS** nanosheets is reported in **Figure 6**, showing that PL signals collected on **1-NS** and **2-NS** are considerably lower than those of the corresponding crystals, as a result of the smaller quantity of material investigated in the nanosheet suspensions. Some evidence of efficient Yb^{III} emission sensitization by photoexcited ligands (antenna effect) was provided by the fact that lanthanide-centered emission dominate over the ligand- centered emission in both heteroleptic compounds, as can be easily deduced from the Vis/NIR signal amplitudes (**Figure 6 c,d**). Multiexponential decays with shorter average lifetimes were found in the corresponding nanosheet suspensions (**Figure 6g**), which could be attributed (i) to an increase in lanthanide nonradiative recombination centers within the crystal structure as a result of the exfoliation process, and (ii) to solvent-related additional vibrational quenching of the lanthanide emission previously discussed for **3-NS**.[49,50]

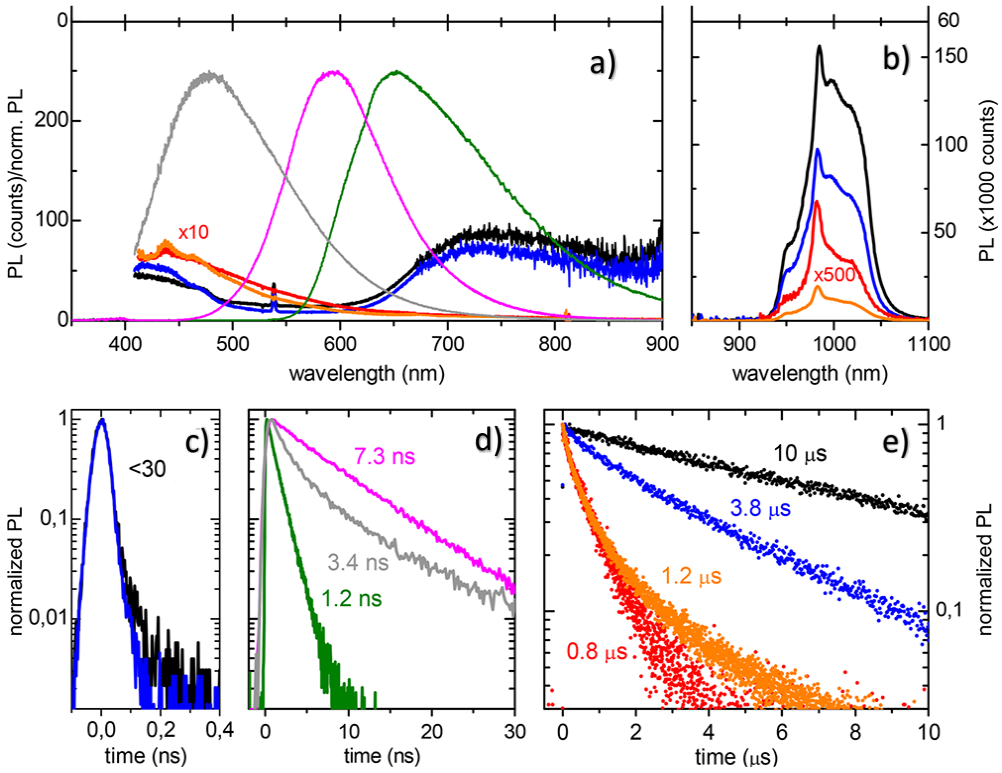

Figure 6. Optical and photophysical characterization of crystals of compounds **1** (black lines/dots) and **2** (blue lines/dots) and isopropanol suspensions of **1-NS** (red lines/dots) and **2-NS** (orange lines/dots); reference data on crystals of $[Ph_4P]_2DOBDC$ (magenta lines), $[Ph_4P]_2F_4BDC$ (gray lines), and $[Ph_4P]_2[ClCNAn]$ (green lines) are also shown. a) PL spectra in the vis−NIR spectral range; b) PL spectra across the Yb^{III} absorption/emission spectral range; c,d) Ligand-centered PL decay profiles. (e) Lanthanide-centered NIR-PL decay profiles. Average lifetimes obtained from multiexponential fit curves are indicated.[43]

Deep insight into the **1-NS** and **2-NS** photophysics could be gained by perturbing their isopropanol suspensions via addition of small quantities of aliphatic and aromatic solvents (CH_3CN, CH_3NO_2, $C_6H_5NH_2$, $C_6H_5CH_3$, $C_6H_5NO_2$, C_6H_5CN). Among aromatic solvents, electron-withdrawing (−CN, $-NO_2$) and electron-donating groups ($-CH_3$, $-NH_2$) in the benzene ring were selected. Here, the photophysical response of the nanosheets was analyzed using a PL multiprobe approach under pulsed photoexcitation, where not only the integrated PL signal (i.e., $\int_0^\infty PL(t)dt$) was used as the optical probe, but also the initial PL signal ($PL_0 = PL(0)$) and the PL lifetime $\tau = \int_0^\infty PL(t)dt/PL_0$. For a multi-exponential decay function, τ coincides with the amplitude-weighted average of the characteristic times of the single exponential

components. In fact, the overall PL quantum yield of the Ln^{III} coordination compounds can be written as $QY = \eta_S QY_i$, where η_S is the lanthanide sensitization efficiency and QY_i is the intrinsic lanthanide PL quantum yield. If the activation time of the NIR PL signal of the lanthanide ions is much faster than its decay time, which is very much often the case, as in these compounds (**Figure 7g**), the initial PL signal amplitude, PL_0, is proportional to η_S, whereas the PL lifetime τ is always proportional to QY_i.

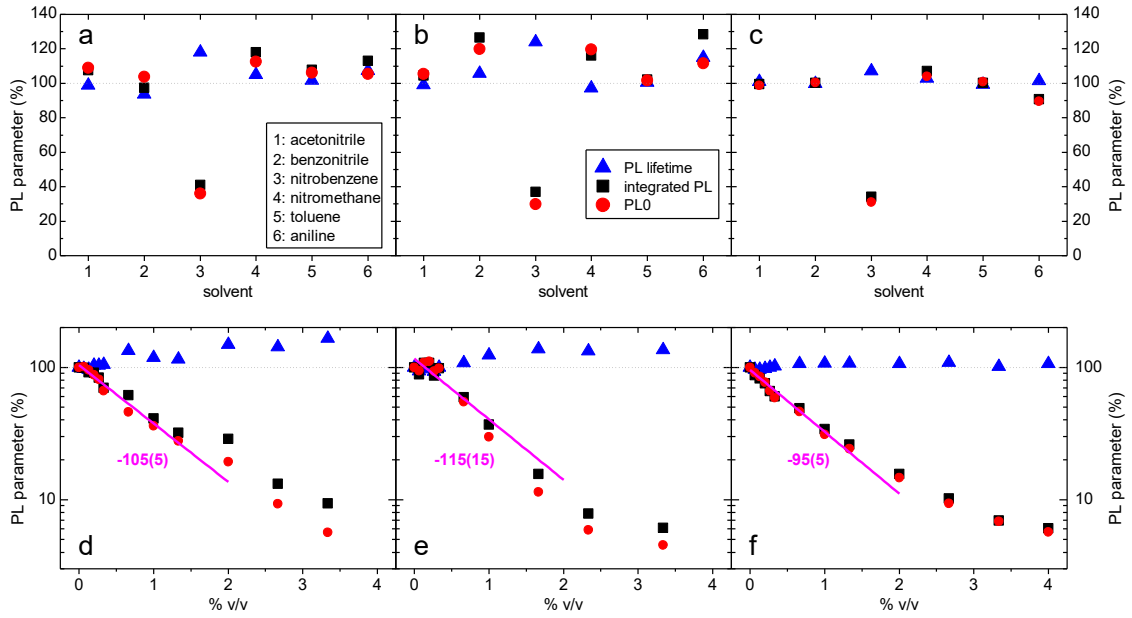

Figure 7. Multiprobe photoluminescence studies on isopropanol suspensions of **1-NS, 2-NS and 3-NS**. (a) Percentage values of PL parameters (PL lifetime, time-integrated PL, and PL_0 = initial PL) upon addition of different solvents (1% v/v) to a **1-NS** suspension. (b) Same as in (a) but for a **2-NS** suspension. (c) Sample as in (a) but for a **3-NS** suspension. Dashed horizontal lines in panels (a-c) mark the 100% reference value. Solvent legend and PL parameter legend apply to all panels. (d) Percentage values of PL parameters versus percentage quantity of nitrobenzene added to a **1-NS** suspension (% v/v). Magenta lines: best exponential decay fits to PL_0 data with indication of characteristic sensitivity in %p / (% v/v) units (2 errors).

Hence, a variation in PL_0 and τ can be traced back to a perturbation produced, respectively, in the lanthanide emission quenching and in the antenna effect, hence making the multiparameter analysis of the PL response an effective probe of multiple photophysical processes. As clearly visible in **Figure 7a–c**, the addition of various solvents at 1% v/v concentration produced little or no variation in any of the PL parameters, with the exception

made for nitrobenzene, to which the nanosheet suspensions reacted with a reduction in PL_0 and simultaneously in the integrated PL signal. The very weak response observed in τ was readily interpreted as a negligible sensitivity of vibrational quenching of the Yb^{III} emission to small changes in the solvent composition. This is reasonable because the addition of small quantities of different solvents (that is, the analytes) produces only a little variation in the density of vibrational oscillators in the medium surrounding the Yb^{III} ions.[49] A sizable reduction ON PL_0 was observed in both heteroleptic compounds **1-NS** and **2-NS** and in the homoleptic one **(3-NS**) and could therefore be traced back to a specific excited-state interaction between nitrobenzene and the $ClCNAn^{2-}$ ligand. A photoinduced charge transfer (PCT)[30] from the $ClCNAn^{2-}$ ligand to nitrobenzene was suggested as interaction mechanism. Owing to the strong electron-withdrawing power of the $-NO_2$ group, nitrobenzene is more electron deficient than the $ClCNAn^{2-}$ ligand; this results in an electronic level alignment where the lowest unoccupied molecular orbital (LUMO) of $ClCNAn^{2-}$ has higher energy than the LUMO of nitrobenzene, thus enabling PCT from $ClCNAn^{2-}$ (photoexcited electron donor) to nitrobenzene (electron acceptor) with subsequent loss in Yb^{III} emission sensitization efficiency and reduction in PL_0.[30] This interaction mechanism has in fact been widely used in the fluorescence turn-OFF detection of electron deficient analytes using fluorescent MOFs.[51] It is worth noting that for fluorescence **turn-OFF** to occur with high sensitivity, the PCT toward the analyte must be much faster than the ISC process occurring within the CP itself. This is clearly a challenging task as the heavy-atom effect due to the lanthanide greatly accelerates ISC. To evaluate the sensitivity of the PL **turn-OFF** process, nitrobenzene titration curves were measured for suspensions of **1-NS** and **2-NS (Figure 7d**–**f**). A reference titration curve was produced for the suspension of **3-NS** to assess the role of the $ClCNAn^{2-}$ as the sole ligand. Increasing the nitrobenzene concentration resulted in a progressive reduction in PL_0 and integrated PL in all compounds; only a negligible effect was found on τ for analyte concentrations as large as 4% v/v. Titration curves were fitted with a single exponential decay function $\% p = 100\% \cdot \exp[-c/c_0]$, where % p represents the signal percentage amplitude, c is the nitrobenzene concentration, and c_0 is the characteristic concentration of the decay. This analysis yielded $c_0 \sim 1\%$ v/v, or equivalently, low concentration sensitivities of about −100% p/(% v/v). As mentioned before, this moderate sensitivity was ascribed to the ultrafast ISC

process at the basis of antenna effect toward the Yb^{III}[52] ions. Remarkably, the homoleptic **3-NS** displays almost the same sensitivity to nitrobenzene as the heteroleptic **1-NS** and **2-NS**, allowing us to infer that the $ClCNAn^{2-}$ ligand plays a dominant role in the Yb^{III} sensitization. In **1-NS**, where the $DOBDC^{2-}$ and $ClCNAN^{2-}$ ligands seem to compete against each other in absorbing the 355 nm laser pump light (**Figure 7a**), this result hints to an unfavorable energy level alignment between the triplet state of $DOBDC^{2-}$and the $^2F_{5/2}$ energy level of Yb^{III}, resulting in inefficient ligand-to-lanthanide energy transfer. Besides, the lack of Yb^{III} emission sensitization by the F_4BDC^{2-} ligand in **2-NS** could be easily understood as a consequence of the large singlet and triplet energies of F_4BDC^{2-} (>34 000 and >27 000 cm^{-1}, respectively),[53] making both photoabsorption and energy-transfer toward the lanthanide unefficient processes.

5.2.2 2D Materials based on UV-Vis Emitters

5.2.2.1 Synthesis and crystal structure of Bulk CPs

Homoleptic layered neutral 2D CPs based on Visible Lanthanides (Ln^{III}= Tb, and Eu) Tb^{III} $ClCNAn^{2-}$ based neutral 2-D CP is formed by self-assembly of Tb^{III} ions and monoprotonated chlorocyanilate in aqueous solution (**Figure 8**) and was further recrystallized in DMSO to obtain single crystals suitable for X-Ray diffraction.

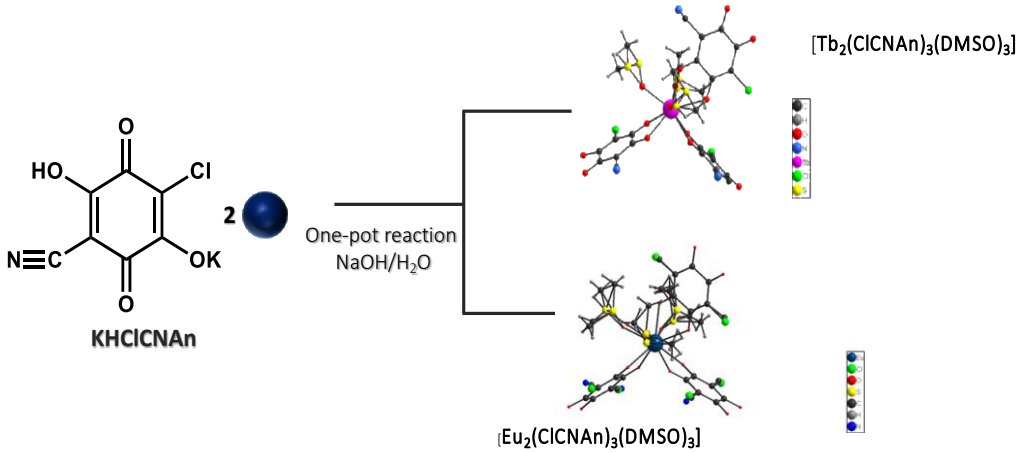

Figure 8. Schematic representation of the synthesis of compounds **4** and **5.**

Compound **4** e **5** are isostructural and crystallize in the monoclinic $P2_1/n$ space group. The discussion will be then focused on **4** (Tb-CP). The asymmetric unit contains one Tb^{III} ion, one and a half molecules of $ClCNAn^{2-}$ ligands and three DMSO molecules (Figure 9a), and hence can be formulated as $Tb_2(ClCNAn)_3(DMSO)_6$. In the $ClCNAn^{2-}$ ligand, due to the presence of an inversion center, chloro and cyano substituents are disordered in one of the half independent anilate, as commonly observed in $ClCNAn^{2-}$-based 2D CPs.[23,43,54–56] Sulfur atoms from the DMSO solvent molecules are disordered.

Tb^{III} ion is nine-coordinated by six oxygen atoms from $ClCNAn^{2-}$ ligands and other three oxygen atoms from DMSO molecules (**Figure 9a**), forming a slightly distorted tricapped trigonal prismatic geometry (**Figure 9b**). Tb–O bond lengths and O–Tb–O bond angles fall in the range between 2.335-2.479 Å and 63.60-142.57°. The shortest Tb···Tb distance is 8.807 Å. These distances are similar to those observed in Dy-$ClCNAn^{2-}$ CP.[57]

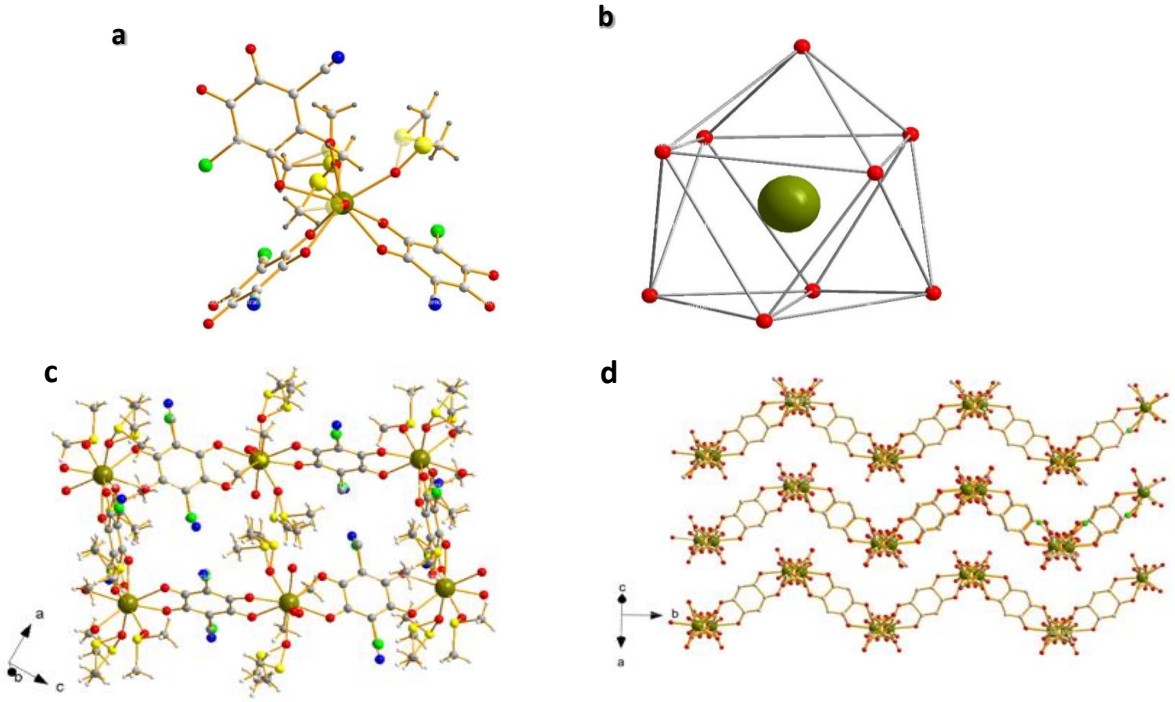

Figure 9. a) Coordination environment around Tb^{III}; **b)** distorted tricapped trigonal prismatic geometry around Tb^{III}; **c)** View of one rectangular cavity in *ac* plane; **d**) View of three consecutive layers in the *abc* plane. Colour code: Tb- dark green; O- red; C- grey; S-yellow; Cl- green; N- blue.

The structure consists of a 2D neutral coordination network, where three bidentate $ClCNAn^{2-}$ ligands are bridged between three neighboring Tb^{III} ions forming distorted hexagonal cavities (6.3 topology) (**Figure 9**). The angles between Tb^{III} at the connecting node are 93° and 100° and Tb-Tb diagonal distances are 19.02 and 20.06 Å, respectively. The obtained geometry is shown to be quite distorted from the regular honeycomb hexagonal network (120°).

In the structure shown in **Figure 9a**, 2D layers are arranged in wave-like manner, where the neighboring layers are eclipsed along the *a* axis forming distorted hexagonal cavities. As commonly seen in lanthanide-anilate based CPs,[23,54–56] there is overlap of 2D layers as the coordinated DMSO molecules face toward neighboring layers and cavities (**Figure 9c**). A similar kind of structure was reported for $[Ln_2(ClCNAn)_3(DMSO)_6]_n$ Ln^{III}- Dy[57]and Pr [54].

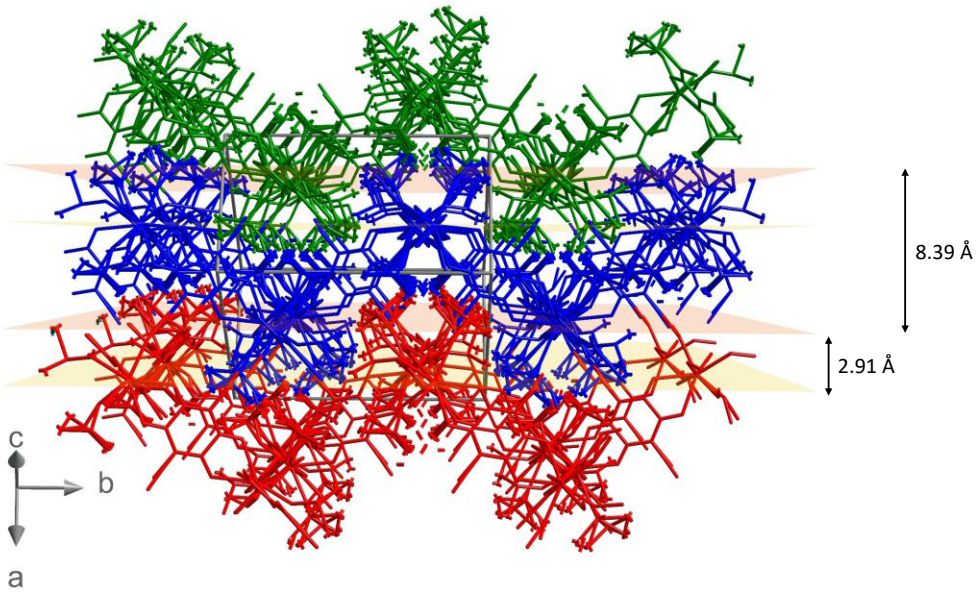

Figure 10. Perspective view of **4** in the *b–c plane*. View of 2D.

In **Figure 10**, the interlayer distance, **8.39 Å** and the overlap between two layers, **2.91 Å**, are reported. The number of layers (***n***) of a 2D crystal slab, of thickness ***h***, can thus be calculated as: $n = 1 + (h - h_0)/d$, where h_0 is the sum between the interlayer distance and the overlap of two layers.

5.2.2.2 Magnetic Characterization

Magnetic measurements were carried out with a fine powder sample of **1** as a function of temperature (**Figure 11**). The $\chi_m T$ value at room temperature (25.1 cm^3 K mol^{-1}) corresponds to two magnetically independent Tb^{III} cations (both exhibiting J = 6, g = 3/2 and theoretical $\chi_m T \approx 11.81$ cm^3 K mol^{-1})[58]. As expected for Tb^{III}, the $\chi_m T$ value decreases when the temperature is decreased, because of the depopulation of the highest crystal-field levels. The high anisotropy of the Tb^{III} centers does not allow to detect any additional super-exchange interactions promoted by the bridging organic ligands. Dynamic (AC) magnetic susceptibility measurements were performed down to 2 K at different frequencies (**Figure 11**). No out-of-phase χ'' signal was observed, not even when an additional DC magnetic field was applied, indicating no SMM (Single Molecular Magnet) behavior for this compound.

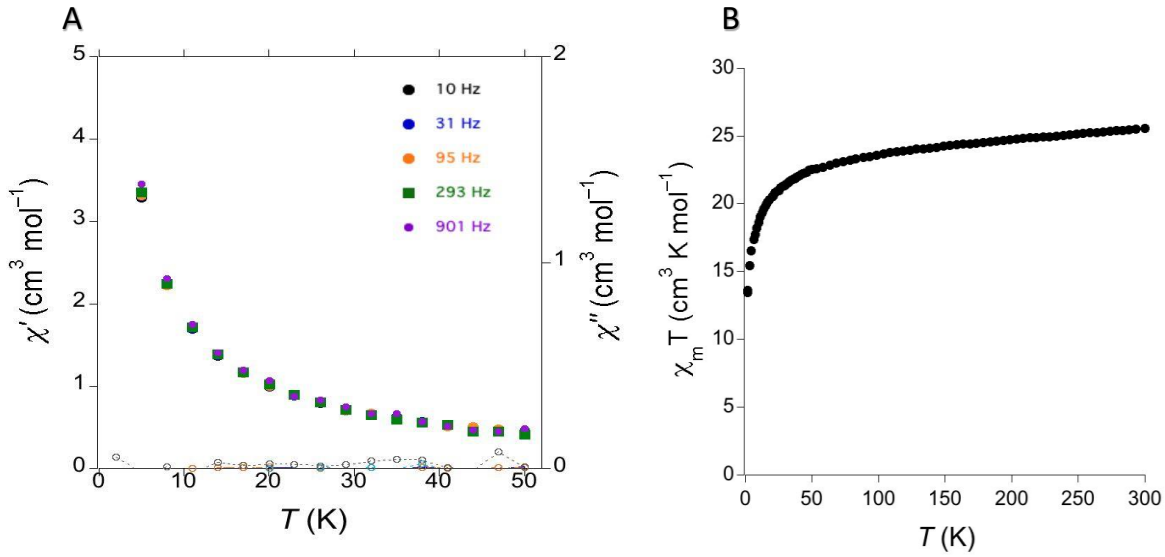

Figure 11. **A)** Plot of the $\chi_m T$ product as a function of temperature for **4**. **B)** In-phase (χ') and out-of-phase (χ'') dynamic susceptibility for **4** at different frequencies as a function of temperature.

5.2.2.3 Synthesis of Nanosheets

Nanosheets of compounds **4** hereafter, **4-NS**, were fabricated through the top-down sonication-assisted exfoliation method. Delamination was achieved by sonicating the dried powder of **4** bulk CPs (1 mg) samples in isopropanol (1 mL) for 15 min at room temperature. The surnactant of the obtained suspension was removed after sonication and let it stand

for 1h. **4-NS** suspensions in isopropanol were dropcast onto SiO_2/Si substrates (20 µL) and carbon-coated copper grids (5 µL) for AFM.

5.2.2.4 Morphological characterization

Morphological characterization of **4- NS** was performed by AFM, on dropcast suspensions, obtained by crystal sonication, revealing the 2D nature of **4** bulk size CP (**Figure 12a-b**). Remarkably micrometer-sized nanosheets were obtained, with heights ranging from one to four in number of layers, as clearly shown in **Figure 12b**.[59]

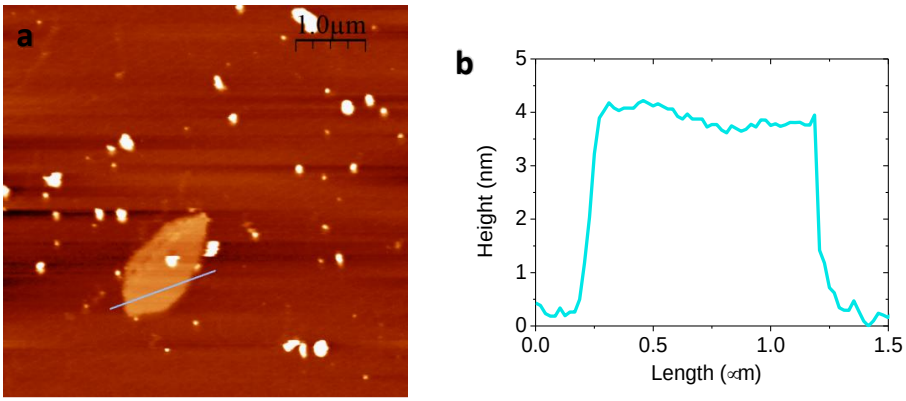

Figure 12. AFM characterization of dropcast nanosheets of **4-NS**. **a**) Topography (height) image of nanosheets. **b**) Height profile of **1-NS** along the line shown in panel (**a**).

5.3 Experimental Section

5.3.1 Materials

Reagents were purchased from Zentek (TCI) and used without further purifications. The solvents, of HPLC grade, were purchased from Thermofisher Scientific Alfa-Aesar. **KHClCNAn** and **$[Ph_4P]_2$[ClCNAn]** were synthesized as reported in literature. [23]

5.3.2 Materials based on NIR-Emitters

5.3.2.1 Synthesis of CPs

$[Yb_4(ClCNAn)_5(DOBDC)_1(DMSO)_{10}]_n.(DMSO)_2$ (1) and $[Yb_2(ClCNAn)_2(F_4BDC)(DMSO)_6]_n$ (2) **$[Yb_2(ClCNAn)_3(DMF)_6]n\cdot(DCM)_x$ (3)** were synthesized (**Figure 13**) and characterized as reported in literature.[23,43,60]

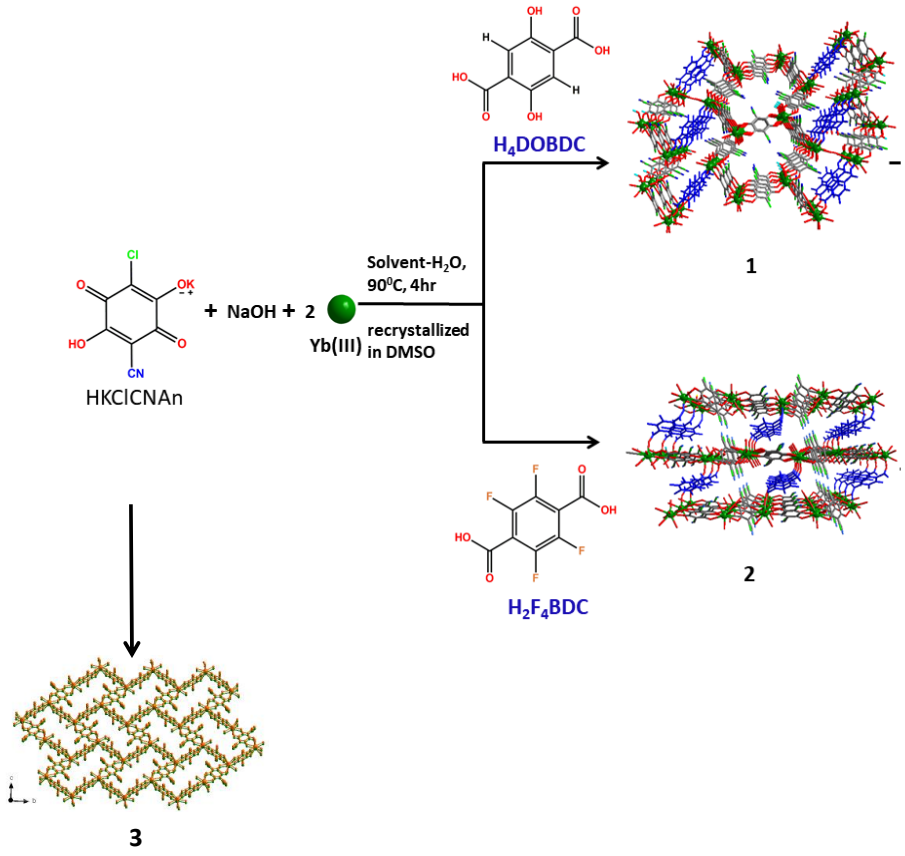

Figure 13. Schematic representation of the synthesis of compounds **1**,**2** and **3.**

5.3.2.2 Synthesis of Nanosheets

Nanosheets of compounds **1**, **2** and, for comparison, **3-NS** (**3**=homoleptic $\{[Yb_2(ClCNAn)_3(DMF)_6\}_nCP)$,[46] hereafter **1-NS**, **2-NS**, **3-NS**, were fabricated through the top-down sonication-assisted exfoliation method. Delamination was achieved by sonicating the dried powder of **1-3** bulk CPs (1 mg) samples in isopropanol (1 mL) for 15 min at room temperature. The surnatant of the obtained suspension was removed after sonication and let it stand for 1h. Then, the solution was used undiluted and kept under stirring during the photophysical measurements. Photophysical measurements were performed on the latter suspension after adding different solvents with a concentration of 1% v/v (3 µL of solvent in 300µL of suspension). **1-3 NS** suspensions in isopropanol were dropcast onto SiO2/Si substrates (20 µL) and carbon-coated copper grids (5 µL) for AFM.

5.3.2.3 AFM Characterization

Nanosheet topology was investigated by AFM (NT-MDT Smena instrument) performed in non-contact mode using sharp Si tips (NT-MDT ETALON HA_NC). Topography (height) images were analyzed using a free software (WSxM version 5.0).[61]

5.3.2.4 Morphology measurements

TEM and HR-TEM images were obtained with a JEM 2010 UHR instrument equipped with a Gatan Imaging Filter (GIF) with a 15 eV window and a 794 slow scan CCD camera.

5.3.2.5 PXRD studies

PXRD analyses were carried out by a Seifert X3000 instrument with a θ−θ Bragg−Brentano focalizing geometry, CuKα anode (λ =1.54056 Å), graphite monochromator on the diffracted beam, and scintillation counter. The samples were analysed by using a zero background (zbg) sample holder. PXRD patterns on bulk samples were recorded on the as-prepared powder (~5mg) whereas PXRD patterns on nanosheets were obtained by dropping the sonicated iso-propanol dispersion on the zbg silicon crystal surface, leaving the drop dry and repeating the process until a ~3 mg of layered sample was reached.

5.3.2.6 Optical Characterization and sensing studies

Continuous-wave (Cw) diffuse reflectance of crystals of coordination compounds was measured using a dual-beam spectrophotometer equipped with an integrating sphere accessory (Agilent Cary 5000 UV−vis−NIR). Time-resolved ligand-centered PL was excited at 360 nm by 200 fs long pulses delivered by an optical parametric amplifier (Light Conversion TOPAS-C) pumped by a regenerative Ti:sapphire amplifier (Coherent Libra-HE) running at a repetition frequency of 1 kHz, wavelength dispersed by single grating spectrometer (Princeton Instruments Acton SpectraPro2300i) and detected by a Vis streak camera (Hamamatsu C1091). Ligand-centered PL spectra were acquired under photoexcitation by a passively Q-switched powerchip laser (Teem Photonics PNV-M02510) delivering 310 ps-long pulses at a 355 nm wavelength and a 1 kHz repetition rate, using a grating spectrometer (Princeton Instruments Acton SpectraPro 2300i) equipped with a Vis array detector (AndorNewton^{EM}). For lanthanide-centered emission spectra, a NIR array detector (AndoriDusInGaAs 1.7 μm) was used in place of the Vis array detector. Time-resolved lanthanide-centered PL measurements were done using a NIR photomultiplier (Hamamatsu H10330A-75 connected to a 1 GHz digital oscilloscope (Tektronik TDS 5104). Energy densities used for photoexcitation were <500 μJ/cm^2 per pulse, corresponding to excitation levels much less than one excited state per ligand per pulse in all cases. PL measurements on ethanol nanosheet suspensions were done with the suspensions in 1-mm-thick quartz cuvettes. All PL decay curves were analyzed using bi/three-exponential decay functions $\mathbf{PL}(t) = \sum_0^n A_k \mathbf{exp}\,(-t/\tau_k)$ with amplitudes A_k and time constants τ_k. Initial PL amplitudes ($\mathbf{PL_0}$) and amplitude-weighted average lifetimes (τ) were computed as $\mathbf{PL_0} = \sum_0^n A_k$and $\tau = \int_0^\infty \mathbf{PL}(t)dt/\mathbf{PL_0} = \sum_0^n A_k\tau_k/\sum_0^n A_k$, respectively.

5.3.3 2D Materials based on UV- Vis Emitters

5.3.3.1 Synthesis of $[Tb_2(ClCNAn)_3(DMSO)_6]_n$.

An aqueous solution of $Tb(NO_3)_3 \cdot 5H_2O$ was added dropwise to an aqueous red solution of KHClCN and NaOH, showing an immediate color change to purple. After stirring at 90°C for ca. 4h, a purple precipitate appeared. The mixture was cooled down to room temperature and the powder was collected from the mother liquor by under vacuum filtration. The

powder was then washed several times with fresh water. Compound **1** was recrystallized in DMSO to give red crystals suitable for X-ray analysis after 1 week.

5.3.3.2 Synthesis of $[Eu_2(ClCNAn)_3(DMSO)_6]_n$. This compound was synthesized with a similar synthetic approach using $Eu(NO_3)_3 \cdot 5H_2O$, instead of $Tb(NO_3)_3 \cdot 5H_2O$.

5.3.3.3 Crystal structure of 4 and 5 CPs

A single crystal of the compound was mounted on glass fiber loop using a viscous hydrocarbon oil to coat the crystal and then transferred directly to the cold nitrogen stream for data collection. Data collection was performed at 150 K on an Agilent Supernova with Cu Kα (λ = 1.54184 Å). The structure was solved by direct methods with the *SIR97* program and refined against all F^2 values with the *SHELXL-97* program using the *WinGX* graphical user interface. All H atoms were placed in calculated positions and refined isotropically with a riding model. Non-H atoms were refined anisotropically except for the disordered C (C4, C8, C12) from cyano, disorder C (C13B, C14B, C17A, C18A, C18B) and S (S3A, S3B) atoms from DMSO molecules respectively. A summary crystallographic data of **4** and **5** is listed in **Table 1**.

Table 1. Crystallographic data of the compound **4** and **5**

Empirical formula	$C_{33}H_{36}Cl_3N_3O_{18}S_6Tb_2$ (**4**)	$C_{16.5}H_{18}Cl_{1.5}EuN_{1.5}O_9S_3$ (**5**)
Fw	**1379.20**	**682.64**
Crystal color	**Red**	**Red**
Crystal size (mm^3)	**0.02*0.04*0.07**	**0.201*0.012*0.012**
Temperature (K)	**150**	**100(2)**
Wavelength (Å)	**1.54184**	**0.71075**
Crystal system, Z	**Monoclinic, 2**	**Monoclinic**
Space group	***P*2$_1$/n**	**P2$_1$/n**
a (Å)	**9.6868(2)**	**9.65100(10)**
b (Å)	**16.3511(3)**	**16.3236(2)**
c (Å)	**15.1558(3)**	**15.17170(10)**
A	**90.00**	**90.00**

	B	**93.683(2)**	**92.9870(10)**
	Γ	**90.00**	**90**
[a]$R1(F)$ = $\Sigma\|\|F_0\|-$	V (Å³)	**2395.57(8)**	**2386.89(4)**
	ρcalc (g.cm^{-3})	**1.912**	**2386.89(4)**
	μ(CuKα) (mm^{-1})	**18.945**	
	θ range (°)	**3.981-73.587**	**2.445-27.480**
	Data collected	**19515**	
	Data unique	**4767**	
	Data observed	**4408**	
	Number of parameters / restraints	**388/65**	**506/887**
	R(int)	**0.0486**	
	R1(F),[a] I > 2σ(I)	**0.0490**	
	wR2(F2),[b] all data	**0.1253**	**0.1046**
	S(F2),[c] all data	**1.106**	

$|F_C||/\Sigma|F_0|$; [b]$wR2(F^2) = [\Sigma w(F_0^2\text{-}F_C^2)^2/\Sigma wF_0^4]^{1/2}$; [c]$S(F^2) = [\Sigma w(F_0^2\text{-}F_C^2)^2/(n+r\text{-}p)]^{1/2}$.

5.3.3.4 Magnetic Measurements

Magnetic measurements were carried out by using a Quantum Design MPMS-XL magnetometer. The magnetic susceptibility data were recorded in the temperature range of 2-300K in an external field of 1000 Oe. The Diamagnetic corrections were calculated by using Pascal's constants. (ref) The dynamic magntetic susceptibility data were obtained in the frequency range of 0.1-1000 Hz in an oscillating field of 3 Oe.

5.3.3.5 AFM characterization

A NT-MDT Solver-Pro atomic-force microscopy (AFM) was used to study the topography and roughness of nanosheets. AFM measurements were performed at 0.5-1 Hz scan speed in semicontact mode in air. Topography image analysis and calculation of surface roughness were performed by using WSxM 5.0 Develop3.2 software.[61]

5.4 Conclusions and Perspectives

Novel robust and crystalline 2D nanosheets of novel heteroleptic 2D-layered NIR-Vis. emissive lanthanide CPs, **1-NS**, **2-NS** and **4-NS,** were successfully obtained, by using the well known sonication-assisted solution method. The synthesis and structural characterization of the bulky sized corresponding 2D neutral CPs, with a special emphasis on the lanthanide coordination environment, exfoliation planes, and distances between them being clearly identified, were also reported . **4** represents the first example of homoleptic CP based on a visible emitting lanthanide and chlorocyanoanilate ligand, while **1** and **2** were the first examples of heteroleptic lanthanide MOFs/CPs based on anilate and carboxylate ligands [ACS AMN[. **1-NS**, **2-NS** and **4-NS** were fabricated by exfoliation of **1** and **2** and **4** bulky sized CPs down to few monolayers and lateral micrometric size has been observed by AFM. PXRD and HR-TEM measurements, performed on **1-2-NS** clearly showed the preservation of crystallinity upon exfoliation, which is an indication of the robustness of the 2D nanosheets. Advanced photophysical studies on **1-NS** and **2-NS** have been undertaken, highlighting the antenna effect of the heterosubstituted anilate linker and the downsizing effect on the lifetime of the decay process. Their robustness makes the 2D nanosheets ideal nanoplatforms to perform advanced photophysical studies by an innovative multiprobe approach, based on the study of small perturbation of lifetime photoluminescence (PL) and integrated PL, induced by different solvents, both aromatic and aliphatic, bearing electro-withdrawing and electro-donating groups. PL turn-off toward nitrobenzene was observed which can be understood in terms of a very efficient ISC process from the anilate to the Yb^{III} center compared to the competitive PCT process from the anilate to nitrobenzene.

As perspectives, photoluminescence studies on **4** e **5**, both bulk size CPs and nanosheets, based on Tb^{III} and Eu^{III} Vis Emitting ions, should be performed, in order to investigate their capabilities to recognize transition metal ions in aqueous environment. These results contribute to the development of research on 2D nanosheets nanomaterials, and in particular they show how to design and fabricate robust and crystalline nanosheets and simultaneously give a roadmap, based on advanced multiprobe photophysical studies, toward challenging applications, such as the design of prototype nanoplatforms for sensing and detection of explosives as TNT or picric acid, which represent a task of paramount

importance for homeland security. Nanosheet technology based on Vis. Lanthanide CPs may also represent a challenge for sensing and detecting inorganic pollutants such as heavy metal ions in water, which have drawn much attention due to their toxicity, long half-life and nonbiodegradability. Noteworthy environmental pollution is increasing and posing serious threat to the ecosystem and human health.

5.5 References

1 A. Mohanty, U. P. Singh, R. J. Butcher, N. Das and P. Roy, *CrystEngComm*, 2020, **22**, 4468–4477.

2 Z. Hao, X. Song, M. Zhu, X. Meng, S. Zhao, S. Su, W. Yang, S. Song and H. Zhang, *J. Mater. Chem. A*, 2013, **1**, 11043–11050.

3 J. C. G. Bünzli and S. V. Eliseeva, *J. Rare Earths*, 2010, **28**, 824–842.

4 Q. Wang and D. Astruc, *Chem. Rev.*, 2020, **120**, 1438–1511.

5 K. M. L. Taylor-Pashow, J. Della Rocca, Z. Xie, S. Tran and W. Lin, *J. Am. Chem. Soc.*, 2009, **131**, 14261–14263.

6 Y. Zhang, G. Li, D. Geng, M. Shang, C. Peng and J. Lin, *Inorg. Chem.*, 2012, **51**, 11655–11664.

7 Y. Zhang, X. Li, K. Li, H. Lian, M. Shang and J. Lin, *ACS Appl. Mater. Interfaces*, 2015, **7**, 2715–2725.

8 J. G. Mao, *Coord. Chem. Rev.*, 2007, **251**, 1493–1520.

9 J. C. G. Bünzli and C. Piguet, *Chem. Soc. Rev.*, 2005, **34**, 1048–1077.

10 L. J. Xu, G. T. Xu and Z. N. Chen, *Coord. Chem. Rev.*, 2014, **273**–**274**, 47–62.

11 H. Weng and B. Yan, *Dalt. Trans.*, 2016, **45**, 8795–8801.

12 G. E. Gomez, M. D. S. Afonso, H. A. Baldoni, F. Roncaroli and G. J. A. A. Soler-Illia, *Sensors (Switzerland)*, , DOI:10.3390/s19051260.

13 X. Lian, D. Zhao, Y. Cui, Y. Yang and G. Qian, *Chem. Commun.*, 2015, **51**, 17676–17679.

14 D. Wang, J. Liu and Z. Liu, *J. Solid State Chem.*, 2017, **251**, 243–247.

15 B. Liu, L. Hou, W. P. Wu, A. N. Dou and Y. Y. Wang, *Dalt. Trans.*, 2015, **44**, 4423–4427.

16 G. Ji, J. Liu, X. Gao, W. Sun, J. Wang, S. Zhao and Z. Liu, *J. Mater. Chem. A*, 2017, **5**,

10200–10205.

17 Z. Hu, B. J. Deibert and J. Li, *Chem. Soc. Rev.*, 2014, **43**, 5815–5840.

18 Z. Xiaoxiong, Z. Wenjun, L. Cuiliu, Q. Xiaohong and Z. Chengyu, *Inorg. Chem.*, , DOI:10.1021/acs.inorgchem.8b03555.

19 Y. Cui, B. Chen and G. Qian, *Coord. Chem. Rev.*, 2014, **273**–**274**, 76–86.

20 Y. Su, J. Yu, Y. Li, S. F. Z. Phua, G. Liu, W. Q. Lim, X. Yang, R. Ganguly, C. Dang, C. Yang and Y. Zhao, *Commun. Chem.*, , DOI:10.1038/s42004-018-0016-0.

21 J. Xu, X. Chen, Y. Xu, Y. Du and C. Yan, *Adv. Mater.*, 2020, **32**, 1–17.

22 M. Atzori, F. Artizzu, L. Marchiò, D. Loche, A. Caneschi, A. Serpe, P. Deplano, N. Avarvari and M. L. Mercuri, *Dalt. Trans.*, 2015, **44**, 15786–15802.

23 S. Ashoka Sahadevan, N. Monni, A. Abhervé, D. Marongiu, V. Sarritzu, N. Sestu, M. Saba, A. Mura, G. Bongiovanni, C. Cannas, F. Quochi, N. Avarvari and M. L. Mercuri, *Chem. Mater.*, 2018, **30**, 6575–6586.

24 C. Tan, P. Yu, Y. Hu, J. Chen, Y. Huang, Y. Cai, Z. Luo, B. Li, Q. Lu, L. Wang, Z. Liu and H. Zhang, *J. Am. Chem. Soc.*, 2015, **137**, 10430–10436.

25 M. Zhao, Y. Wang, Q. Ma, Y. Huang, X. Zhang, J. Ping, Z. Zhang, Q. Lu, Y. Yu, H. Xu, Y. Zhao and H. Zhang, *Adv. Mater.*, 2015, **27**, 7372–7378.

26 S. Guo and S. Dong, *J. Mater. Chem.*, 2011, **21**, 18503–18516.

27 D. Tian, R. Y. Chen, J. Xu, Y. W. Li and X. H. Bu, *APL Mater.*, , DOI:10.1063/1.4904879.

28 X. L. Huang, L. Liu, M. L. Gao and Z. B. Han, *RSC Adv.*, 2016, **6**, 87945–87949.

29 W. Huang, Y. Sunami, H. Kimura and S. Zhang, *Nanomaterials*, , DOI:10.3390/nano8070519.

30 V. K. Maka, A. Mukhopadhyay, G. Savitha and J. N. Moorthy, *Nanoscale*, 2018, **10**, 22389–22399.

31 F. Y. Yi, D. Chen, M. K. Wu, L. Han and H. L. Jiang, *Chempluschem*, 2016, **81**, 675–690.

32 L. M. Gaetke, H. S. Chow-Johnson and C. K. Chow, *Arch. Toxicol.*, 2014, **88**, 1929–1938.

33 C. Song, W. Yang, N. Zhou, R. Qian, Y. Zhang, K. Lou, R. Wang and W. Wang, *Chem. Commun.*, 2015, **51**, 4443–4446.

34 T. Liu, J. X. Che, Y. Z. Hu, X. W. Dong, X. Y. Liu and C. M. Che, *Chem. - A Eur. J.*, 2014,

20, 14090–14095.

35 B. Chen, L. Wang, Y. Xiao, F. R. Fronczek, M. Xue, Y. Cui and G. Qian, *Angew. Chemie - Int. Ed.*, 2009, **48**, 500–503.

36 Q. Tang, S. Liu, Y. Liu, J. Miao, S. Li, L. Zhang, Z. Shi and Z. Zheng, *Inorg. Chem.*, 2013, **52**, 2799–2801.

37 Y. Wu, G. P. Yang, Y. Zhao, W. P. Wu, B. Liu and Y. Y. Wang, *Dalt. Trans.*, 2015, **44**, 3271–3277.

38 W. Yan, C. Zhang, S. Chen, L. Han and H. Zheng, *ACS Appl. Mater. Interfaces*, 2017, **9**, 1629–1634.

39 H. Xu, J. Gao, X. Qian, J. Wang, H. He, Y. Cui, Y. Yang, Z. Wang and G. Qian, *J. Mater. Chem. A*, 2016, **4**, 10900–10905.

40 Y. G. Sun, X. F. Gu, F. Ding, P. F. Smet, E. J. Gao, D. Poelman and F. Verpoort, *Cryst. Growth Des.*, 2010, **10**, 1059–1067.

41 J. Liu, H. Yu, L. Wang, Z. Deng, K. ur R. Naveed, A. Nazir and F. Haq, *Inorganica Chim. Acta*, 2018, **483**, 550–564.

42 L. Tang, X. Li, R. Ji, K. S. Teng, G. Tai, J. Ye, C. Wei and S. P. Lau, *J. Mater. Chem.*, 2012, **22**, 5676–5683.

43 S. Ashoka Sahadevan, N. Monni, M. Oggianu, A. Abhervé, D. Marongiu, M. Saba, A. Mura, G. Bongiovanni, V. Mameli, C. Cannas, N. Avarvari, F. Quochi and M. L. Mercuri, *ACS Appl. Nano Mater.*, 2020, **3**, 94–104.

44 A. Abhervé, S. Mañas-Valero, M. Clemente-León and E. Coronado, *Chem. Sci.*, 2015, **6**, 4665–4673.

45 S. Benmansour, A. Abhervé, P. Gómez-Claramunt, C. Vallés-García and C. J. Gómez-García, *ACS Appl. Mater. Interfaces*, 2017, **9**, 26210–26218.

46 S. Ashoka Sahadevan, N. Monni, A. Abhervé, D. Marongiu, V. Sarritzu, N. Sestu, M. Saba, A. Mura, G. Bongiovanni, C. Cannas, F. Quochi, N. Avarvari, M. L. Mercuri, A. Abherve, D. Marongiu, V. Sarritzu, N. Sestu, M. Saba, A. Mura, G. Bongiovanni, C. Cannas, F. Quochi, N. Avarvari and M. L. Mercuri, *Chem. Mater.*, 2018, **30**, 6575–6586.

47 A. Harvey, J. B. Boland, I. Godwin, M. Siepi, E. Morales-narváez, N. Domingo, M. Singh, E. Della Gaspera, T. Ahmed, F. Wang, Z. Wang, Q. Wang, M. M. Bernal, L. Álvarez, E. Giovanelli, A. Arnáiz and L. Ruiz-gonzález, *2D Mater.*, 2016, **3**, 035014.

48 O. I. Lebedev, F. Millange, C. Serre, G. Van Tendeloo and G. Férey, *Chem. Mater.*, 2005, **17**, 6525–6527.

49 F. Quochi, R. Orrù, F. Cordella, A. Mura, G. Bongiovanni, F. Artizzu, P. Deplano, M. L. Mercuri, L. Pilia and A. Serpe, *J. Appl. Phys.*, 2006, **99**, 4–7.

50 A. Monguzzi, R. Tubino, F. Meinardi, A. O. Biroli, M. Pizzotti, F. Demartin, F. Quochi, F. Cordelia and M. A. Loi, *Chem. Mater.*, 2009, **21**, 128–135.

51 S. R. Zhang, D. Y. Du, J. S. Qin, S. J. Bao, S. L. Li, W. W. He, Y. Q. Lan, P. Shen and Z. M. Su, *Chem. - A Eur. J.*, 2014, **20**, 3589–3594.

52 F. Quochi, M. Saba, F. Artizzu, M. L. Mercuri, P. Deplano, A. Mura and G. Bongiovanni, *J. Phys. Chem. Lett.*, 2010, **1**, 2733–2737.

53 X. Lian, D. Zhao, Y. Cui, Y. Yang and G. Qian, *Chem. Commun.*, 2015, **51**, 17676–17679.

54 P. Gómez-Claramunt, S. Benmansour, A. Hernández-Paredes, C. Cerezo-Navarrete, C. Rodríguez-Fernández, J. Canet-Ferrer, A. Cantarero and C. Gómez-García, *Magnetochemistry*, 2018, **4**, 6.

55 S. Benmansour, I. Pérez-Herráez, G. López-Martínez and C. J. Gómez García, *Polyhedron*, 2017, **135**, 17–25.

56 S. Benmansour, A. Hernández-Paredes and C. J. Gómez-García, *J. Coord. Chem.*, 2018, **71**, 845–863.

57 S. A. Sahadevan, N. Monni, A. Abhervé, G. Cosquer, M. Oggianu, G. Ennas, M. Yamashita, N. Avarvari and M. L. Mercuri, *Inorg. Chem.*, 2019, **58**, 13988–13998.

58 C. Benelli and D. Gatteschi, *Chem. Rev.*, 2002, **102**, 2369–2387.

59 D. Leith, *Aerosol Sci. Technol.*, 1987, **6**, 153–161.

60 M. Atzori, F. Artizzu, L. Marchiò, D. Loche, A. Caneschi, A. Serpe, P. Deplano, N. Avarvari and M. L. Mercuri, *Dalt. Trans.*, 2015, **44**, 15786–15802.

61 I. Horcas, R. Fernández, J. M. Gómez-Rodríguez, J. Colchero, J. Gómez-Herrero and A. M. Baro, *Rev. Sci. Instrum.*, 1991, 78

Summary

Conclusions and Perspectives

The present Work contributes to the ongoing research on Luminescent sensors with the goal to develop novel luminescent chemosensors and/or sensing platforms with promising applications in the real-time detection/monitoring of environmental pollutants. Particularly, dye-functionalized fluorescent on-chip silicon platforms and NIR-Vis. emitting lanthanide based on 2D nanosheets have been developed by the rational design of the molecular building blocks. FITC and ClCNAn^{2-}/carboxylate derivatives were properly tailored for the detection of Cu^{II} ions and nitroaromatics.

The old-fashioned rhodamine fluorophore has been employed for developing hybrid ratiometric fluorescent platforms and intensity-based fluorescent chemosensors. The DPP fluorophore, usually employed in several fields, as Organic Field-Effect Transistors (OFTEs) and Organic Photovoltaics (OPVs), but scarcely used in sensing field, due to its versatility in fine tuning the chemical make-up, has been properly tailored for the preliminary detection of mercury toxic metal cation.

The Tube Map of the present Work is summarized below, highlighting the Four Main Stations, representing **Chapter 2**, **3**, **4** and **5**, in Yellow, Magenta, light Blue and Ferrari Red (red 245 DPP pigment), respectively.

Chapter 2. *Silicon-based Fluorescent Platforms for Copper(II) Detection in Water*

Dye-functionalized Fluorescent silicon-based chips were reported as a challenging strategy for remote detection of metal ions in aqueous solution, over conventional analytical techiniques and fluorescent molecular chemosensors. A fluorescent silicon-based Platform was fabricated by conjugation of a fluorescein derivative (FITC) to an amino-modified silicon chip, capable to detect copper (II) in water, showing high sensitivity and selectivity, a limit of detection compatible with the recommended upper limits for copper (II) in drinking water and good reversibility, by using a standard metal-chelating agent as EDTA. This approach can lead to effective fluorescent sensors for heavy metal ions. The original fluorophore-analyte interaction mechanism at the basis of the reported fluorescence quenching, as well as the potential of performance improvement, were also reported. The herein presented platform architecture is very versatile, allowing, in principle, to tailor the selectivity towards other metal ions ot other analytes, by changing the fluorophore or anchoring group (for example by replacing FITC with DPP derivatives for toxic metal ions, prepared in Chapter 4, *vide infra*) and provides a favorable outlook for integration of fluorescent chemosensors with silicon photonics technology, in remote analysis systems for real-time water monitoring. Noteworthy, even silicon chips could be change with plasmonic nanoplatforms (both linear ore core/shell), leading to an enhancement of the optical properties of grafted fluorophores and resulting in increased sensitivity towards a target analyte.

Chapter 3. *Hybrid Ratiometric Fluorescent Platforms*

A hybrid fluorescent ratiometric probe, consisting of a dansyl moiety as donor unit and a rhodamine moiety as acceptor unit, has been synthesized and characterized. Both rhodamine and dansyl acceptor/donor units were selected since they exhibit the required spectral-overlap between the absorption band of the acceptor unit (rhodamine) and the emission band of the donor unit (dansyl), a crucial prerequisite for a FRET process. This hybrid system has been investigated, in a wide pH range, by a multi-technique approach, involving UV-Visible, PL and time-resolved PL spectroscopies, potentiometric titrations and

Mass Spectrometry. The proton mediated rhodamine spirolactam/ring-opening mechanism and the photophysical mechanism (FRET) at the basis of energy-transfer, was inferred by spectrophotometric and potentiometric titrations, supported by DFT calculations. Particularly, theoretical calculations have been shown the potential to predict the occurrence of the FRET process. In fact, the Frontier Orbitals study highlighted that the HOMO-LUMO gap decreases as a consequence of **RhO-L$_3$** ring-opening, which exhibit strong absorption in the visible region, in highly acidic conditions (pH <*ca.* 3). The protons interaction with **RhO-L$_3$** probe influence significantly HOMO/LUMO energy levels of rhodamine and dansyl moiety and it was found that the HOMO–LUMO energy gap of the H_4L^{4+} species (≈2.3 eV) becomes lower than those of the **RhO-L$_3$** chemosensor (**RhO-L$_3$** ≈ 4.0 eV). Remarkably when **RhO-L$_3$** probe is in its spirolactam form, the HOMO–LUMO energy gap of acceptor rhodamine moiety is greater than that one of dansyl donor, suppressing the dansyl-to-rhodamine energy transfer. However, in acidic conditions (pH <*ca.*3), spirolactam ring is opened up, as a consequence of proton interaction, showing a significant decrease of the energy gap in the rhodamine moiety, matching dansyl unit energy gap and, therefore, favoring FRET process. As perspective, a systematic study on several donor/acceptor combinations of model FRET-based chemosensors is required, to confirm these findings. Dansyl- and rhodamine-centered PL intensity titration experiments are in progress to detect and quantify the FRET process. Furthermore, donor–acceptor pair distance (typically 10–100 Å) in the present hybrid ratiometric platform should be determined in order to rationalize the FRET distance dependency and its efficiency.

Chapter 4. *New Rhodamines and Thiophene-DiketopyrroloPyrroles as Fluorescent Chemosensors*

Rhodamine and Diketopoyrrolopyrrole derivatives have been prepared with the aim to develop fluorescent chemosensors able to detect Hg^{II}. In particularly this chapter is mainly focused on the research performed at the University of Angers, Laboratoire Moltech-Anjou, under the supervision of Prof. N. Avarvari and, unfortunately, interrupted for COVID-19 emergency. Several fluorophores derivatives, mono and dialkylated, have been synthesized and characterized by fluorescence spectroscopy. Following the well- known thymine-Hg^{II}

binding process, where the nitrogen group of is able to interact with Hg^{II}, **DPP-L_1** and **DPP-L_2** have been synthesized as monoalkylated derivatives. Absorption and fluorescence studies on **DPP-L_1** showed a variation in its photophysical properties, upon addition of Hg^{II}, due to an aggregation process Hg^{II}-mediated, resulting in a luminescence quenching. Furthermore, **DPP-L_3** and **DPP-L_4**, conjugating the bipyridine moiety to DPP core, have been synthesized and characterized. Future work will involve the study of sensing performances of the synthesized DPP-fluorescent probes, towards several metal cations in aqueous environment. The probes showing the best performance will be grafted, *via* the layer-by-layer functionalization approach, on silicon-based platforms to fabricate silicon-integrated fluorescent devices for remote detection of a wide range of metal ions in water (*vide supra*).

Chapter 5. Luminescent Nanosheets as Unique Platforms for Chemical Sensing

CPs may represent a challenge for sensing and detecting environmental pollutants such as heavy metal ions in water and nitroaromatic compounds, which have drawn much attention due to their toxicity, long half-life and nonbiodegradability. This chapter reported on the fabrication and characterization of novel robust and crystalline 2D nanosheets of heteroleptic 2D-layered NIR-Vis.-Emissive lanthanide CPs, **1-NS**, **2-NS** and **4-NS**. They were successfully obtained, by using the well-known sonication-assisted solution method and studied by AFM, HR-TEM and PXRD. AFM showed that they are formed by few monolayers and lateral micrometric size, while HRTEM and PXRD, performed on **1-2-NS**, clearly indicate that, upon exfoliation, crystallinity is retained up to the nanoscale level, significant evidence of their robustness. **4** represents the first example of a homoleptic bulk CP based on the Tb^{III} visible-emitting lanthanide and chlorocyanoanilate linker, while **1** and **2** were the first examples of heteroleptic lanthanide MOFs/CPs based on anilate and carboxylate ligands. Due to their robustness, **1-2-NS** are ideal nanoplatforms for the detection of nitrobenzene. Advanced photophysical studies performed by an innovative multiprobe approach, based on the study of small perturbation of lifetime photoluminescence (PL) and integrated PL, induced by different solvents, remarkably reveal PL turn-off toward nitrobenzene. The observed PL quenching can be understood in terms of a very efficient ISC process from the

anilate to the Yb^{III} center compared to the competitive PCT process from the anilate to nitrobenzene. As perspectives, photophysical studies on **4-NS,** based on Tb^{III} Vis Emitter CP, should be performed, in order to investigate their capabilities to detect transition metal ions in aqueous environment. These results contribute to the ongoing research on the design and fabrication of robust and crystalline luminescent nanosheets, as suitable prototype nanoplatforms for sensing applications, also by properly tailoring both linkers and metals nodes of the corresponding 2D bulk size CPs/MOFs.

Annexes

ANNEXES I

General overview on Luminescence and Lanthanide luminescent properties

1.1 Photoluminescence

Photoluminescence is defined as an optical property of a substances which absorbs photon and release them radiatively. At room temperature, elementary particles are in their elementary state. If these particles are exposed to an electromagnetic radiation, the absorption of photons with a proper energy can take place. this process causes the formation of exited state with a consequent dissipation of energy in various forms[1] (**Figure 1**). Depending on the nature of the exited state, it is possible to divide the emission of light into two categories: fluorescence and phosphorescence.

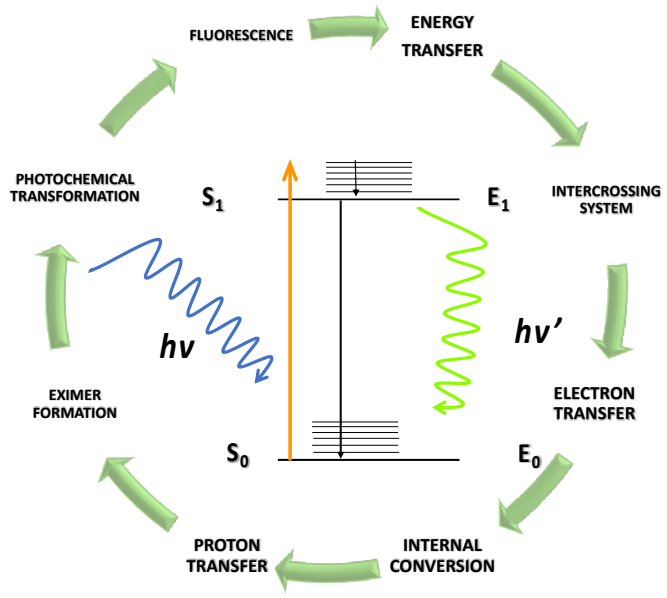

Figure 1. Possible dissipation pathways of exited molecules

Photon with a significant energy, colliding with molecules, is able to promote an electron to higher molecular orbitals, producing electronically exited states. The exited state is energetically unstable, thus, by a variety of processes, lose the excess of energy. The Perrin-

Jablonsky diagram shows the most important processes that may happen after photon absorption [1](**Figure 2**).

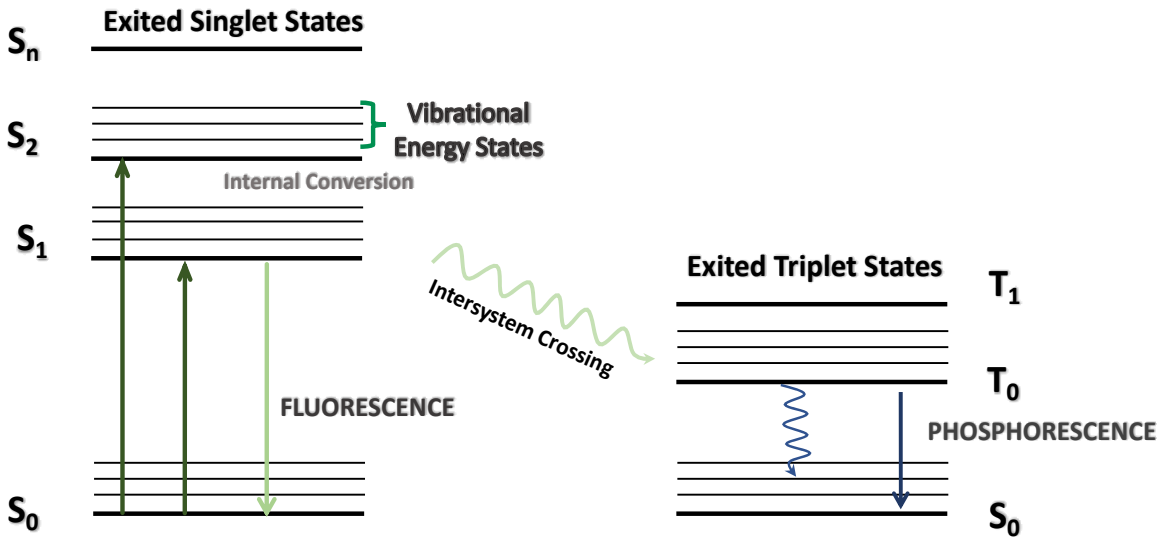

Figure 2. Perrin-Jamblonsky Diagram

Afterward the light absorption, the vibrational levels of some upper excited states are populated with electron density. These electrons immediately relax to the lowest vibrational level of S_1 by vibrational relaxations by a process is called internal conversion. All the other photochemical processes (fluorescence, quenching etc.) are more likely to happen from the lowest vibrational state of S_1.[2] Depending on the nature of the excited molecules, the excited electron at S_1 may undergo three different processes: emission of photons *via* fluorescence emission, intersystem crossing to the triplet state and releasing the excess energy by internal conversion as shown in **Figure 2**. Phosphorescence is the last step in the Intersystem Crossing, that is possible only if the electron in the S1 state undergo a spin conversion. This transition is possible only in few conditions such as presence of a heavy atom and/or exciton coupling within a molecule. Phosphorescence is a lower energetic-radiation and because of multiplicity of its state (T_1), the radiative decay if compared to fluorescence, is slower if compared to fluorescence. Fluorescence is the result of three stage process that occurs on certain compounds known as fluorophores. In the first step, a photon of energy ***hv*** is produced by a source and absorbed by a fluorophore,

causing an exited electronic single state (S_1). The exited state exists for a finite time. During this time, the compound is subject to conformational changes and interacts with the molecular environment. The energy of S_1 is partially dissipated leading to a relaxed singlet exited state (S_1') from which fluorescence emission originates. In some cases, not all the molecules initially excited return to the ground state indeed other processes such as collisional quenching, fluorescence resonance energy transfer (FRET) can be allowed. When a photon of energy **hv'** is emitted, the fluorophore returns to the ground state (S_0). The energy of this proton is lower because of the energy dissipation during the excited state., and therefore of longer wavelength, than the excitation photon ***hv.***

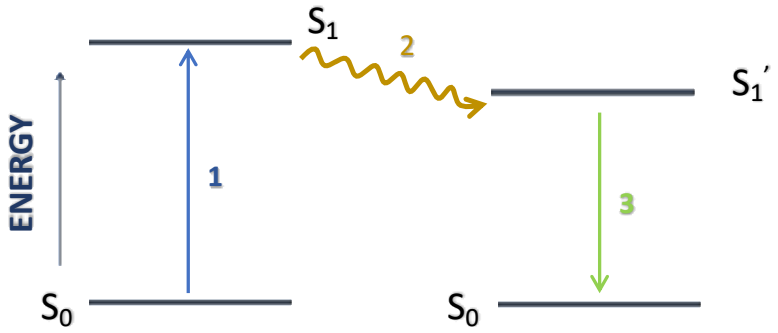

Figure 3. Schematic representation illustrating the process involved during fluorescence emission

The difference (usually in frequency units) between the spectral positions of band maxima of the absorption and luminescence (***hv-hv')*** is called Stokes' shift. The Stokes' shift is fundamental to the sensitivity of the fluorescence technique because it allows emission photons to be detected against a low background.

The most important photophysical parameters, in the fluorescence process, are the fluorescent quantum yield Φ and the lifetime **τ**. The quantum yield is the ratio of the number of photons emitted by S_1 to the number of photons absorbed by S_0. It is possible to calculate this parameter by the equation, reported below, where K_f and K_{nr} are the rate of he rates of radiative and nonradiative transitions, respectively.

A high quantum yield implies a high fluorescence intensity. Moreover, the fluorescence quantum yield of a molecule may also be determined by comparing the area under its

fluorescence spectrum with a spectrum of a reference compound whose quantum yield is known.

$$\Phi = k_f / k_f + k_{nr}$$

The fluorescence lifetime is the time that a molecule remains in its excited state and it is determined by time-resolved measurements. The equation, reported below, show that the fluorescence lifetime is inversely proportional to the sum of the rate constants.[3]

$$T = 1 / k_f + k_{nr}$$

1.2 Lanthanide Luminescence

Their interesting feature is photoluminescence. All of the Ln^{III}, except La^{III} ($4f^0$) and Lu^{III} ($4f^{14}$), exhibit luminescent emissions, which cover the entire spectrum. Eu^{III}, Tb^{III}, Sm^{III}, and Tm^{III} emit in the visible region with the color red, green, orange, and blue, respectively. Pr^{3+}, Nd^{III}, Sm^{III}, Dy^{III}, Ho^{III} , Er^{III}, Tm^{III} and Yb^{III} show emissions the near-infrared region, while Ce^{III} shows a broadband emission from 370 to 410 nm because of the 5d–4f transition. Because of their luminescence, lanthanides can find applications in several fields ranging from lasers, telecommunications, sensing to molecular thermometers and bioimaging.

There are three types of optical transitions in lanthanide compounds:

1. **Allowed f↔d transitions**

configurational $4f^n \leftrightarrow 4f^{n-1}\ 5d^1$ transition are parity allowed. They show broader bands than f-f transitions and their energy is highly dependent on the ligand-field strength, since 5d orbitals have large radial expansion, allowing extensive tuning of the absorption and/or emission wavelengths. However, these transitions are highly energetic so that they are usually

2. **Allowed charge-transfer (CT) transitions**

CT transitions, either LMCT or MLCT are also allowed. As they correspond to either reduction or oxidation of the metal ion, it usually occurs at high energies.

3. Forbidden Intraconfigurational f↔f transitions

Absorption or emission of photons is promoted by operators linked to the nature of light:

- the odd-parity electric dipole operator (ED)
- even-parity magnetic dipole operator (MD)
- the electric quadrupole operator (EQ)

Laporte's parity selection rule implies that ED 4f-4f transitions are forbidden. However, when the lanthanide ion undergoes the influence of a ligand-field, non-centrosymmetric interactions mix electronic states of opposite parity into 4f wavefunctions, which relax the selection rule and the transitions become partially allowed. These transitions are then called induced (or forced) electric dipole transition. Major contributions to their intensity are due to the mixing of $4f^n$ configuration with opposite parity $4f^{n-1}5d^1$ configuration, LMCT states, and/or vibrational levels. Some induced ED transitions are highly sensitive to small changes in the chemical environment of the metal ion and are denoted hypersensitive or sometimes pseudo- quadrupolar transitions because they follow the selection rules of EQ transitions. While the intensity of regular ED transitions varies by factors 2-5 depending on the composition of the inner coordination sphere of the metal ion, hypersensitive transitions can be enhanced up to 200-fold.

Parameter characterizing the emission of Ln^{III} are the lifetime of the excited state and the quantum yield.

$$\frac{\boldsymbol{number\ of\ photons\ emitted}}{\boldsymbol{number\ of\ photons\ absorbed}} = \boldsymbol{Q}$$

The quantum yield depends on the rate at which the excited level is depopulated, k_{obs}, and on the radiative rate k_{rad}.

1.1.2 Sensitized lanthanide luminescence

As most of the 4f transitions are forbidden by selection rules, and, although several mechanisms, such as the coupling with vibrational states, may relax them to some extent, the absorption cross section (molar extinction coefficient: $\varepsilon < 10\ mol^{-1}m^3cm^{-1}$) and the emission intensity after a direct excitation of the lanthanide ion is very low.

This problem can overcome by "antenna effect", which employs a strong absorbing ligand, called chromophore, in order to sensitize the Ln^{III} ion.

The process of energy transfer from organic ligands to the lanthanide ion involves mainly in three steps, as reported in **Figure 4**:

1. the organic ligand absorbs light upon excitation **(1)**
2. the excitation energy is then transferred into Ln^{III} excited states through intramolecular energy transfer **(2)**
3. Ln^{III} ions undergo a radiative process by characteristic luminescence **(3)**

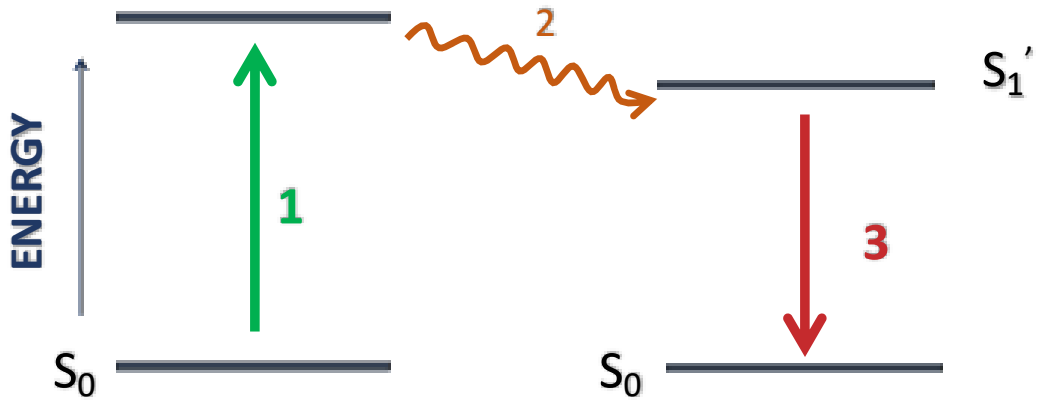

Figure 4. Schematic representation of antenna effect and sensitized luminescence

After the indirect excitation by energy transfer, the lanthanide ion may undergo a radiative transition to a lower 4f-state by a characteristic line-like photoluminescence, or may be deactivated by radiationless process.

There are two other types of electronic transitions of LnIII ions: broad charge–transfer transitions (ligand–metal charge transfer (LMCT) and metal–ligand charge transfer (MLCT)) and broad 4f–5d transitions. They usually occur with high energies, resulting in rare observation in coordination compounds. However, the excitation energy of Sm^{3+}, Eu^{3+}, and Yb^{3+} can be transferred from an LMCT state to their 4f levels when the LMCT state lies

at a high enough energy level. It is of great importance to investigate the numerous energy transfer processes for well-tuning the luminescent properties of LnMOFs.

1.1.3 Luminescence Quenching

The excited states of lanthanide ions do not decay exclusively by radiative processes. If the excited state and the next lower state energy gap is relatively small, luminescence will be in strong competition with the non-radiative decay of the excited state. The electronic excitation energy can also be dissipated by vibrations of the matrix, by a process known as multiphoton relaxation. In other words, phonon relaxations correspond to the collisional decay of an excited energy level, due to the crystalline lattice vibrations. It can occur through coupling of the lanthanide energy levels with the vibrational modes in the direct surrounding of the lanthanide ion. As the quantum yield of a luminescent lanthanide ion depends on the energy gap between the lowest-lying excited state of the metal ion and the highest sublevel of its ground multiplet, the smaller this gap, easier is its de-excitation by non-radiative deactivation processes, for instance through vibrations of bound ligands, particularly high energy vibrations such as O–H or C–H.

These quenching effects lead to shorten luminescent lifetimes ($\mathbf{T_{obs}}$) some orders of magnitude than the natural radiative emission lifetime ($\mathbf{T_r}$) of the free lanthanide ion. The overall rate constant ($\mathbf{T_{obs}}$) for such deactivation processes, is inversely proportional to the measured lifetime, is given by:

$$\kappa_{obs} = 1/T_{obs}$$

The radiationless deactivation, not only vibrations intervene but, also, back energy-transfer processes as well as quenching by charge-transfer states occurs, which are not always easy to identify. The best way to minimize vibration-induced deactivation processes is to design a rigid metal- ion environment, devoid of high-energy oscillators and protecting the Ln^{III} ion from solvent interaction. Such an environment contributes to reduce collision-induced deactivation in solution. However, considerable weakening of the quenching ability of O-H vibrations is observed in some cases if the coordinated water molecules are involved in strong intra- or inter-molecular H-bonding.

The efficiency of the NIR Ln^{III} ion luminescence is severely limited by quenching phenomena, as relatively low energy-gap between excited and ground states of NIR Ln^{III} ions can easily be bridged by high-energy vibrations (O-H, N-H, C H, C O, etc.) and their overtones (Figure A3.5). To overcome this situation, deuteration (C–D) and halogenation (C–F) of the organic ligands has been proven as remedy: absorptions are decreased (C–D) or absent (C–F) because the third overtone of C–D is located at 1.5 µs and the third overtone of C–F is located at 2.6 µs. Halogenation is preferred for the C-band window (infrared) because the third overtone of the C–D vibration absorbs in it. In addition, fluorination does not modify significantly the energy of the triplet levels, so the resonant transfer to the lanthanide ion is not affected. In the late 1990s, several papers were reported with the improved NIR photoluminescence of several deuterated and fluorinated Nd^{III} β-diketonate complexes in solution.

ANNEXES II

Overview on Anilate Ligands

The Anilic Acids are synthesized starting from 2,5-dihydroxy-1,4-benzoquinone (DHBQ), changing the hydrogen in 3 and 6 position. In **Table 1** are reported some anilic acid derivatives. Molecular formula of Anilic acids can be written as $H_2X_2C_6O_4$ (H_2X_2An) where X indicates the substituent and C_6O_4 anilate skeleton.

Table. 1. Names, molecular Formulas and acronyms of the anilic acid presented in literature.

Substituent	Formula	Anilic Acid Name	Acronyms	Anilate dianion name	Acrinyms	Ref.
H	$H_2C_6O_4$	Hydranilic Acid	H_2H_2An	Hydranilate	H_2An^{2-}	4
Cl	$H_2Cl_2C_6O_4$	Choloranilic Acid	H_2Cl_2An	Chloranilate	Cl_2An^{2-}	5
Br	$H_2Br_2C_6O_4$	Bromanilic Acid	H_2Br_2An	Bromoanilate	Br_2An^{2-}	6
F	$H_2F_2C_6O_4$	Fluoranilic Acid	H_2F_2An	Fluoranilate	F_2An^{2-}	6
NH_2	$H_6N_2C_6O_4$	Aminanilic Acid	$H_2(NH_2)_2An$	Aminanilate	$(NH_2)_2An^{2-}$	7
OH	$H_4C_6O_6$	Hydroxyanilic Acid	$H_2(OH_2)_2An$	Hydroxyanilate	$(OH_2)_2An^2$	7
CN	$H_2N_2C_8O_4$	Cyananilic Acid	$H_2(CN)_2An$	Cyananilic Acid	$(CN)_2An^2$	8
CN/Cl	$H_2ClNC_7O_4$	Chlorocyananilic Acid	$H_2ClCNAn$	Chlorocyananilate	$ClCNAn^2$	9
NO_2	$H_6N_2C_6O_4$	Nitranilic Acid	$H_2(NO_2)_2An$	Nitroanilate	$(NO_2)_2An^{2-}$	4

CH_3	$H_8C_8O_4$	Methylanilic Acid	$H_2(CH_3)_2An$	Methylanilate	$(CH_3)_2An^{2-}$	5
CH_2CH_3	$H_{12}C_{10}O_4$	Ethylanilic Acid	$H_2(CH_3CH_2)_2An$	Ethylanilate	$(CH_3CH_2)_2An^{2-}$	4
C_6H_5	$H_{12}C_{18}O_4$	Phenylanilic Acid	H_2Ph_2An	Phenylanilate	Ph_2An^{2-}	9
C_4H_3S	$H_8C_{14}O_4S_2$	Thiophenyl Anilic Acid	H_2Th_2An	Thiophenyl Anilate	Th_2An^{2-}	10
$C_6H_5O_2S$	$H_8C_{14}O_4S_2$	3,4-ethylene dioxythiophenylic Acid	H_2EDOT_2An	,4-ethylene dioxythiophenylate	$EDOT_2An^{2-}$	10

Anilic Acids **(1)** can undergo a mono and double deprotonation process of the two hydroxyl groups giving rise to the monoanionic **(2)** and dianionic **(3)** forms as reported in **Figure 5.**

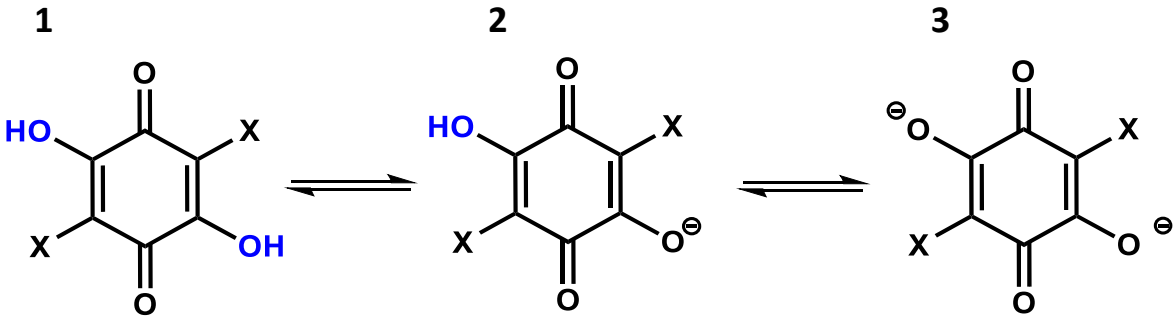

Figure 5. Protonation equilibria for a generic anilic acid

The molecular and crystal structures of the protonated anilic acids are characterized by: (i) a centrosymmetric quasi-quinonoid structure with C=O and C=C distances in the 1.215–1.235 Å and 1.332–1.355 Å ranges, respectively; (ii) a planar structure of the benzoquinone ring; and (iii) moderate-strong H-Bonding and π-stacking interactions in the crystal structure. The molecular and crystal structures of alkali metal salts of some anilic acids have also been reported. The X-ray analysis reveals that the carbon ring system for the anilate in their dianionic form takes the planar conformation but is not in a quinoidal form, having four C–C bonds of equal length (1.404–1.435 Å range) and two considerably longer C–C bonds (1.535–1.551 Å range) whose bond distances vary as a function of the substituents. Moreover, the four C–O bonds are of equal length (1.220–1.248 Å range). This description can be represented with four resonance structures that, in turn, can be combined in one form with delocalized π-electrons along the O–C–C(–X)–C–O bonds (**Figure 6**).

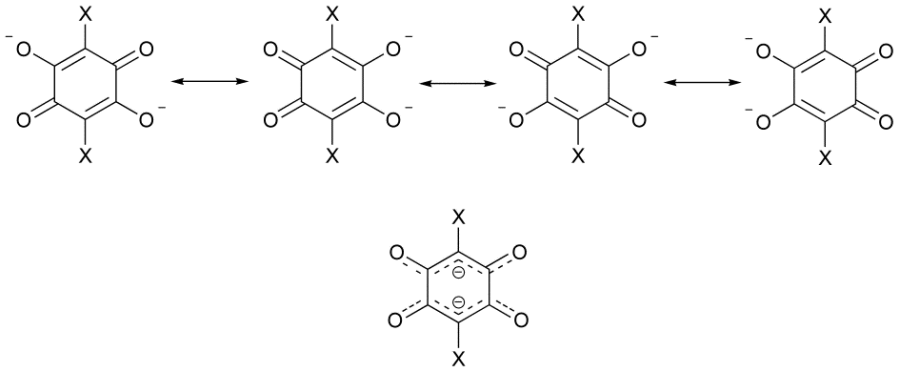

Figure 6. Resonance structure of a generic anilate in the dianionic form

Despite the remarkable similarity in their molecular structure (*vide infra*), the various substituted anilic acids cannot be prepared by a common synthetic procedure. In the following, an overview of the synthetic methods reported in the literature to achieve some anilic acids are reported in **Figure 7.**

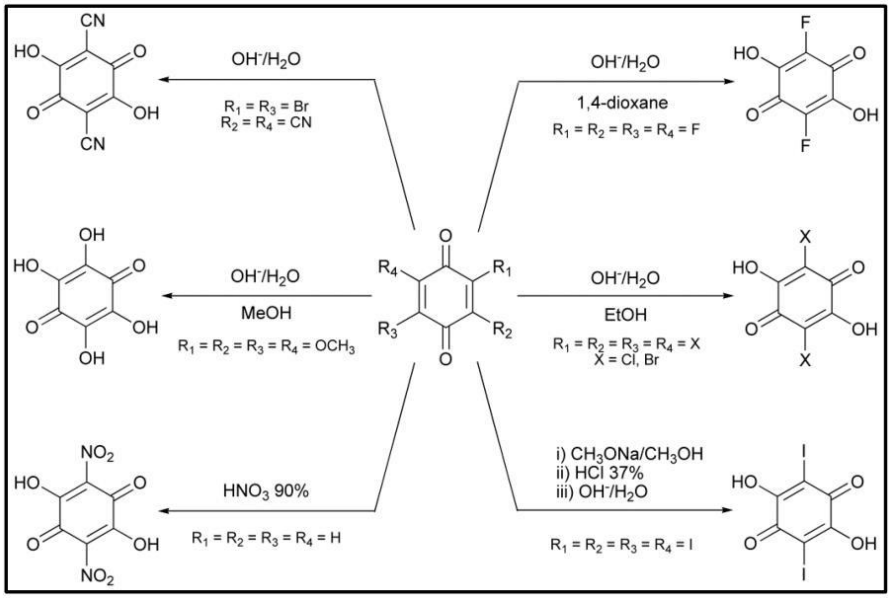

Figure 7. Overview of the synthetic procedures for the preparation of the H_2X_2An (X = F, Cl, Br, I, NO_2, OH, CN) anilic acids.

A simple change of one chloro substituent on the chloranilate ligand with a cyano group affects the electronic properties of the anilate moiety inducing unprecedented luminescence properties in the class of anilate-based ligands and their metal complexes. $ClCNAn^{2-}$ is a unique example of a heterosubstituted anilate ligand, was synthesized by treating 2,3-dicyano- 5,6-dichloro-1,4-benzoquinone with a concentrated water solution of potassium hydroxide, and then acidifying with concentrated hydrochloric acid[11], as shown in **Figure 8**. The dianionic form of this ligand ($ClCNAn^{2-}$) is a green luminophore, with maximum emission band around 550 nm.

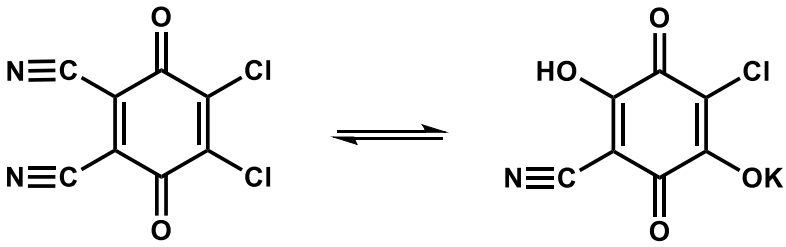

Figure 8. Synthetic procedure for the preparation of KHClCNAn

An overview of the coordination modes shown by the anilate dianions is reported in **Figure 9**. It is noteworthy that among the described coordination modes, I and II are the most common, whereas III, IV and V have been only rarely observed.

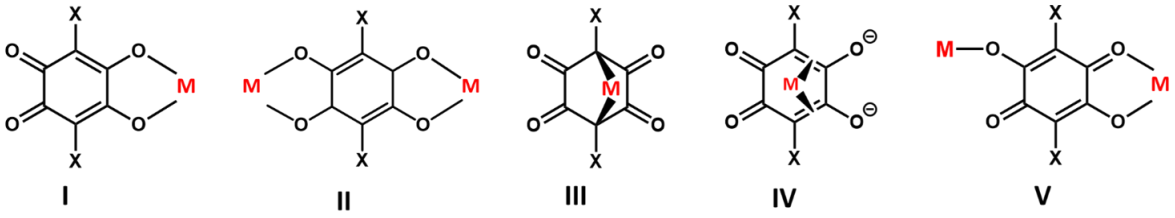

Figure 9. Coordination modes exhibited by the anilate dianions: 1,2-bidentate (I), bis-1,2-bidentate (II), 1,4-bidentate (III), π-bonding (V), 1,2-bidentate/monodentate (V).

When X_2An^{2-} coordinates in the 1,2 bidentate mode (I) exhibits the o-quinone-like form with coordinating C-O bonds that are considerably longer than the uncoordinated C-O

bonds, but when anilate acts as bridging ligand the coordination mode is bis-1,2-bidentate(II). 1,4- bidentate coordination mode (III) is when the ligand coordinates the metal by means of the carbon atoms in 1,4-position showing the bis-carbanion form. It can also coordinate by localized π-electrons in the π-bonding coordination mode (IV). Furthermore, it can act as a bridging ligand but contrary to mode II, one of the two sides coordinates with only one oxygen, in the 1,2-bidentate/monodentate coordination mode (V). This wide range of coordination modes make the anilate ligands very versatile, moreover the presence of different substituents on the benzoquinone ring yield different intermolecular interactions (H- Bonding, Halogen-Bonding, $\pi-\pi$ stacking and dipolar interactions) inside the material. Changing the nature of substituent in 3,6-position is also possible to tune the properties of these materials.

Anilates are interesting building blocks given: (i) their redox properties; (ii) their ability to mediate magnetic superexchange interactions when the ligand coordinates two metals ions in the 1,2-bis-bidentate coordination mode; (iii) the possibility of modulating the strength of this magnetic superexchange interaction by varying the substituents (X) on the 3,6 position of the anilato-ring; moreover the presence of different substituents in the anilato moiety give rise to intermolecular interactions such as H-Bonding, Halogen-Bonding, $\pi-\pi$ stacking and dipolar interactions which may influence the physical properties of the resulting material. These features provide an effective tool for engineering a great variety of new materials.

ANNEXES III

EXFOLIATION METHODS

The development and the study of 2-D materials is a hot topic in material science and nanotechnology since graphene was discovered by Novoselov[12] in 2004, by using adhesive tapes for mechanical exfoliation. Owing to the ultrathin thickness at atomic scale, these materials possess novel properties in many fields, such as carrier concentration, mobility and thermal conductivity. The fabrication of 2-D materials can be performed by two synthetic strategies: top – down exfoliation, [13,14] and bottom -up approach[13,15–17]

The bottom-up approach requires precursors reacting together in their molecular form to synthesize sheets of 2D materials. The top- down exfoliation approach consists of the exfoliation of a bulk layered material to monolayer or few layer 2D sheets. Most commonly used methods for top-down exfoliation are:

1) Micromechanical exfoliation, well known as scotch-tape method (**Figure 10**), is a simple and an efficient way to produce the cleanest, highly crystalline and atomically thin microsheets of a layered material. However, it is difficult to get uniform samples through mechanical exfoliation, as it gives randomly dispersed layers on the substrates.

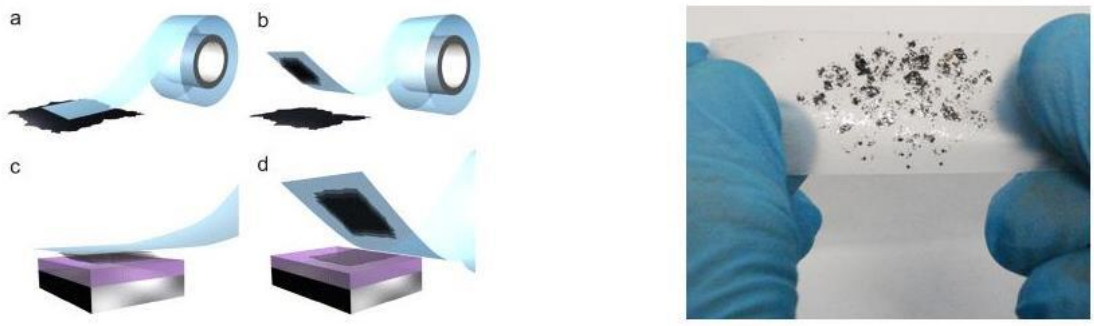

Figure 10. Schematic representation mechanical exfoliation by Scoth-tape

2) Liquid exfoliation includes several synthesis techniques *i.e.* ion intercalation, ion exchange and. Nanosheets are fabricated by soaking the bulk materials into

appropriate solvents and using proper ultrasound. Firstly, ions are intercalated between the layers in a liquid environment, weakening the interlayer interactions. Then, the sonication leads to a dispersion of nanosheets. in the sonication-assisted exfoliation the crucial step is the choice of solvents. A good solvent, i.e. with appropriate surface energy, the exfoliated nanosheets are stabilized against reaggregation. Otherwise, in a bad solvent, reaggregation and sedimentation will occur. Ultrasonication does not allow good control over the size and thickness of flakes; however, the ability to produce large quantities of 2-D materials dispersed in liquid makes it quite useful. Compared with mechanical exfoliation, it has a high yield with rather low cost.

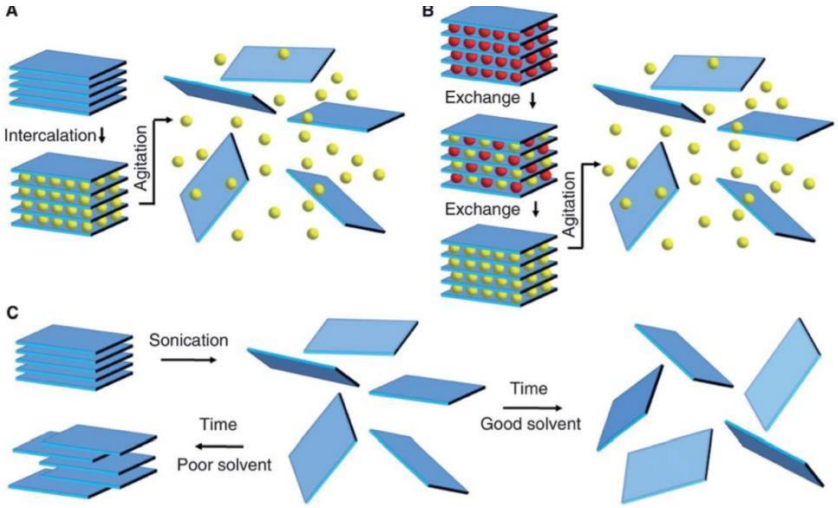

Figure 11. Schematic representation of liquid exfoliation mechanism

2D exfoliated materials can be characterized by using different techniques. The most commonly used tools for determining their morphology and dimensionality are optical microscopy, AFM, TEM, and Raman spectroscopy.

References

1 J. R. Lakowicz, *Principles of fluorescence spectroscopy*, 2006.

2 B. Valeur, *Related Titles from WILEY-VCH Analytical Atomic Spectrometry with*

Flames and Plasmas Handbook of Analytical Techniques Single-Molecule Detection in Solution . Methods and Applications, 2001, vol. 2.

3 M. Y. Berezin and S. Achilefu, *Chem. Rev.*, 2010, **110**, 2641–2684.

4 D. Reactions, T. Synthesis and P. I. Some, 1954, 2183–2186.

5 O. Chlovanil, 1868, 6–14.

6 H. A. Torrey and W. H. Hunter, *J. Am. Chem. Soc.*, 1912, **34**, 702–716.

7 T. Akutagawa and T. Nakamura, *Cryst. Growth Des.*, 2006, **6**, 70–74.

8 M. B. Zaman, J. Toyoda, Y. Morita, S. Nakamura, H. Yamochi, G. Saito, K. Nishimura, N. Yoneyama, T. Enoki and K. Nakasuji, *J. Mater. Chem.*, 2001, **11**, 2212–2216.

9 R. E. Rehwoldt, B. L. Chasen and J. B. Li, *Anal. Chem.*, 1966, **38**, 1018–1019.

10 M. Atzori, F. Pop, T. Cauchy, M. L. Mercuri and N. Avarvari, *Org. Biomol. Chem.*, 2014, **12**, 8752–8763.

11 M. Atzori, F. Artizzu, L. Marchiò, D. Loche, A. Caneschi, A. Serpe, P. Deplano, N. Avarvari and M. L. Mercuri, *Dalt. Trans.*, 2015, **44**, 15786–15802.

12 I. V. G. and A. A. F. K. S. Novoselov, A. K. Geim, S. V. Morozov, D. Jiang, Y. Zhang, S. V. Dubonos, 2016, **306**, 666–669.

13 M. Zhao, Y. Wang, Q. Ma, Y. Huang, X. Zhang, J. Ping, Z. Zhang, Q. Lu, Y. Yu, H. Xu, Y. Zhao and H. Zhang, *Adv. Mater.*, 2015, **27**, 7372–7378.

14 J. M. Tour, *Chem. Mater.*, 2014, **26**, 163–171.

15 A. S. Sarkar and E. Stratakis, *Adv. Sci.*, 2020, **7**, 1–36.

16 L. Yan, S. Gonca, G. Zhu, W. Zhang and X. Chen, *J. Mater. Chem. B*, 2019, **7**, 5583–5601.

17 W. Ma, L. Wang, J. Xue and H. Cui, *RSC Adv.*, 2016, **6**, 85367–85373.